Flow and dynamics of driven and active amorphous materials : a multi-scale modeling approach

Magali Le Goff

Université Grenoble Alpes

THÈSE

Pour obtenir le grade de

DOCTEUR DE L'UNIVERSITE GRENOBLE ALPES

Spécialité : **Physique théorique**

Arrêté ministériel : 25 mai 2016

Présentée par

Magali LE GOFF

Thèse dirigée par **Kirsten MARTENS, Chargée de Recherche (CNRS)** et
codirigée par **Eric BERTIN, Directeur de Recherche (CNRS)**

préparée au sein du **Laboratoire Interdisciplinaire de Physique (UMR 5588)**
dans **l'École Doctorale de Physique**

Écoulement et dynamique de matériaux amorphes forcés et actifs : une approche multi-échelle

Thèse soutenue le **lundi 15 mars 2021**
devant le jury composé de :

Monsieur Jérôme WEISS
Directeur de Recherche CNRS, Laboratoire ISTerre, Université Grenoble Alpes (Président du Jury)

Monsieur Ludovic BERTHIER
Directeur de Recherche CNRS, Laboratoire Charles Coulomb, Université de Montpellier (Rapporteur)

Monsieur Damien VANDEMBROUCQ
Directeur de Recherche CNRS, Laboratoire PMMH, Sorbonne Université (Rapporteur)

Madame Hélène DELANOË-AYARI
Maître de conférence HDR, Institut Lumière Matière, Université Lyon 1 (Examinatrice)

Monsieur Martin LENZ
Directeur de Recherche CNRS, Laboratoires LPTMS et PMMH, Université Paris-Saclay et Sorbonne Université (Examinateur)

Monsieur Sébastien MANNEVILLE
Professeur à l'École Normale Supérieure de Lyon (Examinateur)

"*Ce n'est pas tant la nature qui m'intéresse que les forces de la nature.* "

Paul Cézanne

Abstract

Flow and dynamics of driven and active amorphous materials: a multi-scale modeling approach

by Magali Le Goff

Soft glassy materials below their glass transition and far beyond jamming (at low temperature and high density) exhibit divergent relaxation timescales and behave essentially as solids in the absence of driving or biological activity. In this thesis, we investigate the dynamics, rheology and large scale organization of various types of athermally driven soft amorphous materials resulting either from an externally imposed driving (shear or vibration), from a local activity, or both. The main questions behind the different projects constituting this thesis are: how do distinct sources of mechanical noise affect the fluidization and large scale organization of soft amorphous materials and how do we account for them in coarse-grained descriptions? To this aim, we use a multi-scale modeling approach, from microscopic simulations to continuum modeling, with a main focus on mesoscale elasto-plastic models.

The first topic of this thesis concerns shear localization in the flow of soft amorphous materials. We first consider the case of inertial dynamics at the microscopic scale as a rate-weakening mechanism and show, using a continuum model, that permanent shear bands observed in particle-based simulations can be explained in terms of softening due to kinetic heating of the system under shear, with a shear rate-dependent kinetic temperature.

In a second part, we study how permanent shear bands are affected by an external source of noise leading to the random activation of plastic rearrangements. We show, using a mesoscale elasto-plastic model with two different models of noise, that an increasing external noise leads to vanishing shear bands, and that the transition from heterogeneous to homogeneous flow can be interpreted as a nonequilibrium critical point. Our findings suggest that the critical exponents associated with this transition do not depend on the details of the activation dynamics for the noise, and are also consistent with recent experimental results on vibrated granular media.

Fluidization by a rate-independent noise is an ubiquitous phenomenon, observed not only in vibrated granular media, but also in active or biological systems, where the noise is of active origin. In a third part, we study how active sources of noise resulting from the active deformation of particles can induce a fluidization of the system. Using inputs from microscopic simulations, we build a tensorial mesoscale elasto-plastic model for the dynamics of actively deforming particles. Our first results suggest that this active elasto-plastic model exhibits a fluidization transition similar to the one reported in particle-based simulations and also shares similarities with inert amorphous systems driven with an oscillatory shear protocol.

In a last part, motivated by experiments in the lab, we study the emergence of collective oscillations of the cell velocity in a model of confined epithelial tissue. We consider a Voronoi-based model of epithelium and find that a feedback mechanism between the cell self-propulsion direction and velocity is required to observe oscillations, and that the type of oscillation observed depends upon the confinement length as reported in experiments.

Écoulement et dynamique de matériaux amorphes forcés et actifs : modélisation multi-échelle

Les matériaux amorphes loin de leur transition vitreuse et de blocage (basse température et haute densité) relaxent sur des échelles de temps inaccessibles expérimentalement et, en l'absence de forçage, ont essentiellement un comportement de solide élastique. Dans cette thèse, nous étudions la dynamique, la rhéologie et l'organisation à grande échelle de différents systèmes vitreux "mous" soumis à un forçage soit externe (cisaillement ou vibration) soit résultant d'une activité (biologique) locale. La principale question scientifique à l'origine de ce travail peut être formulée ainsi : "Comment des sources distinctes de bruit mécanique peuvent-elles affecter la fluidisation et l'organisation à grande échelle de matériaux amorphes et comment peut-on décrire ces effets à l'échelle mésoscopique ?" Nous abordons cette question en employant une approche de modélisation multi-échelle, allant de simulations de particules à des modèles continus en se concentrant particulièrement sur les modèles élasto-plastiques à l'échelle mésoscopique.

Le premier thème abordé dans cette thèse concerne l'écoulement hétérogène de matériaux amorphes, sous la forme de bandes de cisaillements. Nous considérons tout d'abord le cas d'un mécanisme d'auto-fluidisation induit par une dynamique inertielle et proposons un modèle continu basé sur une description de l'inertie en terme de température cinétique. Nous montrons que ce modèle décrit l'émergence de bandes de cisaillement telles qu'observées dans des simulations de particules.

Dans une deuxième partie, nous étudions comment une source de bruit externe à l'origine de l'activation d'évènements plastiques (sous la forme de vibrations par exemple) affecte un tel écoulement hétérogène. Nous montrons, à l'aide d'un modèle élasto-plastique sur réseau, qu'augmenter le bruit externe conduit à une disparition des bandes de cisaillement et que cette transition entre un écoulement hétérogène et un écoulement homogène peut s'interpréter comme un point critique hors équilibre. Nos résultats suggèrent par ailleurs que les exposant critiques sont indépendants du détail de la dynamique d'activation du bruit et compatibles avec des expériences récentes sur des granulaires cisaillés et vibrés.

La fluidisation de fluides à seuil par des sources de bruit indépendantes de l'écoulement peut être observée dans divers contextes, comme par exemple dans des systèmes actifs ou biologiques. Dans une troisième partie, nous étudions comment une source de bruit d'origine active, résultant de la déformation active de particules, peut induire la fluidisation d'un matériau amorphe. En se basant sur un modèle microscopique de particules dont le rayon oscille au cours du temps, nous construisons un modèle élasto-plastique tensoriel actif. Nos premiers résultats montrent que ce modèle présente une transition de fluidisation similaire à celle observée dans les simulations microscopiques, analogue à la transition vers l'écoulement rapportée dans les travaux de cisaillement oscillatoire des systèmes amorphes inertes.

Dans une dernière partie, nous présentons un travail réalisé en collaboration avec des expérimentateurs du LIPhy sur l'émergence de dynamique oscillatoire dans la migration collective de cellules dans un tissu épithélial confiné. A l'aide d'un modèle de type Voronoi, nous montrons qu'un mécanisme de rétroaction entre la direction de l'auto-propulsion des cellules et de leur vitesse est nécessaire pour observer des oscillations, et que le type d'oscillations observé dépend de la longueur du confinement, tel qu'observé dans les expériences.

Contents

List of Figures

List of Tables

Chapter 1

Introduction and context

Résumé : Introduction et contexte de la thèse

Les systèmes denses désordonnés constituent une large classe de matériaux, allant des verres, aux suspensions granulaires denses jusqu'aux tissus biologiques.

Les verres traditionnels sont généralement obtenus par trempe d'un liquide en dessous de sa température de transition vitreuse T_g, en évitant la cristallisation. Lorsque la température du liquide est abaissée, la viscosité du liquide dit "surfondu" augmente, jusqu'à atteindre des valeurs tellement grandes que le système semble solide aux échelles de temps accessibles expérimentalement. En d'autres termes, le système relaxe sur des échelles de temps beaucoup plus grandes que la durée typique d'une expérience. Cette transition entre un état "fluide" et un état apparemment "solide" est appelée transition vitreuse, et se produit à une température T_g, définie empiriquement.

La physique des systèmes vitreux couvre cependant un champ plus large que celui des liquides surfondus. Un système est dit "vitreux" si son temps de relaxation typique est grand devant la durée typique d'une expérience ou d'une simulation numérique. Avec cette définition, de nombreux systèmes tombent dans la catégorie des systèmes vitreux, comme le montre la Fig. 1.1. Il y a bien sûr d'une part les verres d'oxydes, les verres métalliques ou les verres de polymères, constitués de particules de taille variant entre 0.1 et 10 nanomètres environ. Ces matériaux ont un module élastique de l'ordre du GigaPascal, et auront tendance à se fracturer lorsque soumis à un forçage mécanique suffisamment important. Il existe d'autre part des systèmes vitreux "mous" tels que les mousses ou les émulsions. Ces systèmes sont composés de bulles ou gouttelettes de taille allant du micromètre au millimètre, et leur module élastique est beaucoup plus faible que celui des verres durs (de l'ordre de quelques centaines de Pascal). Lorsque ces matériaux sont déformés, ils auront tendance à s'écouler comme un fluide si la contrainte appliquée est supérieure à une contrainte seuil. Ces "fluides à seuil" constituent eux-mêmes une large classe de matériaux, puisqu'ils incluent, outre ces deux exemples, les suspensions denses (colloïdales ou granulaires), les milieux granulaires secs, ou, comme proposé plus récemment, les tissus biologiques (Preziosi et al., 2010; Matoz-Fernandez et al., 2017a; Popovic et al., 2020).

Tous les systèmes denses désordonnés partagent un certain nombre de propriétés communes. Ils exhibent à la fois des propriétés solides et des propriétés fluides. L'encombrement stérique lié à la grande densité de particules en interaction (qui peuvent être des atomes, des grains, des cellules) limite le mouvement de ces particules, et les mécanismes de relaxation résultants sont non triviaux. Par ailleurs, comme la phase vitreuse (solide) ne correspond pas à un minimum d'énergie libre du système, le système continue d'évoluer très lentement au cours du temps, donnant lieu à des propriétés dites de "vieillissement". D'autres propriétés physiques remarquables des verres peuvent être citées, comme par exemple le fluage, la réponse non linéaire, le "rajeunissement", etc.

Lorsque la taille des particules est suffisamment grande pour que les fluctuations thermiques soient négligeables, on parle de système "athermique". Il faut alors appliquer un forçage pour observer une dynamique dans de tels systèmes. Dans cette thèse, nous nous intéressons à deux classes de systèmes denses désordonnés athermiques : les systèmes forcés et les systèmes actifs. Alors que dans les systèmes forcés (soumis à un cisaillement par exemple), l'injection d'énergie se fait à l'échelle macroscopique à travers les parois, l'énergie est convertie localement dans les systèmes actifs. En d'autres termes, un système actif est constitué de particules capables de prélever de l'énergie (sous forme chimique par exemple) dans leur environnement afin de réaliser des processus actifs, comme par exemple se déplacer ou se diviser.

Plusieurs analogies ont été proposées dans la littérature entre les systèmes denses thermiques ou forcés et les systèmes actifs. En particulier, l'étude de la transition solide-liquide dans des systèmes de particules actives (essentiellement auto-propulsées) et les analogies possibles avec la transition vitreuse à l'équilibre ont suscité un intérêt grandissant au cours de cette dernière décennie (Berthier et al., 2019; Janssen, 2019). De façon plus générale, on peut se demander comment décrire l'activité biologique de façon effective, en supposant celle-ci comme étant à l'origine de sources de bruit additionnelles dans la dynamique de solides désordonnés. Des questions émergent alors sur les caractéristiques de ce bruit : ressemble-t-il à un bruit thermique, et pour quels types de dynamique active ? Et de façon encore plus générale : quel est le rôle de sources de bruit additionnelles dans la dynamique de solides désordonnés ? Quel seront les conséquences sur la rhéologie et l'organisation de l'écoulement ?

C'est autour de ces questions que s'organise le travail présenté dans cette thèse. La thèse est constituée de chapitres relativement indépendants, et abordant différents aspects de la dynamique des solides amorphes forcés et actifs. Nous focalisons notre étude sur les systèmes athermiques et le rôle de sources de bruit additionnelles dans leur dynamique et leur rhéologie (bruit résultant de la dynamique microscopique ou d'origine externe). La modélisation de ces mécanismes sera abordée à différentes échelles de description, dans le but d'établir un lien entre les modèles microscopiques et des approches plus phénoménologiques à l'échelle macroscopique ou mésoscopique. Nous abordons en particulier les aspects suivants:

- **Quelles sont les conséquences de mécanismes d'autofluidisation (liés à une source de bruit endogène) sur l'organisation de l'écoulement ?** Nous nous intéressons en particulier (dans le Chapitre 3) au cas où une dynamique inertielle est responsable d'une instabilité de l'écoulement homogène et de la formation de bandes de cisaillement (tel qu'observé dans des simulations microscopiques à température nulle), et proposons une description continue à l'aide d'un champ de température cinétique décrivant le "bruit" généré par la dynamique inertielle.

- **Quelles conséquences pour l'écoulement lors de la compétition de mécanismes d'autofluidisation (bruit endogène) et d'une fluidisation par un bruit externe ?** Dans le Chapitre 4, nous montrons, dans le cadre d'un modèle élasto-plastique à l'échelle mésoscopique, que la compétition de ces deux mécanismes peut conduire à l'émergence d'un point critique, tel qu'observé dans des expériences de granulaires cisaillés et vibrés par Wortel et al. (2016).

- **Les modèles élasto-plastiques, décrivant de nombreux aspects de la rhéologie des fluides à seuil cisaillés, peuvent-il être étendus pour décrire des systèmes denses actifs où le forçage serait alors local?** Dans le Chapitre 5, nous proposons un modèle élasto-plastique décrivant une

assemblée dense de particules dont la dynamique résulte d'oscillations du volume des particules et étudions la transition solide-fluide induite par l'amplitude des oscillations.

Les différentes questions soulevées ci-dessus nécessitent d'introduire une partie de l'état de l'art concernant la physique des systèmes denses forcés et actifs ainsi que certaines approches de modélisation. L'objectif du Chapitre 1 est d'introduire d'une part la phénoménologie des systèmes denses, en particulier la rhéologie des systèmes désordonnés athermiques, d'autre part la phénoménologie des systèmes denses actifs, et enfin, les approches de modélisation à différentes échelles de description. Le cas de la modélisation élasto-plastique à l'échelle mésoscopique sera brièvement introduit, mais sera abordé plus en détail dans le Chapitre 2, qui lui est dédié. Un résumé en français des trois grandes parties du Chapitre 1 est donné ci dessous.

Rhéologie des systèmes désordonnés athermiques

La rhéologie de systèmes désordonnés athermiques constitue un domaine de recherche actif. Ces systèmes ont ceci de remarquable qu'ils présentent un comportement de solide élastique au repos ou lorsqu'une faible contrainte est appliquée, et s'écoulent comme des fluides (écoulement plastique sous la forme de réarrangements localisés de particules) lorsque la contrainte appliquée Σ dépasse une contrainte seuil Σ_y. On parle alors de "fluide à seuil".

Une direction de recherche importante consiste à étudier la transition de mise en écoulement (*yielding* en anglais), soit (i) en imposant une déformation à un matériau initialement au repos et en étudiant la dynamique (transitoire) lorsque celui-ci commence à s'écouler, soit (ii) en imposant un écoulement stationnaire à petit taux de déformation ($\dot{\gamma} \to 0$) et en étudiant la dynamique de la relaxation dans le système. Dans le cas (i), la transition vers l'écoulement peut dans certains cas être discontinue et associée à un écoulement hétérogène (par bandes) de façon transitoire. La phase de déformation élastique pouvant fortement dépendre de l'état inital du matériau, des études récentes basées sur un protocole de cisaillement oscillatoire ont permis d'étudier plus en détail les mécanismes microscopiques en jeu lors de la transition vers l'écoulement. Dans le cas (ii), de nombreuses études indiquent un écoulement intermittent à faible taux de cisaillement, au cours duquel des phases de "chargement élastique" alternent avec des phases de relaxation plastique brutales dans le matériau. Ces avalanches de plasticité ont été étudiées dans le contexte des transitions de phase hors équilibre comme associée à l'existence d'un point critique, au voisinage duquel le taux de cisaillement $\dot{\gamma}$ évolue comme $\dot{\gamma} \sim (\Sigma - \Sigma_y)^{1/n}$ (reformulation de la loi rhéologique de Herschel-Bulkley).

Le régime d'écoulement stationnaire à taux de cisaillement $\dot{\gamma}$ fini présente aussi une phénoménologie riche. Alors que dans le cas de fluides à seuil "simples", l'écoulement stationnaire est homogène, il peut, dans les cas où il existe un mécanisme "d'auto-fluidisation", être hétérogène. On parle dans ce cas de bandes de cisaillement permanentes, qui peuvent s'expliquer par des effets de couplage entre l'écoulement et la microstructure (thixotropie) ou la concentration locale du matériau. Des approches théoriques consistant à coupler l'écoulement (décrit par des champs de contrainte et de vitesse) avec un champ auxiliaire décrivant la structure ou la concentration du système ont permis de prédire l'existence de bandes de cisaillement dans ces systèmes. Dans le cas de systèmes désordonnés qui ne présentent pas d'évolution de structure ou de concentration particulière sous écoulement (typiquement le cas pour des systèmes de particules molles répulsives), il n'existe pas de consensus sur l'origine des

bandes de cisaillement. Plusieurs scénarios ont été proposés pour expliquer l'autofluidisation dans ces systèmes, comme par exemple l'existence d'une échelle de temps microscopique liée à la restructuration du système après une déformation plastique locale (Coussot et al., 2010). Une dynamique inertielle peut également entraîner une fluidisation du système, par des effets cinétiques (Nicolas et al., 2016). Cette autofluidisation est d'ailleurs associée à des bandes de cisaillement permanentes, tel que le montrent des travaux récents menés dans le groupe à Grenoble. Le premier chapitre de résultats de cette thèse consistera à proposer un modèle effectif couplant les équations pour l'écoulement à des équations décrivant l'évolution d'une "température cinétique", résultant d'une dynamique sous-amortie, afin de décrire les bandes de cisaillement permanentes observées dans des simulations de particules inertielles.

Cet écoulement hétérogène, par bandes, est parfois interprété dans la littérature comme un scénario de séparation de phase associé à une transition du premier ordre dans le contexte des transitions de phases hors équilibre. Par analogie avec un scénario d'équilibre, on peut imaginer que, en variant un paramètre décrivant une forme de bruit dans le système (analogue à la température), ce régime de séparation de phase puisse se terminer par un point critique. C'est en effet ce qui a été suggéré récemment par des expériences sur des milieux granulaires cisaillés et soumis à des vibrations verticales (Wortel et al., 2016). Alors que la rhéologie en l'absence de vibration présente un comportement de fluide à seuil avec un régime d'autofluidisation (évolution non monotone de la contrainte en fonction du taux de cisaillement), les vibrations induisent une fluidisation à faible contrainte, et, sous l'effet de grandes amplitudes de vibrations, la rhéologie devient monotone. La transition entre une rhéologie non monotone et une rhéologie monotone est associée à des fluctuations géantes du taux de cisaillement, évoquant une dynamique critique à la transition. Les approches de modélisation macroscopiques telles qu'utilisées dans le Chapitre 3 ne permettent toutefois pas de décrire les fluctuations dans la dynamique des systèmes denses désordonnés. Les modèles élasto-plastiques (EP) sur réseau, intermédiaires entre une description microscopique à l'échelle des particules et une description macroscopique, permettent une description à grande échelle de la dynamique et des fluctuations des fluides à seuil. Dans le Chapitre 4, nous étendons un modèle EP décrivant un fluide à seuil avec un régime d'autofluidisation de façon à introduire un bruit externe dans la dynamique. Nous montrons alors qu'un bruit externe, sous la forme d'activation de réarrangements plastiques localisés, est capable de fluidiser le système à faible contrainte, et qu'un point critique émerge pour une amplitude de bruit critique. Dans les modèles considérés, le bruit mécanique additionnel est générique, et son origine n'est pas spécifiée. Ce bruit pourrait résulter de vibrations mécaniques (comme dans les granulaires), d'évènements locaux comme la coalescence dans les mousses par exemple, ou encore d'une activité biologique locale.

Quel lien peut être établi entre la dynamique de fluides à seuil en présence de sources de bruit additionnelles et la dynamique de systèmes actifs denses, où l'activité locale est elle-même source de bruit mécanique? Pour comprendre quelles analogies peuvent être établies, il convient d'abord de résumer la phénoménologie des systèmes actifs denses tels que les tissus biologiques.

Dynamique des systèmes actifs denses

Les systèmes actifs denses ou vitreux ont suscité un intérêt grandissant ces dernières années, comme en témoignent les revues récentes sur le sujet (Berthier et al., 2019; Janssen, 2019). Plusieurs exemples de systèmes, d'origine synthétique et biologique, seront donnés dans le corps du chapitre d'introduction, et nous n'évoquerons ici que

certains aspects de la dynamique des tissus biologiques, exemple emblématique de système actif dense.

Les tissus biologiques sont constitués d'une assemblée de cellules, objets déformables pouvant réaliser différents types de processus actifs tels que contraction, auto-propulsion, croissance, division ou mort cellulaire. Les propriétés mécaniques des tissus épithéliaux, constitués d'une monocouche de cellules jointives, sont particulièrement étudiées dans le domaine de la biophysique, d'une part puisqu'elles jouent un rôle important dans le développement embryonnaire, et d'autre part parce que la dynamique de ces tissus présente certaines similarités avec celle des verres. Suivant les conditions expérimentales (densité de cellules, tissu sain ou pathologique, etc.), des états "fluides" ou "solides" du tissu ont été décrits, associés à la présence ou non de réarrangements de cellules (autrement dit, d'échanges de voisins ou intercalations).

L'étude des transitions solide-liquide dans les systèmes actifs a même dépassé le cadre de la biophysique, puisque celles-ci constituent des exemples de transitions de phase dans des systèmes hors équilibre. Plusieurs analogies ont été proposées dans la littérature entre les transitions solide-liquide dans les systèmes actifs et les systèmes denses thermiques ou forcés. Dans le cas des systèmes de particules auto-propulsées par exemple, qui constituent l'un des systèmes actifs les plus étudiés, la transition entre un état solide et un état fluide (en augmentant la force d'autopropulsion) est analogue à une transition vitreuse d'équilibre dans un système thermique si le temps de corrélation de la direction de propulsion est suffisamment faible (Berthier et al., 2019). Des déviations au cas d'équilibre sont cependant observées lorsque le temps de persistence de la direction de propulsion augmente, et il n'existe pas d'analogie simple dans ce régime. La dynamique observée à la transition dans la limite des longs temps de persistance semble, elle, être analogue à la transition de "mise en écoulement" (*yielding*) dans les systèmes amorphes athermiques soumis à un cisaillement (Mandal et al., 2020a). Cet exemple montre qu'il n'existe pas de scénario simple (et générique) pour décrire les transitions solide-fluide dans les systèmes actifs, et que les analogies possibles avec des systèmes non actifs peuvent différer fortement suivant la région du diagramme de phase explorée.

Outre les aspects de fluidisation, de nombreuses études portent sur l'émergence de mouvements collectifs dans les systèmes denses de particules auto-propulsées, souvent en lien avec la dynamique collective des cellules observée dans les tissus (Alert et al., 2019). Dans le Chapitre 6, nous étudions l'émergence de mouvement collectif de cellules sous la forme d'oscillations de vitesse dans un modèle microscopique de tissu (de type Voronoi).

Même si l'autopropulsion constitue le type d'activité le plus étudié, on peut citer d'autres systèmes actifs fluidisés sous l'effet d'une activité locale. Les systèmes constitués de particules pouvant se diviser ou mourir par exemple, modèles simples de tissus biologiques, présentent un comportement de fluide viscoélastique, dont le temps de relaxation est fixé par le taux de mort ou de division. Cet effet peut être compris au niveau champ moyen dans un modèle mésoscopique conçu initialement pour la rhéologie de fluides à seuil, en considérant une source supplémentaire de bruit mécanique, indépendant de l'écoulement, tel que montré par Matoz-Fernandez et al. (2017a). Les courbes d'écoulement obtenues dans ce cas sont d'ailleurs semblables à celles obtenues pour des milieux granulaires soumis à un cisaillement et à des vibrations, suggérant une analogie possible entre les deux systèmes.

Enfin, un autre type de système actif, constitué de particules dont le volume peut fluctuer au cours du temps, a été utilisé pour modéliser la dynamique de tissus biologiques (dont le volume des cellules fluctue) ainsi que des changements de conformation de protéines dans le cytoplasme de bactéries (Tjhung et al., 2017; Oyama

et al., 2019). Ce modèle présente une transition de fluidisation lorsque l'amplitude des fluctuations de volume est variée, et la nature de cette transition dépend de la dynamique temporelle du changement de volume. Lorsque le volume des particules évolue périodiquement, la transition est discontinue, analogue à une transition de mise en écoulement telle qu'observée dans des systèmes amorphes soumis à un cisaillement oscillatoire. Lorsque le volume évolue suivant un processus stochastique corrélé en temps (bruit coloré), la transition est continue, et analogue au cas des particules auto-propulsées. Afin de tester ces analogies, nous proposons, dans le Chapitre 5, un modèle élasto-plastique à l'échelle mésoscopique décrivant le même type de dynamique active, où le forçage résulte de la déformation active de particules. Nous montrons qu'il existe bien une transition solide-fluide dans ce modèle lorsque l'amplitude des oscillations augmente, et que cette transition partage des caractéristiques communes avec la transition de mise en écoulement observée dans un protocole de cisaillement oscillatoire.

Pour résumer ces deux parties, le lien entre les échelles de description microscopiques et macroscopiques commence à être bien compris dans le cas des solides amorphes cisaillés grâce, entre autres, au développement de modèles mésoscopiques. Ce lien est cependant moins clair dans le cas des systèmes actifs. Plusieurs approches de modélisation existent et nous en présentons quelques unes dans la dernière partie. Dans cette thèse, en nous basant sur les diverses analogies proposées dans la littérature entre systèmes forcés et systèmes actifs, nous explorons la voie des modèles mésoscopiques élasto-plastiques actifs.

Approches de modélisation pour les systèmes denses forcés et actifs

La modélisation des systèmes présentés préalablement peut s'envisager à différentes échelles de description.

Les simulations numériques de modèles microscopiques, ou "expériences numériques" sont largement utilisées pour étudier les systèmes denses désordonnés puisqu'elles permettent un contrôle précis des paramètres d'intérêt et donnent accès à des informations sur la structure et les trajectoires résolues à l'échelle des particules. Suivant le but visé, ces simulations peuvent soit employer des modèles réalistes d'interaction (si le but est de reproduire le comportement d'un matériau en particulier), soit utiliser des modèles d'interaction simples (Lennard-Jones par exemple) afin d'identifier des propriétés génériques des matériaux amorphes denses. Ce type d'approche présente l'avantage de donner accès à un grand nombre d'observables, qui permettent de guider la construction de modèles théoriques à plus grande échelle, comme des modèles sur réseau ou des théories continues.

En particulier, les études mettant en évidence un scénario générique pour la déformation plastique des solides désordonnés ont conduit à l'émergence de modèles mésoscopiques sur réseau, permettant de s'affranchir d'une description détaillée à l'échelle des particules. Dans ces modèles élasto-plastiques, un matériau est modélisé comme une collection de blocs mésoscopiques dont la taille correspond à la taille typique d'un groupe de particules subissant un réarrangement plastique. Le nombre de particules impliquées dans un tel réarrangement dépend en réalité du système considéré (de quatre bulles dans une mousse bidimensionnelle, à quelques dizaines d'atomes dans un verre de silice par exemple), mais l'échelle mésoscopique considérée permet de s'affranchir de ces différences et de se focaliser sur la physique à grande échelle de ces systèmes. L'élasticité joue un rôle essentiel dans ces systèmes, et donne lieu à des interactions entre les blocs mésoscopiques distants. Lorsqu'un bloc se déforme de façon plastique (i.e. lorsqu'il y a un réarrangement localisé de particules), alors il y a

localement relaxation de la contrainte, et redistribution aux autres sites du système via un propagateur élastique. Il existe plusieurs façons de traiter ces interactions, qui seront présentées dans le corps du chapitre.

Outre les approches microscopiques et mésoscopiques, les approches de modélisation à l'échelle macroscopique (ou modèles continus) consistent à décrire l'état d'un système par des champs de contrainte, de déformation, et éventuellement des champs auxiliaires décrivant par exemple la structure ou une température effective dans le système.

Ces trois types d'approche de modélisation sont employées de façon complémentaire pour aborder les questions de cette thèse, même si les principaux développements sont réalisés en utilisant des modèles mésoscopiques. Dans le Chapitre 3, des observations faites dans des simulations de particules (par V.Vasisht, alors post-doctorant dans le groupe) ont motivé le développement d'un modèle continu qui est ensuite étudié analytiquement et numériquement, et dont les résultats peuvent être comparés aux simulations microscopiques. Dans le Chapitre 4, nous étudions le rôle d'une source de bruit additionnelle dans la rhéologie de solides amorphes en introduisant un nouveau mécanisme d'activation d'évènements plastiques dans un modèle élasto-plastique à l'échelle mésoscopique. Dans le Chapitre 5, nous proposons de construire un modèle élasto-plastique pour les systèmes denses actifs, basé sur l'étude d'un modèle de particules actives introduit par Tjhung et al. (2017). Enfin, dans le Chapitre 6, l'étude de mouvements collectifs dans des tissus épithéliaux est basée sur un modèle microscopique de tissu biologique (de type modèle de Voronoi actif) que nous comparons à des expériences réalisées au laboratoire.

Introduction

Let us consider a dense assembly of units, which can be molecules, colloids, droplets, cells, grains or even macroscopic units like robots, animals, individuals, etc. For small densities, these units can easily move, and their motion is enabled by thermal fluctuations if particles are small enough, or chemical reactions, internal motors, etc. We will refer to these systems as being in a "fluid"-like state. As the density is increased, particles are prevented to move over large distances. The competition between particle crowding and energy injection will result in a transition from a fluid to a dynamically arrested state, where the particles are caged by their neighbors and their motion is limited to small "in-cage" displacements. We will refer to these systems as being in an arrested "solid"-like state. For systems made of identical particles in thermal equilibrium, such an increase in density can lead to crystallization. For other systems where the particle size is distributed for instance, the arrested state will more likely be disordered, and we get what is called an "amorphous solid". The transition between an equilibrium fluid and an arrested disordered state is called the glass transition.

The behavior of amorphous solids below the glass transition may depend upon the nature of their constituents. When the elementary units are large enough to neglect Brownian motion (micron-sized particles or larger), the materials are said to be athermal. This the case of dry granular packings, dense granular suspensions, foams, emulsions, or dense assemblies of biological cells, and this is the class of materials we will be considering in this thesis. For these systems, a driving force is required to activate their dynamics and induce configurational changes.[1]

A drive can be applied externally by imposing a shear deformation or stress to the material for instance. In these driven systems, energy is injected at the macroscopic scale through the boundaries. On the other hand, active forces (of biological origin for instance) acting at the particle scale can also induce a dynamics. "Active particles" generally refer to particles with the ability to consume energy (taken from their environment) in order to perform directed active motion or other types of active processes such as deformation, division, etc. With this definition, biological cells can for instance be seen as active particles. Although it can seem that a sheared granular suspension and a living biological tissue have little in common, several recent studies highlight possible analogies between driven and active dense disordered systems (Bi et al., 2014; Tjhung et al., 2017; Tjhung et al., 2020; Mandal et al., 2020a; Henkes et al., 2020; Morse et al., 2020).

In driven systems, even though the driving is homogeneous and continuous, the response of the system to shear can be localized and intermittent, due to the interplay of disorder and elasticity. The role of the mechanical noise arising in such systems is central and many efforts have been made to describe it theoretically (Nicolas et al., 2018a). Additional sources of mechanical noise can also affect the dynamics of amorphous systems, originating either from external perturbations (e.g., mechanical vibrations) or from internal processes (e.g., coarsening in foams or biological activity).

A general question motivating this thesis is: how do distinct sources of mechanical noise affect the fluidization and the organization of the flow of soft amorphous materials?

[1] The classification of thermal vs athermal systems may depend upon the question and protocol used in a particular study. For instance, while thermal fluctuations are not sufficient to activate particle rearrangements in dry granular media, the temperature is known to play an important role in granular dynamics through dilation effects or by affecting the properties of frictional contacts (Divoux et al., 2008; Géminard et al., 2010).

Why studying dense active systems?

There have been increasing evidences that some of the phenomena observed in biological systems can be understood in the framework of the physics of dense systems (such as jamming or glassy physics). For instance, it has been recently observed that the compaction dynamics during the self-assembly of progenitor cell aggregates behaves similarly as relaxing granular piles (Smeets et al., 2019). Other examples include bacterial colonies undergoing self-driven jamming (Delarue et al., 2016), or glassy dynamics observed in biological tissues (Angelini et al., 2011; Schoetz et al., 2013) or in the cytoplasm of cells (Nishizawa et al., 2017).

Glass-like transitions in living tissues, and more generally the origin of the mechanical properties of tissues (solid- or fluid-like states), have attracted an increasing interest in the past decade since they are thought to play an important role in biological processes such as embryonic development, wound healing, or cancer progression (Park et al., 2016; Oswald et al., 2017). For example, the fluid- or solid-like behavior of tissues can influence the spreading of malignant tumors (Streitberger et al., 2020). Understanding the mechanisms driving the fluid-to-solid transitions in biological tissues thus remains an important challenge. More generally, understanding how emergent material properties and tissue rheology are determined by single-cell properties such as the nature of interactions or the forces exerted at the local scale has now become an important goal in the field.

What will be this thesis about?

In this thesis, we will question how small changes in the microscopic dynamics affect the large scale properties of athermal dense disordered systems. In particular, we will focus on how distinct sources of mechanical noise affect the fluidization and the organization of the flow of soft amorphous materials, which will be the main focus of chapters 3, 4 and 5. The possible analogies between the description of active biological systems and athermally driven systems will be mainly discussed in Chapter 5.

In Chapter 3, motivated by molecular simulations of sheared underdamped disordered particle systems exhibiting shear localization, we study how a flow instability induced by inertia can be described at the continuum level by introducing a kinetic temperature field. In Chapter 4, we study the effect of an additional source of noise on the rheology in terms of new activated plastic events in the dynamics within a mesoscale elasto-plastic model, and the emergence of critical dynamics for systems exhibiting a shear banding instability. In Chapter 5, we consider another type of mechanical noise, arising due to the perturbation of stress and strain fields by actively deforming particles. Inspired by the work of Tjhung et al. (2017), we build a mesoscale model to study the solid-to-fluid transition induced by activity and we present the first preliminary results obtained with this model. The work presented in Chapter 6 was motivated by experiments in LIPhy and concerns a slightly different topic than the rest of the thesis. It concerns the emergence of collective velocity oscillations in a model of confined epithelial monolayer.

The different projects of this thesis cover a wide range of topics at the interface between the physics of driven and active dense disordered systems, from flow localization in yield stress fluids to the emergence of collective migration modes in models of biological tissues. Modeling approaches at various scales are used, from particle-based simulations to continuum modeling approaches, with a main focus on mesoscale elasto-plastic modeling.

Organization of the chapter

In this chapter, we present the context, both phenomenological (sections 1.1, 1.2, 1.3) and methodological (section 1.4), that motivated the questions raised in this thesis. A large number of studies regarding the comparison of passive amorphous systems and dense active systems have focused on how a biological activity affects the glass transition (Berthier et al., 2011; Janssen, 2019). Hence, although our work focuses on athermally driven systems, we summarize in this chapter the important findings regarding the active glass transition, and, prior to that, introduce the phenomenology of passive glasses.

Section 1.1 concerns the physics of dense systems. We present the phenomenology of glassy materials and introduce the different types of solid-to-fluid transitions (glass, jamming, yielding) observed in passive systems. This section is mainly based on the review paper by Berthier et al. (2011): "Theoretical perspectives on the glass transition and amorphous materials".

In section 1.2, we focus on the flow properties of athermal amorphous materials undergoing a yielding transition. We first present the macroscopic rheology, before explaining the mechanism for plasticity in amorphous materials and the shear banding phenomenon. We finally present a few studies investigating the role of additional sources of mechanical noise in the flow of soft amorphous materials. This section is mainly based on the following review papers: Bonn et al. (2017): "Yield stress materials in soft condensed matter", Nicolas et al. (2018a): "Deformation and flow of amorphous solids: insights from elasto-plastic models", Divoux et al. (2016): "Shear Banding of Complex Fluids".

In section 1.3, we present the phenomenology of active glassy systems. We first give examples of biological and synthetic systems falling into this category and then discuss how different types of activity influence the dynamics. This section is mainly based on the following review papers: Berthier et al. (2019): "Perspective: nonequilibrium glassy dynamics in dense systems of active particles", Janssen (2019): "Active glasses" and Khalilgharibi et al. (2016): "The dynamic mechanical properties of cellularised aggregates".

In section 1.4 we introduce the modeling approaches for dense driven and active systems at various lengthscales, from particle-based or vertex-based models at the microscopic scale, to mesoscopic approaches (that enable to get rid of microscopic details) and continuum approaches at the macroscopic level.

Finally, the scientific context given in this chapter enables us to introduce in more details the questions raised in this thesis in section 1.5.

1.1 Phenomenology of amorphous systems

1.1.1 Introduction

Glassy or amorphous materials are ubiquitous in our everyday life and widely used in industrial applications. Nonetheless, a complete theoretical description of this state of matter is still lacking and remains an important challenge for modern statistical physics. A remarkable aspect of glasses is that they share similarities with both liquids and crystalline solids: their structure exhibits no structural order like liquids, but they behave mechanically as solids. This makes their theoretical description particularly difficult, and there has been, so far, no derivation of a complete and well accepted theory of disordered materials (see Berthier et al. (2011) for a review). In this section, we will not review the (numerous) different theoretical approaches to the

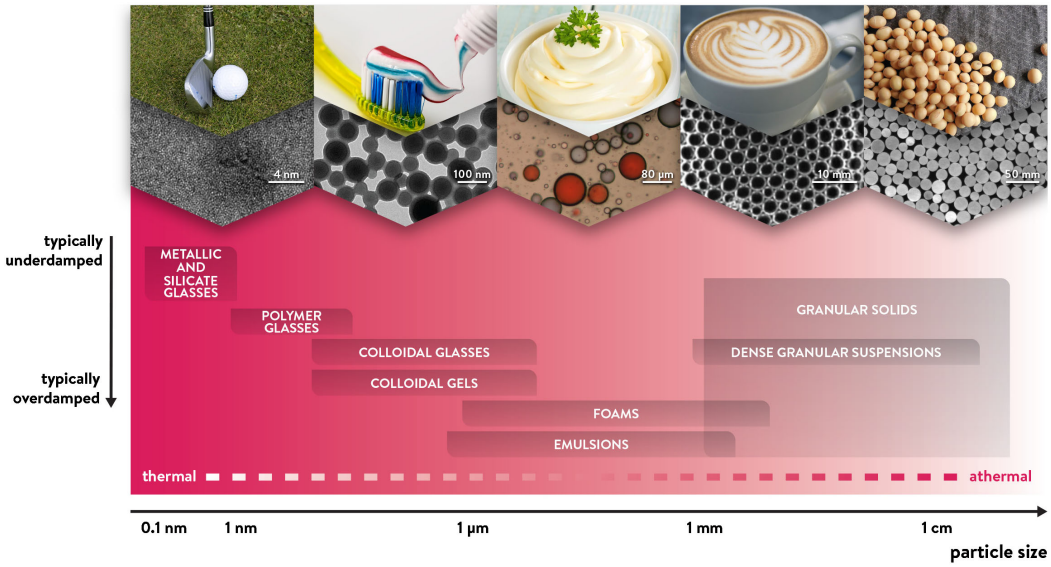

FIGURE 1.1: From Nicolas et al. (2018a) (see references therein): **Overview of amorphous solids**. From left to right, top row: (1) golf club made of metallic glass, (2) toothpaste, (3) mayonnaise, (4) coffee foam, and (5) soya beans. Second row: (1) Transmission electron microscopy (TEM) image of a fractured bulk metallic glass (2) TEM image of blend (PLLA/PS) nanoparticles. (3) Emulsion of water droplets in silicon oil observed with an optical microscope. (4) Soap foam picture. (5) Thin nylon cylinders of different diameters. Below: different amorphous materials classified by their size (left to right) and by the damping regime (top to bottom) of their constituents.

glass transition, but rather focus on the main phenomenological aspects of amorphous materials.

A glass can be obtained by rapid quench of a liquid below its glass temperature T_g. A rapid quench is necessary in order to prevent crystallization. Unlike the first-order transition leading to a crystal phase, the glass "transition" is not a thermodynamic transition since the glass transition temperature T_g is only empirically defined. It corresponds to the temperature at which the viscosity reaches 10^{12} Pa $\cdot$ s, preventing the observation of flow on experimental timescales. However, liquids quenched to the glass phase continue to evolve very slowly towards an equilibrium state they cannot reach on experimental timescales. As a consequence, all the macroscopic observables are time dependent and slowly evolve in time in out-of-equilibrium states, leading to the so-called "aging" of glasses.

The glass transition is also observed in systems made of units much larger than molecular sizes in which the dynamics is controlled by the volume fraction, as in colloidal suspensions (with some polydispersity to avoid crystallization). Dynamical arrest occurs at a critical volume fraction ϕ_g that depends on the details of interactions between particles ($\phi_g \simeq 0.58$ for hard spheres for example).

The subject of "glass physics" is actually much broader than the study of the fluid-to-solid transition observed upon an increase of density or decrease in temperature in molecular and colloidal systems. Materials are said to be "glassy" when their typical relaxation timescale becomes larger (possibly by several orders of magnitude) than the typical duration of an experiment or a numerical simulation. With this generic definition, a large number of systems fall into the class of glassy materials. Examples of such systems are shown in Fig. 1.1 (Nicolas et al., 2018a). Materials such as metallic

or oxide glasses as well as polymer glasses, termed as "hard amorphous materials", are made of units with a typical linear size comprised between 0.1 and 10 nanometers. Their elastic modulus is in the tens to hundreds of GigaPascal range, and they will tend to break if submitted to large stresses, undergoing only little plastic deformation before failure. On the other hand, foams and emulsions, made of micrometer to millimeter size bubbles or droplets are often called "soft amorphous materials". They remain solids at rest due to surface tension, but their elastic modulus is much smaller than metallic glasses and is in the range of a few hundred Pascals. When deformed with a stress exceeding their yield stress, they tend to reach a plastic flow regime. These so-called "Yield Stress Fluids" (YSF) encompass also other types of systems: colloidal pastes, granular materials and dense granular suspensions, and will be the main focus of this thesis.

For all these materials, glassy dynamics can be observed in some part of their phase diagram. It is associated with a rich phenomenology: solid and liquid behaviors, non-trivial relaxation, dynamic heterogeneity, aging, nonlinear response, creep, rejuvenation, memory effects, etc. (Berthier et al., 2011). In summary, these examples show that glass physics covers a broad range of lengthscales and a large variety of materials.

1.1.2 Signatures of glassy behavior

Let us introduce in this section the main characteristics of glassy dynamics (as observed in glass forming liquids), that will also be useful to introduce the physics of dense active systems in section 1.3.

Dynamical arrest and kinetic fragility

The hallmark of glassiness is the dramatic increase of the viscosity in the supercooled liquid state, which is the metastable state achieved when cooling the system fast enough to avoid crystallization. The temperature dependence of the viscosity (or equivalently of the relaxation time), usually represented in an "Angell plot" (Angell, 1991) gives insights into the nature of the relaxation mechanisms in the supercooled liquid. Supercooled liquids can thus be classified depending upon their "kinetic fragility": "strong" glass formers have an Arrhenius-type relaxation, and "fragile" glass formers exhibit a super-Arrhenius relaxation, with the viscosity being well fitted by $\eta = \exp DT_0/(T - T_0)$ (Vogel-Fulcher-Tamman fit). The physical picture in that case is that there is an increase of energy barriers when lowering the temperature, suggesting that glass formation is a collective phenomenon for fragile supercooled liquids. This fitting form also suggests a divergence of the viscosity at finite temperature T_0, possible indicator of a phase transition.

Other possible indicators of a phase transition were also suggested by looking at thermodynamic aspects (excess entropy of the supercooled liquid with respect to the entropy of the crystal, providing information about the number of metastable states), although this point was discussed in the literature (Berthier et al., 2011). Let us mention that although some aspects of the phenomenology (diverging timescale and singularity in the thermodynamics) could suggest that the glass transition is a problem not so different from studying other phase transitions, the difficulty of studying the glass transition comes from the fact that static correlation functions are quite featureless in the supercooled regime, despite dramatic changes in the dynamics.

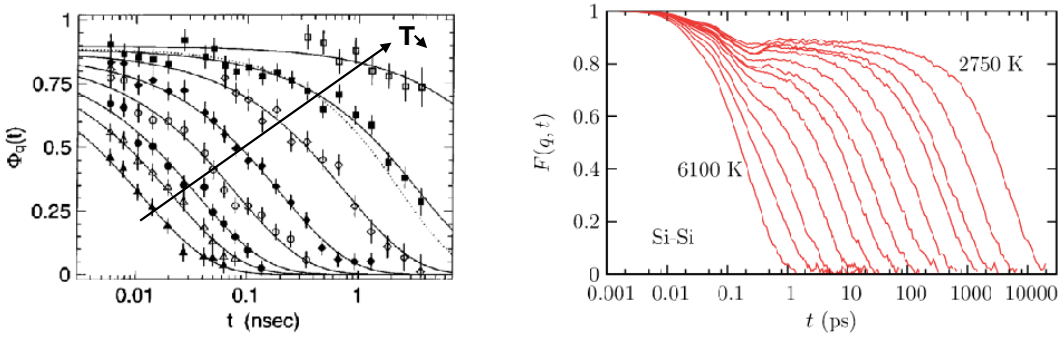

FIGURE 1.2: **Intermediate scattering functions**. (left) From Wuttke et al. (1996): Obtained in neutron scattering experiments on glycerol, $\phi_{\vec{q}(t)=F(\vec{q},t)/F(\vec{q},0)}$ with $\vec{q}$ corresponding to the first peak in the static structure factor and (right) From Horbach et al. (2001): obtained from computer simulations of a silica model.

For instance, the structure factor, defined as

$$S(\vec{q}) = \langle \frac{1}{N} \rho_{\vec{q}} \rho_{-\vec{q}} \rangle \tag{1.1}$$

with $\rho_{\vec{q}}$ the Fourier component of the density field, N the number of particles, does not provide indications of a diverging lengthscale at the transition. Signatures of the glass phase are however found when turning to dynamical correlation functions.

Dynamical correlation functions

The intermediate scattering function $F(\vec{q}, t)$ (Fourier transform of the Van Hove function) is a useful quantity since it is accessible in light and neutron scattering experiments:

$$F(\vec{q}, t) = \langle \frac{1}{N} \rho_{\vec{q}}(t) \rho_{-\vec{q}}(0) \rangle \tag{1.2}$$

The intermediate scattering function $F(\vec{q}, t)$ is actually the autocorrelation function at time interval t of density fluctuations for a given mode $\vec{q}$. Examples of intermediate scattering function curves are shown in Fig. 1.2 for both experiments and computer simulations of glass forming systems. At short time, there is a small plateau (ballistic regime where the interaction does not affect the motion of particles) followed by a relaxation. This first regime (very short times) is not accessible in experiments. At high temperature, the relaxation is simply exponential. When the temperature approaches the glass transition, a plateau appears due to particles vibrating inside a cage formed by their neighbors. This caging effects lasts longer and longer as the temperature is decreased. Cage-breaking eventually occurs at longer timescales, leading to a second relaxation phase ("α-relaxation"). At low temperature, the timescale of relaxation becomes larger and the exponential form becomes stretched. The behavior of the intermediate scattering function in the supercooled liquid regime suggests that by decreasing further the temperature to be in the glass phase, the "caging" will last forever.

Numerical simulations of glasses have enabled researchers to measure individual particle displacements (more details on simulation methods in section 1.4). In particular, the mean squared displacement can be computed from individual particle trajectories, as depicted in Fig. 1.3(a). At short times, the mean squared displacement follows a ballistic regime. At high temperatures, this regime is immediately

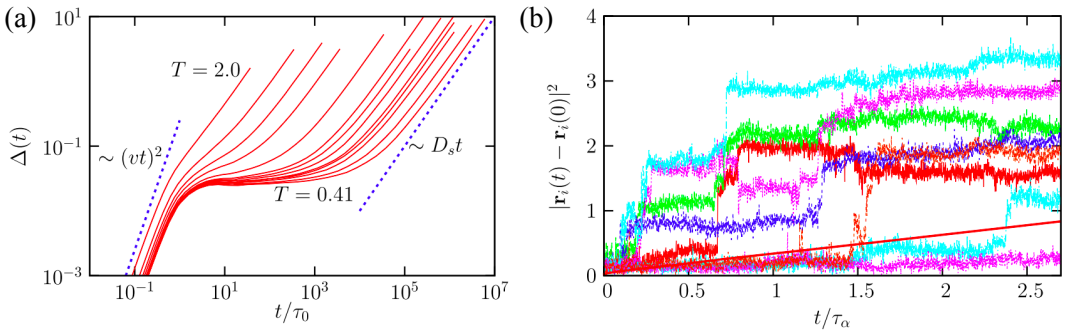

FIGURE 1.3: From Berthier et al. (2011): (a) **Mean squared displacement** of individual particles in computer simulations of a simple model of a glass-forming liquid composed of Lennard-Jones particles for various temperatures (decreasing temperatures from left to right). (b) **Time-resolved squared displacements** of individual particles.

followed by a diffusive regime, while at low temperature, it reaches first a plateau regime at intermediate timescales. As for the intermediate scattering function, the plateau is related to particles vibrating in a cage formed by their neighbors. Particles eventually escape their cage to reach the long time diffusive regime. The duration of the plateau increases as the temperature is decreased.

When looking at trajectories of individual particles (Fig. 1.3(b)), one observes that an individual particle undergoes a succession of periods during which it vibrates around a mean position interrupted by rapid jumps. Moreover, when particles of some regions are vibrating around their mean position, particles in other regions may undergo large displacements. This dynamics cannot be inferred from average properties, highlighting the importance of fluctuations around the average dynamical behavior in glass forming systems.

Several studies show that the relaxation is spatially heterogeneous, with slow and fast relaxing regions. Since supercooled liquids are ergodic, a fast relaxing region will eventually become slow and vice-versa, meaning that these heterogeneities have a finite lifetime. These heterogeneities, characterized using 4-points correlation functions, are thought to explain the non-exponential relaxation behavior of the intermediate scattering function. Moreover, regions of fast and slow moving particles are correlated over a dynamical lengthscale that grows upon approaching the glass transition. These dynamical heterogeneities, which result directly from crowding, lead to important collective phenomena in glassy materials, which is also an important feature of active glasses.

Concluding remarks

Dynamical slowdown, two-step dynamical correlation functions and dynamical heterogeneities are the main aspects that are usually considered when addressing the question of the existence of a signature of glassy behavior in a system (e.g., active system). There are however other important aspects of glassy dynamics that we will not discuss here, such as violation of the Stokes-Einstein relation, stretched exponential dynamics, aging, etc. (Berthier et al., 2011).

The potential energy landscape (PEL) picture, as introduced by Goldstein (1969), is useful to understand some features of the dynamics of glassy systems, such as aging mechanisms. Aging, as mentioned in introduction, is generically described as a non-equilibrium phenomenon occurring when a system gradually evolves towards

an underlying equilibrium state. In the PEL representation, the whole configuration of the system (particles positions and velocities) is considered as a "state point" Γ evolving on top of a hypersurface $V(\Gamma)$ representing the total potential energy. The hypersurface $V(\Gamma)$ is a high-dimensional object since its dimension is proportional to the number of particles N. It can be viewed as a rugged landscape with a large number of local minima (that grow exponentially with N). Glassy states do not minimize the free energy of the system (unlike crystals), and aging observed in thermal systems is simply an evolution towards the lowest-energy states through random thermally activated barrier-crossing events. As the state point of the system reaches deeper and deeper minima, the jumps become more rare and the dynamics slows down.

1.1.3 Other fluid-to-solid transitions

In the previous section, we presented the phenomenological behavior of glass forming liquids. Fluid-to-solid transitions are actually ubiquitous and can be found in very diverse systems. First of all, let us recall that colloidal suspensions also undergo a glass transition upon compression (or increase of volume fraction), going from a (metastable) thermal equilibrium state to an arrested state, similarly to glass forming liquids (Hunter et al., 2012). Then, in athermal systems (non-Brownian suspensions, foams, granular media), a fluid-to-solid transition upon an increase in volume fraction is also observed, and is called the (geometrical) "jamming transition" (Liu et al., 2010).[2] Finally, while soft glassy materials deep in the glass phase behave like solids at rest, they can start to flow like fluids when driven with a sufficient stress, exhibiting a solid-to-fluid transition upon the applied load (Bonn et al., 2017).

These different scenarios of fluid-to-solid transitions have been summarized in the well-known "jamming diagram" of Liu et al. (1998), depicted in Fig. 1.4(left), where the three different axes indicate how an increase of temperature, a decrease of density or an increase in loading can lead to a transition from an arrested solid-like state to a fluid-like state. In this diagram, thermal and athermal systems appear as a single "jammed" phase, while theoretical studies suggested that the jamming transition occurs well inside the nonergodic glassy phase (Jacquin et al., 2011). This diagram is thus limited to an "illustrative" purpose as these three transitions (glass, jamming, yielding) are very different in nature, and concern usually different types of systems (or at least different regions of their phase diagram) (Ikeda et al., 2012).

Fluid-to-solid transitions in active systems

Transitions from a fluid-like to a solid-like state are ubiquitous, not only for molecular, colloidal or granular systems, but also in a large variety of active or biological systems, where the constituents of the material can be active colloids, cells, or self-propelled grains (Sadati et al., 2013; Berthier et al., 2019; Janssen, 2019). It is thus tempting to draw analogies between dense passive and active systems, as illustrated for instance in Fig. 1.4(right) by the hypothetical jamming phase diagram for cell monolayers proposed by Sadati et al. (2013). Biological systems can undergo solid-to-fluid transitions linked to a large variety of biochemical and biophysical factors. In this diagram for instance, a cellular monolayer becomes fluid upon a decrease in density, an increase of motility or a decrease of cell-cell adhesion. As in amorphous solids, different types of transitions may be observed depending on the type of biological activity, and this point will be addressed in more details in section 1.3.

[2] Another phenomenon termed as "shear-induced jamming" occurs when an applied shear strain yields rigidity in suspensions (Bertrand et al., 2002).

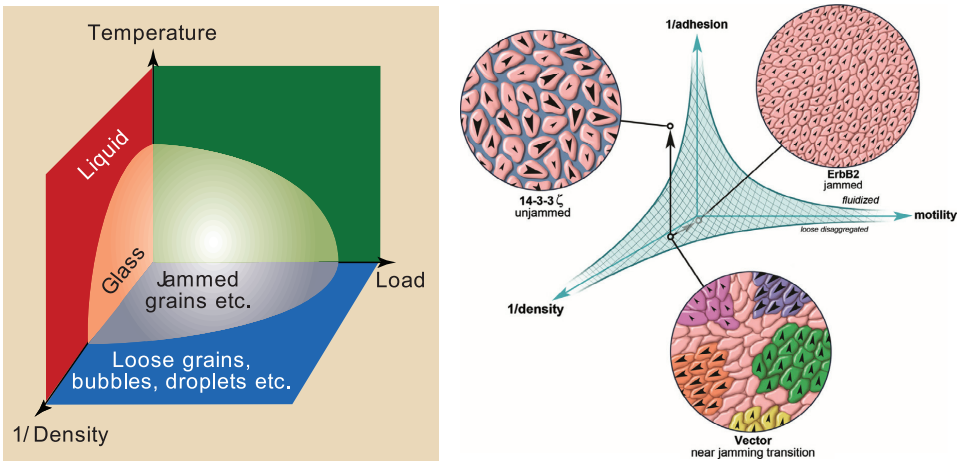

FIGURE 1.4: **Hypothetical "jamming" phase diagrams**. (Left) From Liu et al. (1998): different routes to undergo a transition between solid-like and fluid-like states: by increasing the temperature, decreasing the density or increasing the driving load. (Right) From Sadati et al. (2013): Hypothetical phase diagram for cellular monolayers that could become fluid-like upon an increase in cell motility, a decrease in density or a decrease in cell-cell adhesion.

Depending upon the scientific community, the fluid-solid transitions in active systems have often been referred to as active "jamming" transitions rather than glass transitions. The distinction between jamming and glass transitions has however been made quite clear in the recent years (Ikeda et al., 2012). According to recent review papers on the topic (Berthier et al., 2019; Janssen, 2019), the competition between crowding and particle agitation (due to thermal or active processes such as cell motility) generally leads to a glass transition, while jamming is seen as a geometric transition (no agitation, no dynamics) between rigid and non-rigid states. With this definition, particles with non zero activity cannot undergo jamming.

Fluid-to-solid transitions in driven (sheared) systems

Arrested materials can also be driven out of equilibrium by driving forces under the form of an externally applied mechanical load. Unlike in the case of active forces, energy injection occurs at a macroscopic scale, e.g., by imposing a shear flow or applying a constant shear stress. An arrested material with no source of agitation (negligible thermal fluctuations, no activity), subjected to an external load responds essentially as an elastic solid for small applied stresses. For larger stresses, the response becomes non linear, and for stresses larger than a "yield stress", the system starts to deform plastically and eventually flows at a fixed rate with a potentially driving-dependent viscosity, like a complex fluid. The yielding transition is thus another form of solid-to-fluid transition upon the application of a shear stress. Note that dense amorphous systems can also be driven by applying a fixed deformation rate. In that case, the system is never dynamically arrested and constantly undergoes plastic rearrangements, which will be discussed in the next section.

The response of dense amorphous materials to an external load has become an active field of research in the past decades (Bonn et al., 2017; Nicolas et al., 2018a) and is one of the main topics of this thesis. In the next section, we will review the main features of the rheology of dense amorphous systems, focusing on the case where thermal fluctuations play a negligible role (athermally driven systems).

Summary of section 1.1

- A glass can be obtained by rapid quench of a molecular liquid below its glass temperature or by increasing the density of a colloidal suspension above a critical volume fraction.
- A glassy behavior is characterized by divergent relaxation timescales that can be revealed by dynamical correlations functions, whereas static correlation functions are quite featureless in the supercooled regime.
- Two-step dynamics of the dynamical correlation functions and mean squared displacement of particles in a supercooled liquid reveal a caging effect; in the glass phase, a particle would remain caged by its neighbors forever.
- The relaxation is spatially heterogeneous with slow and fast relaxing regions. These dynamical heterogeneities lead to important collective phenomena.
- Athermal (non-active) systems undergo a transition from a fluid-like to a solid-like state upon an increase of density called the jamming transition.
- Materials below their glass or jamming transition behave as solids at rest but can start to flow like fluids when a sufficient load is applied, undergoing a solid-to-fluid transition termed as"yielding".
- Solid-to-fluid transitions have also been evidenced in active or biological systems such as cells and tissues and analogies with solid-to-fluid transitions in inert systems have been proposed.

1.2 Rheology of athermally driven amorphous materials

How do soft solids flow upon loading? We describe in this part the mechanisms for the flow of soft amorphous materials such as foams, emulsions, dense granular or colloidal suspensions or granular media. We first describe the rheology and the phenomenology of the flow, before discussing the mechanisms at the origin of plasticity in amorphous solids. We then explain the phenomenon of shear banding and present a few studies addressing the role of external sources of noise on the flow of yield stress fluids.

1.2.1 Phenomenology of the flow

Macroscopic rheology

When shearing amorphous materials using a rheometer, one can control either the torque or the angular velocity, which is equivalent to either imposing the shear stress Σ or the shear rate $\dot{\gamma}$ in the system. Fig. 1.5(a) depicts the typical stress-strain curve measured when imposing a constant shear rate $\dot{\gamma}$ to a dense amorphous system (shear start-up protocol). For small applied deformations, the system responds essentially elastically as depicted by the linear stress-strain evolution in Fig. 1.5(a). When the stress becomes larger, the system starts to exhibit irreversible plastic deformation. If the stress becomes larger than a threshold called the (static) "yield stress", the material yields: this results in irreversible plastic deformation for hard brittle materials such

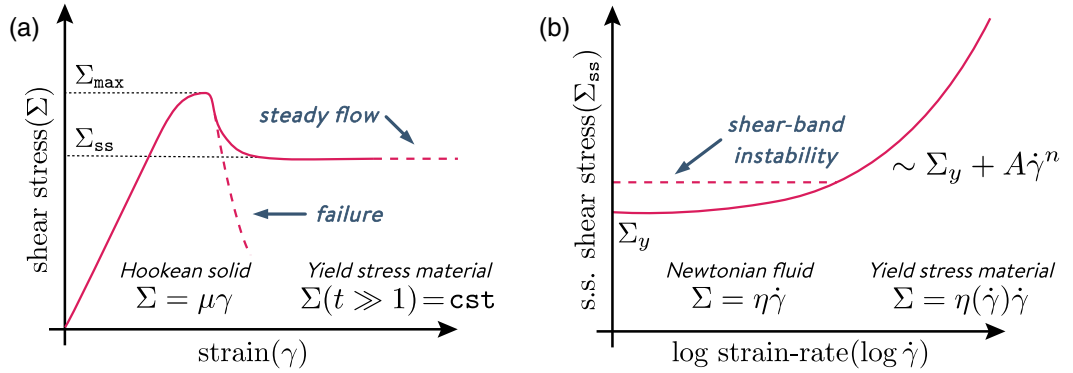

FIGURE 1.5: From Nicolas et al. (2018a): **Schematic macroscopic response of amorphous solids to an applied deformation**. (a) Macroscopic shear stress Σ as a function of the applied shear strain γ, with a stress overshoot Σ_{max} that can be followed either by failure (for "hard" materials) or by a steady state plastic flow (for "soft" glassy materials). (b) Flow curve: steady-state shear stress as a function of the applied strain rate.

as silica glass (Taylor, 1949; Kermouche et al., 2016) and steady-state plastic flow for the soft amorphous materials we are interested in.

The steady state flow of soft amorphous materials is usually characterized by the flow curve, that is, the relation between the applied shear rate $\dot{\gamma}$ and the macroscopic shear stress Σ in steady state, as depicted in Fig. 1.5(b). For many soft amorphous systems, the flow curve can be fitted by a Herschel-Bulkley (HB) equation (Herschel et al., 1926):

$$\Sigma = \Sigma_y + A\dot{\gamma}^n \tag{1.3}$$

with Σ_y the dynamical yield stress, A a constant and an exponent n close to 0.5.

Avalanches in the slow flow regime ($\dot{\gamma} \to 0$)

An important question concerns the link between the macroscopic rheology and the spatial organization of the flow of amorphous solids in the slow flowing regime ($\dot{\gamma} \to 0$). Although the response to shear depicted in the scheme of Fig. 1.5(a) seems smooth and very different in the case of hard and soft materials, looking carefully at experimental stress-strain curves reveals that the actual response is jagged. Fig. 1.6(b) depicts the stress as a function of strain for a sheared bubble raft (shown in Fig. 1.6(a)) (Lauridsen et al., 2002). Instead of smooth deformation, one observes a succession of loading phases of the material until a breaking point, where an abrupt relaxation occurs, as in "stick-slip" phenomena. In other words, potential energy V accumulates in the material in the form of elastic strain until some rupture threshold, leading to a plastic event releasing the stored energy associated with a stress drop. The distributions of stress drops observed in the stress strain curve at small shear rates (Fig. 1.6(c)) exhibit a power-law behavior that is related to the presence of long-range elastic interactions in the system (Nicolas et al., 2018a) that we will further discuss in section 1.2.3.

Dynamics at the yielding transition and insights from oscillatory shear

Beside studies of avalanches in sheared amorphous solids, various studies have been dedicated to the transition to failure or to a steady-state flow in amorphous solids

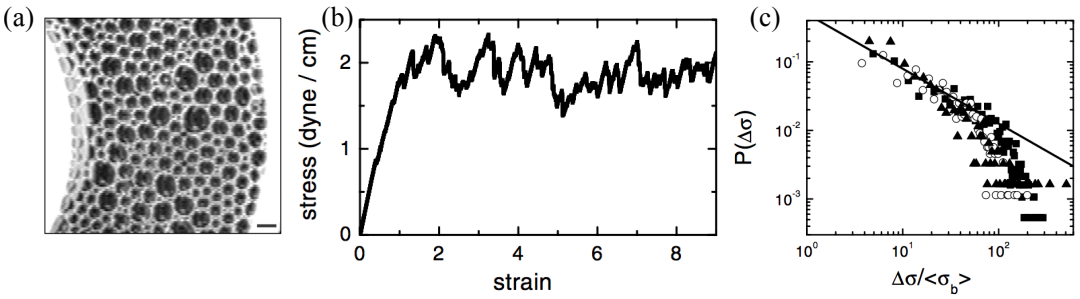

FIGURE 1.6: From Lauridsen et al. (2002): **Avalanche dynamics in a bubble raft**. (a) Image of a section of a typical bubble raft (scale bar: 3.6 mm). (b) Stress versus strain for a strain rate $\dot{\gamma} = 3.1 \cdot 10^{-3}\mathrm{s}^{-1}$. (c) Stress drop probability distribution function.

upon increasing strain, as depicted in Fig. 1.5(a), termed as "yielding transition". Understanding the microscopic mechanisms at the origin of changes in mechanical behavior and avalanches between pre- and post-yielding deformation has implications in glass physics (Jaiswal et al., 2016; Wisitsorasak et al., 2017; Jin et al., 2018) but also in mechanical engineering (Telford, 2004).

Studying the pre-yielding regime can however be difficult due to large sample-to-sample variations when imposing a uniform shear flow, in contrast with the universal behavior seen in the post-yielding regime. Oscillatory shear driving thus offers a convenient approach to probe the mechanical behavior below and above yielding, as demonstrated by various recent numerical works (Fiocco et al., 2014; Leishangthem et al., 2017; Yeh et al., 2020). Note that dynamic oscillatory shear tests are commonly used in rheological experiments. Small amplitude oscillations are generally used to probe the linear viscoelastic response of complex fluids, while large amplitude oscillations (LAOS) can be used to probe the non linear response and the onset of plastic deformation.

Studies based on oscillatory shear driving in athermal conditions have demonstrated that yielding is associated with irreversibility of particle trajectories (Fiocco et al., 2014; Regev et al., 2015; Kawasaki et al., 2016). The transition is associated with a sudden change in particle dynamics, evolving from nondiffusive motion to irreversible diffusive motion upon increasing the amplitude of oscillatory strain, γ_0, as depicted in Fig. 1.7(a) (Kawasaki et al., 2016). Moreover, the stress as a function of maximum strain (denoted $\gamma_{\max}$ in the quasi-static protocol of Leishangthem et al. (2017)) under oscillatory driving is found to vary abruptly at the yield point even if it varies smoothly in uniform strain as it is generally the case for soft amorphous materials (Fig. 1.7(c)). For strain amplitudes γ_0 below the yield strain γ_y, hardening effects are observed, leading to an increase of glass stability sometimes termed as "mechanical annealing". This is reflected in the energy of the system which decreases with increasing strain until the yield point γ_y (Fig. 1.7(d)). For strain amplitudes above yielding, the system deforms plastically and accesses higher energy states, leading to an increase of energy with γ_0. The yielding point is thus characterized by a minimum in the system's energy (at least for soft amorphous materials exhibiting ductile yielding behavior, and more generally by a cusp for materials exhibiting brittle yielding (Yeh et al., 2020)). It was also found that the number of cycles required to reach steady state increases when approaching the yield point (Fig. 1.7(b)). Studies of particle-based simulations as well as a mesoscale model have further revealed that the deformation in the regime $\gamma_0 > \gamma_y$ (but close to γ_y) can be heterogeneous and organize into macroscopic shear bands (see section 1.2.4) (Radhakrishnan et al., 2016;

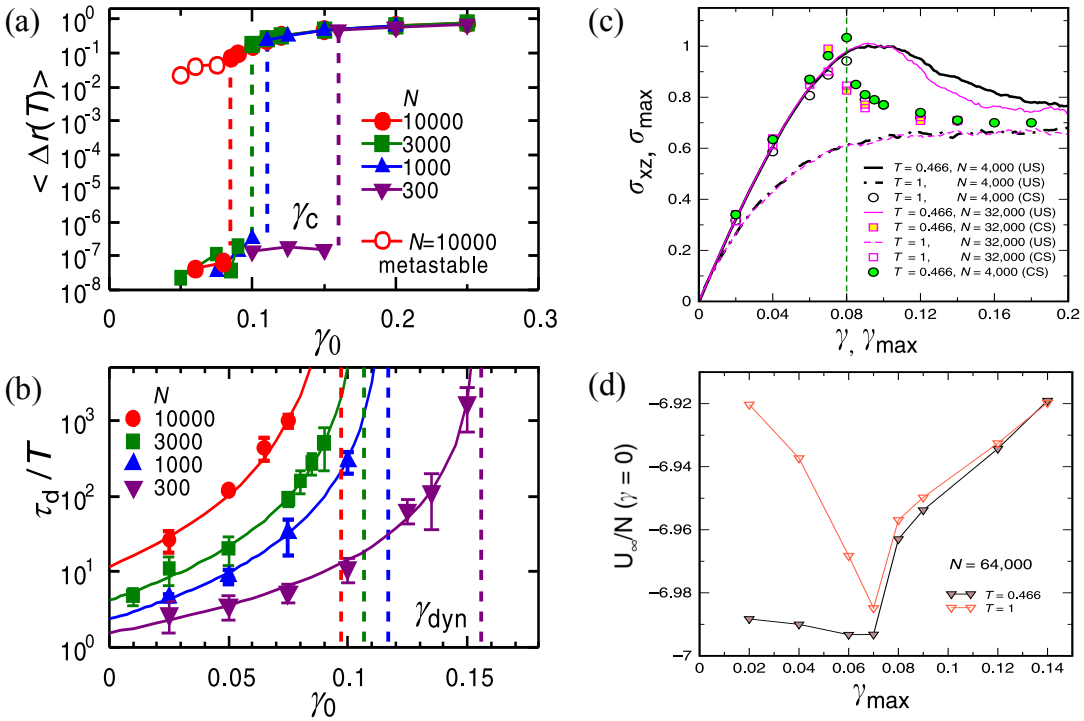

FIGURE 1.7: **Yielding transition under oscillatory shear driving**. From Kawasaki et al. (2016): (a) Time averaged displacement during one cycle of oscillation for various strain amplitudes and system sizes. (b) Divergence of the average time to reach an immobile state (zero displacement). From Leishangthem et al. (2017): (c) Average stress-strain curve for uniform (solid lines) and oscillatory shear with an athermal quasi-static shear protocol (symbols). (d) Asymptotic energy per particle measured at a strain $\gamma = 0$ as a function of the maximum strain amplitude $\gamma_{\max}$.

Yeh et al., 2020; Liu et al., 2020b).

Recent works have further shown that the nature of yielding can depend upon the glass stability (well annealed versus poorly annealed samples), changing from brittle to ductile yielding behavior and associated with distinct shear band formation mechanisms (Ozawa et al., 2018; Yeh et al., 2020).

In summary, the transition to flow in soft amorphous materials is characterized by the appearance of irreversible plastic deformation. What is the nature of the microscopic processes leading to plastic deformation in amorphous solids?

1.2.2 Localized plastic rearrangements

Since direct visualization of atoms or molecules displacements in atomic or molecular glasses is impossible, early works in the 1970's made use of the analogy between bubbles rafts and glasses to study plastic deformation in glasses (Argon et al., 1979). The analogy between the deformation of foams and metals was already pointed out in crystals by Bragg et al. (1947), who evidenced that yielding in a bubble raft started with a dislocation. Argon et al. (1979) evidenced rapid localized rearrangements involving a few number of bubbles, and singularities in the deformation. In foams, these shear transformations were identified by Princen et al. (1986) as local topological changes involving four neighboring bubbles coming to share a vertex, also called "T1 events", as depicted in Fig. 1.8. At mechanical equilibrium, bubbles in a bidimensional

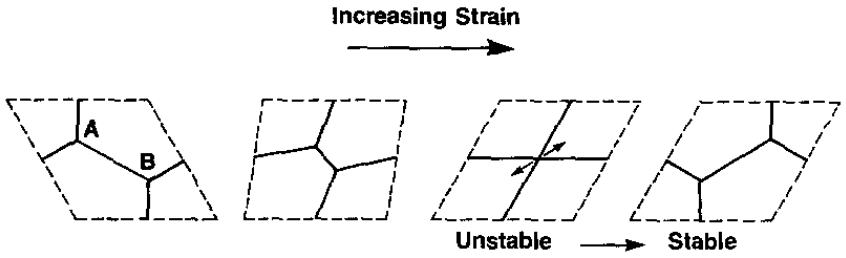

FIGURE 1.8: From Princen et al. (1986): **Sketch of a shear transformation, or "T1 event"** in a bidimensional foam.

foam meet at an angle of 120 degrees, leading to vertices shared by three neighboring bubbles. When sheared, the bubbles deform elastically until they reach a configuration where four neighboring bubbles share a vertex. This four-fold vertex configuration being unstable, a transition to the above configuration is observed, associated with the "flip" of one soap film, the so called "T1 transition".

Shear transformations were also evidenced in experiments on colloidal glasses by Schall et al. (2007) and granular media by Amon et al. (2012). Atomistic simulations have also shed light on the nature of these shear transformations, due to the difficulty to perform measurements at the particle scale in experiments (Falk et al., 1998; Maloney et al., 2006; Tanguy et al., 2006).

Characterizing plastic rearrangements

Particle rearrangements in amorphous materials correspond to local inelastic deformations of the material. Various quantitative tools to describe them have been introduced, as for instance the "D^2_{min}" introduced by Falk et al. (1998). In practice, such tools rely on subtracting the local affine elastic deformation in order to measure nonaffine transformations characterizing plastic rearrangements.

Generally speaking, these methods have evidenced that at low shear rate, plastic events are strongly localized, with a few active regions separated by regions of (locally) affine elastic deformation. The characteristics of plastic rearrangements may vary depending upon the material under consideration. First, the size of the rearrangement can vary from a few particles in foams, emulsions, colloidal suspensions, to tens or a hundred of atoms in metallic glasses. The shape of the rearrangement may also vary, and thermally activated rearrangements may differ from mechanically activated ones (Nicolas et al., 2018a). This picture of clearly separated plastic events should however be nuanced in the case of hard particles like grains (Bouzid et al., 2015).

A detailed numerical characterization of plastic events in amorphous silicon has been conducted by Albaret et al. (2016). By fitting the particles displacement during a plastic event to the elastic response to an idealized circular shear transformation (see section 1.2.3), the authors have been able to extract the size and typical plastic strain of the rearranging cluster of particles, finding that a robust quantity to characterize rearrangements is the product of the strain ε^* with the inclusion volume V_{in}. They also show that the transformation undergone by the group of rearranging particles is mostly shear, as the mean strain $\text{Tr}(\varepsilon^*)/3$ doesn't exceed 5 % of the shear components and its sign (dilation or contraction) depends on the details of the interaction potential. Moreover, using the fitted values of ε^* and of a (strain-dependent) shear modulus, they have been able to reproduce the macroscopic stress-strain curve, indicating that plastic rearrangements surrounded by an elastic response of the medium constitute the key mechanism of plasticity in amorphous solids.

Predicting plastic rearrangements

Understanding what leads a specific region of the material to rearrange is a long standing question in the field (Nicolas et al., 2018a). A common general idea is that the deformation will take place in "weak" zones of the material, where particles have an increased mobility.

The idea that the local free volume per particle correlates with the ability of a region to undergo plastic rearrangements has been introduced long ago, and is a key ingredient for various modeling approaches for glassy materials, such as the Shear Transformation Zone (STZ) theory introduced by Falk et al. (1998). Regions with small elastic moduli have also been shown to be correlated with an increased average plastic activity, but no general criterion has been found (Tsamados et al., 2009). Studies of the vibrational modes of amorphous packings have revealed that particles associated with the softest modes are more likely to rearrange (Rottler et al., 2014). More recently, numerical measurements of local yield stresses (by applying an affine deformation of the outer medium) by Patinet et al. (2016) have offered a promising approach to predict future plastic rearrangements. Alternative approaches based on machine learning techniques have also been developed (Cubuk et al., 2015; Zhang et al., 2020). Overall, identifying the relevant structural indicators to predict plastic rearrangements is still an ongoing active research field (Richard et al., 2020).

Concluding remarks

Localized particle rearrangements are a generic feature of the plasticity of amorphous solids and have been evidenced both in experiments and simulations. The characteristics of these shear transformations (size, shape) may depend on the details of the system under consideration. Predicting where plastic rearrangements will occur is still an open question, despite access to local quantities in numerical simulations. Simulations have in particular enabled one to characterize in detail the long-range stress and strain response to such a shear transformation, which leads to non-local effects in the dynamics.

1.2.3 Non-local effects

Once a shear transformation has occurred, it deforms the medium over large distances and may trigger other rearrangements in the material, thus leading to non-local effects.

Stress redistribution following a shear transformation

A single shear transformation (ST) can be approximated (in 2d) as a deformation $\varepsilon^* = \varepsilon_{xy}$. This corresponds to a stretch along the direction $\theta = \pi/4$ (modulo π) and a contraction along the perpendicular direction. The induced displacement field in the surrounding elastic matrix follows the same symmetry, with displacements pointing outwards the ST along the directions $\theta = \pi/4$ and displacement pointing inwards along the direction $\theta = 3\pi/4$, and has thus a dipolar symmetry in the far field. The deformation field (i.e., the symmetrized gradient of the displacement field) has therefore a quadrupolar symmetry. Following incompressible linear elasticity, the stress response to a punctual shear transformation (located at the origin) for an infinite system as computed by Picard et al. (2004) has thus the following form (and is displayed in Fig. 1.9(c)):

$$\sigma_{xy} \propto \frac{\cos(4\theta)}{r^2} \tag{1.4}$$

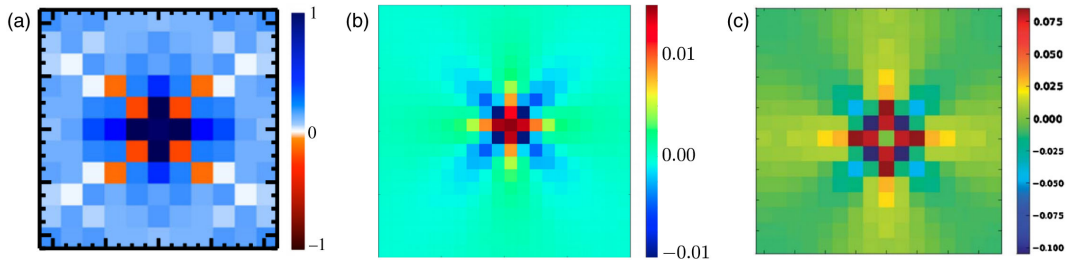

FIGURE 1.9: From Nicolas et al. (2018a): **Average shear stress redistribution around a shear transformation**. (a) From Desmond et al. (2015): Experimental measurements in dense emulsions. (b) From Puosi et al. (2014): average response measured in molecular simulations (binary Lennard-Jones glass). (c) Simplified theoretical form. The values of shear stress (colorbar) are not comparable between the different panels and the central blocks are artificially colored in panels (b) and (c).

Experiments on colloidal suspensions or dense emulsions (Schall et al., 2007; Desmond et al., 2015) as well as numerical simulations have confirmed this form for the far field, as shown in Fig. 1.9(a) and (b).

Eq. 1.4 is valid in the far field (as it is computed for a punctual shear transformation). Following the computation of Eshelby (1957), it is possible to compute the stress response in the near field as well. Eshelby's inclusion solution describes well the average displacement field induced by an ideal circular ST in molecular simulations of glasses (Puosi et al., 2014). Deviations from Eshelby's solutions are due to several aspects such as: the fluctuations due to heterogeneous elastic constants in the material, the difference between an idealized circular ST and an actual plastic rearrangements, as well as the effect of walls and finite system sizes.

Evidence and consequences of non-local effects

Beside the direct measurements of long-range strain and stress fields, non-local effects can be studied by looking at the correlations of the plastic deformation field which also obey a long-range decay with a quadrupolar form, as evidenced in experiments of colloidal glasses or granular media for instance (Schall et al., 2007; Le Bouil et al., 2014). The stress redistribution induced by a plastic event in an Eshelby fashion activates new plastic events, thus inducing correlations with the same geometry as the stress redistribution.

Consequences of these non-local effects have been evidenced in channel flows of dense emulsions by Goyon et al. (2008) or in sheared granular media by Nichol et al. (2010). These studies reveal that immobile regions in a sheared system can exhibit a vanishing yield stress and hence a fluid-like behavior although they are not flowing. This can be explained by the long-range interactions discussed above, as the redistribution of stress following local plastic events is responsible for mechanical fluctuations in the system.

These non-local effects have a strong impact on the modeling of the flow of soft glassy materials, as it excludes the possibility for an intrinsic local flow rule. Interactions between different regions of the material must then be incorporated into the modeling approaches, and different possible strategies will be explained in section 1.4 and Chapter 2. Beside treating explicitly spatial interactions between different regions of the material, some modeling approaches have focused on the mechanical fluctuations resulting from this coupling.

Mechanical fluctuations in athermal systems

The mechanical noise generated by localized plastic rearrangements (perturbations of the stress and strain fields in the material due to long-range elastic interactions) is a key ingredient to understand the dynamics of these systems, as it can trigger new rearrangements in an avalanche-like fashion.

A widely used approach to model the flow of soft glassy materials consists in interpreting the fluctuating mechanical noise as an effective activation temperature as done in the context of the "Soft Glassy Rheology" model (Sollich et al., 1997). In this model, shear lowers the energy barrier that needs to be overcome to realize a plastic event and a temperature-like parameter χ controls the activation dynamics, accounting for mechanical noise.

This approach has however been challenged in the context of athermal systems by Nicolas et al. (2014a), based on the escape time statistics of a mesoscale region subjected only to the "kicks" due to the mechanical noise resulting from plastic events in an elastic medium. They find that the escape time statistics does not follow an Arrhenius-type activation dynamics as it would be expected from a thermally activated process, but exhibits rather a power-law dependence on the energy barrier. These findings point towards the non-existence of a mechanical noise temperature, and suggest that modeling approaches should include mechanical fluctuations in a self-consistent manner (Hébraud et al., 1998).

The physical picture is that mechanical noise fluctuations, by tilting the PEL (as done by shear), persistently modify the local energy landscape thus leading to a cumulative effect, while thermal fluctuations have a short-time effect and exceptional sequences of fluctuations would be required to observe a cumulative effect leading to barrier-crossing. Note that self-consistent modeling for the noise seems to be an important point when modeling athermal systems. However, the picture may be very different in the case of thermal systems, where shear might be seen as "facilitating" thermally activated events, potentially leading to different statistics for the noise.

Concluding remarks

Elastic interactions in amorphous solids induce mechanical noise in the system and are responsible for non-local effects that can be seen for instance in the correlations between plastic events. These cooperative effects yield rich flow behaviors such as avalanches in the low shear rate limit, and, in some cases, heterogeneous flow patterns in the form of macroscopic shear bands that can be either transient or permanent.

1.2.4 Heterogeneous flow

When subjected to a homogeneous shear stress above the yield stress value, soft amorphous materials start to flow. This flow can be either homogeneous or heterogeneous, exhibiting "shear localization" or "shear banding" (Divoux et al., 2016). This shear banding phenomenon can be either transient or permanent.

Transient shear banding is usually associated with a stress overshoot in the stress-strain curve measured in shear start-up experiments, as shown schematically in Fig. 1.5(a). In that case, shear bands can persist for a long time that depends upon the initial age of the system, the applied shear rate and the damping (Vasisht et al., 2019). The flow will nonetheless eventually reach a homogeneous steady state if the flow curve is monotonic (i.e., of Herschel-Bulkley type, as shown in Fig. 1.5(b)). Note that, as mentioned earlier, shear bands are also reported in the case of oscillatory shear driving (Radhakrishnan et al., 2016; Yeh et al., 2020), and are also thought to be related to

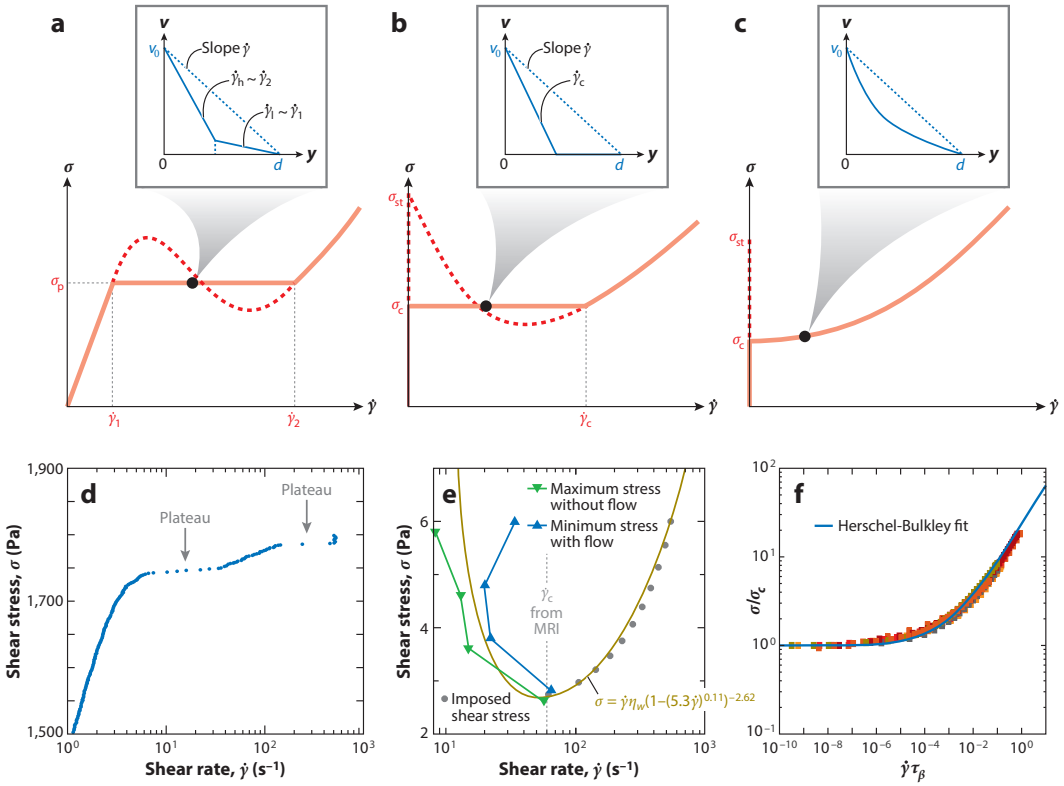

FIGURE 1.10: From Divoux et al. (2016): **Shear banding in complex and yield stress fluids**. Sketches of flow curves σ versus $\dot{\gamma}$ and velocity profiles $v(y)$ (along the gradient direction y) expected in (a) complex fluids undergoing a mechanical instability or a shear-induced transition (b) a yield stress material with steady state shear banding below a critical shear rate $\dot{\gamma}_c$; (c) a yield stress material with a Herschel-Bulkley rheology which flows homogeneously in steady state. Flow curves illustrated for (d) a cubic phase of a triblock copolymer made of ethylene and propylene oxide, showing two successive stress plateaus (Eiser et al., 2000); (e) a colloidal suspension of Ludox silica spheres (Møller et al., 2008); and (f) microgels with different cross-link densities made of acrylate chains bearing methacrylic acid units (Cloitre et al., 2003).

a stress overshoot in the stress-strain curve, although there is no unifying picture of shear banding at the yielding transition yet.

On the other hand, steady state or permanent shear bands are usually related to an underlying material instability. They have been reported in a large class of systems (not only yield stress fluids) and have been widely studied in the past decades (Olmsted, 2008; Schall et al., 2010; Fielding, 2014; Divoux et al., 2016). Among the different scenarios leading to permanent shear banding, the case of polymeric systems and wormlike micelle solutions seems to be well understood. The typical scenario observed in these systems is shown in Fig. 1.10(a). Shear induced structuration leads to the coexistence of regions flowing at different shear rates $\dot{\gamma}_1$ and $\dot{\gamma}_2$, even when the system is driven homogeneously (Lerouge et al., 2009; Olmsted, 2008; Divoux et al., 2016; Dhont, 1999; Dhont et al., 2008; Fielding et al., 2003). In the framework of continuum mechanics, these permanent shear bands have been understood as a consequence of a material instability, e.g., resulting from a non-monotonic constitutive flow curve (Fig. 1.10(a)). The negative-slope part of the flow curve being mechanically unstable (Yerushalmi et al., 1970), it is usually not observed in experiments (at least for sufficiently large systems). A stress plateau associated with phase coexistence is observed instead, as shown in Fig. 1.10(d), with the two boundaries of the plateau determining the shear rates in the two bands respectively. When the globally applied shear rate lies within the stress plateau range, the applied shear-rate is generally decomposed into volume-weighted averages of the shear rates in the two bands, obeying a so-called classic "lever rule".

Permanent shear bands in yield stress fluids

Permanent shear banding was also reported in the case of dense amorphous materials that are the focus of this thesis (Schall et al., 2010; Fielding, 2014; Divoux et al., 2010). Fig. 1.10(b) depicts a typical permanent shear banding scenario in yield stress materials. The material separates into a flowing region (at a shear rate $\dot{\gamma}_c$) and an arrested region, while the stress remains homogeneous in the system.

Although there is lack of consensus on the origin of shear banding in yield stress fluids, the mechanisms leading to permanent shear banding have been identified in a few cases, such as flow-structure or flow-concentration coupling. Regarding flow-structure coupling, an example of experimental data is shown in Fig. 1.10(e) for a dense colloidal system (made of attractive colloids) (Møller et al., 2008), exhibiting a non-monotonic flow curve (where the unstable part is accessed through measurements in the transient state). This type of system is usually strongly shear-history dependent (thixotropic), because the microstructure evolves with the flow. Theoretical approaches based on coupling the flow fields with the micro-structure have been successful in predicting permanent shear bands (Fielding et al., 2009; Mansard et al., 2011). In dense hard sphere suspensions, shear banding can occur due to a flow-concentration coupling mechanism (Besseling et al., 2010; Jin et al., 2014; Gross et al., 2018). Similarly to flow-structure coupling, theoretical approaches based on coupling the flow fields with the concentration field have been able to predict permanent shear bands.

The case of dense suspensions of soft particles, where neither significant structural nor volume fraction inhomogeneities are observed (Ovarlez et al., 2013; Bonn et al., 2017), remains however unclear. The role of attractive or adhesive interactions, proposed to lead to permanent shear banding, is debated in the literature (Bécu et al., 2006; Chaudhuri et al., 2012; Ovarlez et al., 2013). Alternatively, an intrinsic timescale for "restructuration" at the microscopic scale is suggested as a mechanism to induce local weakening leading to shear banding (Coussot et al., 2010; Martens et al., 2012).

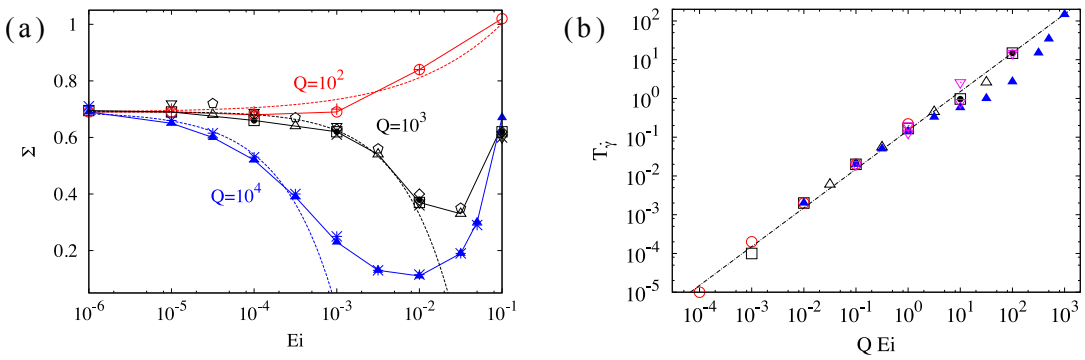

FIGURE 1.11: From Nicolas et al. (2016). **Non-monotonic flow curves and kinetic temperature due to inertia** in a binary Lennard-Jones glass. (a) Flow curve for athermal underdamped systems (data points and solid lines) for three different values of the damping coefficient (from top to bottom $Q = 10^2$, $Q = 10^3$ and $Q = 10^4$). The damping coefficient is defined as $Q = \tau_{\text{damp}}/\tau_{\text{vib}}$, with $\tau_{\text{damp}} = m/\zeta$ (with ζ the damping coefficient, m the mass of the particle) and $\tau_{\text{vib}} = \sqrt{ma^2/\varepsilon}$ (with a and ε being the average diameter and energy scale of the interaction potential for the particles). The x-axis corresponds to $\text{Ei} = \dot{\gamma}\tau_{\text{vib}}$. Dotted lines indicate fits using a function of the kinetic temperature in the system. (b) Kinetic temperature due to shear as a function of QEi measured in underdamped samples, in the athermal case (apart from $\triangledown$ symbols where $T_{\dot{\gamma}} = T_{\text{K}} - T_0$ with $T_0 = 0.2$).

The underlying idea is that once a region of the material has deformed plastically, a typical time is needed to reform bounds or adhesion between particles, before the material can locally sustain elastic stress again. This induces a softening of the system (decrease in stress) with an increase in shear rate, thus leading to a non-monotonic constitutive flow curve. This mechanism was proposed to explain the emergence of shear bands in dense suspensions of associative microgels with short-range attractive forces (Mattiello, 2018; Cloitre, 2018). It was also shown to induce shear bands in a mesoscale elasto-plastic model for the flow of soft glassy materials by Martens et al. (2012). This class of models (and their use to model shear bands) will be introduced in more detail further section 1.4 and Chapter 2. In Chapter 4, we will study how an external noise can affect shear bands induced by a long restructuring time in a mesoscale elasto-plastic model.

Inertia as a mechanism for shear banding in soft glassy materials?

Recent works, looking at the role of inertia on the flow behavior of yield stress materials (Salerno et al., 2012; Karimi et al., 2016; Karimi et al., 2017; Nicolas et al., 2016) have demonstrated rate-weakening mechanisms resulting in non-monotonic macroscopic flow curves, as shown in Fig. 1.11(a). This effect has been rationalized by Nicolas et al. (2016) in terms of kinetic heating of the system due to inertia. A kinetic temperature due to shear in the system can be measured (by removing the thermal temperature contribution or considering athermal simulations), and is found to increase with increasing shear rate and decreasing damping (see Fig. 1.11(b).) The idea to define a temperature derived from the local kinetic energy is a well established concept in the framework of sheared granular materials (Campbell et al., 1985; Walton et al., 1986; Losert et al., 2000). However, although it has been shown that the inertial heating effect on the microscopic scale can indeed lead to non-monotonic flow

curves (Nicolas et al., 2016), no evidence of shear localization due to inertial effects has been reported in that first study. Shear bands were reported in a finite-element-based elasto-plastic model with inertial dynamics by Karimi et al. (2016) and were shown not to obey a lever-rule, but this effect was attributed to the small systems sizes considered in this study and the characteristics of the shear bands remained unclear.

More recently, particle-based simulations performed in the group in Grenoble by Vasisht et al. (2018) have evidenced permanent shear bands in systems with underdamped dynamics when considering sufficiently large system sizes (we will further present these results in Chapter 3). One of the works conducted in this thesis in collaboration with V. Vasisht and J.L. Barrat consists in building an effective continuum model based on a kinetic temperature field description coupled to the flow fields (similarly to the flow-structure or flow-concentration coupling approaches mentioned above) in order to describe the permanent shear banding instability observed in particle-based simulations of inertial systems.

1.2.5 Fluidization of yield stress fluids by flow-independent noises

In section 1.2.3, we discussed the properties of the mechanical noise in the flow of soft glassy materials arising from elastic coupling within the material. Besides this self-generated mechanical noise there can be additional (external or internal) sources of noise, which can be regarded as a first approximation as independent of the shear-induced one. This is for example the case of thermally induced (Chattoraj et al., 2010; Ikeda et al., 2012) or vibration activated irreversible deformations. Other mostly rate-independent fluctuations can also result from local processes such as coarsening in foams (Cohen-Addad et al., 2004), or internal active processes (Mandal et al., 2016; Tjhung et al., 2017; Matoz-Fernandez et al., 2017a). One important aspect of such external noise sources is that they can induce a fluidization of the system at small imposed external stresses.

Fluidization by mechanical vibrations

In the case of granular materials, it appears that very small vibrations amplitudes are sufficient to fluidize the system (vanishing yield stress), as shown by the flow curves obtained for various vibration magnitudes in Fig. 1.12(a-b). The same phenomenology was reported in the case of wet granular suspensions (Fig. 1.12(c)) (Hanotin, 2014; Gaudel et al., 2017). The rheology in the low shear rate regime is close to being Newtonian for wet granular suspensions (Hanotin et al., 2012; Gaudel et al., 2017) (see inset of Fig. 1.12(c)), while more complex behaviors can be observed for dry granular media (see the flow curves of Dijksman et al. (2011), Fig. 1.12(b)).

The elimination of the yield stress by small amplitude vibrations was confirmed in creep experiments by Pons et al. (2015) where vibrated granular systems would eventually flow for applied stress values below the dynamical yield stress of the system. A whole literature is actually dedicated to the study of the effect of mechanical vibrations on the rheology of granular media. Without being exhaustive, we can cite for instance the works by D'anna et al. (2003), Caballero-Robledo et al. (2009), Jia et al. (2011), Hanotin et al. (2012), Melhus et al. (2012), and Gnoli et al. (2016). A comparison between the effect of random noise with periodic vibrations in numerical simulations of sheared granular media, done by Melhus et al. (2012), suggested that a relevant quantity to rationalize the fludization effect was the injected power, regardless of the details of the dynamics. Note that studies of the response of sheared granular media to external vibrations have often been conducted in the context of understanding dynamic earthquake triggering (Melhus et al., 2012; Griffa et al., 2013). It was

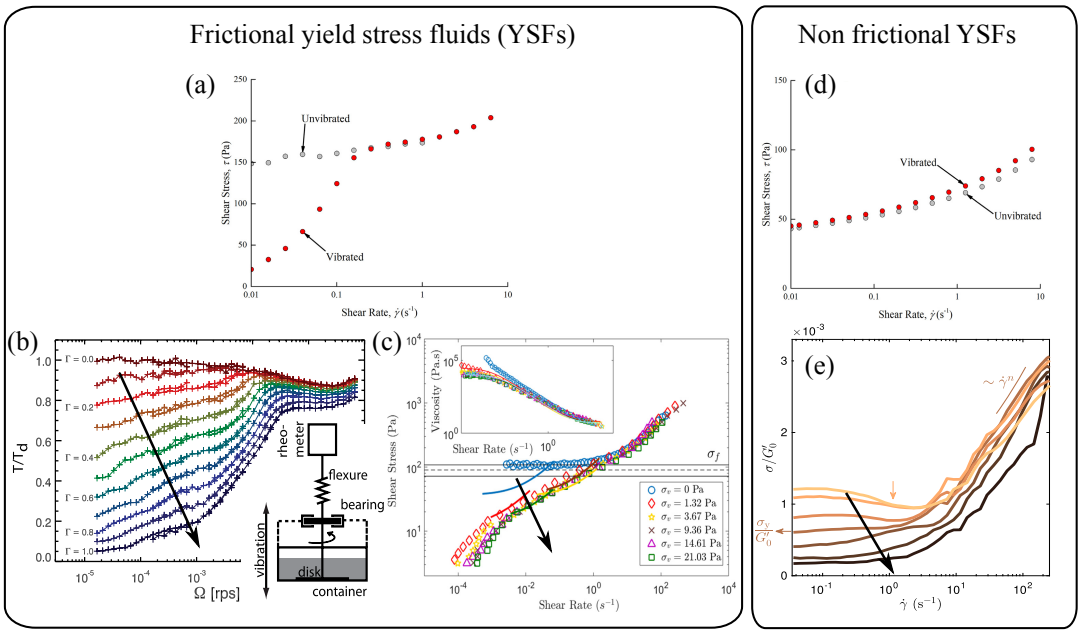

FIGURE 1.12: **Effect of vibration on frictional and non frictional yield stress fluids** (left and right panel respectively, with the arrows showing increasing vibration amplitudes). (a) From Koch et al. (2019): Flow curve for a wet granular medium exhibiting an elimination of the yield stress when vibration is applied by inserting a vibrating probe in the medium. (b) From Dijksman et al. (2011): flow curve of a dry granular material with small amplitude vertical vibrations exhibiting an elimination of the yield stress for any amplitude of vibration. (c) From Gaudel et al. (2017): flow curve for a wet vibrated granular suspension exhibiting a qualitatively similar behavior as (b). (d) From Koch et al. (2019): Flow curve of Carbopol in water, using the same protocol as in (a), not qualitatively altered by vibration. (e) From Gibaud et al. (2020): calcite gel subjected to ultrasonic vibrations (45 kHz) exhibiting a decrease of yield stress with an increase in the vibration magnitude.

for instance found that stick-slip events triggered in presence of vibrations occur in advance compared to samples that are only sheared (Griffa et al., 2013), and this may have an impact in understanding fault dynamics in geophysics.

Different results on the effect of mechanical vibrations were however reported in the case of non-frictional yield stress fluids. A direct comparison between frictional and non-frictional YSFs was done in a study by Koch et al. (2019). Fig. 1.12(a) and (d) depict the flow curves obtained for uniformly vibrated samples in the case of (a) a suspension of glass beads in silicon oil (hard frictional system) and (b) of carbopol (soft frictionless system). While small vibrations amplitudes are sufficient to fluidize a wet granular suspension, this does not affect the rheology of carbopol. This can be understood qualitatively due to the nature of plasticity in these two classes of materials. While in frictional systems, plasticity can occurs both at the particle level (neighbor exchanges) and at the contact (asperity) level, it is restricted to neighbor exchanges in frictionless systems (Andreotti et al., 2013; McNamara et al., 2016). The amplitude of the perturbation needed to induce plasticity in frictionless systems is thus expected to be higher than in the frictional case, since a local stress threshold for neighbor exchanges must be overcome.

Recent experiments using ultrasonic vibrations to tune the rheological properties

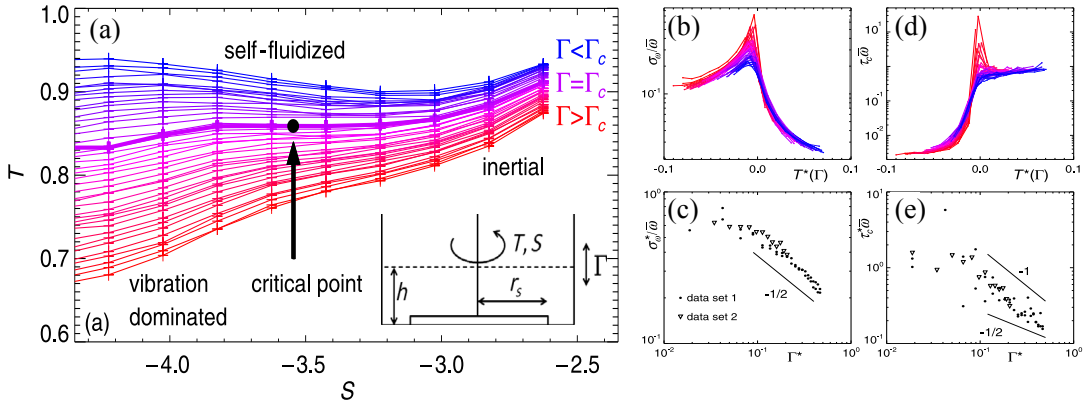

FIGURE 1.13: From Wortel et al. (2016): **Critical dynamics at finite shear and vibration rates in granular media**. (a) Flow curves obtained in a vibrated granular media sheared in a split-bottom cell (schematic): dimensionless torque T as function of the rotation rate (ω) expressed by the dimensionless parameter $S = \log(\omega)$ for various vibration magnitudes Γ, changing from a monotonic to non monotonic behavior for a critical magnitude Γ_c. (b) Fluctuation magnitude (standard deviation of the rotation rate) as a function of the torque T. (c) Maximum fluctuation magnitude as a function of the reduced vibration magnitude $\Gamma^* = \Gamma - \Gamma_c$ exhibiting a power-law decay. (d) Correlation time of the rotation rate as a function of T. (e) Maximum correlation time as a function of Γ^*

of colloidal gels (Gibaud et al., 2020) have evidenced that the rheology of frictionless yield stress fluids (such as calcite gel) could be affected by mechanical vibrations. Instead of an elimination of the yield stress, a systematic decrease of the yield stress with an increase of the vibration intensity is observed (Fig. 1.12(e)).

Competition between self-generated noise and external noise

The flow curves shown in Fig. 1.12(b) and (e) in absence of mechanical vibration exhibit a negative slope for a range of shear rate $\dot{\gamma} < \dot{\gamma}_c$, $\dot{\gamma}_c$ corresponding to the shear rate at which the flow curve exhibits a positive slope again, and varies depending upon the system. As discussed in the previous section (1.2.4), this branch is usually interpreted as the signature of a flow instability that can lead to localized (shear-banded) or metastable flow. Interestingly, in these two cases, this non-monotonic flow curve progressively gives rise to a monotonically increasing flow curve upon increasing vibration magnitude.

In the case of frictional granular systems, this transition from a non-monotonic to a monotonic flow curve (Fig. 1.13(a)) was linked to the existence of a critical point in a study by Wortel et al. (2016). This scenario was supported by measurements of increasingly large fluctuations of the macroscopic shear rate at the approach of the transition, as shown in Fig. 1.13(b-c). It was found that both the magnitude and the correlation time of the fluctuations diverge at the transition, obeying power-law scalings (Fig. 1.13(b-e)).

In the framework of statistical physics, the characteristics of a critical point (exponents describing the scaling of both average quantities and fluctuations) are supposed not to depend on details of the system, but rather only on generic properties shared by a broad class of systems. Do soft glassy materials share a generic critical point in the case of a competition between self-generated and external sources of noise? Can

it be captured using a minimal model for the flow of YSFs? This will be one of the questions addressed in this thesis (Chapter 4).

Internal active noise as another type of flow-independent noise

We mainly discussed so far the case of external sources of noise. Local events such as those induced by a biological activity can also contribute to the mechanical noise in the system, and induce a fluidization of systems exhibiting a yield stress in absence of activity (Mandal et al., 2016; Tjhung et al., 2017; Matoz-Fernandez et al., 2017a; Czajkowski et al., 2019). The next section is dedicated to the dynamics of dense active systems, with a specific focus on the fluidization mechanisms induced by a local activity and the possible analogies between driven and active systems.

Summary of section 1.2

- Soft glassy materials (deep in the glass phase) behave as an elastic solid at rest and can reach a steady state plastic flow if the applied stress exceeds a dynamical yield stress, with a non linear rheology in the flowing regime.
- In the slow driving regime, the stress response to an applied strain is characterized by a succession of loading phases and abrupt relaxation phases as in stick-slip phenomena and the distribution of stress drops follows a power-law behavior related to long-range elastic interactions in the system.
- The "yielding" transition upon increasing strain can be studied using oscillatory shear driving, revealing a sharp transition between a regime of reversible particle trajectories at small strain and a regime where the system deforms plastically and in which particle trajectories become irreversible.
- Plasticity occurs through localized rearrangements of particles that disturb the elastic strain and stress fields in the material, inducing a mechanical noise that can activate other plastic events, thus leading to correlations between localized plastic events and cooperative effects.
- Permanent shear bands can be observed when the rheology is non-monotonic, due to rate weakening effect that can result from diverse microscopic processes like, e.g., flow-structure coupling or inertia at the microscopic scale. Shear weakening due to inertia can be rationalized as a kinetic heating effect inducing softening in the system. Whether kinetic heating due to inertia can actually lead to shear banding and how it can be described at the continuum level remains an open question (Chapter 3).
- Beside the self-generated noise due to plastic events, external sources of noise (independent of the shear rate) can also affect the dynamics and fluidize the system. Such external sources of noise encompass for example thermal noise, external mechanical perturbation or local sources of biological activity. The type of softening or fluidization observed may depend upon the nature of the external noise (Chapter 4 and 5).
- The competition of endogenous noise leading to a rate-weakening effect and fluidizing external noise (mechanical vibrations) has been shown to lead to critical dynamics in experiments on granular systems. The genericity of this scenario remains however to be tested (Chapter 4).

1.3 Dense active materials

Dense active systems, or "active glasses" have been intensively studied in the past decade, as revealed by various recent reviews on the subject (Berthier et al., 2019; Janssen, 2019). Examples of such systems encompass assemblies of biological cells at high density forming a tissue or a biofilm, intracellular medium, or synthetic active systems such as dense suspensions of colloids powered by chemical reactions. These systems have been shown to exhibit glassy dynamics and dynamical arrest although

they are far from equilibrium as, in most cases, thermal fluctuations play no role and the dynamics results from a local (possibly biological) activity. Depending upon the type of activity, the transition to arrested states can take various different forms (Berthier et al., 2019). Moreover, although biological activity is often seen as a factor that tends to fluidize a system that would be glassy in the absence of activity, it was shown in the case of self-propelled particles that departure from equilibrium due to activity can both enhance or diminish glassy dynamics (Berthier et al., 2017).

Beside the interest to study active systems in the framework of non-equilibrium statistical mechanics, motivation to study dense active materials comes from the fact that it is now clear that mechanics plays an important role in various biological processes. It is for instance well accepted that the mechanical properties of biological tissues play an important role in physiological processes such as embryonic development, wound healing and cancer invasion (Alert et al., 2019). Understanding what governs the mechanical properties of dense tissues from the perspective of (active) dense amorphous materials is thus a novel and promising research area. A remarkable example is given by the work of Bi et al. (2015) and Park et al. (2015), where the authors show that the solid-to-fluid transition observed in asthmatic epithelial tissues is related to an underlying geometric jamming transition appearing in a vertex model for epithelial tissues.[3]

This section is organized as follows. We first review some experimental studies of glassy dynamics in active materials. We then emphasize how distinct sources of activity (self-propulsion in different persistence regimes, cell division or death, volume fluctuations) can lead to transitions to dynamical arrest with very different features, and how they can be understood by drawing analogy with (either equilibrium or driven) passive systems. We finally present studies addressing the mechanical response of cells aggregates to deformation and discuss the mechanical response of a material to local active events, and how it could be used as a building block of coarse-grained theoretical descriptions.

1.3.1 Evidences of glassy dynamics in dense active systems

Many phenomena associated with glass physics have been reported in active matter systems in the last decade. In this section, we summarize the main findings regarding glassy dynamics in active matter systems like active colloids, intracellular medium and biological tissues.

Synthetic dense active matter systems

Active colloidal systems have been designed using Janus particles for instance (particles made of one part covered with a catalyst leading to self-propulsion). While many studies focus on the single particle or the low density regime of active colloidal systems, the dense regime was only studied recently (Klongvessa et al., 2019a; Klongvessa et al., 2019b). In this study, glassy dynamics was evidenced upon increasing the density of colloids, and the dynamics was shown to exhibit a nonmonotonic behavior upon tuning the self-propulsion, preventing a simple mapping onto a passive glassy system.

[3]Let us remind that although the terms jamming and glassy are often encountered in the active glass literature, we will refer to the term "glass transition" whenever we are talking about a transition leading to dynamical arrest as a result of a competition between crowding and particle motion (motored by thermal fluctuations or active processes such as self-propulsion), while jamming implies a purely geometrical transition in absence of any dynamics (thermal or active), as suggested by recent review papers on the topic (Berthier et al., 2019; Janssen, 2019).

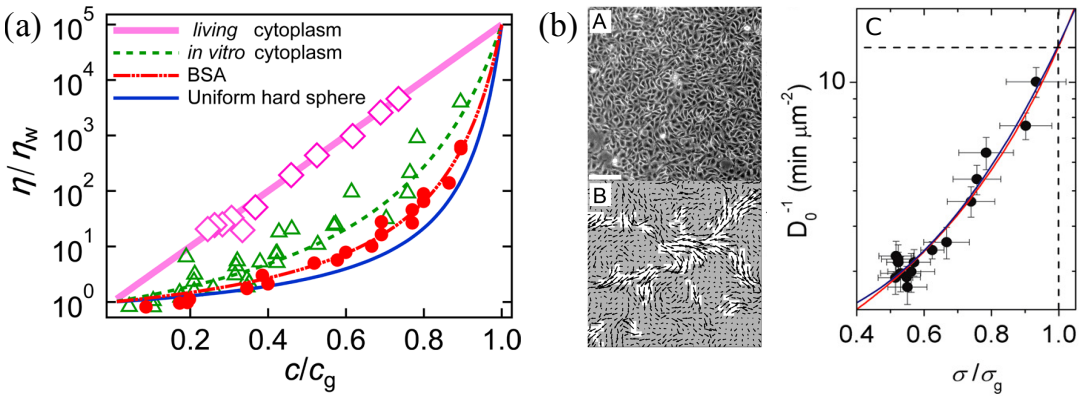

FIGURE 1.14: **Glassy dynamics in biological systems**. (a) From Nishizawa et al. (2017), bacterial cytoplasm: Relative viscosity as a function of the scaled concentration c/c_g (Angell plot) for a bovine serum albumin (BSA) solution (red circles), for cell extracts from E. coli (green triangles), and for cytoplasm in a living cell (pink diamonds). The thick solid line indicates Arrhenius behavior. (b) From Angelini et al. (2011), epithelial tissue: A, B: Confluent epithelial monolayer of MDCK cells exhibiting spatially heterogeneous motion. C: Inverse of the self diffusion coefficient of cells as a function of the scaled cell density σ/σ_g.

Let us mention that other synthetic active matter systems exist, such as colloidal rolling particles (Bricard et al., 2013) or granular systems driven at the level of individual particles through shaking of their substrate (Deseigne et al., 2010), but most studies were conducted in intermediate density regimes.

Intracellular dynamics

The link between intracellular cytoplasmic properties and glass-like properties was first established by Zhou et al. (2009). The mechanical properties of eukaryotic cells are generally thought to be governed by the properties of their cytoskeleton as well as the content of their intracellular space. In their study, Zhou et al. (2009) find that the intracellular space becomes progressively stiffer with increasing osmotic compression, accompanied by a slowing down of the relaxation in the cytoplasm, analogous to the colloidal glass transition (Mattsson et al., 2009). Is is further found that altering the metabolic activity of the cell (by depleting ATP) affects the glass transition, supporting the idea that nonequilibrium processes may modulate the glassy behavior.

Bacterial cells, unlike eukaryotic cells lack motor proteins enabling propulsion of macromolecules in the cytoplasm, and transport properties are thought to by dominated by crowding effects, as found by Parry et al. (2014). They also find that while metabolically inactive bacteria exhibit glassy dynamics (very slow and dynamically heterogeneous transport properties), metabolic activity fluidizes the cytoplasm.

In another study, Nishizawa et al. (2017) study both eukaryotic and prokaryotic cells, in both *in vivo* and *in vitro* conditions, where the metabolic components and cytoskeleton of the cell have been removed. Their results are depicted in Fig. 1.14(a). They find that living cells are usually associated with a strong glass former kinetic behavior (Arrhenius-type growth of the viscosity upon crowding) and that inactive cells (*in vitro* conditions) exhibit a fragile kinetic behavior. Interestingly, computer simulations of a minimal model for actively deforming particles by Oyama et al. (2019) yield similar conclusions (model further discussed in section 1.3.2).

Intercellular dynamics (biological tissues)

An increasing number of studies indicates that glass physics is also encountered at the intercellular level in multicellular systems such as biological tissues. Most of the recent studies are conducted on epithelial monolayers: two-dimensional confluent amorphous cell sheets (i.e., with a packing fraction of unity).

Madin–Darby Canine Kidney (MDCK) monolayers are a widely used model system to study the dynamics of epithelial tissues (Fig. 1.14(b)-A). In their study, Angelini et al. (2011) evidence both a slowing down of the relaxation dynamics (as quantified from, e.g., the self-diffusion coefficient of cells in Fig. 1.14(b)-C) and an increase in the dynamical heterogeneity across the MDCK monolayer as the cell density increases during the experiment. Slowing down of the dynamics with increasing cell density is also reported by Garcia et al. (2015) in another type of epithelium, constituted of human bronchial epithelial cells (HBEC). Interestingly, non-trivial correlations in the instantaneous cell velocity are found, which constitutes a major difference with equilibrium systems, where instantaneous velocities are uncorrelated. The interpretation of Garcia et al. (2015) is however slightly different as it points towards aging features that do not depend on the density, but rather on maturation of cell-cell and cell-substrate adhesions during the experiment, which has no equivalent in the physics of passive glasses. It is also important to mention that although the phenomenology of epithelial monolayers resembles, in some aspects, that of conventional glass-forming systems, the relaxation mechanisms at play in these systems have a fundamentally different origin. In epithelial layers, the dynamics is governed by the self-generated propulsion of cells, but also by additional active processes such as cell division (mitosis), programmed cell death (apoptosis) and active cell deformations such as volume fluctuations. All these processes are absent in inert systems such as colloidal glass-forming systems, and their impact onto the dynamics and the transition to dynamical arrest will be addressed in the next section (section 1.3.2).

As already mentioned in the introduction, studying the glassy behavior of an epithelial tissue may be relevant for pathological conditions such as asthma, as realized by Park et al. (2015). Their study of HBEC monolayers reveals that the cell dynamics of non-asthmatic donors undergoes a transition from a fluid-like state to a glass-like state as the tissue matures over time, while asthmatic epithelia remain mobile and exhibit a delayed glass-like transition. They also remark that fluid-like tissues are characterized by an average shape ratio between the cell perimeter and the square root of the cell area larger than 3.81 while solid-like tissues are characterized by small values of this shape ratio. The link between structural (or geometrical) and dynamical properties of tissues plays a crucial role in understanding the rigidity transitions observed in dense tissues (Bi et al., 2014; Bi et al., 2015). In particular, it has led to the development of numerous vertex-based models for the dynamics of tissues, which will be further discussed in section 1.4.

Glassy dynamics was also reported in three-dimensional assemblies of cells, as shown for instance in tissue explants of zebrafish embryos by Schoetz et al. (2013). It now is believed that solid-to-fluid transitions may play an important role during development, where both phases of collective cell migration and arrested glass-like states are observed (Park et al., 2016). This has been evidenced *in vivo* by Mongera et al. (2018) in a recent work studying the process of zebrafish vertebrate body axis elongation. During this developmental process, the mean displacement of progenitor cells is found to decrease as they move from a region (mesodermal progenitor zone, MPZ) to another (presomitic mesoderm, PSM), where they get arrested. By performing measurements of the local mechanical response, Mongera et al. (2018) further

evidence the existence of a yield stress in the tissue, with a gradual increase from MPZ to PSM correlated with the concentration of adhesion proteins. The study also reveals stress fluctuations above the yield stress in the MPZ phase (and below the yield stress in the PSM), consistent with a picture of fluidization by active processes at the cell-cell contact level generating stress fluctuations leading to cell intercalations and hence to a fluid-like behavior. This study thus suggests that a spatio-temporal control of fluid-like and solid-like properties of tissues may represent a mechanism at play during embryonic morphogenesis.

Concluding remarks

It is now clear that dense active and living systems exhibit several hallmarks of glassy dynamics. This has been evidenced both at the intracellular and intercellular level, in two and three dimensions, and in various biological contexts (in healthy and pathological tissues, in developing tissues, etc.).

Beside developmental processes, let us mention that glassy dynamics also potentially plays an important role in cancer invasion (see Park et al. (2016) and Oswald et al. (2017) for a review), which is related to the ability of cells to move collectively. Actually, the topic of collective cell migration is even a broader topic than the physics of active glasses or the physics of cancer, and has attracted a great interest in the past decade (Ladoux et al., 2017; Alert et al., 2019). A large variety of collective migration modes (flocks, swirls, velocity oscillations, etc.) has been reported in dense tissues, and a more detailed introduction to this topic will be given in Chapter 6, which is dedicated to modeling collective wave-like dynamics of the cell velocities in epithelial monolayers.

Various distinct active processes are at play in living tissues, and it is often difficult to disentangle the contributions of distinct sources of activity. Various experimental approaches exist, such as turning down metabolic activity by depleting ATP, inhibiting cell division or cell contractility using targeted drugs, etc., but they are often difficult to control as many coupled phenomena and feedback mechanisms are at play in biological systems. Computer simulations thus constitute a powerful complementary approach to study active glasses since they allow to tune specifically the relevant parameter controlling activity, and, by resolving single particle trajectories, enable one to compute a large number of observables. Numerical studies have thus shed light on the nature of the solid-fluid transitions observed in dense active systems, and we will review the main outputs of these studies in the next section. The different types of numerical approaches will be the topic of section 1.4.

1.3.2 Solid-to-fluid transitions in dense active matter

In all of the active systems mentioned in the previous section, the motion of particles is controlled by the magnitude of the active driving of biological, chemical, or mechanical origin. The dynamics is fully arrested when activity is turned off, and the particles may start to diffuse and exhibit rich dynamics for finite levels of activity. The description of the transition between a dense amorphous solid and a fluid controlled by active forces remains a largely open question (Berthier et al., 2019). What type of microscopic dynamics can be expected at the transition? How does it depend on the type of activity? Can this be described theoretically using simplified models of active matter? We review in this section the main numerical and theoretical findings regarding active solid-to-fluid transitions for different types of activity: self-propulsion of particles, active deformation, cell division and cell death.

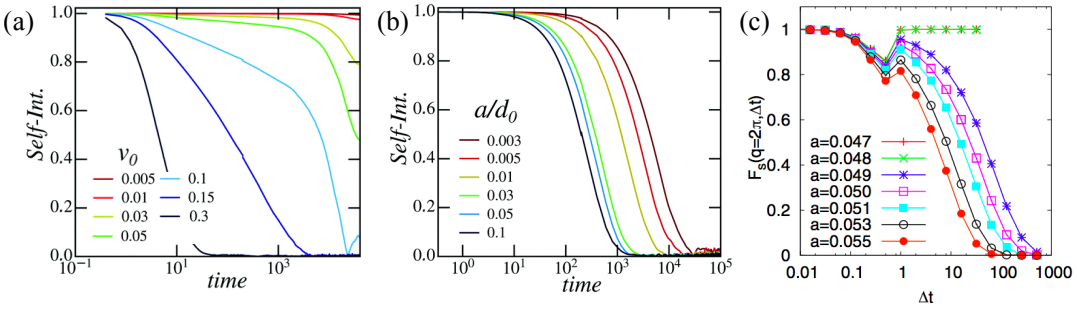

FIGURE 1.15: **Self-intermediate scattering function for distinct local active processes** in 2d particle-based models. (a) From Matoz-Fernandez et al. (2017b): System of self-propelled particles in the small persistence time regime, for various values of the self-propulsion velocity v_0, exhibiting a glass-like transition. (b) System of particles endowed with division and death mechanisms at rates d_0 and a respectively, always exhibiting a fluid-like behavior. (c) From Tjhung et al. (2017): System of actively deforming particles exhibiting a discontinuous fluidization at a deformation amplitude $a = a_c \simeq 0.049$

Self-propulsion

In self-propelled particle systems, the motion of particles is governed, aside from particle interactions, by active self-propulsion forces that are often characterized by two parameters: the magnitude of the self-propulsion force and its persistence time (time before changing direction). This brings two additional parameters, in addition to temperature and density. Temperature is often neglected to reduce the parameter space of the model and we will focus here on athermal active systems. More details on microscopic simulations can be found in section 1.4.

Models of self-propelled particles Let us first present the two main classes of microscopic models used to study the role of self-propulsion: active Brownian particles (ABPs) (Romanczuk et al., 2012) and active Ornstein–Uhlenbeck particles (AOUPs) (Szamel, 2014). In ABP models, particles have a constant self-propulsion velocity and propel along a polarity vector rotating by a slow rotational diffusion. This model, intended to represent active colloids, has been used to study motility-induced phase separation (Cates et al., 2015) but also active glassy dynamics (Ni et al., 2013; Fily et al., 2014), and as a minimal model of epithelial tissues (Henkes et al., 2020). On the other hand, for AOUPs, each component of the self-propulsion velocity follows a Ornstein-Uhlenbeck stochastic process, leading to a persistent random walk dynamics characterized by a persistence time and an effective temperature which quantifies the magnitude of the active force. These two models are generally considered in the overdamped limit and both reduce, in the limit of vanishing persistence time, to a passive Brownian system.

Non-equilibrium glass transition for self-propelled particles In a study of ABP model with a hard sphere potential, Ni et al. (2013) find that when increasing the self-propulsion velocity the apparent volume fraction of the glass transition moves to larger values. Fily et al. (2014), using a soft repulsive potential, also report an arrested phase at low activity and large density. They find that in the limit of small persistence time, the system reduces to an equilibrium system with an effective temperature $T_{\text{eff}} \propto v_0^2$ with v_0 the self-propulsion velocity. The intermediate scattering function measured

for various self-propulsion velocities (Matoz-Fernandez et al., 2017b) is depicted in Fig. 1.15(a) and resembles that of Fig. 1.2 for equilibrium glasses.

A more detailed study of the glass transition was conducted by Berthier and coworkers for the AOUP model with a WCA interaction potential (Weeks et al., 1971) (see Berthier et al. (2019) and references therein). In their work, they fix the effective temperature T_{eff} and study how the glassy behavior is affected by departing from equilibrium, i.e., increasing the persistence time τ_{p}. They find that the structure of the supercooled liquid (as characterized by the pair correlation function) is affected by an increase of τ_{p}, leading, depending upon the T_{eff} range, to an effective short-range attraction resulting from the competition between repulsion and self-propulsion (predominant at low T_{eff}) and/or to an increase of the effective particle radius with τ_{p} (predominant at high T_{eff}) (Berthier et al., 2017). They also evidence non-trivial velocity correlations for finite persistence time, implying a form of collective motion (Szamel et al., 2015). Moreover, increasing the persistence time affects the glass transition in a nonmonotonic way. While at low T_{eff}, an increase in the persistence time shifts the glass transition towards larger densities, the opposite effect is observed for larger T_{eff}. This non-trivial dependence shows that departing from equilibrium can either promote or depress glassy dynamics.

Large persistence time: possible analogy with sheared amorphous solids The large (but finite) persistence time limit of athermal ABPs was recently studied by Mandal et al. (2020a). Interestingly, this regime is characterized by intermittent dynamics in the kinetic energy, as a consequence of long arrested periods followed by bursts of plastic yielding (cage breaking by self-propelled particles) associated with Eshelby deformations fields (see Fig. 1.18(b)), akin to the response of dense amorphous solids to an externally imposed shear (Fig. 1.18(a)). Note that for an infinite persistence time, the system can reach a state of dynamical arrest where all active forces are balanced.

Models with aligning mechanisms Studies attempting to describe epithelial tissues have used more sophisticated models, incorporating aligning mechanisms (see, e.g., the review by Camley et al. (2017)). In the seminal work of Henkes et al. (2011), an additional coupling mechanism incorporated in ABPs tends to align the direction of self-propulsion to the direction of velocity at the single cell level. This results in large-scale coordinated motion, and slow oscillations of the cellular packing. Other types of interactions (Viscek-like for instance (Vicsek et al., 1995)) have been considered to model collective oscillations in epithelial tissues as done by Deforet et al. (2014). We will come back to this point in Chapter 6, when studying a model for the emergence of collective oscillations in an epithelium.

Note that the influence of other forms of motility has also been addressed in the literature, such as, e.g., the solid-to-fluid transition observed in a system of active particles endowed with an active torque (self-rotation mechanism) by Ravazzano et al. (2020) (inspired by the dynamics of microswimmers such as *Chlamydomonas reinhardtii*).

Cell division and apoptosis

Cell division and apoptosis are important phenomena governing the dynamics of biological tissues. Large apoptosis rates can lead to a vanishing tissue, while cell division can lead to tissue growth. If cell death and division are statistically balanced, the system can reach a non-equilibrium steady state.

Matoz-Fernandez et al. (2017b) have studied the effect of cell division and cell death on the dynamics of a numerical model of soft particles. The system exhibits a rich phase diagram, and they find that, in the dense confluent regime, the system is fluidized for any positive rate of cell apoptosis and division, in agreement with Ranft et al. (2010). As a consequence, no glass phase is observed, as illustrated by the self-intermediate scattering function in Fig. 1.2(b), always relaxing at long time for any rate of activity. Similar results are reported by Malmi-Kakkada et al. (2018) in a model of growing tri-dimensional tissue.

This result has however been contrasted in a recent work by Czajkowski et al. (2019), where the authors report the existence of a glassy phase in vertex-based simulations for small enough death and division rates. Various differences between the two models (and dynamical rules) could contribute to these contrasted results, but there is, so far, no consensus on the existence of a solid-like phase in a dense system of particles endowed with division and death processes.

To summarize, including both cell division and apoptosis in the dynamics leads to nonequilibrium steady states where the number of particles is conserved on average. This case has been studied both in the context of particle-based and vertex-based models (Ranft et al., 2010; Matoz-Fernandez et al., 2017b; Czajkowski et al., 2019) and was shown to lead to a visco-elastic behavior, where the long time flow behavior is governed by the rate of cell division/ apoptosis, as proposed theoretically by Ranft et al. (2010).

Note that in the case where cell division is not compensated by cell death, as studied by Tjhung et al. (2020), this leads to a global growth of the tissue. Although energy injection still occurs at the particle scale, this results in a global macroscopic driving, in the form of an expansion rate. The dynamics in that case is similar to that of a soft glassy material subjected to a global shear rate, leading to plasticity and flow. The microscopic dynamics of the system is thus never arrested but shows dynamical features directly controlled by the global radial growth rate. The plasticity observed in that case results both from cell division events and from the global macroscopic driving.

Active deformation

Active deformations of cells in epithelial tissues are a widely observed phenomenon, that can originate from, e.g., active fluctuations of cell-cell interfaces (Guillot et al., 2013) and important cell volume fluctuations (Spring et al., 1982; Zehnder et al., 2015a; Dasgupta et al., 2018). A large variety of spatio-temporal dynamics of active deformations has been reported, from highly fluctuating dynamics to oscillations of synchronized groups of cells (Curran et al., 2017; Zehnder et al., 2015a). Moreover, cell deformation is an active process that may be coupled to both internal and external forces and biochemical signals, potentially leading to complex feedback mechanisms.

Recent works have addressed the solid-to-fluid transition resulting from active fluctuations of the junction tension resulting in cell-cell contact length fluctuations using the framework of vertex models (Krajnc, 2020; Kim et al., 2020). Krajnc et al. (2018) find a solid-to-fluid transition very similar to the transition induced by a change in target shape index in vertex models, suggesting that the mechanism for this transition may be independent of the underlying source of fluctuation. In their study, Kim et al. (2020) develop a computational framework including features of both vertex and particle-based models (accounting for extracellular space) and evidence a solid-to-fluid transition governed by active tension fluctuations occurring both in confluent and non-confluent systems. Their work highlights a complex interplay of cell adhesion,

Parameter	Model	Reference and description	Proposed transition
Target shape index Interfacial tension	Vertex	Bi et al. (2014)	"rigidity"/jamming
	Cellular Potts	Chiang et al. (2016)	glass
Self-propulsion	Particle	Berthier (2014) (AOUPs)	glass
		Fily et al. (2014) (ABPs)	glass
		Mandal et al. (2020a): large persistence time	yielding (avalanche dynamics)
		Ravazzano et al. (2020): self rotation	n.s.
	Vertex and Voronoi	Czajkowski et al. (2019) Bi et al. (2016) and Sussman et al. (2018)	glass
	Cellular Potts	Chiang et al. (2016)	glass
Cell division apoptosis	Particle	Ranft et al. (2010): steady state Matoz-Fernandez et al. (2017b)	none (fluid)
		Tjhung et al. (2020): expanding system	none (rate imposed flow)
	Vertex	Czajkowski et al. (2019): steady state	glass
Active deformation	Particle	Tjhung et al. (2017): oscillatory or random radius fluctuation	discontinuous yielding glass
	Vertex	Krajnc (2020) and Kim et al. (2020): active junctions fluctuations	n.s.

TABLE 1.1: **Examples of solid-to-fluid transitions in numerical models of (athermal) dense active systems** (n.s. stands for non specified)

cell tension and density explaining the mechanical behavior of the tissue, which may reconciliate findings of particle and vertex-based models (see section 1.4).

Cell volume fluctuations have been studied within a particle-based model by Tjhung et al. (2017). In this model, the only source of activity is given by active changes of the particle volume (by prescribing a dynamics for the radius of each particle). In the case of a random driving (persistent random walk of the particle radius), the authors find a fluid-to-solid transition upon decreasing the activity that has the features of an ordinary equilibrium like glassy dynamics. On the other hand, a sharp fluid-to-solid transition is observed for a purely periodic driving (or if the frequencies are weakly distributed), that does not resemble glassy dynamics (see the intermediate scattering function in Fig. 1.2(c)). This transition between an arrested state for small volume fluctuations and a fluidized state occurs at a finite activity magnitude and appears discontinuous, resembling a nonequilibrium first-order transition. The authors argue that, in this case, the proper analogy with the physics of glasses is not with the glass transition itself but rather with the yielding transition of amorphous solids driven with an oscillatory shear protocol. The physical picture is that volume fluctuations act as a slow driving force in the material, and local fluidization occurs when that force exceeds a threshold, as for yielding.

Concluding remarks

It is clear that biological activity can induce a transition from a solid-like to a fluid-like state, although the type of transition can differ depending upon the source of activity (or type of interaction), as summarized in Table 1.1. As illustrated in the last column of Table 1.1, various different analogies have been proposed between the solid-to-fluid transitions observed in dense active systems and in inert systems (thermal or driven).

Recent studies address the origin of these similarities from a theoretical perspective (Morse et al., 2020), although a general framework is still lacking. In particular, the type of dynamics expected at the transition depending upon the type of local activity and its temporal dynamics remains a largely open question.

The case of particles with active volume fluctuations, where the temporal dynamics can be easily tuned from purely oscillatory to colored random noise as done by Tjhung et al. (2017), constitutes an example of simple model to approach questions such as: (i) What are the mechanisms at the origin of the fluidization? (ii) What is the influence of having a local driving versus a global driving in a dense system? (iii) How is the fluidization transition affected by a change in temporal dynamics of the activity? The work of Tjhung et al. (2017), conducted in parallel with studies on the yielding of amorphous solids in oscillatory shear driving (Kawasaki et al., 2016; Yeh et al., 2020), suggests that there are indeed strong similarities between oscillatory volume fluctuations at the particle level and systems sheared with an oscillatory driving. In this thesis, we want to further investigate these similarities at a coarse-grained level, using mesoscale elasto-plastic models for the deformation of amorphous solids. This approach enables us to probe in particular what are the minimal ingredients required to explain the fluidization observed in a system of actively deforming particles (see Chapter 5).

We briefly mentioned the existence of feedback mechanisms between biochemical and mechanical processes in biological tissues. An important consequences of these complex feedback loops is that, unlike inert materials where phase changes (e.g., from a solid-like to a fluid-like state) are controlled by externally tuned parameters such as temperature or density, living materials can tune themselves into different states through regulatory biochemical and/or genetic pathways acting on cell motility, cell cycle and phenotype changes. Famous examples include contact inhibition of cell division (Martz et al., 1972) and contact inhibition of cell locomotion (Mayor et al., 2010) upon an increase in cell density in tissues. To what extent these behaviors can emerge from simple physical rules remains however an open question (Recho et al., 2019; Bertrand et al., 2020; Buttenschön et al., 2020).

The (time-dependent) rheology of tissues is therefore affected by active processes occurring at various length and timescales, and by their regulation due to the cross-talk between mechanical and chemical signaling. In the next section, we present a few experimental studies of tissue rheology and some of the biological processes contributing to the observed behavior.

1.3.3 Rheology of dense active and biological systems

Understanding how local active processes influence the relaxation in dense active systems and hence the macroscopic rheology when a system is subjected to mechanical forcing has been the focus of various studies in the recent years. This has not only implications in modeling the mechanics of biological tissues, but also in understanding biological morphogenetic processes: how do local active events contribute to shaping tissues? How does a tissue maintain mechanical integrity despite large scale flows of cells during developmental stages? (Collinet et al., 2015; Mongera et al., 2018)

Let us mention that the rheology of biological materials is an extended research field that we will not cover here. It is much broader than the mechanics of epithelial tissues and covers for instance the rheology of single cells, as well as its sub-cellular elements constituting the cytoskeleton (actin gels for instance), the rheology of connective or contractile tissues, etc. (Verdier et al., 2009).

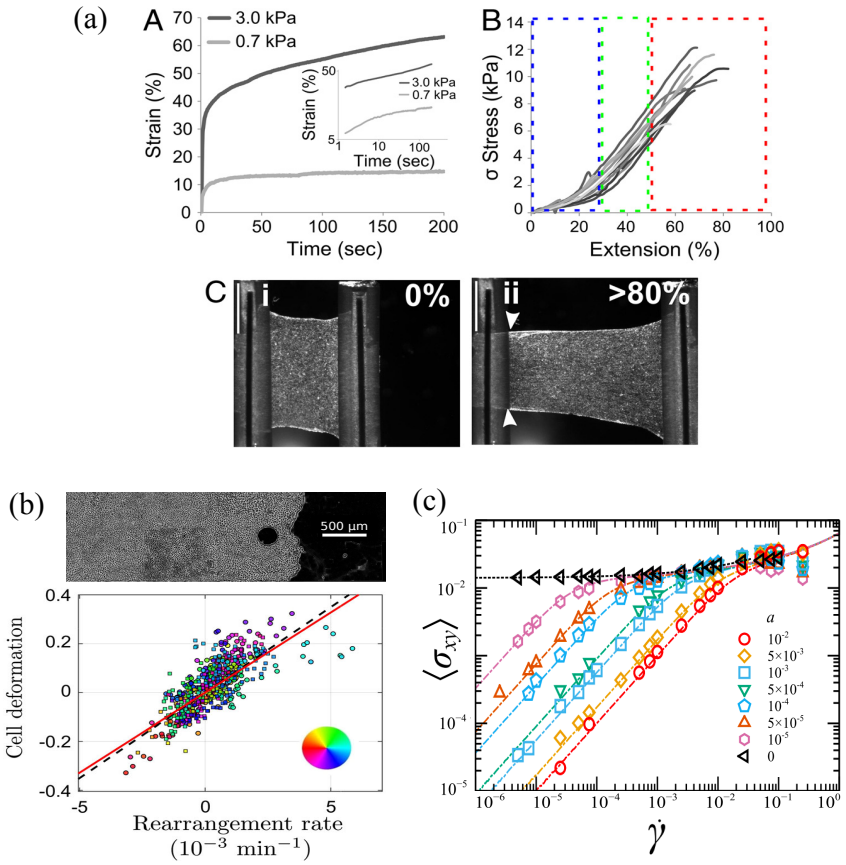

FIGURE 1.16: (a) From Harris et al. (2012): **Mechanical characterization of a cell monolayer**. A: Creep response exhibiting a strain plateau at low stress and a continuous strain increase at high stress. B: Stress-extension curves displaying three distinct regimes of loading: initial loading phase (blue box), linear extension regime (green box) from which an elastic modulus can be calculated, and a plateau (red box) corresponding to plastic deformation and eventual failure. C: Bright field microscopy images of the deformed monolayer under stretch at 0 and >80 % extension. (b) From Tlili et al. (2020): **Experiment of an MDCK epithelial monolayer migrating around a circular obstacle**. Cell deformation as a function of the cell rearrangement rate indicating a viscoelastic behavior with a relaxation time of about 70 min. (c) From Matoz-Fernandez et al. (2017a) **Flow curve for a particle-based model of tissue with cell division and apoptosis** exhibiting a Herschel-Bulkley rheology in absence of activity and a Newtonian rheology at low shear rate with a viscosity depending on the apoptosis rate.

Rheological behavior of tissues

On the experimental side, experiments performed on embryonic tissues (Petridou et al., 2019), multicellular spheroids (Marmottant et al., 2009; Guevorkian et al., 2010), or cell monolayers with or without substrate (Harris et al., 2012; Nnetu et al., 2013; Vincent et al., 2015; Tlili et al., 2020) have evidenced elastic, plastic and viscous flows behavior depending on the forces applied and on the timescale of observation (Wyatt et al., 2016). Fig. 1.16 depicts two examples of experiments performed to characterize the rheological behavior of epithelial monolayers: by imposing a tensile deformation to a freely suspended monolayer (Fig. 1.16(a), from Harris et al. (2012)) or by studying the dynamics of an epithelial tissue migrating around an obstacle on a substrate (Fig. 1.16(b), from Tlili et al. (2020)). These two experiments exhibit elastic, viscoelastic and plastic deformation regimes (see caption of Fig. 1.16).

Living tissues are thus generally seen as viscoelastic materials with both physical and biological mechanisms contributing to their time-dependent material properties. Over relatively short timescales (of the order of 10 seconds), tissues respond essentially as passive elastic media. They often display non-linear response to deformation, suggesting that some constituents may be solicited above a certain strain threshold (Phillips et al., 1978; Harris et al., 2012). On the other hand, on longer timescales (tens of minutes to hours), tissues exhibit a liquid-like behavior, associated with (plastic) cell rearrangements (Phillips et al., 1978; Guevorkian et al., 2010). On intermediate timescales (tens of minutes), cell aggregates behave as viscoelastic materials as many soft matter systems like gels, polymer melts, etc. In this regime, the stress is not totally dissipated, indicating the existence of structures able to sustain elastic deformation and some slow relaxation processes occur leading to slow flow (or creep) behavior (Harris et al., 2012; Guillot et al., 2013).

Processes at the origin of tissue mechanical properties

The different mechanical regimes in tissues can be explained by various dynamical processes occurring at diverse length and timescales as shown in Fig. 1.17 (from Khalilgharibi et al. (2016)).

Intracellular processes The rheological properties of single cells indeed affect the mechanical behavior of the tissue. The cell cytoskeleton is generally thought as the most important mechanical structure of the cell, playing an important role in cell shape and motility. The rheology of the actomyosin network, an important component of the cytoskeleton, has been studied in great detail and depends upon the turnover rate of actin filaments, the dynamics of cross-linker proteins as well as the dynamics of myosin motors (Fletcher et al., 2010). All these processes can moreover be regulated by biochemical signaling pathways. At the continuum level (and within a near-equilibrium assumption), active gel theories have been able to account for the rheological behavior of actomyosin gels (Prost et al., 2015). Myosin contractility is also thought to play an important role in tissue dynamics and rheology. Note that on very short timescales (second or shorter), biochemical reactions within the cell, intracellular fluid flows and poroelastic effects may also have an impact on the tissue mechanical response (Kollmannsberger et al., 2011; Moeendarbary et al., 2013).

Intercellular processes Short time (and small strain) measurements of the mechanical response of tissues reveal stiffness values that can be of the order of or larger than (by a few orders of magnitude) that of single cells. Intercellular junctions are

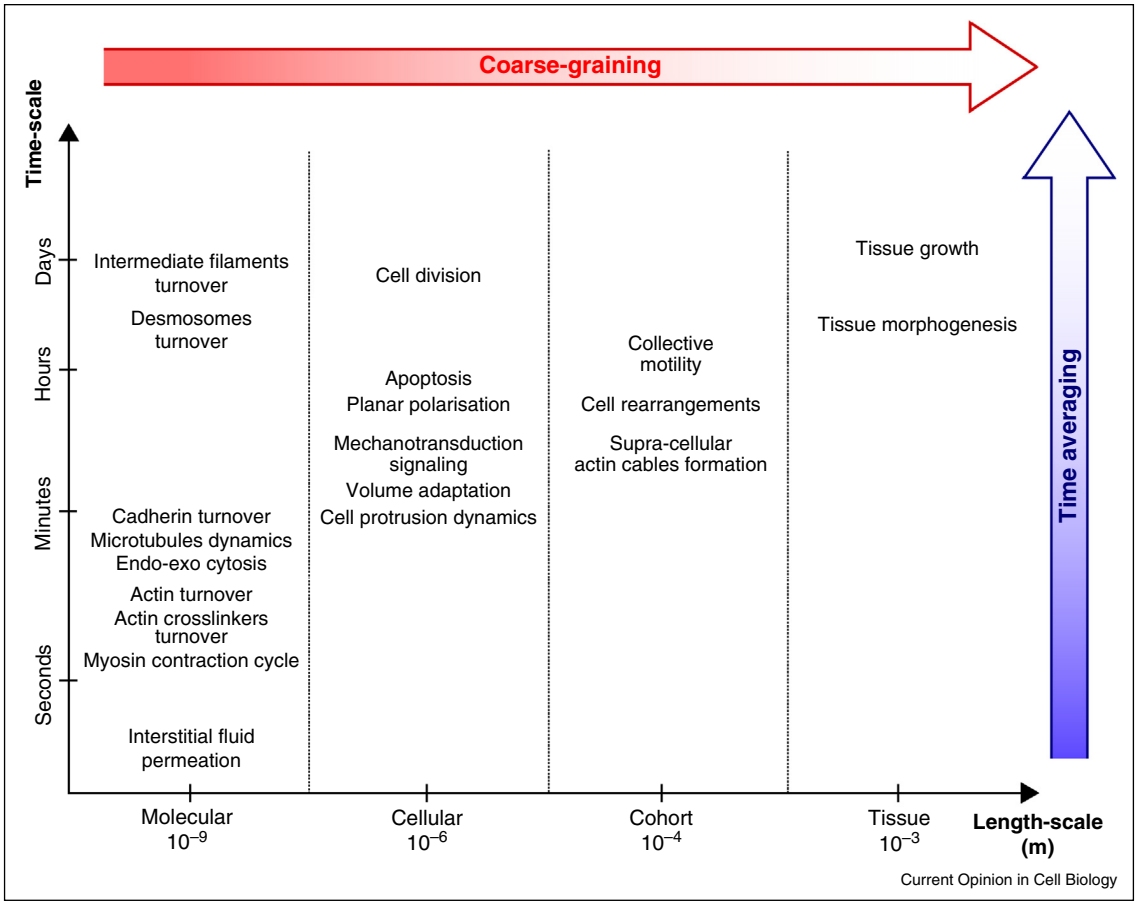

FIGURE 1.17: From Khalilgharibi et al. (2016). **Modeling biological tissues at various lengthscales (molecular, cellular, cohort of cells and tissue) and timescales**. Biological processes contributing to aggregate rheology classified according to their lengthscale and timescale. A computational model can exclude structures smaller than a chosen scale (process known as coarse-graining, red arrow), and can seek to represent dynamics only above a chosen timescale (time averaging, blue).

thus thought to mechanically stabilize the tissue (Guillot et al., 2013). Cell contacts result from the competition of adhesion forces that stabilize cell-cell interfaces and cortical tension exerted by the actomyosin network of each cell that tends to reduce cell contacts (Lecuit et al., 2007). Adhesive contacts between cells (adherens junctions mainly mediated by cadherin molecules) link the actin cytoskeleton of neighboring cells, thus contributing to an overall tissue tension (Harris et al., 2012).

Dynamical processes like mechanotransduction signaling (i.e., transduction of a mechanical signal into a biochemical response) at the junctions or in the cytoskeleton or biochemical turnover within the junction occur at intermediate timescale (minutes to hours) and may contribute to the visco-elastic relaxation observed at intermediate timescales in tissues, like slow creep or viscoelastic flow behaviors. On longer timescales, junction remodeling occurring during cell rearrangements, cell division, extrusion, etc. contributes to the liquid-like behavior (Guillot et al., 2013).

Although these different mechanisms start to be well characterized, the relative importance of junctional actomyosin, cortical tension and cadherin mediated adhesion in explaining tissue mechanics is still an open question in the field (Khalilgharibi et al., 2016). Cellular events like cell rearrangements, divisions, etc., may contribute importantly to tissue mechanical properties. Their impact may further depend on their orientation with respect to the stress field, as evidenced in *Drosophila* embryonic development for instance (Etournay et al., 2015). Such events also disturb the stress and strain fields and can induce mechanical noise in the system, as we will see in the next section.

Modeling biological processes at diverse lengthscales and timescales It is often difficult to capture, within a unique model, the different "short time" phenomena occurring in tissues and at the same time the viscous-like behavior observed on long timescales. Some computational models attempt to describe in detail molecular scale mechanisms and couple biochemical signaling and mechanics, but this approach requires a large number of parameters and can be computationally expensive (Brodland, 2015). A more commonly used approach consists in averaging the processes occurring at length and timescales smaller than the phenomenon under study in order to construct effective rheological parameters (a procedure called "homogeneization" in mechanics). This approach is particularly efficient when there is a clear timescale separation between the phenomenon under study (e.g., long time tissue relaxation) and molecular scale processes (such as actin cytoskeleton turnover).

At the numerical level, particle-based models have been used to understand collective cell dynamics, crowding effects, and the role of particular cell-scale processes like self-propulsion and cell division or apoptosis, as presented in the previous section. Studies addressing more specifically the rheology will be presented in the next section. Particle-based methods are however not suited to describe cell morphologies and the role of cell-cell junctions in tissue rheology, and vertex-based or cellular Potts models are preferred in that case as they explicitly describe cell morphologies and incorporate ingredients such as intercellular adhesion energies, cortical tensions and bulk elasticity.

Finally, coarse-grained descriptions at scales larger than the cell scale lead to continuum models for tissue mechanics. It is interesting to note that while Ranft et al. (2010) model a tissue as an active elastic medium exhibiting an effective viscous behavior at long time, Blanch-Mercader et al. (2017a) show, describing an epithelial monolayer as an active viscous fluid, that an effective tensile elastic modulus can emerge as resulting from active dynamics. These examples illustrate that both elastic and viscous constitutive modeling can be used to describe the dynamics of tissues,

and are able to reproduce experimental observations such as velocity oscillations in epithelial monolayers (see Banerjee et al., 2019 for a review), provided that mechanical variables are coupled to internal degrees of freedom such as contractile activity, cell division or cell polarity. All these modeling approaches will be presented in greater detail in section 1.4.

To summarize, a large number of biological processes at diverse lengthscales and timescales affect the rheology of biological tissues. When it comes to modeling, a practical approach is to choose a particular scale and average ("coarse-grain") the dynamical mechanisms occurring at smaller scales. Even using this coarse-graining procedure, there are still several distinct processes at play in tissue dynamics, as summarized in the second column of Fig. 1.17, such as cell motility, cell division and death, cell volume changes, etc. From a more fundamental point of view, one may be interested in understanding how a specific active process at the cellular scale affects the rheology of the system (in a similar way we asked how it could affect the solid- or fluid-like state in the previous section). In the following, we present a few studies investigating how such processes may affect the rheology of dense active systems.

Tissues as fluidized yield stress materials

Biological tissues can be seen as yield stress materials where active dynamics induces stress fluctuations that lead to fluidization of the system (Matoz-Fernandez et al., 2017a; Mongera et al., 2018; Kim et al., 2020; Popovic et al., 2020). The experimental evidences of glassy behavior and, more generally, of various types of solid-to-fluid transitions induced by activity support this scenario. Understanding how these local active mechanisms (e.g., active fluctuations of junctional tension, cell division and apoptosis events, etc.) are related to the long time visco-elastic relaxation times measured in tissue deformation experiments remains an important question (Ranft et al., 2010; Matoz-Fernandez et al., 2017a; Czajkowski et al., 2019; Tlili et al., 2020). There is no global picture yet, and little is known about the additivity of the different active sources of stress fluctuations in the system (Czajkowski et al., 2019).

Macroscopic picture A theoretical study by Ranft et al. (2010) shows that while the tissue is described as an active elastic medium at short timescales, it behaves effectively as a viscoelastic fluid when accounting for the disturbance of stress field by division and apoptosis events, with a viscoelastic relaxation time set by the rates of division and apoptosis. Matoz-Fernandez et al. (2017a) further find, using particle-based simulations, that the rheology is actually non linear, with a Herschel-Bulkley type flow curve in the absence of biological activity and a fluidized branch at low shear rates (when the shear rate is of the order of the apoptosis rate), reminiscent of the flow curves observed for vibrated granular media, as shown in Fig. 1.16(c).

On the other hand, by studying the rheology of a freely migrating epithelial monolayer using a Stokes experiment, Tlili et al. (2020) reveal a visco-elastic behavior with a relaxation time much shorter than the one associated with cell division, and thus not affected by changes in the division rate (Fig. 1.16(b)). The relaxation time is however found to increase when myosin contractility is inhibited, indicating that in this case, contractility is key to fluidize the tissue. It is also found to depend on the migrating velocity, suggesting a rheo-fluidizing behavior.

Mongera et al. (2018), by performing *in vivo* measurements in zebrafish embryo, evidence a finite yield stress in the tissue and show that fluid-like regions have higher stress fluctuations correlated with higher cell-cell contact length fluctuations. Reducing myosin contractility leads to smaller cell-cell contact length fluctuations and

an increased yield stress value, also supporting the scenario of contractility-mediated fluidization.

Microscopic picture The effect of a specific local active event on the strain and stress fields can be investigated in microscopic simulations of active models. In Fig. 1.18, we show the displacement fields of particles surrounding individual localized events in the case of (a) a localized rearrangement in sheared amorphous solids (Puosi et al., 2014), (b) self-propelled particles with a large persistence time (Mandal et al., 2020a) and (c) division and apoptosis (Czajkowski et al., 2019).

This kind of measurement has been used to characterize the elastic response of a material to a localized rearrangement of particles in sheared systems, which follows an Eshelby-like quadrupolar response with a radial decay $1/r$ for the displacement magnitude (see section 1.2), as depicted in Fig. 1.18(a). Interestingly, similar responses are observed in the case of local active events. In Fig. 1.18(b), Mandal et al. (2020a) study a model of self-propelled particles in a relatively large persistence time regime, where self-propulsion leads to avalanche-like dynamics. They find that cage-breaking events due to self-propulsion forces induce an Eshelby-like displacement field in the surrounding material. In Fig. 1.18(c), Czajkowski et al. (2019) measure the response to individual cell division and apoptosis events in a vertex-based model for epithelial tissues, and also report an elastic response following a $1/r$ radial decay for the displacement magnitude, with an anisotropic response in the case of cell division and an isotropic response in the case of apoptosis.

Mesoscopic picture The long-range elastic response to these local active events supports the idea that activity will generate an additional mechanical noise in the system. This opens new perspectives to model dense active systems at the mesoscopic scale, by including mechanical interactions due to the response to local active events in a similar way it is done for the elastic response to shear transformations in elasto-plastic models for sheared amorphous solids.

This path was already followed at the continuum level by Ranft et al. (2010), by treating tissues as an active elastic medium at short timescales, and considering active stress increment sources due to division and apoptosis events. In the framework of elasto-plastic models, Matoz-Fernandez et al. (2017a) have introduced an additional mechanical noise in the Hébraud-Lequeux mean-field model (Hébraud et al., 1998) to account for the effect of cell division and apoptosis.

In this thesis, we develop spatially-resolved elasto-plastic models to account for active dynamics. A first simple approach is to consider that activity induces additional plastic rearrangements (and hence systematically fluidizes the system) without considering the detailed mechanisms at play. We study this type of model in Chapter 4 for two different activation dynamics. Another approach is to focus on a particular type of activity and to describe explicitly the elastic response of the surrounding material as depicted for self-propulsion, division and apoptosis in Fig. 1.18(b-c). In this case, activity results in active stress sources that can induce plastic rearrangements of particles and hence relaxation in the system. We explore this approach in Chapter 5 to study the fluidization induced by actively deforming particles (in the form of an oscillatory radius change), as studied at the microscopic level by Tjhung et al. (2017).

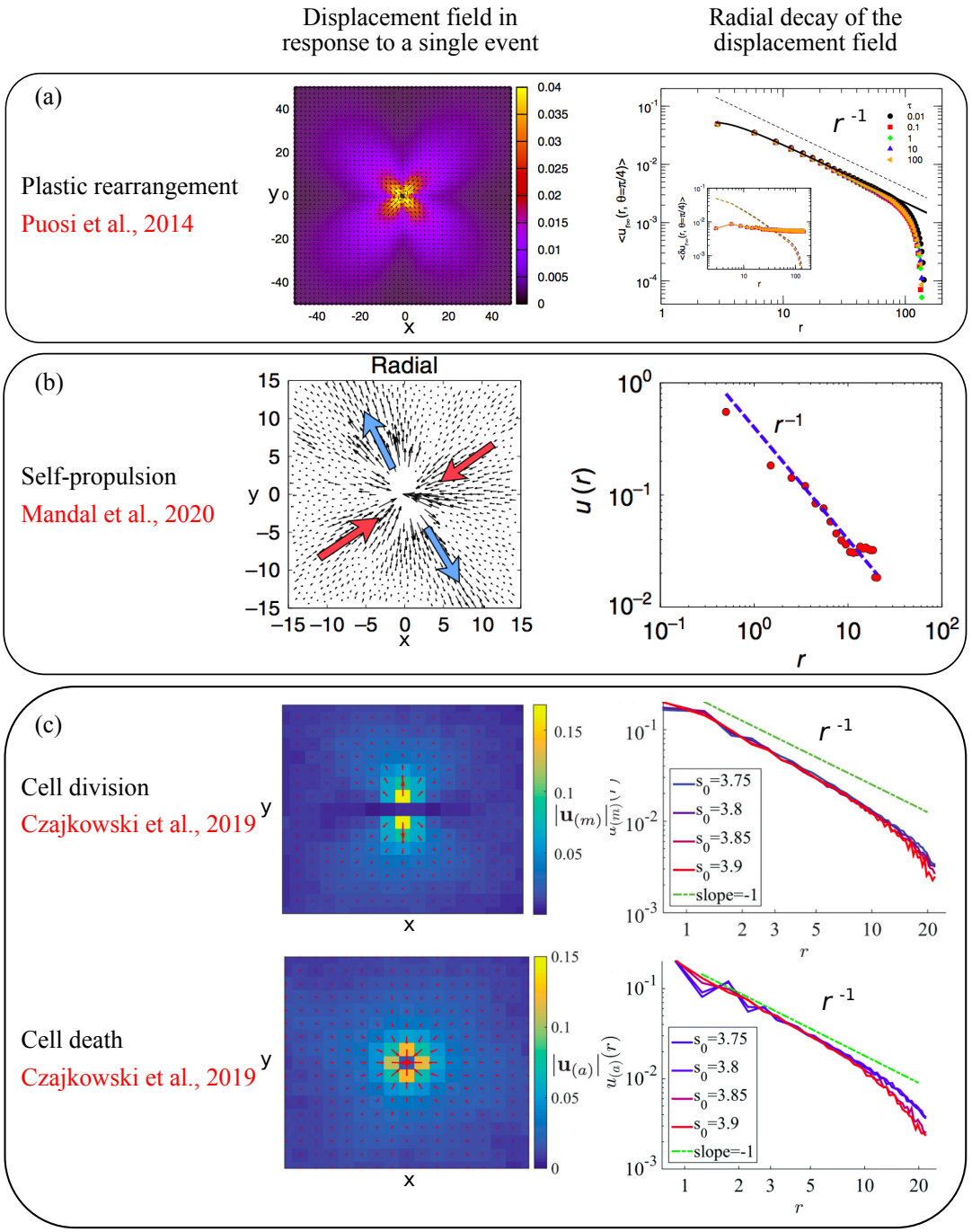

FIGURE 1.18: **Elastic responses to local events in microscopic simulations**. (a) Local plastic rearrangement in a Lennard-Jones glass (Puosi et al., 2014) (b) Self-propulsion of a particle in a Lennard-Jones glass with a long persistent time for the direction of motion (Mandal et al., 2020a). (c) Cell division and cell death in a vertex-based model (Czajkowski et al., 2019). All the dashed lines are guides to the eye with a slope of $1/r$.

Summary of section 1.3

- Various active and biological systems exhibit glassy features in some part of their phase diagram, both at the intra- and intercellular level (e.g., dynamical heterogeneities, dynamical slowdown, caged dynamics).
- Different types of solid-to-fluid transitions have been reported in computer simulations of dense active systems and analogies with glass, yielding and jamming transition in passive systems have been proposed depending upon the type of active dynamics.
- The rheology of biological tissue is characterized by a rich behavior (elastic, plastic and viscous) depending upon the loading and observation time considered, related to a large variety of physical and biochemical processes at various length and timescales.
- It is in general difficult to capture all these effects within a unique theoretical model and various modeling approaches have been developed to describe tissue mechanics. A possible approach to build mechanical models is to consider biological tissues as yield stress materials fluidized by active sources of stress.
- The elastic responses to local active events resemble the response to local plastic rearrangements observed in sheared systems, suggesting a possible common elasto-plastic framework to model the dynamics of sheared and active dense materials.

1.4 Multi-scale modeling of driven and active amorphous materials

We have seen in the previous sections that driven and active amorphous materials exhibit a rich behavior, including large scale coordinated dynamics and dynamical slowdown, and that events occurring at the scale of particles play a crucial role in the dynamics. Modeling this kind of systems is thus particularly challenging since it spans a wide range of length and timescales. We introduce in this last section the main different approaches used to model driven and active soft amorphous materials at various scales, focusing mainly on the approaches used in this thesis (summarized in Table 1.2).

Modeling approaches for dense cellular amorphous materials essentially fall into two classes: discrete cell-based (or microscopic) simulations and continuum models. In discrete cell-based models, individual particles or cells are endowed with some geometric and mechanical properties and the global behavior of the system is obtained by simulating a large number of these particles. This approach enables one to test the effect of specific cell-scale ingredients (and feedback mechanisms) on the large scale properties of the system. There is no other lengthscale incorporated in the model than the one given by the particle size.

On the other hand, building continuum models requires an intermediate lengthscale, which is larger than the particle size and smaller than the spatial extension of the material and beyond which the relevant fields (stress, strain) vary smoothly. The macroscopic rheology is captured through a constitutive equation relating the stress and deformation tensors. It is then incorporated into the model through conservation laws (mass, momentum). One difficulty generally lies in finding the right constitutive equation, which can be left to some phenomenological considerations. A continuum model can then be tested by extracting continuum information (spatially averaged quantities) from other sources such as simulations of discrete models or experiments with particle-scale resolution.

Beside microscopic and continuum approaches, intermediate "mesoscopic" models are based on "coarse-graining" microscopic details, i.e., including only the essential details of the interactions or mechanisms at play, thus enabling one to reduce the degrees of freedom of the system. In this thesis, we will focus on lattice-based mesoscale models,[4] which aim at bridging the gap between microscopic dynamics and macroscopic properties. In these models, continuum fields are discretized onto a lattice, and their evolution is determined by dynamical rules and interactions between lattice sites. Well known mesoscopic models include lattice Boltzmann models for fluid dynamics, which enable one to describe the flow of small scale or heterogeneous systems, where continuum Navier-Stokes approaches find their limits. Here, we focus on mesoscale Elasto-Plastic Models (EPMs) that were developed to describe the rheology of materials exhibiting both solid-like and fluid-like behaviors (Yield Stress Fluids, YSFs), which often deform plastically in a heterogeneous way. Building mesoscopic models relies on either phenomenological rules or coarse-graining of microscopic simulations (usually both).

In this work, we combine modeling approaches at different scales to address the scientific questions introduced in the previous sections. We use continuum modeling to study the emergence of permanent shear bands in particle-based simulations of YSFs

[4] Note that, depending upon the scientific community, "mesoscopic models" may also include particle-based models, as for instance the commonly used Dissipative Particle Dynamics in soft matter simulations where simulating solvent molecules explicitly would be too costly computationally (Schiller et al., 2018).

(Chapter 3), we use mesoscale EPMs to study the effect of additional mechanical noises in the flow of YSFs (Chapters 4 and 5, combined with particle-based simulations), and finally, we use a vertex-based model to study collective cell migration in confined 2d tissues (Chapter 6). These different classes of models are presented in the following. Starting from microscopic approaches (particle-based simulations, vertex models), we will then introduce mesoscale EPMs (which will be described in details in Chapter 2) and briefly introduce continuum modeling approaches.

1.4.1 Microscopic simulations of driven amorphous materials

Computer simulations of microscopic models, or "numerical experiments", are now a widely used tool to study glass-forming materials as they allow for a fine control of the relevant parameters and provide particle-resolved information on the structure and dynamics of the system under consideration.

When the aim is to study the properties of a material with a specific composition at the microscopic scale, the use of advanced molecular dynamics methods involving effective potentials taking into account specific interatomic potentials allows for quantitative predictions of the mechanical properties (Leach et al., 2001). On the other hand, when the purpose is to understand generic properties of amorphous systems, independently of the details of the potential, a commonly used model of amorphous system is a Lennard-Jones particles mixture (which, to avoid crystallization is either bidisperse or polydisperse). Other types of potential are also commonly used, such as the Lennard-Jones potential cut at the minimum (also called Weeks-Chandler-Andersen, WCA), hard-sphere potentials to study colloidal glasses, harmonic spheres to model soft systems such as foams, etc. (Berthier et al., 2011).

In order to obtain glassy states, samples are prepared by a quench of a high-temperature liquid sample and different quenching methods lead to amorphous systems with different structures, which will affect the transient mechanical response to an applied shear. The preparation protocol will however not affect the steady state flow properties, where the memory of the initial state is lost (Bonn et al., 2017; Nicolas et al., 2018b). Obtaining well annealed samples in simulations has been an important challenge in the field, since it requires slow quenches and an important computational effort. Recent methods such as the SWAP Monte Carlo method have led to important advances (Ninarello et al., 2017).

Different types of microscopic dynamics

Different types of dynamics can be used for simulations of glassy systems. Newtonian dynamics, mainly used in numerical work on supercooled liquids, consists in computing the trajectories of individual atoms following Newton's equation of motion. Each atom is characterized by an instantaneous position and velocity and one can define a temperature in the system as being proportional to the total kinetic energy. When modeling larger molecules in a solvent (which is often the case in soft matter physics, where the molecule and the solvent molecules have well separated length and timescales) it is convenient to use stochastic simulations such as Langevin or Dissipative particle dynamics (DPD). These "mesoscale" particle methods enable one to account for dissipative and random forces exerted by the solvent on the particle. Temperature is controlled as in a thermostat, approximating the canonical ensemble in statistical mechanics. It was found that the global relaxation dynamics in glassy systems does not depend on the type of microscopic dynamics used in simulations. It

seems that these details act at very short timescales and do not affect the slow dynamics on much longer timescales (Berthier et al., 2019). The details of the methods specifically used in this thesis will be presented in the corresponding chapters.

Sheared systems

Shearing a sample in particle-based simulations can be done either by deforming a simulation box using periodic boundary conditions (PBC) or by moving a rigid wall extending along the axis of the flow direction. The main difference is that using PBC enable particles to diffuse along the gradient direction over distances larger than the box size, while rigid walls prevent it.[5]

Two different protocols are also often found for the dynamics: either quasi-static shear or finite shear rate. In quasi-static simulations, a small displacement increment is imposed to the top wall in a rigid wall protocol (or a small strain increment to the system in the case of PBC), and the system is then left to relax to its nearest local energy minimum using some energy minimization algorithm, before a new displacement/strain increment is applied. On the other hand, a finite shear rate protocol is achieved by enforcing either a constant velocity translation on the top wall (rigid walls) or by deforming the simulation box at a given shear rate. Quasi-static simulations have been used extensively to study the behavior of amorphous solids in the limit of vanishing shear rates where avalanches occur (Maloney et al., 2004).

1.4.2 Microscopic simulations for active systems

Particle-based simulations

Following the modeling approaches for glasses, minimal particle-based models of active matter have been built considering isotropic particles interacting via soft potentials such as Lennard-Jones, WCA or harmonic potentials. Many studies in the dense regime aim at simulating the dynamics of assemblies of biological cells in a tissue, for which the dynamics is generally considered to be overdamped. The equation of motion for the center of mass of particle i can be written as:

$$\vec{0} = \vec{F}_i^{\text{friction}} + \vec{F}_i^{\text{active}} + \vec{F}_i^{\text{cell-cell interaction}} \tag{1.5}$$

The friction force is usually given by $\vec{F}_i^{\text{friction}} = -\gamma d\vec{x}_i/dt$ (describing, e.g., friction on a solid substrate for two-dimensional systems), $\vec{F}_i^{\text{active}}$ is the active force and $\vec{F}_i^{\text{cell-cell interaction}}$ derives from an interaction potential. As mentioned in section 1.3.2, a large variety of active particle-based models have been built. The most studied type of activity is the self-propulsion of particles, and various models (ABPs, AOUPs) exist (Berthier et al., 2019), including some accounting for aligning interactions (Henkes et al., 2011), that will lead to different forms for $\vec{F}_i^{\text{active}}$. Other types of active processes have been included in particle-based simulations, such as cell division and cell death (Ranft et al., 2010; Matoz-Fernandez et al., 2017a; Tjhung et al., 2020) or volume fluctuations (Tjhung et al., 2017; Oyama et al., 2019), and were shown to lead to different types of fluidization (see section 1.3). Beside active processes, more realistic interaction potentials, including adhesive interactions between particles are used in order to mimic cell-cell adhesion (Drasdo et al., 2007; Schoetz et al., 2013; Matoz-Fernandez et al., 2017b). Matoz-Fernandez et al. (2017b) report that adhesive interactions are responsible for a rich phase diagram, exhibiting a gel-like phase (clusters of cells) for

[5] Note that different types of boundary conditions can also be used for the thermostat: either the heat is exchanged by the walls, or in the bulk.

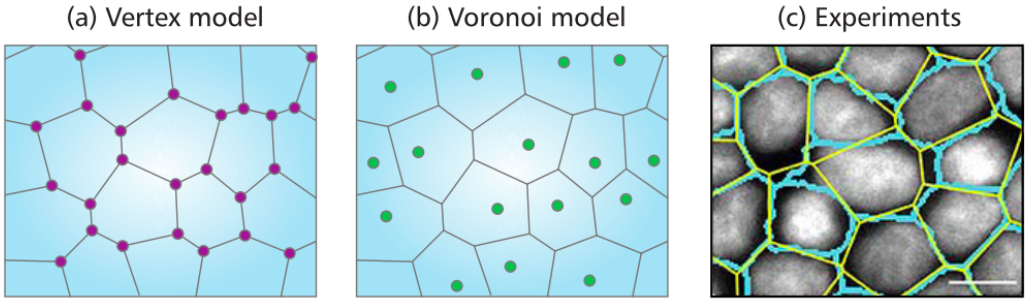

FIGURE 1.19: From Janssen (2019): **Vertex and Voronoi models of epithelial tissues**. Illustration of (a) the vertex model and (b) the Voronoi model for confluent cells. The purple and green circles represent the respective degrees of freedom in these models. Panel (c) shows the differences between the cell boundaries of MDCK cells obtained via imaging methods (blue) and a Voronoi tessellation of the cell nuclei (yellow).

large adhesion strengths. Schoetz et al. (2013) found that tissues tend to be more solid-like when the ratio between cell-cell adhesion and cortical tension is high.

In particle-based models, the transition from solid-like to fluid-like states results from a competition between crowding and activity, and resembles what is observed in inert systems (Berthier et al., 2019). However, in many morphogenetic processes, the tissue is confluent or nearly confluent and so the system cannot become more crowded. Yet, cells are observed to change their behavior from fluid-like to solid-like depending on the developmental stage (Mongera et al., 2018). Another class of models, vertex-based models, seem to be better-suited to account for these types of observations since they are built to describe fully confluent tissues.

Vertex-based models for active systems

Vertex-like models, initially introduced to model inorganic system such as foams or grains growth (Kawasaki et al., 1989; Okuzono et al., 1995), have become very popular to model confluent biological tissues (see Fletcher et al. (2014) for a review). Vertex-like models encompass two types of models: the actual Vertex model and the Voronoi model.

In vertex models, the cells are described by an ensemble of vertices, which are the degrees of freedom on which the forces and the noise are acting (see Fig. 1.19(a)). The energy of a configuration of the system E is computed as:

$$E = \sum_{i=1}^{N_{\text{cells}}} \frac{K_i}{2} \left(A_i - A_0\right)^2 + \sum_{i=1}^{N_{\text{cells}}} \frac{\Gamma_i}{2} P_i^2 + \sum_{\langle \mu,\nu \rangle} \frac{\Lambda_{\mu\nu}}{2} l_{\mu\nu} \tag{1.6}$$

where N_{cells} is the total number of cells, A_i is the area of the cell i, A_0 is the target area, K_i is the area modulus (a constant with units of energy per area squared that can be seen as the rest length of a spring). P_i is the cell perimeter and Γ_i (with units of energy per length squared) is the perimeter modulus that determines how hard it is to change the perimeter P_i. $l_{\mu\nu}$ is the length of the junction between vertices μ and ν and $\Lambda_{\mu\nu}$ is the tension of that junction (with units of energy per length), resulting from a competition between cortical tension and cell-cell adhesion. $\langle \mu, \nu \rangle$ in the last term denotes the sum over all pairs of vertices that share a junction.

This model undergoes a density-independent rigidity transition (sometimes termed as jamming transition) governed by the competition between surface and bulk energy terms, controlled by a control parameter p_0 termed as *effective shape index* with $p_0 = P_0/\sqrt{A_0}$ where $P_0 = -\Lambda/\Gamma$, the perimeter rest length (assuming that Γ_i and $\Lambda_{\mu\nu}$ are the same for all cells and junctions) (Bi et al., 2015). For values $p_0 < p_0^c$ (with $p_0^c \simeq 3.81$) the system's response is essentially that of a solid, while for $p_0 > p_0^c$, the response is fluid-like, and the energy barriers for cell intercalations to occur vanish (Bi et al., 2014). An important feature of the vertex model is that an increased adhesion will lead to larger values of p_0 and hence to a more fluid-like behavior, unlike in particle-based models. A recent model introduced by Kim et al. (2020), sharing features with both particle-based and vertex-based model, may elucidate the dual role of adhesion in models of tissues. They find that while increasing adhesion in a non-confluent system leads to higher volume fraction, making it more solid-like, increasing adhesion in a confluent system leads to lower energy barriers for neighbor exchange and a more fluid-like system.

In the Voronoi model, the cells are modeled as Voronoi volumes defined by their neighbors and the degrees of freedom are the Voronoi cell centers (Fig. 1.19(b)). Approximating cell shapes by the Voronoi tessellation of the center of mass of their nuclei is often found to be a reasonable approximation as shown for instance in Fig. 1.19(c) (Kaliman et al., 2016). The expression of energy in the Voronoi model is the same as in the standard Vertex model.

Both vertex and Voronoi models have been studied in the presence of either thermal noise (equilibrium), or self-propulsion forces with a a finite persistence time (Bi et al., 2016; Czajkowski et al., 2019). Fluid-to-solid transitions with the signature of glassy dynamics have been reported in the model with self-propulsion. Cell division and apoptosis have also been encoded in this type of model (Czajkowski et al., 2019), and a fluid-to-solid transition was also reported, unlike in the case of particle-based simulations with cell division and apoptosis (Matoz-Fernandez et al., 2017a). One thus needs to keep in mind that beside the effect of a particular type of activity, the model choice and the details of rules for the active events may play an important role in determining the type of fluidization due to a biological activity. The fluidization induced by active fluctuations of the junctional tension has been studied in vertex models by prescribing a dynamics (e.g., Ornstein-Uhlenbeck process for instance) to the junction tension $\Lambda_{\mu\nu}$ (Krajnc et al., 2018; Kim et al., 2020).

More complex dynamics have also been incorporated in self-propelled vertex-like models, such as including an alignment mechanism at the single cell level between the direction of self-propulsion and that of velocity. Giavazzi et al. (2018) show that this mechanism could explain the formation of flocks of migrating cells in confluent tissues. More generally, this type of feedback mechanism, also studied in particle-based models, plays an important role in the emergence of collective motion such as flocks or velocity oscillations in models of confluent tissues. We will show in Chapter 6 that this type of feedback mechanism could possibly explain the spatio-temporal oscillations of cell velocities observed experimentally in confined epithelial tissues.

Let us mention that other rules have also been recently included in self-propelled vertex models, such as delayed T1 transitions to account for the fact that remodeling at cell-cell junctions is not an instantaneous process (Das et al., 2020). These delayed T1 transitions are shown to affect the glass transition and lead to an effective cohesion of the tissue, favoring large scale collective motion of cells.

Other microscopic models

Other microscopic models include for instance the cellular Potts model, phase fields models, or models including subcellular elements. The Cellular Potts model is a stochastic model where cells in a monolayer are represented as a subset of sites of a lattice sharing the same cell identity (ID) (the cell ID being analogous to the spin in the original Potts models) (Marée et al., 2007). The model is based on a Hamiltonian that includes interfacial tension, area conservation and active motility, and a Monte Carlo algorithm is used to find the pattern of cell shapes that minimizes the sum of all the cellular energies. Depending on the parameters controlling the interfacial energy and the cell mobility, a transition from fluid-like to solid-like behavior is observed (Chiang et al., 2016). This transition is accompanied by a change of cell shape, as in vertex-based model (shapes are more elongated in the fluid regime where cells can intercalate and more roundish in the solid regime, where cells are caged).

Phase field models are also used in the context of the modeling of active systems such as migrating biological cells (Moure et al., 2019). Cell migration can be thought of as a moving boundary problem, where the boundary represents the cell membrane. The phase field ϕ, defined on the entire domain, indicates the location of the cell ($\phi = 1$ inside the cell and $\phi = 0$ outside) and obeys the evolution equation of a diffusive interface, derived from an energy functional. The velocity of each cell can also have its own active dynamics in order to mimic self-propulsion, and may include feedback mechanisms between the direction of motion and the force, as done in the work of Peyret et al. (2019).

Let us finally mention the existence of models including subcellular elements (subvolumes of the cytoskeleton) and accounting for intra- and intercellular interactions of these elements (Newman, 2005). The advantage of these models is the resulting cell-shape dynamics and the possibility to incorporate intracellular biological mechanisms. They are however costly to simulate in the context of large multi-cellular systems.

Concluding remarks

The choice of a particular microscopic model for dense active matter simulations is highly system and context (question) dependent. Particle-based models have only a few number of parameters and are easy to simulate, which make them suitable for large scale simulations running over long times. However, the particles remain essentially spherical (or circular in 2d) and the interaction potential becomes unrealistic at high density. Potts and Vertex models, relying on an effective energy, have a larger number of parameters and require a larger computational time, but they are more suited to describe changes of cell shape, especially in the large density (confluent) regime. They are moreover well suited for direct comparison with experiments on epithelial tissues. Note that Potts models are suited to describe both confluent and non-confluent tissues. Vertex models, on the other hand, are slightly simpler since they are restricted to confluent tissues, and are widely used to study different types of solid-to-fluid transitions.

Our modeling approach follows the above lines: in Chapter 5, we use a simple particle-based model of actively deforming particles as an input to build a coarse-grained mesoscale model, while in Chapter 6, we use a vertex-based model to describe the dynamics of confined confluent tissues in a more realistic way in order to compare our results to experiments.

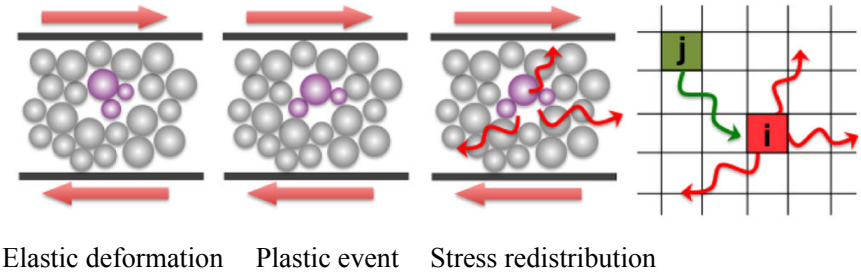

FIGURE 1.20: From Bocquet et al. (2009): **Sketch of plastic deformation in amorphous media**. Deformation occurs via elastic deformation, localized plastic events, and nonlocal redistribution of the elastic stress, potentially triggering other plastic events. These ingredients are incorporated into lattice-based elasto-plastic models with mesoscale blocks interacting via elastic interactions.

1.4.3 Mesoscopic approaches for the flow of amorphous materials

The generic features of the plastic deformation of disordered solids (see section 1.2) have led to the emergence of multiple coarse-grained models. Mesoscale modeling enables one to get rid of microscopic details such as the particle type and size and the interaction potential between particles. Mesoscale elasto-plastic models (EPMs) rely on the ideas of Argon et al. (1979) which consist in considering an elementary unit of plasticity in disordered systems that corresponds to a localized group of rearranging particles, as demonstrated in numerous experimental and simulation works (see section 1.2). A possible formalism for this type of model will be introduced in detail in Chapter 2, and we only give here the general principle and some examples of EPMs.

Let us first remind the generic mechanism for plasticity in amorphous media, as depicted in Fig. 1.20. Flow occurs through a succession of global elastic deformations and localized plastic rearrangements resulting from local yielding events. These events induce non-local elastic redistribution of the stress in the system, thereby creating cooperative flowing regions. In EPMs, the amorphous medium is described in terms of "mesoscopic" blocks, of the typical size of a rearrangement of particles. Each block can thus hold a single "shear transformation" (ST). Depending upon the system (colloidal glass, foam, etc.) a shear transformation can involve a varying number of particles or droplets. This variability is erased at the mesoscopic scale (where the basic length unit is that of a rearrangement), which enables one to focus on the generic large scale physics of deformed amorphous materials. Upon driving, these blocks are loaded elastically until a condition for yielding is fulfilled, which leads to a local plastic deformation associated with stress relaxation and stress redistribution through the elastic interactions.

Various variants of EPMs exist, with different dynamics for the plastic regions and coupling mechanisms between mesoscopic blocks. In particular, two main aspects must be considered in order to choose a particular model: (i) is the coupling between different regions of the material explicitly taken into account (lattice-based spatial EPMs), or is it described in an effective manner through a mechanical noise term (mean-field EPMs)? (ii) Do thermal fluctuations play a role in the activation of plastic rearrangements? Is the activation due to a real thermodynamic or to an effective temperature?

Mean-field elasto-plastic models

Mean-field EPMs discard any explicit spatial information about the location of yielding events, and stress propagation is described in a mean-field way. We briefly introduce two types of mesoscopic models with different spirits: the "Soft Glassy Rheology Model" and the "Hébraud-Lequeux" model.

Soft Glassy Rheology model The Soft Glassy Rheology (SGR) model of Sollich et al. (1997) is based on a Potential Energy Landscape (PEL) representation of the configurations of the system. Each mesoscopic block evolves in a landscape of traps whose depths are randomly drawn from an exponential distribution, as in Bouchaud's trap model (Bouchaud, 1992). The external driving, by deforming each region, facilitates hops from trap to trap, and random kicks due to mechanical noise activate hops at a rate governed by an Arrhenius law with an effective temperature x. Sollich et al. (1997) have proposed a mean-field analysis of this model, based on a master equation for the (joint) probability distribution of the local energy barrier and strain. They find that as the effective temperature x is decreased, the system transits from a Newtonian liquid behavior to a power-law regime and then to a yield stress fluid with a Herschel-Bulkley rheology.

In this model, the mechanical noise temperature x is fixed externally. Another variant of the model was introduced by Fielding et al. (2009), describing the dynamics of x as depending on the rearrangement rate and obeying a diffusive dynamics (but still relaxing to an externally fixed equilibrium value x_0). This variant was shown to exhibit localization, depending upon the form of the coupling to the rearrangement rate.

Note that other models such as the Shear Transformation Zone theory are based on thermally activated events with an effective temperature describing the propensity of a given region to yield (regions associated with a large free volume density) (Falk et al., 1998). Even earlier than these developments, Bulatov et al. (1994) had proposed a lattice-based model with thermal activation of plastic events.

Hébraud-Lequeux model Unlike in the previous cases, the model introduced by Hébraud et al. (1998), neglects any thermal activation processes, doesn't account for any effective temperature and treats the mechanical noise in a self-consistent manner.

The elasto-plastic scenario is essentially the one explained above: the macroscopic drive contributes to an increase of the local stress, until a yielding event occurs at a rate $\tau_{\rm pl}^{-1}$ once the stress has exceeded the (unique) local stress threshold. When yielding occurs, the local stress is instantaneously reset to 0 and some stress is redistributed to the rest of the material inducing mechanical noise in the system. Hébraud et al. (1998) have studied a mean-field version of the model, by describing stress redistribution as a Gaussian white noise, leading to a diffusive contribution to the probability distribution of the stress $P(\sigma;t)$. By choosing a diffusion constant proportional to the average rate of plastic events in the system (with a coupling constant α), this leads to a self-consistent equation. This model predicts a transition from a Newtonian fluid to a yield stress fluid behavior for a coupling constant value $\alpha = 1/2$ (Herschel-Bulkley rheology with an exponent 0.5 for $\alpha < 1/2$). Let us mention that this model was extended by Agoritsas et al. (2015) to account for a distribution of local thresholds σ_c, which did not affect qualitatively the results, whereas the disorder is a key aspect to get a yield stress fluid behavior in SGR model, thus underlying the difference between these two mean-field approaches. Beside the macroscopic rheology, this model was shown to

reproduce the creep behavior of soft amorphous solids (Liu et al., 2018), and extended to account for an additional noise of active origin (Matoz-Fernandez et al., 2017a).

Lattice-based elasto-plastic models

In lattice-based EPMs, the mesoscopic blocks are described as nodes of a regular lattice. Elastic interactions between blocks are treated explicitly, using an Eshelby propagator. The first spatial models that have been introduced are extremal models, accounting for the elastic interactions between blocks but ignoring any dynamical aspects, thus suitable to study the "quasi-static" limit ($\dot{\gamma} \to 0$) of the flow of amorphous systems (Chen et al., 1991; Baret et al., 2002; Dahmen et al., 2009), as in athermal quasi-static (AQS) particle simulations.

The first dynamical model has been introduced by Picard et al. (2005), treating the local dynamics of the deformation and stress fields (with stochastic rules to transit from local elastic to plastic states). This model, based on simple stochastic rules with a unique local yield stress, predicts a yield stress rheology as well as the emergence of shear bands for long durations of plastic events, but does not capture the Herschel-Bulkley exponent (close to 0.5) often observed in soft amorphous materials, and always leads to discontinuous stress-strain curves (with a stress overshoot) in shear start-up conditions. A more realistic model has been introduced later by Nicolas et al. (2013a), based on a distribution of local yield stress and accounting for more realistic rules for the local dynamics. This model leads to a Herschel-Bulkley rheology with an exponent close to 0.5, and to continuous stress-strain curves. Many variants of dynamical lattice-based EPMs now exist, including stress-controlled protocols, and some of these models will be detailed in Chapter 2.

Concluding remarks

In the last decade, EPMs have become a widely used tool to understand the flow of amorphous solids. They have been successful in capturing a large number of features of the rheology of yield stress materials, including transient features (flow curves, creep behavior, shear bands, avalanches, etc.). They are particularly suited to study large scale and long timescales features of amorphous solids, like those arising in critical phenomena (Nicolas et al., 2018a). In Chapter 4, we will address, within a mesoscale EPM, the question of the existence of a critical point at finite shear rate in the presence of an additional source of noise (see section 1.2). Our modeling framework will be presented in Chapter 2.

1.4.4 Continuum approaches

Beside microscopic and mesoscopic models as presented above, continuum models aim at describing a material without accounting for its structure at the particle or cellular scale. In continuum modeling approaches, stress, strain rate, as well as other state variable such as "effective temperatures" or "active stresses" are treated as continuum fields. These quantities are related through macroscopic constitutive laws and momentum and mass conservation determine their dynamical evolution.

Constitutive models for the flow of amorphous materials

Constitutive models for the flow of soft amorphous materials range from those built using bottom up approaches from microscopic descriptions (e.g., mode coupling theories)

or based on mesoscopic models (spatially-resolved mean-field elasto-plastic models), to top-down approaches based on the macroscopic phenomenology.

Microscopic or mesoscopic derived models Mode-coupling theories (MCT) are microscopically derived theories for dense colloidal suspensions, starting from a liquid state description. Initially built to describe the glass transition (approaching from the liquid side), it was then extended to account for flow, based on ergodicity restoration in steady flow (Fuchs et al., 2002). Starting from the probability distribution of the position of Brownian particles (neglecting hydrodynamic interactions), a series of approximations leads to a constitutive equation for the macroscopic stress, using as an input the material's static and dynamic structure factors for the density correlation functions. MCT has been used in a variety of studies addressing steady shear as well as time-dependent shear (Brader et al., 2007). These theories are however based on technically involved calculations and more or less controlled approximations, sometimes hindering their practical use.

Mean-field elasto-plastic models such as Soft Glassy Rheology or Hébraud-Lequeux models predict various features of the flow of soft glassy materials (Hébraud et al., 1998; Fielding et al., 2000; Liu et al., 2018), but are limited to bulk quantities and cannot be used to predict flow in a specific geometry. Spatially-resolved adaptations of these models have thus been introduced to study the flow of yield stress fluids in various geometries and driving protocols, as done for instance in the work of Moorcroft et al. (2011), Radhakrishnan et al. (2016), and Fielding (2020) using the Soft Glassy Rheology framework. Bocquet et al. (2009) have proposed a kinetic elasto-plastic (KEP) model, that can be seen as a spatial extension of the Hébraud-Lequeux model, where interactions between blocks are approximated as stress diffusion in the system. The authors propose a coarse-graining procedure leading to a non-local constitutive law for the flow, where the key dynamic quantity is the local rate of plastic events, or "fluidity". It appears that the fluidity correlates with a "flow cooperativity" lengthscale ξ, which quantifies the spatial extent of plastic activity due to non-local elastic coupling in the system. This model has enabled one to rationalize experimental findings about flow cooperativity and size effects in the flow of yield stress fluids (Goyon et al., 2008).

Microscopic or mesoscopic derived models reproduce well the general features of the flow of soft amorphous materials while keeping track of the underlying physics, but their practical use is often limited when it comes to modeling a flow in complex geometry and/or time-dependent driving protocol. To this end, a large variety of macroscopic phenomenological model were developed, and are often better suited to complex flow geometries and dynamics. On the downside, they usually contain many parameters not easily related to the underlying mesoscopic physics.

Macroscopic phenomenological approaches Early works have proposed phenomenological constitutive relations relating stress and deformation to describe the flow of yield stress fluids, such as the models of Bingham, Herschel-Bulkley, Oldroyd, etc., describing the behavior before yielding either as a rigid or elastic solid, and the flow behavior after yielding either as a Newtonian or power-law fluid. More recently, elasto-visco-plastic models have described materials as viscoelastic solids at low stress, and as a viscoelastic fluid if the stress is above the yield stress (Saramito, 2007).

Macroscopic models for materials undergoing an evolution of their structure with shear (thixotropy) usually contain both an equation for the stress tensor and an auxiliary equation for the time evolution of an internal variable describing the structure

of the material. In most models, the link between the structure and the bulk rheological properties is phenomenological. Kinematic hardening mechanisms have for instance been introduced to model the Bauschinger effect observed in shear-reversal experiments (Dimitriou et al., 2014), although their microscopic origin (polarization of local yield stresses) was only recently investigated (Patinet et al., 2020).

The use of auxiliary fields coupled to the flow is particularly relevant when it comes to modeling heterogeneous flows. Effective temperatures are often used as auxiliary fields to describe strain localization in amorphous solids (Manning et al., 2007). In the case of hard spheres suspensions, shear concentration coupling mechanisms were shown to induce shear localization (Besseling et al., 2010; Gross et al., 2018).

Continuum approaches for dense active and living systems

Various continuum approaches for dense active systems such as biological tissues have been developed. In the most general case, a continuum model describing the dynamics of tissues should include viscous, elastic and plastic behaviors as observed at different timescales and applied forces in experiments, but as mentioned in section 1.3, it is often difficult to capture all these phenomena within a unique model. In practice, continuum models usually focus on a given timescale (and lengthscale) (Khalilgharibi et al., 2016). Building continuum models for tissue mechanics can be done using different approaches: building elasto-visco-plastic models (Preziosi et al., 2010), using a hydrodynamic approach based on a near-equilibrium thermodynamic formalism (Prost et al., 2015; Tlili et al., 2015), etc. We will not go into the details of the derivation of such models, but only give a few examples.

Active gel models constitute a wide class of models where a tissue is described as a fluid or an elastic continuum in which the mechanical variables are coupled to internal degrees of freedom that account for the extent of the chemical reaction (ATP hydrolysis) driving active processes, such as contractility and cell polarization (Ranft et al., 2010; Notbohm et al., 2016; Duclos et al., 2018a). One of the first questions one may ask is whether biological tissues are better described as active elastic solids or as active fluids, as discussed for instance in a recent review by Banerjee et al. (2019). The choice of a particular approach may indeed depend on the type of tissue considered (and the timescale of the phenomenon under study). It is for instance well accepted that the *Drosophila* embryo at early developmental stages can be modeled as a viscous fluid (Wessel et al., 2015). However, in the case of collective cell migration in epithelial tissues on a substrate, models accounting for elastic or viscous description have been able to capture a large number of features, including the emergence of waves patterns in the migration velocity (Banerjee et al., 2019) (see the introduction of Chapter 6 for more details).

The above-cited models, although they reproduce a number of experimental facts and provide testable predictions, often lack a clear link with the underlying cell-scale processes, such as the deformation induced by cell plastic rearrangements or cell division. Other models are based on the decomposition of the total tissue deformation into the contribution of cell shape changes and topological transitions (cell rearrangement, division, and death), as done by Tlili et al. (2015), Popović et al. (2017), and Ishihara et al. (2017). In their study, Ishihara et al. (2017) build a continuum model describing coarse-grained cell shape, based on an energy function similar to vertex-based or cellular Potts models, thus accounting for cellular-level mechanical ingredients such as cell area elasticity and cell junction tension. The model, derived using a thermodynamic framework, is able to reproduce features of developmental dynamics such as

Scale	Approach	Driven systems	Active systems
Microscopic	Particle-based simulations	Maloney et al. (2006) Tanguy et al. (2006)	Berthier et al. (2019)
	Vertex and Voronoi models	Okuzono et al. (1995)	Fletcher et al. (2014)
	Phase field models	Xie et al. (2016)	Raina et al. (2016)
	Cellular Potts models	Jiang et al. (1999)	Graner et al. (1992)
	Sub-cellular elements models		Newman (2005)
Mesoscopic	Lattice-based Elasto-Plastic Models (EPMs)	Nicolas et al. (2018a)	———
Mean-field	Mean-field EPMs	Hébraud et al. (1998)	Matoz-Fernandez et al. (2017a)
no space		Sollich et al. (1997)	
Macroscopic Continuum	Coarse-grained EPMs	Bocquet et al. (2009) Fielding (2020)	———
	Mode coupling theories	Brader et al. (2009)	Nandi et al. (2017)
	Visco-elasto-plastic models	Saramito (2007)	Preziosi et al. (2010)
	Active gel theories		Kruse et al. (2005) (fluid) Notbohm et al. (2016) (elastic)

TABLE 1.2: **Examples of models for driven and active soft dense amorphous systems**. References correspond to review articles or examples of studies based on the corresponding methods (non-exhaustive list).

the relaxation following an axial stretching as well as a non-linear rheology in the form of a shear-thinning rheological behavior.

Another approach to describe the non-linear rheology of tissues starting from a mesoscale description is to include active terms (potentially leading to viscous behavior at long times) in elasto-plastic models describing non-linear flow curves as done at the mean-field level (extending Hébraud-Lequeux model) by Matoz-Fernandez et al. (2017a). Including such active terms into (spatially-resolved) fluidity models (Bocquet et al., 2009) would in principle be another way to obtain continuum models for dense active systems, either by adding a phenomenological active term in the (macroscopic) fluidity model, or by coarse-graining spatially-resolved mesoscale active elasto-plastic models (horizontal lines in Table 1.2). Including active terms in lattice-based mesoscale elasto-plastic models is one of the objective of this thesis (Chapter 5), and could constitute a first step in this direction.

Summary of section 1.4

- Microscopic models allow for a fine control of parameters and provide particle-resolved information. They are suited to study the role of specific microscopic ingredients and characterize in details the spatio-temporal dynamics.
- Mesoscale models like EPMs enable one to get rid of microscopic details (e.g., interaction potential between particles) and include only generic mesoscopic ingredients. They can be used to test mesoscale physics ingredients, and perform large scale and long time studies of the dynamics.
- Continuum models rely on constitutive equations relating the mechanical variables and possible internal variables such as effective temperatures, active stresses, etc. They are either built phenomenologically, using inputs from experiments or microscopic simulations, or derived from microscopic or mesoscopic theories.
- A complementary use of these three approaches can be useful to build continuum models based on microscopic and mesoscopic ingredients. In the case of sheared amorphous solids, particle-based simulations provide inputs like the response to local rearrangements or yield stress distributions that enable one to build spatially-resolved mesoscale EPMs. Mean-field approximations can then lead to continuum models.

1.5 Conclusion and overview of the thesis

Among the large variety of glassy systems, athermal systems require a form of drive to activate their dynamics, that can be either global (shear) or local (biological activity). Sheared amorphous materials share common features that have motivated the development of generic mesoscale elasto-plastic models (EPMs) to describe their plasticity. Their flow is governed by local yielding events and long-range elastic stress redistribution within the material. The mechanical noise induced by elastic interactions plays an important role in the dynamics, as it can trigger important correlations and avalanches in the system. While spatially-resolved EPMs treat explicitly the elastic interactions in the system using an Eshelby propagator, mean-field EPMs neglect spatial correlations and treat elastic interactions as a noise acting on the local stress (Hébraud et al., 1998). Continuum models such as the fluidity model describe the effect of the mechanical noise as leading to non-local effects in the flow equations (Bocquet et al., 2009).

Yield stress materials can exhibit steady state shear localization, but the origin of these flow patterns remains unclear in many cases. Sources of endogenous noise, like local softening or inertial dynamics, can be responsible for self-fluidization and hence lead to shear banding. In this thesis, we study the emergence of shear banding in systems with underdamped dynamics by building a continuum model based on an effective (kinetic) temperature field description of inertia. This model is tested by comparing its predictions to particle-based simulations of a model glass (work in collaboration with V. Vasisht and J.L. Barrat).

Moreover, sources of noise independent of the flow, such as mechanical vibrations in granular media for instance, can affect the rheological properties of soft glassy

materials and even lead to critical dynamics if the material exhibits a rate-weakening behavior (Wortel et al., 2016). It is however not clear if this scenario is generic in fluidized soft glassy materials, and if the critical features depend on microscopic details of the system. The role of an external source of noise has already been studied in a mean-field EPM (Matoz-Fernandez et al., 2017a), and shown to lead to a Newtonian regime at low shear rate. In this thesis, we study the role of additional sources of noise in spatially-resolved EPMs, using different models for the noise. We study in particular how an external noise (in the form of the random activation of plastic events) affects the organization of the flow in an EPM with a rate-weakening mechanism inducing shear bands, and test the scenario of a critical point.

The physics of "active glasses" has recently emerged as a research field and is becoming increasingly popular, not only as a new topic in statistical physics but also as a framework to study materials like biological tissues. Various works evidence glass-like states in tissues, characterized by dynamical heterogeneities and caged dynamics. However, the long-time dynamics of tissues is generally found to be fluid-like and this viscous behavior is often thought to be related to local active processes such as self-propulsion of cells, cell division, apoptosis or self-deformation, leading to a mechanical noise of active origin. How to account for this activity in mesoscopic or macroscopic models is still an open question and various different approaches can be used, by building active fluid or active solid models. Recent numerical works have evidenced long-range elastic responses of the material to local active events, in a way similar to the response of amorphous solids to local plastic rearrangement of particles. It is thus likely that these active microscopic events lead to an additional mechanical noise in the system due to elasticity, which could trigger particle rearrangements and hence fluidize the system. In this thesis, we explore this idea to build an active elasto-plastic model for a system of actively deforming cells, using inputs from active particle simulations.

The main part of this thesis is organized as follows:

- In Chapter 2, we present in more details mesoscale elasto-plastic models using a generic framework that enables us to introduce the variants of the model used in Chapters 4 and 5.

- In Chapter 3, we present a work in collaboration with V. Vashist and J.L. Barrat (LIPhy) in which we propose an effective continuum model to describe a shear banding instability due to inertial dynamics in particle-based simulations. This work is submitted for publication in *Soft Matter* (second author).

- In Chapter 4, using elasto-plastic models, we study how external sources of noise fluidize soft glassy materials. In particular, we show that external sources of noise competing with a self-fluidizing noise can lead to critical dynamics associated with giant fluctuations of the shear rate. This work is published in *Phys. Rev. Lett.* **123**, 108003 (2019) and *J. Phys. Mater.* **3**, 025010 (2020) (first author).

- In Chapter 5, we build an active elasto-plastic model to describe the dynamics of actively deforming particles in order to characterize the solid-to-fluid transition induced by activity (preliminary results, ongoing work).

- In Chapter 6, we present a work conducted in collaboration with experimentalists in LIPhy, for which we have used a vertex-based model in order to model velocity oscillations in confined epithelial tissues. This work is published in *Phys. Rev. Lett.* **122**, 168101 (2019) (second author).

Chapter 2

Mesoscale elasto-plastic models for the flow of amorphous solids

Résumé : Modèles élasto-plastique pour l'écoulement de solides amorphes

Ce chapitre vise à introduire de façon plus détaillée les modèles élasto-plastiques à l'échelle mésoscopique sur lesquels sont basées les études présentées dans les chapitres 4 et 5 de cette thèse.

La plupart des modèles élasto-plastiques récents sont basés sur les travaux de Argon et al. (1979), proposant que l'unité de plasticité élémentaire dans les systèmes denses désordonnés corresponde au réarrangement d'un groupe de particules localisé dans l'espace. Dans ces travaux précurseurs, Argon et al. (1979) mettent en évidence ces réarrangements dans un radeau de bulles (mousse bidimensionnelle constituée d'une monocouche de bulles) polydisperse cisaillé et proposent une analogie entre la déformation des verres métalliques et des mousses, inspiré par les travaux de Bragg et al. (1947). Depuis, ce mécanisme pour la plasticité des solides amorphes a été mis en évidence dans d'autres systèmes (Princen et al., 1986; Schall et al., 2007; Amon et al., 2012) et est généralement accepté. Dans ce scénario, générique à de nombreux systèmes amorphes, des évènements plastiques peuvent être activés soit par des fluctuations thermiques soit sous l'effet d'un forçage. Ceci a motivé la construction de modèles mésoscopiques phénoménologiques pour décrire la dynamique et la rhéologie de solides amorphes (Bulatov et al., 1994; Baret et al., 2002; Picard et al., 2005). Ces modèles sont généralement divisés en deux catégories: (i) les modèles ne prenant pas en compte les corrélations spatiales entre réarrangements plastiques et (ii) les modèles tenant compte des interactions entre évènements plastiques, et décrivant l'activation de cascades de réarrangements plastiques (avalanches). Dans ce chapitre, nous nous concentrons essentiellement sur cette deuxième catégorie de modèles, bien que des modèles simplifiés sans interaction puissent dans certains cas être utilisés pour avoir des prédictions analytiques concernant la rhéologie, comme nous le verrons dans la section 2.4.

Dans une première partie (section 2.1), les ingrédients de la modélisation élasto-plastique, déjà introduits dans le chapitre précédent, sont présentés plus en détail. Plusieurs aspects sont abordés : l'origine de la plasticité dans les solides amorphes sous la forme de réarrangements localisés de particules, le rôle des interactions élastiques à longue portée, le rôle joué par le désordre structurel ainsi que les aspects de dynamique temporelle.

Dans une deuxième partie (section 2.2), une formulation générale de ce type de modèle, telle qu'introduite par Liu (2016) est présentée. Cette formulation permet

d'introduire différentes versions du modèle utilisées dans la littérature: versions tensorielles ou scalaires, protocoles à contrainte ou taux de cisaillement imposé, ainsi que plusieurs variantes pour la dynamique stochastique. Le détail de l'implémentation de ces différentes versions est ensuite présenté dans la section 2.3. Enfin, dans la section 2.4, nous résumons les résultats de la littérature concernant les propriétés de l'écoulement prédit par ce type de modèle, en se concentrant en particulier sur les modèles introduits par Picard et al. (2005) et Nicolas et al. (2013a), puisque ces derniers constituent le socle du travail présenté dans les chapitres 4 et 5.

Introduction

A large number of studies indicate that the macroscopic plastic flow behavior of soft amorphous materials relies on a spatially heterogeneous behavior at smaller scales. Bridging the scales of descriptions at the microscopic level (particle dynamics) and at the macroscopic level (rheological response) remains an important challenge in the physics of dense disordered materials and building approximate models at the mesoscopic scale is a way to approach this question (Nicolas et al., 2018a).

Soft amorphous materials, also called "yield stress fluids" (YSFs), encompassing foams, emulsions, dense suspensions, colloidal glasses, etc., behave essentially as elastic solids when subjected to small stresses or deformations, while they can reach a steady-state flow regime at large stress. Driven amorphous materials are thus an example of systems exhibiting an out of equilibrium steady state, a topic of current interest in statistical physics. On the other hand, understanding their flow behavior in order to predict their mechanical response is an important topic in mechanical engineering. Modeling the flow of soft amorphous materials is thus at the intersection of various research fields, such as statistical physics, solid mechanics and complex fluids rheology.

While the aim, in statistical physics, is generally to understand the general behavior of driven disordered systems using minimal or "toy" models (with a small number of parameters), material scientists often try to model quantitatively the behavior of a given system, employing models with a large number of parameters. Elasto-plastic models (EPMs) lie at the interface of these two approaches. They rely on simple assumptions connecting the microscopic dynamics to the macroscopic flow behavior of amorphous systems and aim at describing the general phenomenology of amorphous materials, regardless of the details of microscopic constituents and interactions. Nonetheless, they generally include a sufficiently large number of parameters so they can predict a realistic macroscopic behavior for a given material.

EPMs are based on the precursor work of Argon (1979), who has first proposed the idea, now well accepted, that the elementary unit of plasticity in amorphous materials corresponds to a spatially localized cluster of rearranging particles in an essentially elastic medium. As a consequence, long-range elastic interactions can lead to cascading rearrangements in the form of avalanches in the material. Let us mention that earlier studies of dislocations in crystalline solids had already shed light on the elasto-plastic deformation of solids and possible analogies between materials constituted of atomic scale and macroscopic scale components (e.g., crystalline solids and mono-dispersed bubble rafts) (Bragg et al., 1947). This generic elasto-plastic scenario, evidenced in many systems (Princen et al., 1986; Schall et al., 2007; Amon et al., 2012), has motivated the construction of phenomenological mesoscale models, based on coarse-grained quantities such as stress and strain fields and material properties described by elastic moduli and local yielding barriers. The ingredients of these mesoscopic models often remain phenomenological, although some models were

successfully fitted to simulations or experiments, such as the fluidity model (Goyon et al., 2008; Mansard et al., 2013). Recent developments have however contributed to establish a quantitative link between EPMs and the microscopic dynamics measured in particle-based simulations (Puosi et al., 2014; Agoritsas et al., 2015; Puosi et al., 2015; Albaret et al., 2016; Patinet et al., 2016). In a very recent work by Liu et al. (2020a), using input quantities from microscopic simulations such as coarse-grained stress and yield stress distributions, a mesoscale EPM has been shown to reproduce features of both the steady state and transient rheology of a Lennard-Jones glass, validating the use of a simple Eshelby-based elasto-plastic description.

In EPMs, an amorphous material is described as an assembly of mesoscopic elements that alternate between an elastic response to driving and plastic relaxation. These models fall into two main categories: (i) mean-field like models that describe the dynamics of a single site (that can either account for fluctuations due to interactions in the system or not depending upon the model considered) and (ii) models with a spatial structure accounting explicitly for interactions between mesoscale blocks. In this chapter, we focus mainly on the second category of models, although we refer in some cases to models without explicit spatial interactions that can be useful to get analytical predictions for the rheology.

Let us now discuss briefly how the different types of modeling approaches discussed so far would be suited to address the questions raised in this thesis. As mentioned in Chapter 1, the flow behavior of YSFs can be studied using particle-based simulations, by choosing a particular microscopic model and performing averages of the relevant quantities. This enables one to study the behavior of both average quantities and fluctuations, as well as getting spatial information on any relevant field, but leads to high computational costs. The average flow behavior of YSFs can be also described at the continuum level using empirical laws such as the Herschel-Bulkley relationship (Herschel et al., 1926), or continuum descriptions, such as visco-elasto-plastic (Marmottant et al., 2007; Saramito, 2007) and fluidity models (Bocquet et al., 2009; Fielding, 2014), but these approaches do not describe the fluctuations of the stress and strain fields resulting from elastic interactions in the system. In spatially-resolved EPMs, elastic interactions between mesoscopic regions of the material are considered, making these models suitable to study the role of mechanical noise in amorphous materials while containing a minimal number of ingredients.

Lattice-based elasto-plastic models are thus good candidates to address the questions raised in this thesis regarding the role of additional sources of mechanical noise in the dynamics and rheology of soft amorphous systems. Our questions are motivated by experiments and simulations on the fluidization of dense disordered systems by sources of noise that can be either external (mechanical vibrations) or due to an internal biological activity. While these studies were performed on a large variety of systems (granular media, colloidal gels, particle or vertex-based models for biological tissues, etc.), a modeling approach based on EPMs enables us to investigate generic noise-induced fluidization scenarii in soft amorphous materials.

Different types of noise can be considered at the mesoscale level. In Chapter 4, we first study a scalar EPM with an additional mechanism of random activation of plastic events (beside those generated by the internal mechanical noise). We then consider in Chapter 5 a tensorial version of the EPM with a local active dynamics that disturbs the local stress and strain field and can lead, indirectly, to the activation of additional plastic events. Since different variants of the model are used in this thesis, we introduce in this chapter the main ingredients of elasto-plastic modeling as well as a generic theoretical framework accounting for the different variants of EPMs that we use.

This chapter is organized as follows: we first present the generic ingredients of elasto-plastic modeling (section 2.1), and then formulate the model using a general framework (section 2.2). Numerical implementation aspects are discussed in section 2.3. In the final section (2.4), we present the properties of the flow obtained by numerical resolution of the EPM, focusing on the scalar and tensorial implementations of the models introduced by Picard et al. (2005) and Nicolas et al. (2013b).

2.1 Ingredients of elasto-plastic modeling

We focus in this chapter on modeling athermal amorphous materials (see Chapter 1, section 1.2), for which external forces are required to activate the dynamics and generate configurational changes. This can be done by imposing shear (or gravity) induced flows (as in granular packings and suspensions, foams, emulsions), or using active forces (as in synthetic or biological active systems).

When sheared, these systems respond elastically to a small applied stress or strain. For larger stresses, they start to exhibit irreversible plastic deformation and reach a steady-state flowing regime if the applied stress exceeds the dynamical yield stress. Plastic deformation occurs via localized plastic rearrangements of particles that disturb the strain and stress field and may then activate new plastic events. Modeling localized plastic events in an elastic matrix as interacting shear transformations is the main building block of coarse-grained elasto-plastic models. The key ingredients behind these models are thus (i) the nature of the local shear transformation or plastic events, (ii) elastic interactions between individual plastic events, (iii) the disorder associated with the amorphous structure of the system and (iv) the dynamical rules that govern the plastic deformation. These four points are discussed below.

2.1.1 Irreversible localized plastic events in an elastic medium

As mentioned in the previous chapter (section 1.2.2), measurements of non-affine motion in experiments or in particle-based simulations of amorphous solids reveal that plastic rearrangements take place at very localized regions while the displacement field in other regions is mostly affine with respect to the global strain. These observations support the scenario of local plastic events embedded in an overall elastic medium which constitutes the foundation of EPMs.

The number of particles involved in a single plastic event can vary depending upon the system under consideration and provides a lengthscale to build coarse-grained models. In EPMs, the size of a mesoscopic block is set by the size of a rearranging cluster of particles, which becomes the elementary unit length of the model. At this mesoscopic level, the details of the rearrangement are thus discarded, enabling one to build generic models for athermal systems.

An important point is that local plastic rearrangements such as “T1” events in bubbles rafts (Argon et al., 1979) are irreversible and the topology remains changed even after releasing the loading, while the rest of the system recovers its initial configuration. This can be described phenomenologically as plastically deforming inclusions in a system deforming elastically under shear. This idea, first proposed by Bulatov et al. (1994), consists in describing an amorphous system as a collection of mesoscopic blocks deforming elastically and that can undergo plastic events (with some activation rules and interactions that will be discussed below).

2.1.2 Elastic interactions

In most spatially-resolved EPMs, once a block has undergone a plastic event, it is treated as an Eshelby inclusion in an elastic matrix, i.e., the stress released by a local plastic event within a block is redistributed through the system according to the Eshelby propagator computed from mechanical equilibrium (Eshelby, 1957) (more details below). The description of interactions between blocks using an Eshelby quadrupolar propagator is supported by experiments and simulations (see section 1.2.3). The main assumptions commonly used in EPMs are (i) that linear elasticity holds everywhere in the material and (ii) that the elastic constants are homogeneous in space.

Regarding the assumption of linear elasticity, it is generally accepted that amorphous materials below the yield stress behave as an isotropic elastic solid. Their bulk elasticity is well described by Hooke's law, with most of the deformation being affine to the global compression. Under shear loading conditions however, particle displacements are highly non-affine to the macroscopic strain, and local shear moduli must be measured carefully from the local stress-strain curve for instance, as done by Mizuno et al. (2013). An amorphous material can thus be seen as an assembly of blocks that satisfy linear elasticity (if the size of the block exceeds typically 5 interatomic distances (Tsamados et al., 2009)).

Elastic constants are however found to be highly heterogeneous and to evolve during the loading (Tsamados et al., 2009; Mizuno et al., 2013). Assuming homogeneous elastic constants thus seems to be an unrealistic hypothesis to describe the deformation of amorphous materials. Puosi et al. (2014) performed detailed measurements of the displacement field generated by a cluster of rearranging particles in a Lennard Jones glass, and found that, when averaging over 50 rearrangements, the response is reasonably well described by an Eshelby kernel assuming spatially constant elastic moduli. It is thus important to keep in mind that, although they describe materials deforming in a heterogeneous fashion at the mesoscopic scale, EPMs describe an averaged ("coarse-grained") microscopic behavior.

Eshelby inclusion

Let us consider a circular inclusion undergoing a plastic deformation $\varepsilon_0^{\mathrm{pl}}$ such that it is transformed into an ellipse embedded in a homogeneous elastic material. The deformed inclusion induces internal elastic strain (and stress) in the material as depicted by the colormap of Fig. 2.1(left) (from Tyukodi et al. (2016a)). Following the approach of Eshelby (1957), is appears that the elastic stress field is constant within the inclusion, while it exhibits a quadrupolar symmetry outside the inclusion (being negative along the axes at 0 and 90 degrees and positive along the directions + and - 45 degrees). The complete expression for the elastic stress field depends on the details of the rearranging region (see McNamara et al. (2016) for instance), but simplifies, in the far field, to:

$$\sigma^{\mathrm{el}} = \mu \varepsilon_0^{\mathrm{pl}} a \frac{\cos(4\theta)}{r^2} \tag{2.1}$$

with μ the shear modulus, $\varepsilon_0^{\mathrm{pl}}$ the plastic strain and a the area of the inclusion. In other words, an increment of plastic strain $\delta\varepsilon_0^{\mathrm{pl}}$ at a position $\vec{x'}$ in the material leads to an increment of stress at position $\vec{x}$ in the material.

$$\delta\sigma^{\mathrm{el}}(\vec{x}) = G\left(\vec{x}, \vec{x'}\right) \delta\varepsilon_0^{\mathrm{pl}}(\vec{x'}) \tag{2.2}$$

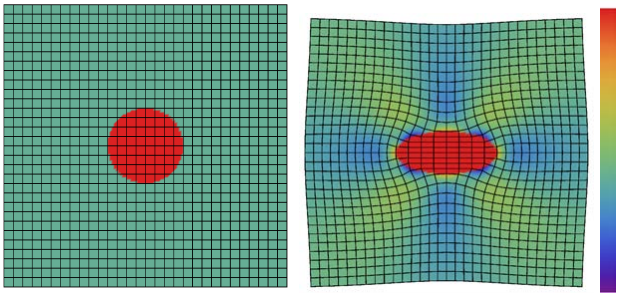

FIGURE 2.1: From Tyukodi et al. (2016a). **Strain fields for a plastic inclusion in an elastic matrix**. A circular inclusion undergoing a pure shear plastic deformation (principal axis of the plastic deformation oriented along 0 and $\pi/2$) inducing elastic strain in the system. The color scale indicates the total strain in the right panel and the mesh is deformed according to the displacement field induced by the inclusion.

with G the so-called Eshelby elastic propagator. The long-range and quadrupolar form of the stress redistributed after a local plastic event are key ingredients of EPMs. The long-range nature (power law decay in $1/r^2$) is at the origin of non-local effects and the anisotropy leads to flow localization in the form of shear bands, associated with the existence of "soft modes" of the interaction kernel (Tyukodi et al., 2016b).

Note that the use of periodic boundary conditions in numerical simulations requires some care due to the long-range nature of the interactions (see Appendix A.1). Beside Eshelby's approach, other approaches to compute the response to localized shear transformations have been introduced. Plastically deforming inclusions embedded in an elastic matrix can for instance be modeled as point-forces in an infinite elastic medium as done by Picard et al. (2004) to compute the far field response.

2.1.3 Including disorder in mesoscale models

An important characteristic of amorphous materials is spatial disorder of their mechanical properties, like local elastic moduli and energy barriers to yield (Baret et al., 2002; Tsamados et al., 2009; Barbot et al., 2018). However, the role played by structural disorder on the rheological properties of amorphous solids remains unclear, as illustrated by the variety of mesoscale models. While a distribution of local energy barriers to yield seems to be a key ingredient to observe a non-Newtonian rheology in the Soft Glassy Rheology model (Sollich et al., 1997), other models do not account for such heterogeneities (Hébraud et al., 1998; Picard et al., 2005).

Two main strategies have been developed to account for disorder in the existing coarse-grained elasto-plastic models: disorder can either be included into the landscape (Baret et al., 2002) or into the dynamics (Picard et al., 2005). Including disorder through the landscape would correspond to quenched disorder. In that case, the value of the local yielding threshold is drawn from a distribution, and is renewed only once the site has yielded (which occurs when the local stress exceeds the local threshold). On the other hand, including disorder using stochastic dynamics can be done for instance using a time-delayed model (Picard et al., 2005). Once the local stress has reached the (uniquely defined) yield stress, yielding does not occur instantaneously, but with a given probability per unit time.

In this thesis, we will use the two types of models depending upon the question raised. It was argued that including a distribution of local yield stress was a more

realistic choice for the dynamics and was shown to lead to a Herschel-Bulkley type flow curve (Nicolas et al., 2014a), as observed in experiments or molecular simulations. On the other hand, time-delayed models are simpler since their flow features simply result from a competition of timescales, and are in some cases more suited to derive simple mean field arguments for the rheology (Martens et al., 2012). The different timescales at play in the flow of amorphous solids are discussed in the following section.

2.1.4 Elasto-plastic dynamics

Material and driving timescales

Various models consider a finite duration of plastic events in the form of a "restructuring time" $\tau_{\rm el}$,[1] time during which the material undergoes local plastic deformation while stress relaxation occurs (Picard et al., 2005; Martens et al., 2012). If $\tau_{\rm el}$ competes with the driving timescale $\tau_{\dot\gamma} = \gamma_y/\dot\gamma$ (with $\dot\gamma$ the shear rate and γ_y the local yield strain) then plastic events are disrupted by the driving, leading to a shear rate dependence of the macroscopic stress (Nicolas et al., 2014a).

At lower driving rates $\tau_{\rm el} \ll \tau_{\dot\gamma}$, individual plastic events are not disrupted by the driving. Avalanches observed in this regime (i.e., the cascades of plastic events triggered by an initially shear-induced event) are however characterized by a duration $\tau_{\rm av}(L)$ which depends upon the system size and can also depend on the delays due to elastic shear wave propagation, although this aspect has often been neglected in EPMs apart from recent studies (Nicolas et al., 2015; Karimi et al., 2016). When neither individual events nor avalanches are disrupted by the driving, the so-called "quasi-static" limit is reached (characterized by $\tau_{\rm el} \ll \tau_{\dot\gamma}$ and $\tau_{\rm av}(L) \ll \tau_{\dot\gamma}$). In this regime, the material's response to shear is independent of the driving rate. As mentioned in Chapter 1, quasi-static particle-based simulations can be performed by applying a strain step followed by an energy minimization step; equivalent approaches have been developed in the context of EPMs, called extremal or quasi-static models (Baret et al., 2002; Talamali et al., 2011).

Criteria for yielding

As discussed in Chapter 1, numerous studies have attempted to correlate plastic events with local properties of amorphous materials (e.g., local density, free volume, shear modulus, etc.) and it was recently argued that the local yield stress is the most relevant quantity to predict plastic events (Patinet et al., 2016). Most EPMs rely on a yielding criteria based on the value of the local yield stress: generally speaking, a plastic event occurs when the value of the local stress exceeds the value of the local yield stress.

The details of the sequence associated with a yielding event may however vary depending upon the model (Nicolas et al., 2018a). The local yield stress can for instance either be fixed or randomly drawn from a distribution after each yielding event. Yielding can be either instantaneous once the threshold is reached, or instead delayed. In that case, the yielding rate above the threshold can either be constant (Picard et al., 2005) or stress-dependent (Nicolas et al., 2013a; Ferrero et al., 2019).

Regarding the dynamics once a site has yielded, plastic events can be either instantaneous (Hébraud et al., 1998; Baret et al., 2002; Lin et al., 2014) or have a finite duration (Picard et al., 2005). It was further argued that choosing a finite strain

[1] The terminology $\tau_{\rm el}$ can be understood as "typical time to become elastic again"; $\tau_{\rm res}$ is also often encountered.

rather than a finite time would appear more physical to set the duration of a plastic event (Nicolas et al., 2014a), but this approach can be problematic at low shear rate.

Constitutive behavior in plastic regions

The constitutive behavior is modified locally when a plastic rearrangement occurs: rearranging regions are generally treated as fluid-like inclusions that relax stress.

An unconstrained inclusion would spontaneously relax its stress σ at a rate τ^{-1}, τ being an intrinsic relaxation timescale of the material. However, due to the constraint of the surrounding elastic medium, the relaxation only occurs at a rate $|G_0|/\tau$, with $0 < |G_0| < 1$ the local value of the elastic stress propagator. Note that while relaxation is at play, elastic loading still occurs as in a Maxwell's viscoelastic model.

The viscous dynamics of the plastically deforming inclusion is not always considered in EPMs, and a common simplification consists in considering instantaneous stress relaxation. While the two approaches are equivalent in the low shear rate (quasi-static) limit, the choice of a particular type of dynamics can influence the flow curve at larger shear rates.

Further, the clear distinction of local elasticity and local plasticity in the EPM remains phenomenological. In practice, this approach is supported (for soft systems) by the numerical work of Albaret et al. (2016), who have been able to account for the macroscopic stress-strain curve of a material based on a decomposition onto local elastic and plastic strain. This distinction can however be relaxed at the mesoscale when using continuum approaches based on a potential energy landscape representation (Jagla, 2007).

2.1.5 Concluding remarks

We presented in this section the main ingredients of mesoscale elasto-plastic models, emphasizing the large variety of dynamical rules for the plasticity and yielding criteria which often remain phenomenological.

The different rules for yielding and recovering an elastic behavior mentioned in section 2.1.4 have often been used in different contexts (e.g., different scientific questions, driving protocols, shear rate regimes), making their comparison difficult. Moreover, while there start to be insight from molecular simulations regarding aspects like the distribution of local yield stress or initial stress configurations (Patinet et al., 2016; Liu et al., 2020a), no microscopic measurements have shed light on the dynamics of the plastic events yet, leaving the choice of a specific rule to purely phenomenological considerations. In practice, the choice of a particular model is often guided by the scientific goals. For example, models accounting for a yield stress distribution and a recovery criterion based on accumulated strain (Nicolas et al., 2014a) reproduce well the Herschel-Bulkley rheology observed in molecular simulations and are suited for comparisons with microscopic simulations (Liu et al., 2016). On the other hand, simpler models based on competing timescales as introduced by Picard et al. (2005) do not yield a very realistic rheological curve, but are suited to test simple arguments and derive theoretical predictions for the rheology using single-site approximations (Martens et al., 2012).

We did not mention implementation issues yet, such as strategies for spatial discretization, the use of pseudo-spectral methods, etc., where an important variety is also observed (Nicolas et al., 2018a). Treating elastic interactions using an Eshelby kernel is a widespread choice in EPMs, and, as discussed earlier, is supported by microscopic data. However, the choice of a particular discretization strategy may have

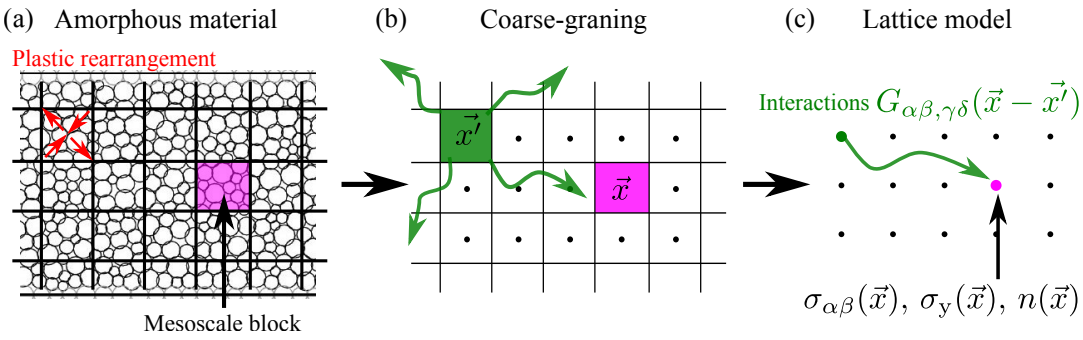

FIGURE 2.2: **Building mesoscale elasto-plastic models**. (a) An amorphous medium (simulation snapshot from Weaire et al. (2010)) is coarse-grained into elementary cells that can deform elastically and undergo plastic rearrangements (depicted with the red arrows) which lead to stress redistribution to the surrounding elastic matrix. (b) This is modeled as interacting blocks: the block undergoing a plastic event (green) redistributes stress to the rest of the system. (c) The state of a cell located in $\vec{x}$ (magenta block) is described by its stress $\sigma_{\alpha\beta}(\vec{x})$, its local threshold $\sigma_y(\vec{x})$ and its plastic activity $n(\vec{x})$. The stress $\delta\sigma_{\alpha\beta}(\vec{x})$ redistributed to the site located in $\vec{x}$ due to a plastic deformation $\varepsilon_{\gamma\delta}(\vec{x'})$ occurring in $\vec{x'}$ is computed using an Eshelby-type elastic propagator $G_{\alpha\beta,\gamma\delta}(\vec{x}-\vec{x'})$

an impact on the outcome of the model. It was for instance suggested that choosing a regular lattice obeying the same symmetries as the elastic kernel would lead to overestimated correlations between plastic events in EPMs (Nicolas et al., 2018a). Some of the technical aspects of the implementation will be further discussed in section 2.3 and in Appendix A.1.

2.2 Formulation

In this section, we introduce a general formalism for the elasto-plastic model including the ingredients introduced above and summarized in Fig. 2.2. We consider a system made of an assembly of elementary (homogeneous) mesoscale blocks, represented as sites of a regular lattice (Fig. 2.2, right panel) which all have the same elastic modulus. Each block can undergo plastic deformation and elastic deformation using a linear elasticity assumption. The dynamics is heterogeneous since blocks can individually undergo plastic events and the interactions between blocks result from the elastic response to plastically deforming blocks, computed from mechanical equilibrium following Eshelby's problem.

Following the approach of Liu (2016), we first describe the elastic response to a heterogeneous plastic deformation field (section 2.2.1). Then, we introduce external driving in the model and explain how to account for either a stress-controlled or a shear-rate-controlled protocol. We finally present the dynamical rules for the local plasticity.

2.2.1 Elastic response to a heterogeneous plastic deformation field

In this first part, we describe the response of an elastic material to a heterogeneous field of plastic deformation (due to localized plastic events).

Displacement and strain fields

We define a displacement field in the material at time $t = t_0 + \Delta t$ with respect to a reference state of the material at time t_0: $\vec{u}(\vec{x}, t_0 + \Delta t) \equiv u_\alpha(x_\beta, t_0 + \Delta t)$ (using indicial notations, i.e., summation over repeated indices, α, β standing for x, y or z). We decompose the displacement field u_α into an elastic contribution and a plastic contribution:

$$u_\alpha = u_\alpha^{\mathrm{el}} + u_\alpha^{\mathrm{pl}} \tag{2.3}$$

A material element centered in $\vec{x} \equiv x_\alpha$, subjected to a displacement $u_\alpha = u_\alpha^{\mathrm{el}} + u_\alpha^{\mathrm{pl}}$ during a time Δt undergoes a total deformation: $\varepsilon_{\alpha\beta}^{\Delta t} = \varepsilon_{\alpha\beta}^{\mathrm{el},\Delta t} + \varepsilon_{\alpha\beta}^{\mathrm{pl},\Delta t}$, with

$$\varepsilon_{\alpha\beta}^{\mathrm{el},\Delta t} = \frac{1}{2}\left(\frac{\partial u_\beta^{\mathrm{el}}}{\partial x_\alpha} + \frac{\partial u_\alpha^{\mathrm{el}}}{\partial x_\beta}\right) \quad \text{and} \quad \varepsilon_{\alpha\beta}^{\mathrm{pl},\Delta t} = \frac{1}{2}\left(\frac{\partial u_\beta^{\mathrm{pl}}}{\partial x_\alpha} + \frac{\partial u_\alpha^{\mathrm{pl}}}{\partial x_\beta}\right) \tag{2.4}$$

The reference state (at $t = t_0$), noted R, can be arbitrarily chosen as long as it respects mechanical equilibrium, i.e., $\frac{\partial \sigma_{\alpha\beta}^R}{\partial x_\beta} = 0$. In linear elasticity, a non-zero stress field in the reference state implies a non-zero elastic deformation field in the reference state: $\sigma_{\alpha\beta}^R = \lambda \delta_{\alpha\beta} \varepsilon_{\gamma\gamma}^{\mathrm{el},R} + 2\mu \varepsilon_{\alpha\beta}^{\mathrm{el},R}$, with λ and μ being the Lamé coefficients.

The plastic deformation field $\varepsilon_{\alpha\beta}^{\mathrm{pl}}$, that can be heterogeneous, describes the contribution of localized irreversible plastic events occurring in the system during a time Δt. We write as $\vec{x}_a$ the position of a plastic event occurring during Δt and $\varepsilon_{\alpha\beta}^{\mathrm{pl},a,\Delta t}$ the plastic strain associated with this event. We can compute the total plastic strain in the system during Δt as (with $A(\vec{x}) = 1$ (or 0) if $\vec{x}$ is inside (or outside) the plastically deforming region):

$$\varepsilon_{\alpha\beta}^{\mathrm{pl},\Delta t} = \sum_{\vec{x}_a} A(\vec{x} - \vec{x}_a) \varepsilon_{\alpha\beta}^{\mathrm{pl},a,\Delta t} \tag{2.5}$$

Mechanical equilibrium

In a static state, the elastic deformation $\varepsilon_{\alpha\beta}^{\mathrm{el},\Delta t}$ during Δt can be seen as the response of a homogeneous elastic material to a heterogeneous plastic strain field $\varepsilon_{\alpha\beta}^{\mathrm{pl},\Delta t}$. Using linear elasticity, the stress perturbation induced after a time Δt (with respect to a reference state R) is given by

$$\sigma_{\alpha\beta}^{\Delta t} = \lambda \delta_{\alpha\beta} \varepsilon_{\gamma\gamma}^{\mathrm{el},\Delta t} + 2\mu \varepsilon_{\alpha\beta}^{\mathrm{el},\Delta t} \tag{2.6}$$

In the following, we drop the Δt labels to lighten notations. Using $\varepsilon_{\alpha\beta}^{\mathrm{el}} = \varepsilon_{\alpha\beta} - \varepsilon_{\alpha\beta}^{\mathrm{pl}}$, mechanical equilibrium reads

$$\frac{\partial \sigma_{\alpha\beta}}{\partial x_\beta} = \frac{\partial}{\partial x_\beta}\left(\lambda \delta_{\alpha\beta}(\varepsilon_{\gamma\gamma} - \varepsilon_{\gamma\gamma}^{\mathrm{pl}}) + 2\mu(\varepsilon_{\alpha\beta} - \varepsilon_{\alpha\beta}^{\mathrm{pl}})\right) = 0 \tag{2.7}$$

which yields:

$$\lambda \frac{\partial \varepsilon_{\gamma\gamma}}{\partial x_\alpha} + 2\mu \frac{\partial \varepsilon_{\alpha\beta}}{\partial x_\beta} = \lambda \frac{\partial \varepsilon_{\gamma\gamma}^{\mathrm{pl}}}{\partial x_\alpha} + 2\mu \frac{\partial \varepsilon_{\alpha\beta}^{\mathrm{pl}}}{\partial x_\beta} \tag{2.8}$$

We rewrite this equation in terms of displacement field:

$$(\lambda + \mu) \frac{\partial}{\partial x_\alpha} \frac{\partial u_\gamma}{\partial x_\gamma} + \mu \frac{\partial}{\partial x_\beta}\left(\frac{\partial u_\alpha}{\partial x_\beta}\right) = \lambda \frac{\partial \varepsilon_{\gamma\gamma}^{\mathrm{pl}}}{\partial x_\alpha} + 2\mu \frac{\partial \varepsilon_{\alpha\beta}^{\mathrm{pl}}}{\partial x_\beta} \tag{2.9}$$

This equation actually reduces to the Navier equation for a static state of the material:

$$(\lambda+\mu)\frac{\partial}{\partial x_\alpha}\frac{\partial u_\gamma}{\partial x_\gamma}+\mu\frac{\partial}{\partial x_\beta}\left(\frac{\partial u_\alpha}{\partial x_\beta}\right)=-f_\alpha \tag{2.10}$$

with a body force $f_\alpha=-\lambda\frac{\partial \varepsilon^{\mathrm{pl}}_{\gamma\gamma}}{\partial x_\alpha}-2\mu\frac{\partial \varepsilon^{\mathrm{pl}}_{\alpha\beta}}{\partial x_\beta}$.

Incompressible medium assumption

If we assume that the elastic medium is incompressible, Eq. 2.10 reduces to:

$$-\frac{\partial P}{\partial x_\alpha}+\mu\frac{\partial^2 u_\alpha}{\partial x_\beta^2}+f_\alpha=0 \tag{2.11}$$

$$\frac{\partial u_\alpha}{\partial x_\alpha}=0 \tag{2.12}$$

Solving the above equation is actually analogous to solving a well-known problem in hydrodynamics, which consist in looking for the flow solution when a force is applied to a point particle immersed in a viscous liquid in the case of an incompressible flow (Stokeslet) (Hancock, 1953). Due to the linearity of this equation, it is conveniently expressed in Fourier space:

$$iq_\alpha\tilde{P}-\mu q_\beta q_\beta\tilde{u_\alpha}+\tilde{f_\alpha}=0 \tag{2.13}$$

$$-iq_\alpha\tilde{u_\alpha}=0 \tag{2.14}$$

By multiplying Eq. 2.13 by the wavevector q_α (taking the divergence of the equation, which yields a Poisson equation for the pressure):

$$iq_\alpha q_\alpha\tilde{P}-\mu q_\alpha q_\beta q_\beta\tilde{u_\alpha}+q_\alpha\tilde{f_\alpha}=0 \tag{2.15}$$

and using the incompressibility condition (Eq. 2.14), we can express the pressure as (with $q^2=q_\alpha q_\alpha$):

$$\tilde{P}=i\frac{q_\alpha\tilde{f_\alpha}}{q^2} \tag{2.16}$$

By inserting the expression for the pressure in Eq. 2.13, we get:

$$\tilde{u_\alpha}=\frac{1}{\mu q^2}\left(\tilde{f_\alpha}-\frac{q_\alpha q_\gamma}{q^2}\tilde{f_\gamma}\right) \tag{2.17}$$

One recognizes here the Oseen tensor, relating the displacement field to the force, with $\tilde{f_\alpha}=2i\mu q_\beta\tilde{\varepsilon}^{\mathrm{pl}}_{\alpha\beta}$. Then, using $\sigma_{\alpha\beta}=2\mu\varepsilon^{\mathrm{el}}_{\alpha\beta}=2\mu\left(\varepsilon_{\alpha\beta}-\varepsilon^{\mathrm{pl}}_{\alpha\beta}\right)$:

$$\tilde{\sigma}_{\alpha\beta}=-i\mu\left(q_\alpha\tilde{u}_\beta+q_\beta\tilde{u}_\alpha\right)-2\mu\tilde{\varepsilon}^{\mathrm{pl}}_{\alpha\beta} \tag{2.18}$$

By inserting Eq. 2.17 into Eq. 2.18, we get:

$$\tilde{\sigma}_{\alpha\beta}=2\mu\left(\frac{\delta_{\beta\delta}q_\alpha q_\gamma+\delta_{\alpha\gamma}q_\beta q_\delta}{q^2}-2\frac{q_\alpha q_\beta q_\gamma q_\delta}{q^4}-\delta_{\alpha\gamma}\delta_{\beta\delta}\right)\tilde{\varepsilon}^{\mathrm{pl}}_{\gamma\delta} \tag{2.19}$$

which can be rewritten as

$$\tilde{\sigma}_{\alpha\beta}=2\mu\tilde{G}^*_{\alpha\beta,\gamma\delta}\tilde{\varepsilon}^{\mathrm{pl}}_{\gamma\delta}\quad\text{with}\quad\tilde{G}^*_{\alpha\beta,\gamma\delta}=\frac{\delta_{\beta\delta}q_\alpha q_\gamma+\delta_{\alpha\gamma}q_\beta q_\delta}{q^2}-2\frac{q_\alpha q_\beta q_\gamma q_\delta}{q^4}-\delta_{\alpha\gamma}\delta_{\beta\delta} \tag{2.20}$$

The propagator $\tilde{G}^*_{\alpha\beta,\gamma\delta}$ is not defined for wavevectors $|\vec{q}| = 0$. The stress response for a zero wavevector is such that the integral over the whole space of the stress response to an internal plastic event is equal to zero. If we note the total stress response function $\tilde{G}_{\alpha\beta,\gamma\delta}$, we thus get:

$$\tilde{G}_{\alpha\beta,\gamma\delta}(|\vec{q}| = 0) = 0 \tag{2.21}$$

$$\tilde{G}_{\alpha\beta,\gamma\delta}(|\vec{q}| \neq 0) = \tilde{G}^*_{\alpha\beta,\gamma\delta} \tag{2.22}$$

To summarize, $\tilde{G}_{\alpha\beta,\gamma\delta}$ describes the stress response to a heterogeneous plastic deformation field in the system, which corresponds to a macroscopically stress-free state. The above expression is general (valid for any dimension and both tensorial and scalar models), and we will specify in the following the two types of models that we use in this thesis.

2.2.2 External driving

Superimposition of stress fields

We note $\sigma^{\text{int}}_{\alpha\beta}$ the internal stress field due to a heterogeneous plastic deformation field, as described above. In real space, it is defined as the convolution of the plastic strain field with the elastic kernel G,

$$\sigma^{\text{int}}(\vec{x}, t) = 2\mu \int d^d\vec{x'} G_{\alpha\beta,\gamma\delta}(\vec{x} - \vec{x'})\varepsilon^{\text{pl}}_{\gamma\delta}(\vec{x'}, t) \tag{2.23}$$

If a driving (external or local) is applied to the material, this will induce an additional stress field in the system, $\sigma^{\text{driv}}_{\alpha\beta}$. The total stress field thus reads:

$$\sigma_{\alpha\beta}(\vec{x}, t) = \sigma^{\text{int}}_{\alpha\beta}(\vec{x}, t) + \sigma^{\text{driv}}_{\alpha\beta}(\vec{x}, t) \tag{2.24}$$

with

$$\frac{1}{V} \int d^d\vec{x'} \sigma^{\text{int}}_{\alpha\beta}(\vec{x}, t) = 0 \tag{2.25}$$

and the macroscopic stress reads

$$\Sigma_{\alpha\beta} = \langle \sigma_{\alpha\beta} \rangle = \frac{1}{V} \int d^d\vec{x'} \sigma_{\alpha\beta}(\vec{x}, t) = \frac{1}{V} \int d^d\vec{x'} \sigma^{\text{driv}}_{\alpha\beta}(\vec{x}, t) \tag{2.26}$$

To summarize, the medium, assumed to be in mechanical equilibrium at all times, is characterized by a heterogeneous plastic deformation field $\varepsilon^{\text{pl}}_{\alpha\beta}$ which induces an internal stress field $\sigma^{\text{int}}_{\alpha\beta}$. An additional stress field due to driving (that can take any arbitrary form), $\sigma^{\text{driv}}_{\alpha\beta}(\vec{x}, t)$ adds up to the internal stress field, yielding the total stress field in the system. In elastic regions (regions that are not undergoing plastic deformation), the elastic strain field is related to the total stress field by linear elasticity, which reads, for an incompressible material: $\sigma_{\alpha\beta} = 2\mu\varepsilon^{\text{el}}_{\alpha\beta}$.

Stress-controlled dynamics

The dynamics of the system results from the fact that at each time, the internal stress field must fulfill mechanical equilibrium in the system. The underlying hypothesis is that the dynamics of the system is overdamped, so that inertial contributions are negligible. From equations 2.23 and 2.24, the state of the system at time t is determined by two independent contributions: the internal plastic deformation field $\varepsilon^{\text{pl}}_{\alpha\beta}(\vec{x}, t)$ and

the external driving $\sigma^{\text{driv}}_{\alpha\beta}(\vec{x},t)$. The time evolution of these two quantities will thus set the dynamics of the system.

Two main aspects must be considered to determine the dynamics of $\varepsilon^{\text{pl}}_{\alpha\beta}(\vec{x},t)$: (i) where and when does a plastic event occur ? When does it terminate? and (ii) When a localized plastic event occurs in a given region, how does the plastic strain evolve with respect to the other variables (e.g., stress)? As mentioned in section 2.1, there exist several ways of modeling the dynamics of $\varepsilon^{\text{pl}}_{\alpha\beta}(\vec{x},t)$, and we will introduce the dynamical rules used in this thesis in the next section.

The dynamics of $\sigma^{\text{driv}}(\vec{x},t)$ depends on the system under consideration and on the driving protocol used. In the case of a passive amorphous system with an externally imposed uniform shear stress, $\sigma^{\text{driv}}_{\alpha\beta}(\vec{x},t) = \sigma^{\text{driv}}_{\alpha\beta}$ is constant over the system. In the case where a uniform pressure gradient is imposed along the x direction in a 2d channel, $\partial P/\partial x = C_{\text{p}}$, mechanical equilibrium and symmetries yield: $\sigma^{\text{driv}}_{xy}(x,y) = C_{\text{p}}y + K_1$ (K_1 being a constant) and $\sigma^{\text{driv}}_{xx} = -\sigma^{\text{driv}}_{yy} = K_2$ (K_2, a constant). Finally, in the case where local active processes induce heterogeneous stresses in an active or biological system, $\sigma^{\text{driv}}_{\alpha\beta}(\vec{x},t)$ can take an arbitrary form depending upon the type of activity. We will see an example in Chapter 5, where the local driving results from the (coarse-grained) response to the active deformation of particles.

In the framework introduced in this section, it is natural to model flows using a stress-controlled driving protocol. However, it is common, both in experiments and simulations, to impose the macroscopic shear rate rather than the macroscopic stress to the system. This framework can be generalized to account for shear-rate-controlled driving protocols.

Shear-rate-controlled dynamics

The global strain in the system is defined as:

$$\langle \varepsilon_{\alpha\beta}(t)\rangle = \frac{1}{L^d}\int d\vec{x}^d \varepsilon_{\alpha\beta}(\vec{x},t) = \langle \varepsilon^{\text{pl}}_{\alpha\beta}(t)\rangle + \langle \varepsilon^{\text{el}}_{\alpha\beta}(t)\rangle \tag{2.27}$$

The elastic strain is further decomposed into two parts: one resulting from the internal stress $\sigma^{\text{int}}_{\alpha\beta}$, whose average is equal to 0 (by definition of $\sigma^{\text{int}}_{\alpha\beta}$), $\langle \varepsilon^{\text{el,int}}_{\alpha\beta}(t)\rangle = 0$, and one resulting from the driving stress $\sigma^{\text{driv}}_{\alpha\beta}$, $\langle \varepsilon^{\text{el,driv}}_{\alpha\beta}(t)\rangle \neq 0$. In order to impose a global deformation rate $\langle \dot{\varepsilon}_{\alpha\beta}\rangle$ to the system, one needs to adjust the value of the driving stress depending upon the total deformation rate:

$$\dot{\sigma}^{\text{driv}}_{\alpha\beta}(t) = 2\mu\left(\langle \dot{\varepsilon}_{\alpha\beta}(t)\rangle - \langle \dot{\varepsilon}^{\text{pl}}_{\alpha\beta}(t)\rangle\right) \tag{2.28}$$

The dynamics of the local stress reads:

$$\frac{\partial \sigma_{\alpha\beta}(\vec{x},t)}{\partial t} = \dot{\sigma}^{\text{driv}}_{\alpha\beta}(t) + \dot{\sigma}^{\text{int}}_{\alpha\beta}(\vec{x},t) \tag{2.29}$$

Using Eq. 2.28 and Eq. 2.23, we get:

$$\frac{\partial \sigma_{\alpha\beta}(\vec{x},t)}{\partial t} = 2\mu\left(\langle \dot{\varepsilon}_{\alpha\beta}(t)\rangle - \langle \dot{\varepsilon}^{\text{pl}}_{\alpha\beta}(t)\rangle\right) + \frac{\partial}{\partial t}2\mu\int d^d\vec{x'} G_{\alpha\beta,\gamma\delta}(\vec{x}-\vec{x'})\varepsilon^{\text{pl}}_{\gamma\delta}(\vec{x'},t) \tag{2.30}$$

We finally get, by introducing the shear rate $\dot{\gamma} = 2\mu\langle \dot{\varepsilon_{\alpha\beta}}(t)$:

$$\frac{\partial \sigma_{\alpha\beta}(\vec{x},t)}{\partial t} = \mu\dot{\gamma} + 2\mu\int d^d\vec{x'}\left(G_{\alpha\beta,\gamma\delta}(\vec{x}-\vec{x'}) - \frac{1}{V}\right)\frac{\partial \varepsilon^{\text{pl}}_{\gamma\delta}(\vec{x'},t)}{\partial t} \tag{2.31}$$

When using shear-controlled protocols, it is thus convenient to define the propagator $G^{\text{shear}}_{\alpha\beta,\gamma\delta}(\vec{x}-\vec{x'}) = G_{\alpha\beta,\gamma\delta}(\vec{x}-\vec{x'}) - \frac{1}{V}$ for which the integral of $\sigma^{\text{int}}_{\alpha\beta}$ over the whole volume is not zero.

2.2.3 Dynamics of the local plasticity

If a mesoscopic block centered in $\vec{x}$ deforms plastically ($\varepsilon^{\text{pl}}_{\alpha\beta}(\vec{x},t) \neq 0$), then the block is said to be in a "plastic state". We introduce a Boolean variable, $n(\vec{x},t)$, to account for the local state: $n(\vec{x},t) = 0$ when the block deforms elastically and $n(\vec{x},t) = 1$ when the block deforms plastically. The evolution rules for $n(\vec{x},t)$ encode the physical mechanisms governing the elasto-plastic behavior of amorphous materials.

The transition from an elastic to a plastic state occurs once the local stress exceeds a local threshold (local yield stress σ_{y}) and is determined by a von Mises yield criterion $\sigma_{\text{v}} > \sigma_{\text{y}}$, with in 2d:

$$\sigma_{\text{v}} = \sqrt{\frac{(\sigma_{xx} - \sigma_{yy})^2 + 4\sigma_{xy}^2}{2}} \tag{2.32}$$

The choice for the local barrier values σ_{y} and the yielding rules may differ between the different elasto-plastic models found in the literature. In the following, we use two different sets of stochastic rules: in Chapter 4 we use the model introduced by Picard et al. (2005) based on transition rates and where all sites have the same barrier σ_{y} and in Chapter 5 we use a model based on distributed yield stress values as introduced by Nicolas et al. (2014a).

Dynamics of the plastic deformation

Once a site has yielded ($n(\vec{x},t) = 1$), plastic deformation accumulates locally. As mentioned earlier, each mesoscopic block is then modeled as a viscoelastic Maxwell element i.e., with an Hookean spring (undergoing elastic deformation $\varepsilon^{\text{el}}_{ij}$) in series with a dashpot (undergoing plastic deformation $\varepsilon^{\text{pl}}_{ij}$). The local plastic strain rate is thus given by:

$$\frac{\partial \varepsilon^{\text{pl}}_{\alpha\beta}(\vec{x},t)}{\partial t} = n(\vec{x},t)\frac{\sigma_{\alpha\beta}(\vec{x},t)}{2\mu\tau} \tag{2.33}$$

with τ the timescale associated with viscous damping, which sets the time units of the model.

Stochastic dynamics for the local activity $n(\vec{x},t)$ in Picard's model

In Picard's model, to account for the fact that a region has a finite probability to yield when the local stress becomes too large, a stochastic dynamics for $n(\vec{x},t)$ is introduced with a transition rate $1/\tau_{\text{pl}}$ for the transition $n : 0 \xrightarrow{1/\tau_{\text{pl}}} 1$ if $\sigma_{\text{v}} > \sigma_{\text{y}}$. The yield stress σ_{y} has a unique value and is identical for all the blocks. Once it has yielded, a site becomes elastic again after a typical time τ_{el}: $n : 1 \xrightarrow{1/\tau_{\text{el}}} 0$. The typical evolution of a local stress is depicted in Fig. 2.3.

Stochastic dynamics based on a yield stress distribution

An alternative approach is to consider instantaneous yielding once the local stress has exceeded a threshold σ_{y}, the yield stress value σ_{y} being a random variable renewed after each yielding event (Nicolas et al., 2014a).

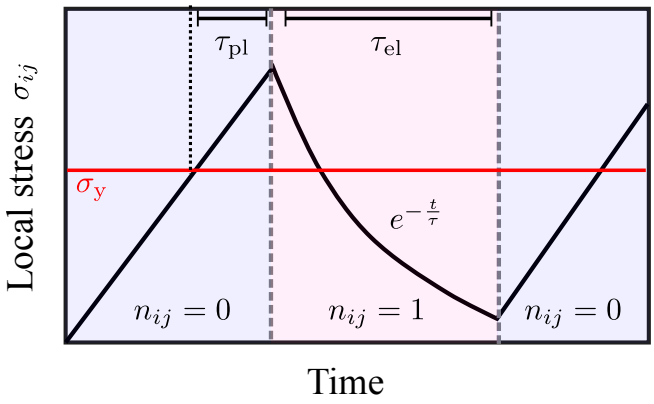

FIGURE 2.3: **Sketch of the local stress dynamics in the model introduced by Picard et al. (2005).**

The local threshold σ_{y} is drawn form a probability distribution independently for each block. A stress threshold σ_{y} would correspond to an energy barrier $E_{\text{y}} = \frac{|\sigma_{\text{y}}|^2}{4\mu}$. We consider an exponential distribution of energy barriers (as in the Soft Glass Rheology model (Sollich et al., 1997)), bounded by a minimum value $E_{\text{y}}^{\min}$ and a maximum value $E_{\text{y}}^{\max}$:

$$P(E_{\text{y}}) = \Theta(E_{\text{y}} - E_{\text{y}}^{\min})\Theta(E_{\text{y}}^{\max} - E_{\text{y}})\lambda \exp -\lambda(E_{\text{y}} - E_{\text{y}}^{\min}) \tag{2.34}$$

with $\Theta(x)$ the Heaviside function and λ a parameter chosen such that the average yield strain γ_{y} takes a realistic value (as compared to experiments), around, e.g., 10% for emulsions (Hébraud et al., 1997). Note that no upper bound for the energy barrier distribution was considered in the original implementation of this model ($E_{\text{y}}^{\max} \to \infty$) (Nicolas et al., 2014a). We added this feature to ensure that, when using stress-controlled protocols, the system would not always become arrested in the long time limit as a consequence of a statistical hardening effect (because all the barriers would eventually become larger than the local stress).

Regarding the elastic recovery, Nicolas et al. (2014a) proposed a criterion based on the accumulated plastic strain, arguing it was a more realistic physical picture than setting a fixed duration of events. In our work, we will however consider the same recovery rule as in Picard's model (with a fixed event duration τ_{el}), to avoid potential issues in the low driving limit (where the rule of Nicolas et al. (2014a) can lead to never ending plastic events).

2.3 Implementation

The formulation presented above was general, and neither the spatial dimension nor the tensoriality of the model was specified. In this thesis, we focus on 2d elasto-plastic models. Note that the dimensionality of the model is found to affect only slightly the dynamical features of the flow such as avalanche dynamics (Liu et al., 2016).

We use different variants of the elasto-plastic model introduced previously: scalar and tensorial implementations, stress- and strain-controlled protocol, and, as already mentioned, different sets of stochastic rules. Let us now present these different variants, discuss some aspects of their numerical implementation before comparing their rheological behavior in section 2.4.

Scalar and tensorial models

Both scalar and tensorial implementations of elasto-plastic models have been used in the literature (Nicolas et al., 2018a). It is known that the direction of the plastic events is biased by the external driving (Nicolas et al., 2018b). When the driving is uniform (such as simple shear), it can be convenient to consider only one stress component, σ_{xy}, corresponding to the geometry of an externally imposed strain γ_{xy}. Scalar models are however simplifications of the general model formulated above since stress redistribution via the elastic propagator leads to non-zero values for the other stress components, as shown in Fig. 2.4.

Tensorial implementations have thus also been considered. It was however found that the effect of tensoriality on the rheology and avalanche properties was not significant (Nicolas et al., 2014b; Budrikis et al., 2017). However, in the case of heterogeneous driving such as bending, torsion or indentation tests on hard glassy materials (Budrikis et al., 2017) or microchannel flows of soft glassy materials (Nicolas et al., 2013a), a tensorial implementation of EPMs is necessary. In this thesis, we will consider another case of heterogeneous driving in EPMs, due to a localized (biological) activity acting as a heterogeneous source of stress in the system. Let us now introduce a 2d tensorial implementation of the EPM, as introduced by Nicolas et al. (2013a).

2d tensorial model: We consider a two-dimensional uniform elastic incompressible medium, for which the deviatoric part of the strain and stress tensors read:

$$\varepsilon = \begin{pmatrix} \varepsilon_{xx} & \varepsilon_{xy} \\ \varepsilon_{xy} & \varepsilon_{yy} \end{pmatrix} \text{ and } \sigma = \begin{pmatrix} \sigma_{xx} & \sigma_{xy} \\ \sigma_{xy} & \sigma_{yy} \end{pmatrix} \tag{2.35}$$

with $\varepsilon_{xx} + \varepsilon_{yy} = 0$ and $\sigma_{xx} + \sigma_{yy} = 0$. There are only two independent strain and stress components and the notations can be condensed as:

$$\varepsilon = \begin{pmatrix} \frac{\varepsilon_{xx} - \varepsilon_{yy}}{2} \\ \varepsilon_{xy} \end{pmatrix} \text{ and } \sigma = \begin{pmatrix} \frac{\sigma_{xx} - \sigma_{yy}}{2} \\ \sigma_{xy} \end{pmatrix} \tag{2.36}$$

with $\frac{\varepsilon_{xx} - \varepsilon_{yy}}{2} = \varepsilon_{xx}$ and $\frac{\sigma_{xx} - \sigma_{yy}}{2} = \sigma_{xx}$. We express the stress tensor as a function of the plastic strain tensor in Fourier space, following the above calculation, with $\tilde{G}^{\mathrm{T}}_{2\mathrm{d}}$ the elastic kernel describing the stress redistribution due to plastic deformation in the system,

$$\begin{pmatrix} \tilde{\sigma}_{xx} \\ \tilde{\sigma}_{xy} \end{pmatrix} = 2\mu \tilde{G}^{\mathrm{T}}_{2\mathrm{d}} \begin{pmatrix} \tilde{\varepsilon}^{\mathrm{pl}}_{xx} \\ \tilde{\varepsilon}^{\mathrm{pl}}_{xy} \end{pmatrix} \tag{2.37}$$

From Eq. 2.20, we get:

$$\tilde{G}^{\mathrm{T}}_{2\mathrm{d}} = \frac{1}{q^4} \begin{bmatrix} -(q_x^2 - q_y^2)^2 & -2q_x q_y (q_x^2 - q_y^2) \\ -2q_x q_y (q_x^2 - q_y^2) & -4q_x^2 q_y^2 \end{bmatrix} \tag{2.38}$$

The stress response to a plastic event of plastic strain $\varepsilon^{\mathrm{pl}}_{xy}$ in the center of the system is depicted in Fig. 2.4.

2d scalar model: In the commonly used scalar EPMs (as introduced by Picard et al. (2005)), the assumption is that all the plastic events contributing to the flow have the same geometry as the macroscopically applied shear flow, i.e., we consider a single component of the strain and stress tensor, ε_{xy} and σ_{xy}, thus leading to:

$$\tilde{\sigma}_{xy} = 2\mu \tilde{G}^{\mathrm{S}}_{2\mathrm{d}} \tilde{\varepsilon}^{\mathrm{pl}}_{xy} \tag{2.39}$$

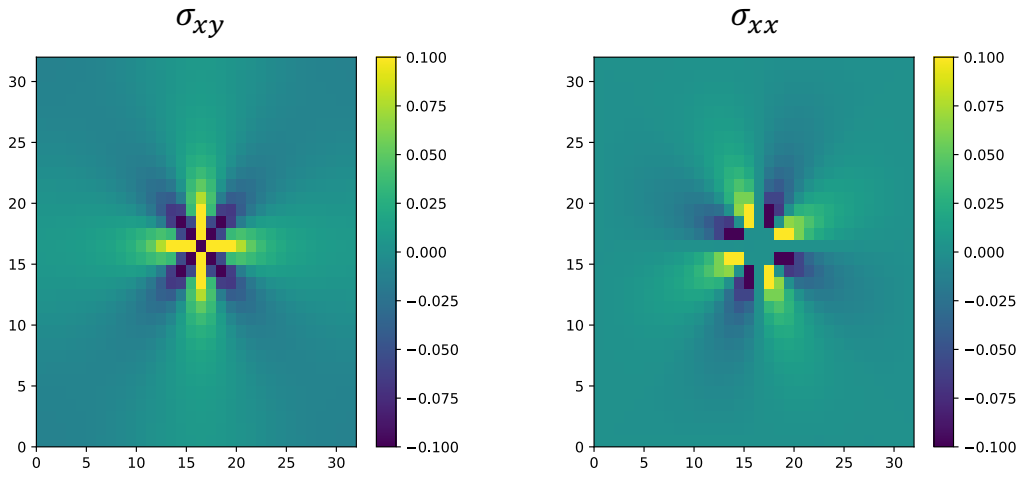

FIGURE 2.4: **Stress response to a plastic event** of plastic strain $\varepsilon^{\mathrm{pl}}_{xy}$ ($\varepsilon^{\mathrm{pl}}_{xx} = 0$) induced artificially in the center of the system for a lattice size $L_x = L_y = 32$. Left panel: σ_{xy}. Right panel: σ_{xx}

and the propagator reduces to the $\left(\tilde{G}^{\mathrm{T}}_{2\mathrm{d}}\right)_{22}$ component of Eq. 2.38.

$$\tilde{G}^{\mathrm{S}}_{2\mathrm{d}} = -\frac{4q_x^2 q_y^2}{q^4} \tag{2.40}$$

Note that, in this part, we did not specify the full form of the propagators $\tilde{G}^{\mathrm{T}}_{2\mathrm{d}}$ and $\tilde{G}^{\mathrm{S}}_{2\mathrm{d}}$ since it depends on the driving protocol (strain- or stress-controlled protocol).

Driving protocols

Numerical simulations of the elasto-plastic model have mostly considered strain-controlled (fixed $\dot{\gamma}$) rather than stress-controlled (fixed Σ) driving protocols. We use in this thesis both types of dynamics as they give access to different features of the flow.

We discretize the model introduced in section 2.2 on a two-dimensional lattice. The lattice indices (i, j) represent the discretized coordinates along x and y directions respectively. When using a stress-controlled protocol with a driving stress $\sigma^{\mathrm{driv}}_{\alpha\beta}$, the dynamics for the local plastic strain at site (i, j) reads:

$$\frac{d}{dt}\gamma^{\mathrm{pl}}_{\alpha\beta}(i,j) = \frac{n(i,j)\sigma_{\alpha\beta}(i,j)}{\mu\tau} = n(i,j)\frac{\sigma^{\mathrm{driv}}_{\alpha\beta}(i,j) + \sigma^{\mathrm{int}}_{\alpha\beta}(i,j)}{\mu\tau} \tag{2.41}$$

with

$$\sigma^{\mathrm{int}}_{\alpha\beta}(i,j) = \mu \sum_{i',j'} G^{2\mathrm{d}}_{\alpha\beta,\gamma\delta}(i,j,i',j')\gamma^{\mathrm{pl}}_{\gamma\delta}(i',j') \tag{2.42}$$

with $\gamma^{\mathrm{pl}}_{\gamma\delta}(i',j') = 2\varepsilon^{\mathrm{pl}}_{\gamma\delta}(i',j')$. The propagator $G^{2\mathrm{d}}$ is such that the average redistributed stress is zero.

When using a strain-controlled protocol with an imposed shear rate $\dot{\gamma}$, the dynamics for the local stress at site (i, j) is described by:

$$\frac{d}{dt}\sigma_{\alpha\beta}(i,j) = \mu\dot{\gamma} + \mu \sum_{i',j'} G^{2\mathrm{d,shear}}_{\alpha\beta,\gamma\delta}(i,j,i',j')\frac{d}{dt}\gamma^{\mathrm{pl}}_{\gamma\delta}(i',j') \tag{2.43}$$

with $d\gamma^{\rm pl}_{\gamma\delta}(i,j)/dt = n(i,j)\sigma_{\alpha\beta}(i,j)/\mu\tau$.

The propagator $G^{\rm 2d,shear}$ is related to G^{2d} by $G^{\rm 2d,shear} = G^{2d} - 1/L^2$, because, unlike $G^{\rm 2d}$, $G^{\rm 2d,shear}$ describes the full stress field response to a plastic deformation (and not only the stress fluctuations).

In the numerical implementation of the elasto-plastic model, we consider a discretized space and, as we focus on bulk properties, it is convenient to work with a bounded system with periodic boundary conditions. Various numerical approaches have been developed to compute the convolution product in Eq. 2.42 and Eq. 2.43. Taking advantage of the periodic boundary conditions, we use a pseudo-spectral method which consists in discretizing the elastic propagator in Fourier space which enables us to compute the convolution as a local operation on the Fourier modes. The numerical implementation of the model is presented in more details in Appendix A.1.

2.4 Some flow properties of elasto-plastic models

In this section, we review general flow properties of the elasto-plastic models introduced in the first part of the chapter.

We simulate the two models presented above: Picard's model (called model 1 in the following) and the model with a yield stress distribution and fixed recovery time (model 2) on a 2d lattice using strain- and stress-controlled protocols and scalar and tensorial implementations using the methods presented in Appendix A.1. The elastic modulus $\mu = 1$ sets the stress units and the relaxation time τ sets the time units of the model. To simulate model 1, we set the timescales of the model $\tau_{\rm pl} = \tau_{\rm el} = \tau = 1$ and the local yield stress $\sigma_{\rm y} = 1$. To simulate model 2, we choose a yield stress distribution with the following parameters: $E_{\rm y}^{\rm min} = 2.5 \cdot 10^{-4}$, $E_{\rm y}^{\rm max} = 1.8225 \cdot 10^{-2}$ and $\lambda = 701.67$ (Nicolas et al., 2014a), and an elastic recovery time $\tau_{\rm el} = \tau = 1$.

2.4.1 Rheological behavior

In Fig. 2.5(a) and (b), we show, for models 1 and 2, the stress Σ_{xy} as a function of strain γ_{xy} obtained by imposing a constant shear rate $\dot\gamma_{xy}$ starting from an initial state characterized by $\sigma_{xy} = 0$ and $n = 0$ for all the sites (shear start-up protocol). There is a clear overshoot in Picard's model due to the fact that all the sites must reach a stress greater than $\sigma_{\rm y} = 1$, leading to an abrupt yielding of the system. On the other hand, no stress overshoot is observed in model 2, where the local yield stress values are drawn from a distribution. In this case, sites with small barriers will yield first, leading to a smooth stress-strain response.

Numerical flow curves (stress $\overline{\Sigma_{xy}}$ versus shear rate $\overline{\dot\gamma_{xy}}$ in steady state) are shown in Fig. 2.5(c) and (d). The rheology is only slightly affected by the tensoriality of the model (Fig. 2.5(c)), as found by Nicolas et al. (2014a). Stress-controlled and strain-controlled protocols also yield the same steady-state rheology, as shown in Fig. 2.5(d) (Liu et al., 2018).

The two models lead to a yield stress fluid behavior. The flow curve of model 2 can be fitted to a Herschel-Bulkley form with an exponent comprised between 0.5 and 0.7 at sufficiently low shear rates (see legend of Fig. 2.5(d)). In Picard's model, the dynamical yield stress (value of the stress plateau observed at low shear rate) differs from the static yield stress value (value at the overshoot, determined by the uniquely defined local yield stress). An important aspect of Picard's model is that all the rheological data can be collapsed if the shear stress is rescaled by σ_y, the time by τ and the shear rate by $\dot\gamma_{\rm c} = \sigma_y/\mu\tau$ (Picard et al., 2005). The model can thus be made dimensionless and the only parameters left are $\tau_{\rm pl}$ and $\tau_{\rm el}$.

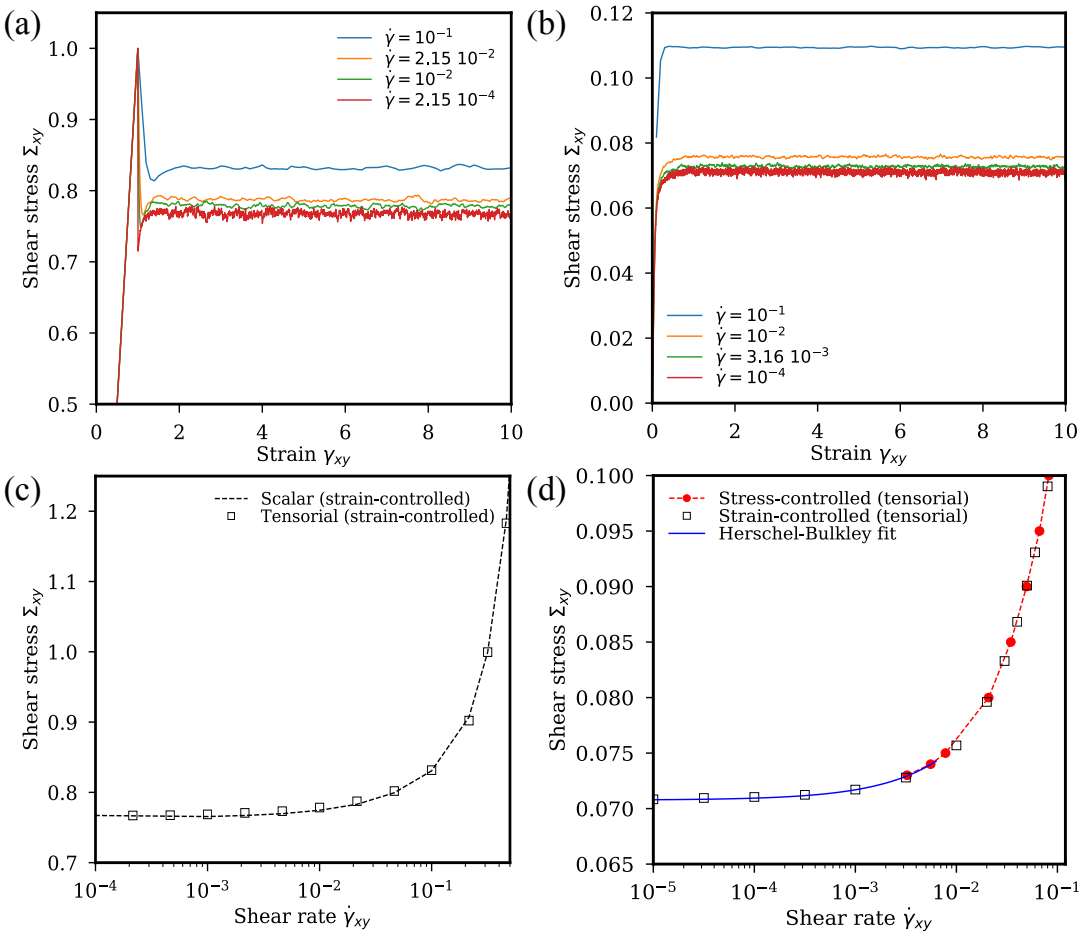

FIGURE 2.5: **Rheological behavior of two different elasto-plastic models** obtained from simulations of a 2d system of size $N = 128 \times 128$. (1) Picard's model (a-c) and (2) model based on a yield stress distribution with a fixed elastic recovery time (b-d). (a) Stress as a function of strain for different imposed shear rates in a tensorial version of Picard's model (1) exhibiting an overshoot. (b) For the tensorial version of model (2), no stress overshoot is observed. (c) Shear stress versus shear rate in model (1) for both scalar and tensorial versions of the model using a strain-rate controlled protocol. (d) Shear stress versus shear rate in a tensorial version of model (2) for stress-controlled and strain-controlled protocols. The curve is fitted with a Herschel-Bulkley form at low shear rates ($\dot{\gamma}_{xy} \lesssim 10^{-2}$): $\Sigma_{xy} = \Sigma_y + A\dot{\gamma}_{xy}^n$ with an exponent n comprised between 0.5 and 0.7 depending upon the exact fitting range.

The effect of these two timescales on the macroscopic flow curve is shown in Appendix A.2 (Fig. A.1). $\tau_{\rm el}$ describes the time needed to regain an elastic behavior once a site has yielded locally. This time may be related to the physico-chemistry of the material and to the adhesion properties of its constituents, as suggested by Coussot et al. (2010). Coussot et al. (2010) have further proposed that a longer restructuring time could lead to local softening and be at the origin of shear banding. This aspect was investigated using Picard's EPM by Martens et al. (2012).

2.4.2 Nonmonotonic constitutive flow curve and shear bands

Martens et al. (2012) have shown that the bulk rheology of Picard's model can be captured using an analytically solvable approximation, by considering an effective single-site dynamics. The advantage of considering a single-site dynamics is that it ensures that the resulting rheology is that of a homogeneous system, giving access to the constitutive (possibly nonmonotonic) flow curve.

Single-site elasto-plastic model

Let us consider a scalar EPM, with $\sigma \equiv \sigma_{xy}$ and $\dot\gamma \equiv \dot\gamma_{xy}$. In the EPM, the dynamics of the stress on a site (i,j) is written as:

$$\frac{\partial \sigma(i,j)}{\partial t} = \dot\gamma^{\rm eff}(i,j) + G(0,0)n(i,j)\sigma(i,j) \tag{2.44}$$

with $G(0,0) < 0$ the value of the stress propagator at the origin (describing the local plastic relaxation) and $\dot\gamma^{\rm eff}(i,j)$ the effective local shear rate due to the external drive and to the stress redistribution due to plastic events elsewhere in the system, $\dot\gamma^{\rm eff}(i,j) = \dot\gamma + \sum_{i',j'} G(i-i',j-j')n(i',j')\sigma(i',j')$. The single-site model relies on the assumption that this effective shear rate is spatially homogeneous, and neglects any fluctuations around its mean value $\dot\Gamma$. In this case, the evolution of stress $\sigma(t)$ on a single site reads:

$$\frac{\partial \sigma(t)}{\partial t} = \dot\Gamma - g n(t)\sigma(t) \tag{2.45}$$

with $g = |G(0,0)|$ the absolute value of the stress propagator at the origin, which can depend on the system size in the spatial model, but which remains approximately constant for large systems ($g \simeq 0.57$). The dynamics of the activity $n(t)$ remains unchanged with respect to the spatial model (see section 2.2.3: $n : 0 \xrightarrow{1/\tau_{pl}} 1$ if $\sigma > \sigma_{\rm y}$ and τ_{el}: $n : 1 \xrightarrow{1/\tau_{el}} 0$).

In a first step, one can simulate the above stochastic dynamics for the single-site EPM (Eq. 2.45). The steady state flow curves thus obtained by averaging the stress in steady state are depicted by the symbols in Fig. 2.6(a) (Martens et al., 2012).

Martens et al. (2012) derived an analytical expression for the flow curve, depicted by the solid lines in Fig. 2.6(a). The full derivation of the model is shown in Appendix A.3, we recall here only the main points. The time averaged stress $\langle\sigma\rangle_t$ can be computed as

$$\langle\sigma\rangle_t = \frac{\tau_{\rm in}\langle\sigma_{\rm in}\rangle_t + \tau_{\rm act}\langle\sigma_{\rm act}\rangle_t}{\tau_{\rm in} + \tau_{\rm act}} \tag{2.46}$$

with $\tau_{\rm in}$ and $\tau_{\rm act}$ the average times spent in the inactive and active phase respectively, and $\langle\sigma_{\rm in}\rangle_t$ and $\langle\sigma_{\rm act}\rangle_t$ the associated average stress values. The computation of $\tau_{\rm in}$, $\tau_{\rm act}$, $\langle\sigma_{\rm in}\rangle_t$ and $\langle\sigma_{\rm act}\rangle_t$ relies on the hypothesis that the driving is sufficiently slow $\dot\Gamma < g$ and the restructuring time $\tau_{\rm el}$ sufficiently large to decorrelate the typical stress

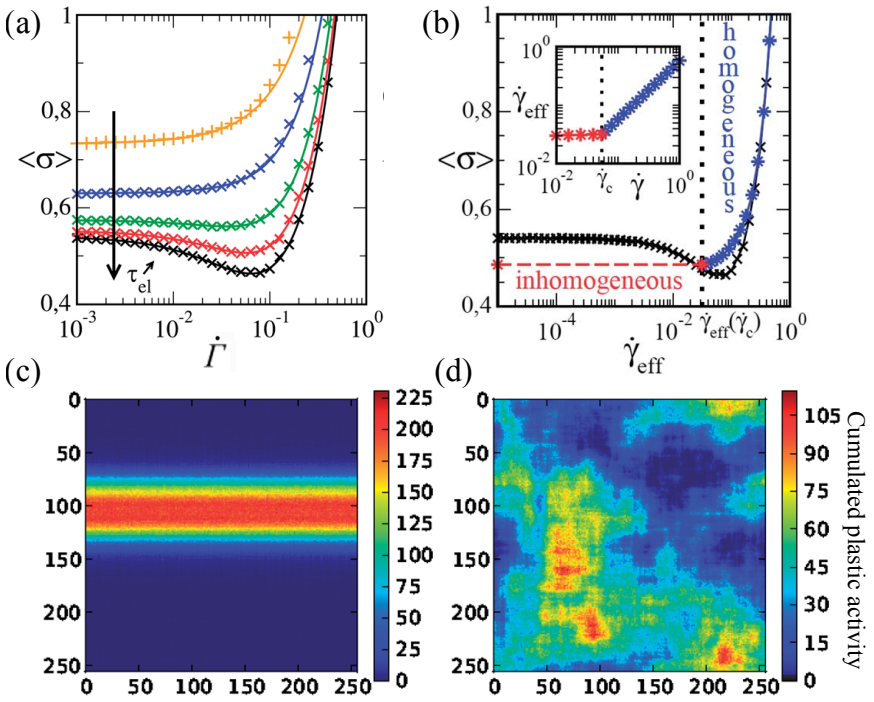

FIGURE 2.6: From Martens et al. (2012). **Shear localization in Picard's elasto-plastic model**. (a) Flow curves in the single-site EPM: numerical values (symbols) and analytical expressions (solid lines) for restructuring times $\tau_{\rm el} = 1, 2.5, 5, 7.5, 10$. (b) Flow curve for $\tau_{\rm el} = 10$ in the single-site EPM (black $\times$) and in the 2d spatial model (blue $*$), plotted as a function of the effective shear rate (see text), with the vertical dotted line indicating the critical value of $\dot{\gamma}^c_{\rm eff}$ separating homogeneous and shear banded flow. Inset: effective shear rate $\dot{\gamma}_{\rm eff}$ vs $\dot{\gamma}$. (c) Map of plastic activity accumulated over a strain window $\Delta\gamma = 100$ with a long-range quadrupolar elastic propagator exhibiting permanent shear bands. (d) Same map with a short range kernel: no shear bands.

values from the change of activity, and by performing an ensemble average over the time spent in the active and inactive phases. Flow curves obtained using the analytical model are shown as solid lines in Fig. 2.6(a) for various values of the restructuring time τ_{el}. Above a critical value of the restructuring time, τ_{el}^{c}, the flow curve for the single-site EPM exhibits a minimum. For a given value of the stress $\langle\sigma\rangle_t$, two solutions of effective shear rate exist, which can lead to phase coexistence in the form of a shear banding instability in the spatial elasto-plastic model.

The flow curves obtained from the single-site dynamics (black cross symbols) and from the full spatial model (blue stars symbols) are compared in Fig. 2.6(b), to test the validity of the single-site approximation to approximate the full model rheology. While the two curves are identical at large shear rate, there seems to be a stronger impact of the fluctuations of the effective shear rate on the dynamics at smaller shear rates, leading to a shift of the minimum of the flow curve. Overall, the single-site EPM describes qualitatively the behavior of the full spatial model, but the fluctuations of the effective shear rate cannot be discarded to get a quantitative description at low shear rate.

Shear banding scenario

From the observed minimum in the homogeneous flow curve, one expects that the plasticity localizes in some specific regions of the system in simulations of the spatial model. This is what Martens et al. (2012) observed, as depicted in Fig. 2.6(c). Their study further suggests that the structure of the flow localization is strongly affected by the nature of elastic interactions: while the Eshelby-type long-range propagator produces well-defined shear bands (Fig. 2.6(c)), a short-range propagator produces localized regions of activity with smooth interfaces (Fig. 2.6(d)).

When imposing the shear rate to the system, the measured flow curve exhibits a stress plateau in the unstable region (see Appendix A.2, Fig. A.1(b)). In this regime, the homogeneous flow being unstable, the system separates in two regions: a flowing and a non-flowing band, sharing the same stress in order to fulfill mechanical equilibrium. When varying the shear rate in this regime, the stress and the maximum shear rate in the system remain constant and only the width of the band varies so as to conserve the externally applied shear rate in the overall system, following a so-called "lever rule". This is similar to a liquid-gas phase separation scenario in equilibrium thermodynamics, and analogies between shear banding and first-order phase transitions are often drawn (Fardin et al., 2012). Note however that, unlike in equilibrium phase transitions, there is no general understanding of the criterion leading to the selection of a specific stress plateau value in complex fluids (Olmsted, 2008; Fardin et al., 2012).

When instead of imposing a fixed strain rate, the stress of the system is controlled, the applied stress cannot, in practice, correspond precisely to the plateau value and hence the flow remains homogeneous. The flow instability can however manifest in the form of hysteresis when applying ramps of increasing/decreasing stresses to the system (as shown in granular media by Dijksman et al. (2011) for instance).

Our last remark concerns finite size effects. For an infinite system, the system will separate between a flowing band and a non-flowing band (as sketched by the dashed line in Fig. 2.6(b)) and the stress plateau will extend to $\dot{\gamma} \to 0$. For a finite system however, the shear rate in the non-flowing band does not vanish and hence the extent of the stress plateau is limited by a system-size-dependent low shear rate value, as shown by the negative slope in the flow curve at $\dot{\gamma} \simeq 10^{-3}$ in Fig. A.1(b).

We introduced in this part two different variants of the EPM and discussed their macroscopic rheology and flow organization at finite shear rate. Let us mention that a large number of studies have rather focused on the behavior of EPMs at low shear rates, in the regime where avalanche dynamics and important cooperative effects are observed (Nicolas et al., 2018a).

Although EPMs give access to macroscopic quantities such as stress, strain rate and erase particle-level details, it is possible to reconstruct the trajectories of fictitious particles that would follow the long-range displacement field induced by the plastic rearrangements. This allows one to study for instance the diffusion and relaxation of tracer particles in sheared systems, as done for instance by Martens et al. (2011).

Tracer particles and cooperative dynamics

In order to study relaxation in the system, we introduce fictitious (non-interacting) tracer particles whose trajectories follows the non-affine motion originating from the long-range displacement fields induced by plastic events.

We compute the displacement field associated with each plastic event using the Oseen tensor (Eq. 2.17). We assign to each lattice site a tracer particle and the fictitious trajectory of tracer particles is built progressively by adding up contributions from all plastic events. The mean square displacement of these tracer particles can then be computed from the trajectories and a diffusion coefficient $D = \dot{\gamma}\tilde{D}$ can be extracted with $\tilde{D} = \frac{\Delta r^2}{4\Delta\gamma}$ (Martens et al., 2011). Martens et al. (2011) find a direct connection between the diffusion coefficient of tracer particles and the size of cooperative regions at low shear rates, with a strong dependence on the shear rate but also on the system size, revealing the importance of non-local effects in the dynamics.

2.5 Conclusion

Lattice-based elasto-plastic models such as Picard's model allow one to model qualitatively the flow of soft glassy materials with a minimal number of ingredients. Refined models including, e.g., yield stress distributions may be suited to reproduce more quantitatively the experimental rheological behaviors (Nicolas et al., 2018a).

The main advantage of Picard's model is its simplicity: as all the dynamical rules are set by constant rates, the phenomenology of the model can be easily understood in terms of competing timescales. It also makes possible the analytical derivation of the flow curve within a single-site dynamics approximation (Martens et al., 2012). In order to study the role of an external fluidizing noise in the flow of YSFs, we will, in Chapter 4, extend Picard's model to account for the random activation of additional plastic events, considering either a constant rate (additional timescale in Picard's model), or a stress-dependent rate.

Models including local stress barriers distributions are richer since the distribution is itself evolving dynamically. Since a barrier is renewed only when a site yields, larger barriers accumulate, inducing a hardening of the system. This effect, that can be seen as "mechanical annealing" is believed to play an important role at the yielding transition in oscillatory shear driving (Priezjev, 2018; Yeh et al., 2020). In Chapter 5, we will build an EPM for the dynamics of actively deforming particles in the form of an oscillatory radius change. Tjhung et al. (2017) have proposed that the solid-to-fluid transition observed upon an increased oscillation amplitude is analogous to the yielding transition observed in amorphous solids under oscillatory shear. Hence we expect the dynamic evolution of the yield stress distribution to be an important

ingredient of the model. We will base our active EPM on the model 2 presented in this chapter.

Chapter 3

Permanent shear band instability induced by inertial dynamics

Résumé : Bandes de cisaillement permanentes induites par une dynamique inertielle

Dans ce chapitre, nous étudions l'apparition d'une instabilité de l'écoulement homogène au sein d'un matériau désordonné dense cisaillé sous l'effet d'une dynamique inertielle. Nous proposons pour cela un modèle continu couplant les équations de l'écoulement à une variable auxiliaire (température cinétique), que nous comparons à des simulations de particules sous-amorties réalisées dans le groupe par V. Vasisht.

Cette instabilité de l'écoulement homogène se manifeste sous la forme de bandes de cisaillement dans des simulations de dynamique moléculaire de systèmes denses désordonnés avec une dynamique inertielle (simulations réalisées à l'aide de LAMMPS par V. Vasisht). L'effet d'une dynamique inertielle sur la courbe rhéologique (contrainte en fonction du taux de cisaillement) de fluides à seuils avait déjà été étudié par Nicolas et al. (2016), en mettant en évidence que l'inertie induit une non-monotonie de la courbe d'écoulement (existence d'un régime où la contrainte diminue lorsque le taux de cisaillement augmente). Comme évoqué dans l'introduction, ce type de courbe rhéologique peut être associé à une instabilité de type bandes de cisaillement. Cependant, aucune hétérogénéité de l'écoulement sous forme de bandes n'avait été observée dans ces précédentes simulations. Récemment, les simulations à grande échelle réalisées par V. Vasisht (résultats résumés en première partie du chapitre) ont permis de mettre en évidence de telles bandes de cisaillement, ainsi que l'existence d'une longueur minimale ℓ_c nécessaire pour que l'instabilité puisse se développer dans le système.

Nous proposons dans ce chapitre un modèle décrivant l'émergence de ces bandes et prédisant la forme des profils d'écoulement dans l'état stationnaire. En suivant l'approche proposée par Nicolas et al. (2016), nous décrivons l'inertie de façon effective, en considérant un système sur-amorti (où l'inertie joue un rôle négligeable dans la dynamique) dans lequel une température cinétique aurait un effet fluidisant sur la rhéologie. Cette température cinétique, si elle est mesurée dans un système athermique, n'est non nulle que si la dynamique des particules est sous-amortie et dépend de façon monotone du taux de cisaillement. L'effet de fluidisation produit par la température cinétique dépend donc du taux de cisaillement, et permet de décrire les courbes d'écoulement non monotones observées dans les simulations de particules.

Afin d'étudier la dynamique de l'écoulement, nous introduisons un modèle continu décrivant la dynamique de deux champs couplés: le champ de vitesse dans le matériau, $v_x(y,t)$ et le champ de température cinétique, $\tilde{T}(y,t)$. Nous utilisons un modèle unidimensionnel, dans lequel nous décrivons l'évolution de la composante de

vitesse $v_x(y,t)$ (supposée invariante suivant la direction de l'écoulement x dans l'état stationnaire) suivant la direction du gradient de vitesse y. Dans un premier temps, une analyse de stabilité linéaire de l'écoulement stationnaire homogène permet de montrer que si la température cinétique a un effet fluidisant, alors une instabilité apparaîtra si la taille du système est plus grande que la longueur d'onde associée à cette instabilité. Ce scénario est en effet vérifié quantitativement dans les simulations de dynamique moléculaire. Dans un second temps, la dynamique du modèle est étudiée numériquement, et permet de vérifier que dans le cas où la solution homogène est instable, alors le système évolue vers un état d'écoulement hétérogène stationnaire. Dans une troisième partie, nous étudions le modèle dans l'état stationnaire, et montrons que les profils d'écoulement prédits par le modèle sont similaires à ceux obtenus dans les simulations de particules. En particulier, les extrema du profil de taux de cisaillement ne sont pas indépendants du taux de cisaillement imposé. En d'autres termes, le système ne suit pas une "loi du levier", comme attendu dans un scénario classique de séparation de phase. Enfin, dans une dernière partie, nous utilisons une analogie mécanique (avec une équation de type pendule) pour expliquer la phénoménologie du modèle, et en particulier l'absence de "loi du levier" observée.

Introduction

Flow instabilities in disordered materials are ubiquitous and have been widely studied in the last few decades (see for instance reviews by Schall et al. (2010), Fielding (2014), and Divoux et al. (2016)). These flow instabilities manifest in terms of strong spatial inhomogeneities in the flow, e.g., in the form of shear bands, even when the material is homogeneously driven. Such instabilities can be either transient (although long persisting) and related to an overshoot in the stress-strain curve in a shear start-up protocol, or permanent and related to a rate-weakening effect (Fielding, 2014). For both types of flow instabilities there exist continuum approaches based on coupling mechanical variables to auxiliary fields such as local concentration (Dhont, 1999; Dhont et al., 2008; Olmsted, 2008), local temperature (Dafermos et al., 1983; Shi et al., 2007; Manning et al., 2007; Hinkle et al., 2017; Katsaounis et al., 2017) or local microstructure (Dhont, 1999; Dhont et al., 2008).

Despite these various approaches to understand flow instabilities under homogeneous driving, the origin of permanent shear localization in dense disordered solids is still debated in the literature. In this chapter, we propose a theoretical framework for the formation of permanent shear bands in dense disordered solids where the dynamics is influenced by a rate-weakening effect induced by microscopic inertia (Nicolas et al., 2016).

As discussed in the introduction of this thesis, many different scenarii can lead to permanent shear banding. Although there is lack of consensus on the origin of shear banding in dense disordered solids, in the case of shear history-dependent materials (Coussot et al., 2002b; Ragouilliaux et al., 2007; Møller et al., 2008) and dense hard sphere suspensions (Besseling et al., 2010), theoretical approaches based on coupling flow fields with either the micro-structure (Fielding et al., 2009; Mansard et al., 2011) or concentration field (Besseling et al., 2010; Gross et al., 2018; Jin et al., 2014) have been successful in predicting permanent shear bands.

On the other hand, dense suspensions of soft athermal particles do not exhibit strong structural or volume fraction inhomogeneities (Ovarlez et al., 2013; Bonn et al., 2017), and the possible mechanisms for shear band formation remain unclear.

Proposed mechanisms for shear band formation include attractive or adhesive interactions (Bécu et al., 2006; Ovarlez et al., 2013; Chaudhuri et al., 2012), or an intrinsic timescale for "restructuration" at the microscopic scale that would lead to local weakening and hence to shear banding (Coussot et al., 2010). This second mechanism, which has been shown to lead to shear bands in elasto-plastic models by Martens et al. (2012) (see Chapter 2) will be further studied in Chapter 4.

In this chapter, we focus on another rate-weakening mechanism, due to inertial dynamics at the microscopic scale (Salerno et al., 2012; Karimi et al., 2016; Karimi et al., 2017; Nicolas et al., 2016). Inertia has been shown to lead to nonmonotonic macroscopic flow curves and this effect has been rationalized by Nicolas et al. (2016) in terms of kinetic heating of the system (see Chapter 1, Fig. 1.11). However, although inertial heating effects on the microscopic scale have been shown to lead to nonmonotonic flow curves by Nicolas et al. (2016), no evidence of shear localization has been reported in that study.

In this work, we show using particle-based simulations and continuum modeling that kinetic heating due to inertia can indeed lead to local softening and hence shear banding. Particle-based simulations were performed in the group in LIPhy by V. Vasisht, and motivated the development of the model presented in this chapter in collaboration with K. Martens and J.L. Barrat.

This chapter is organized as follows: in a first part we briefly introduce the particle-based model used in the simulations (more details can be found in Appendix B) and describe the nonmonotonic rheology observed in underdamped conditions as well as the emergence of shear bands for large systems (simulations performed by V. Vasisht). In a second part, we propose a continuum model based on a kinetic temperature description of inertia, following the ideas of Nicolas et al. (2016). By performing a linear stability analysis of the homogeneous flow solution, we show that the model exhibits an instability due to a softening effect induced by kinetic heating, and compute the wavelength associated with this instability, which matches the results obtained in particle-based simulations. We then study the non-linear dynamics by numerically integrating the continuum model and evidence that the instability actually leads to steady-state shear bands. However, the steady-state profiles observed both in particle based simulations and in the continuum model do not obey a "lever rule" as in usual shear banding scenarios. We rationalize this finding in a last part, using a mechanical analogy.

3.1 Steady-state shear band instability in particle-based simulations with inertial dynamics

In this part, we summarize the numerical results obtained by V. Vasisht that motivated the development of a continuum model to explain the emergence of shear bands in systems with inertial dynamics.

3.1.1 Particle-based model

The model disordered solid considered in the particle-based simulation consists of a dense assembly of polydisperse spheres (volume fraction $\phi = 70\%$), interacting via a truncated and shifted Lennard-Jones potential (Weeks et al., 1971). After a standard annealing preparation, the system is subjected to a shear deformation at a fixed shear rate $\dot{\gamma}$ using Lees-Edwards boundary conditions (LEBC) and evolved using dissipative

particle dynamics (DPD) (see Appendix B). In the following, $[x, y, z]$ dimensions refer to flow, gradient and vorticity directions respectively.

In order to study the role played by inertia in the rheology, various values of dissipation constants ζ are considered. We introduce the inertial quality factor Q, similar to Nicolas et al. (2016), which is defined as $Q = \frac{\tau_{\text{damp}}}{\tau_{\text{vib}}}$, where $\tau_{\text{damp}} = m/\zeta$ and $\tau_{\text{vib}} = \sqrt{ma^2/\varepsilon}$, with ζ the damping coefficient, ε the energy scale of the interaction potential, m the mass and a the average diameter of the particles. For an overdamped system, $Q \leq 1$, the steady-state flow curve is monotonic and can be well fitted by a Herschel-Bulkley (HB) law $\sigma(\dot{\gamma}) = \sigma_{\text{y}} + A\dot{\gamma}^n$, with $\sigma_{\text{y}} \approx 2.5$ the yield stress, a coefficient $A \approx 16.5$ and the HB exponent $n \approx 0.5$. As the inertial quality factor Q increases, the dynamics becomes underdamped and the flow curves exhibit a nonmonotonic behavior as shown by Nicolas et al. (2016) (see Chapter 1, Fig. 1.11).

3.1.2 Nonmonotonic flow curve

Fig. 3.1(a) depicts an example of flow curve obtained for an inertial quality factor $Q = 10^4$. For a cubic system ($L_x = L_y = L_z = 42a$, around 10^5 particles), we observe a nonmonotonic flow curve which is attributed to the underdamped dynamics (Nicolas et al., 2016). The flow curve has a minimum at $\dot{\gamma} \approx 0.1\tau_{\text{vib}}^{-1}$. Hence one could expect a flow instability in the region of shear rates $\dot{\gamma} < 0.1\tau_{\text{vib}}^{-1}$, where the flow curve exhibits a negative slope. Similar to the observations of Nicolas et al. (2016) we did not find any shear instabilities in the velocity profiles. These results remain unchanged even for a non-cubic geometry, where $L_x = L_z = 42a; L_y = 120a$.

With further increase in L_y we observe a lowering of the steady-state stress for shear rates below $\dot{\gamma} = 0.1\tau_{\text{vib}}^{-1}$, while the flow curve remains unchanged in the positive-sloped region, suggesting the appearance of a new flow regime for large systems in the regime $\dot{\gamma} < 0.1\tau_{\text{vib}}^{-1}$.

3.1.3 Permanent shear instability

For a larger system ($L_y = 360a$), we show, in Fig. 3.1(b)-(c), (for a shear rate $\dot{\gamma} = 10^{-2}\tau_{\text{vib}}^{-1}$), that the system exhibits permanent shear heterogeneities along the gradient direction in the flow regime mentioned above. Note that the local shear rates and stresses were computed after the system had been sheared for around $\gamma = 60$ (or 6000% strain) and averaged over a strain window of $\Delta\gamma = 0.20$. It is clear that the system has reached a steady state both from the load curve (see Appendix B) and from the homogeneous stress profile displayed in Fig. 3.1(c).

These simulation results indicate that the instability resulting from a negative slope in the flow curve can only be observed above a minimum system size that can accommodate the corresponding instability wavelength. In the following, we propose a continuum model based on the ideas of Nicolas et al. (2016), in order to predict the minimum length scale required to allow for such an inertia-induced flow instability.

3.2 Continuum model

3.2.1 Kinetic temperature due to inertia

The basic idea of our approach, initially proposed by Nicolas et al. (2016), consists in interpreting inertia as causing a heating effect in the system. If we consider that inertia is introducing a kinetic temperature $\tilde{T}$ to the athermal dynamics, quantified through an excess of kinetic energy (Losert et al., 2000; Nicolas et al., 2016; Karimi et al.,

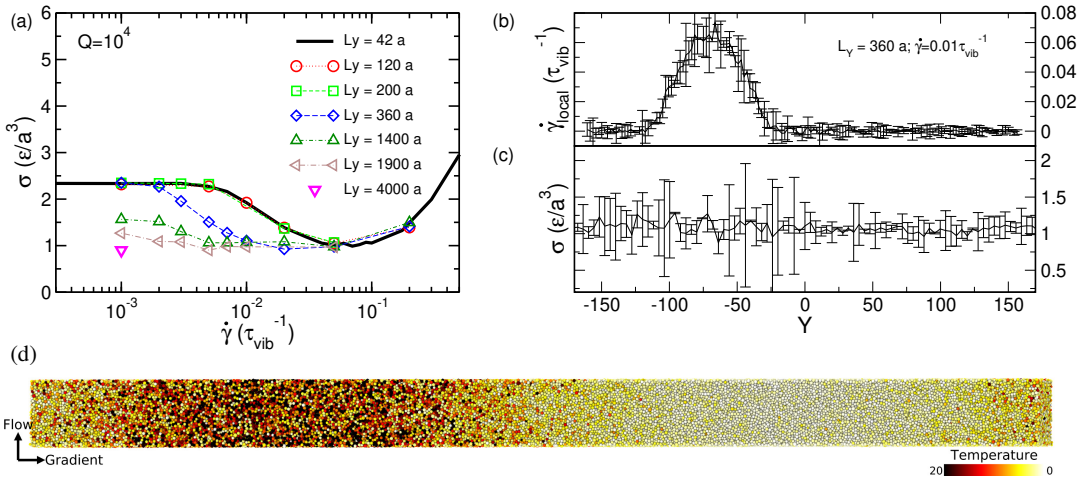

FIGURE 3.1: **Nonmonotonic flow curves and shear bands in underdamped particle-based simulations**. (a) Steady-state stress as a function of the applied shear rate for an athermal underdamped system ($Q = 10^4$) for different system sizes. (b) Steady-state local shear rate profile along y (the coordinate along the gradient direction), averaged over a strain window of $\Delta\gamma = 0.2$, computed for a system size $N = 240731$ and $L_Y = 360a$ at $\dot{\gamma} = 10^{-2}\tau_{\text{vib}}^{-1}$. (c) Corresponding stress profile. (d) 3D rendering of a configuration from simulation trajectory depicting shear localization ($Q = 10^4$, $N = 240731$, $L_Y = 360a$, $\dot{\gamma} = 10^{-2}\tau_{\text{vib}}^{-1}$). The colormap is based on the kinetic temperature $\tilde{T}$, varying from white to black (from $\tilde{T} = 0\epsilon/k_B$ to $20\epsilon/k_B$).

2016), one can interpret the nonmonotonic flow rheology of athermally driven inertial systems $\sigma(\dot{\gamma}; Q, T = 0)$ effectively as an overdamped rheology at a finite shear-rate dependent temperature $\sigma(\dot{\gamma}; Q = 1, \tilde{T}(\dot{\gamma}))$.

These ideas are tested in particle-based simulations in Fig. 3.2. We show flow curves (solid lines) obtained for an overdamped system ($Q = 1$) at different temperatures T, as well as the flow curve for an underdamped athermal system ($Q = 10^4$, $T = 0$) (filled red circles). We can see that the stress values obtained in the overdamped case at a finite (true) temperature can coincide with the stress values obtained in the underdamped case at $T = 0$, provided a shear-rate dependence of the kinetic temperature in the system is assumed. The measured kinetic temperature in the underdamped system versus the true temperature for similar stress and shear rates values (values taken at the intersection of the underdamped curve represented by the red dots in Fig. 3.2 and the overdamped finite temperature curves) is displayed in Appendix B (Fig. B.1), showing a strong correlation of these two quantities (although there is not a 1:1 ratio).

We can thus interpret the underdamped rheology as the rheology of an overdamped system with a finite rate-dependent kinetic temperature. The shear stress σ is thus not only a function of the shear rate $\dot{\gamma}$, but also of the kinetic temperature $\tilde{T}$: $\sigma = \sigma(\dot{\gamma}, \tilde{T})$.

3.2.2 Formulation of the model

Starting from the above hypothesis, that the shear stress $\sigma = \sigma(\dot{\gamma}, \tilde{T})$ is not solely depending on the shear rate $\dot{\gamma}$ but also on the kinetic temperature $\tilde{T}$ accounting for inertial effects, we aim for a derivation of continuum equations describing the evolution of the local shear rate and the local kinetic temperature.

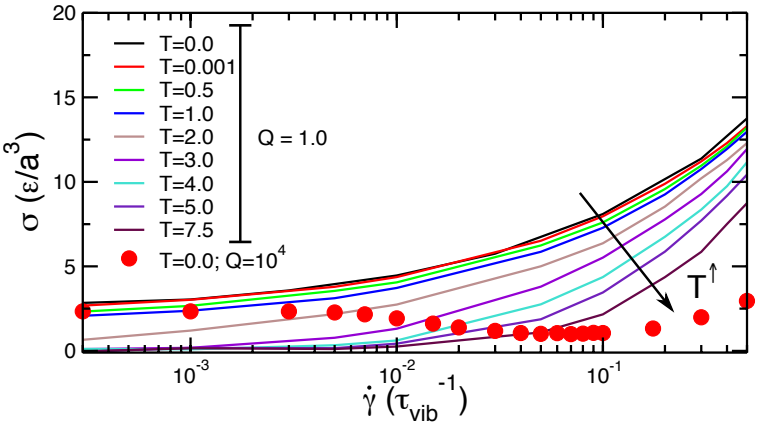

FIGURE 3.2: **Flow curves for underdamped athermal and overdamped thermal simulations**. Overdamped simulations ($Q = 1$) performed at finite temperature are represented as solid lines (for a system size of $N = 10^4$ particles). The filled circles represent the flow curve from an underdamped simulation ($Q = 10^4$, $N = 10^5$) at $T = 0$.

To fix the notations we assume in the following a specific driving protocol at a fixed externally applied shear rate $\dot{\gamma} = \partial v_x/\partial y$ in a 3d planar geometry (flow direction x, gradient direction y, and vorticity direction z). Using the continuity equations for momentum and energy, we derive the time evolution equations for the shear component of the velocity $v_x(y,t)$ and the kinetic temperature $\tilde{T}(y,t)$ similarly as Katsaounis et al. (2017):

$$\rho \frac{\partial v_x}{\partial t} = \frac{\partial \sigma}{\partial y} = \frac{\partial \sigma}{\partial \tilde{T}} \frac{\partial \tilde{T}}{\partial y} + \frac{\partial \sigma}{\partial \dot{\gamma}} \frac{\partial^2 v_x}{\partial y^2} \tag{3.1}$$

$$c_{\mathrm{v}} \frac{\partial \tilde{T}}{\partial t} = \lambda_{\mathrm{T}} \frac{\partial^2 \tilde{T}}{\partial y^2} + \frac{\partial v_x}{\partial y} \sigma \left(\frac{\partial v_x}{\partial y}, \tilde{T} \right) - \frac{c_{\mathrm{v}}}{\tau} \tilde{T} \, . \tag{3.2}$$

where ρ is the system density, c_{v} the volumetric heat capacity, λ_{T} the thermal conductivity and τ the typical time to remove the kinetic energy (originating from the external shear) by the thermostat (at zero temperature).

In the above model equations, the second term in Eq. 3.1, $\partial\sigma/\partial y$, is the usual expression obtained from momentum conservation in systems with a simple flow curve relation solely depending on the shear rate. The new part in Eq. 3.1 is the term introducing a dependence of the shear stress on the kinetic temperature $\partial\sigma/\partial\tilde{T}$. This derivative is negative accounting for a local shear-weakening effect introduced by the local heating, which we expect to be the source of our shear instability. The second equation simply describes the heat evolution as a diffusive process together with a source term given by the drive and a sink term given by the thermostat at zero temperature.

3.2.3 Homogeneous steady state

From equations 3.1 and 3.2, it appears that in steady state ($\partial\sigma/\partial t = 0$; $\partial\sigma/\partial y = 0$; $\partial\tilde{T}/\partial t = 0$) and for a uniform flow ($\partial\dot{\gamma}/\partial y = 0$) and temperature field ($\partial\tilde{T}/\partial y = 0$), the temperature and shear rate in the (homogeneous) system are related by:

$$\tilde{T} = \frac{\tau}{c_V} \sigma(\dot{\gamma}) \dot{\gamma} \tag{3.3}$$

This relation is tested in particle based simulations using data for systems exhibiting a nonmonotonic flow curve (underdamped, $Q = 10^4$) but small enough so they have a homogeneous steady state ($L_x = L_y = L_z = 42a$). In Fig. 3.3(a), we show the kinetic temperature $\tilde{T}$ measured as $0.5\langle m v_z \rangle^2$, with v_z the particles velocity component in the neutral vorticity direction (which is not influenced by the affine flow) as a function of the imposed shear rate $\dot{\gamma}$. We also show the value of $\tilde{T}$ computed from Eq. 3.3, using the values of $\sigma(\dot{\gamma})$, τ and c_v measured in particles based simulations. In simulations, λ_T and c_v are system properties fixed by the interaction potential and τ is fixed by the dissipation coefficient ζ (see Appendix B).

The good match between $\tilde{T}$ computed from the model (by inputting simulation parameters) and $\tilde{T}$ directly measured in the simulations indicates that the continuum model accounting for a kinetic temperature describes well underdamped simulations in the homogeneous flow regime.

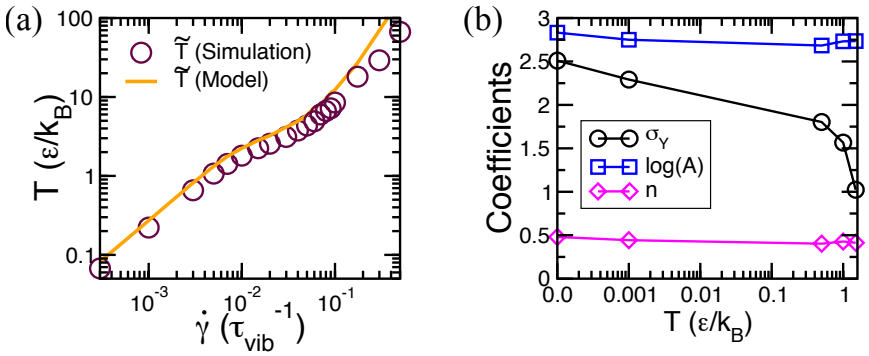

FIGURE 3.3: **Kinetic temperature in underdamped simulations and flow curve fits.** (a) Comparison of kinetic temperature $\tilde{T}$ measured in simulations of underdamped athermal simulations ($Q = 10^4$) with $\tilde{T}$ predicted from the continuum model (Eq. 3.3), for different shear rates. (b) Temperature dependence of the yield stress (σ_y), the coefficient (A) and the exponent (n) obtained from fitting the overdamped flow curves with the Herschel-Bulkley equation $\sigma(\dot{\gamma}) = \sigma_y + A\dot{\gamma}^n$.

3.2.4 Constitutive flow curves

One of the assumptions of our approach is that the shear stress σ depends explicitly on both the shear rate $\dot{\gamma}$ and the kinetic temperature $\tilde{T}$.

Constitutive flow curve in particle-based simulations

In the particle-based simulations, there is a clear dependence of the stress on the shear rate and the (true) temperature (Fig. 3.2). If we fit the flow curves obtained in overdamped particle-based simulations for a given temperature T with a HB expression $\sigma = \sigma_y(T) + A(T)\dot{\gamma}^{n(T)}$, it appears from Fig. 3.3(b) (where the fitting parameters are reported), that the main dependence with the temperature lies in the term $\sigma_y(T)$, and only a little dependence with temperature is observed for A and n. An expression of type:

$$\sigma = \sigma_y(T = 0) + A\dot{\gamma}^n + f(T) \tag{3.4}$$

would thus reasonably capture the rheological behavior of the system. We could not however find a simple analytical expression for $f(T)$ that describes well the simulation data. Moreover, the form of the constitutive flow curve (and hence $f(T)$) can depend

on the details of the model (such as the interaction potential, the thermostat, etc.), as shown by the differences between the flow curve of Nicolas et al. (2016) (see Chapter 1, Fig. 1.11) and the simulation data of V. Vasisht (Fig. 3.1), so the form of $f(T)$ would probably not be general.

In the following, we will either assume a simple expression for $f(T)$ in order to study the theoretical model, or measure numerically $\frac{\partial \sigma}{\partial \tilde{T}}$ when doing quantitative comparisons between the model and simulation data.

Constitutive flow curve to study the model

In the following, in order to study the continuum model introduced above, we use a function $f(T) = -BT^{\alpha}$, leading to a constitutive flow curve:

$$\sigma = \sigma_{\mathrm{y}}^{0} + A\dot{\gamma}^{n} - BT^{\alpha} \tag{3.5}$$

By using the relation between temperature and shear rate for a homogeneous steady state (Eq. 3.3), we get an implicit expression relating the shear stress and the shear rate:

$$\sigma = \sigma_{\mathrm{y}}^{0} + A\dot{\gamma}^{n} - B\left(\frac{\tau}{c_V}\sigma\dot{\gamma}\right)^{\alpha} \tag{3.6}$$

The value of σ_{y}^{0} and n are chosen to match approximately the flow curve for an overdamped system in particle-based simulations (corresponding to $T = 0$). The values of B and α are chosen such that the minimum of the flow curve is located at values of shear rate $\dot{\gamma}_{\mathrm{min}}$ and stress σ_{min} close to the values observed in numerical simulations (for a quality factor $Q = 10^4$). The values of $\tau = 350$ and $c_v = 3$ are measured in particle-based simulations, as explained in Appendix B. The flow curve obtained by solving numerically Eq. 3.6 with $\sigma_{\mathrm{y}}^{0} = 2.7$, $n = 0.5$, $B = 2.3$ and $\alpha = 0.3$ is depicted in Fig. 3.4. The minimum of the flow curve is located at $\dot{\gamma}_{\mathrm{min}} = 3.42 \cdot 10^{-2}$ and $\sigma_{\mathrm{min}} = 1.2208$.

Note that better fits to particle-based simulations were obtained when choosing a shear rate dependence of the exponent $\alpha(\dot{\gamma})$ (enabling for instance to recover a positively sloped flow curve at low shear rate values as observed in particle-based simulations). There is however no physical justification to such form, and keeping a simple form for $f(T)$ enables us to perform the theoretical analysis presented in Section 3.2.7.

3.2.5 Stability analysis and system size dependence

Linear stability analysis

A simple stationary solution of equations 3.1 and 3.2 corresponds to a uniform flow and homogeneous temperature in the system: $\partial\dot{\gamma}/\partial y = 0$ and $\partial\tilde{T}/\partial y = 0$. In this case, the temperature and shear rate are related by: $\tilde{T}^{*} = \frac{\tau}{c_v}\sigma(\dot{\gamma}^{*})\dot{\gamma}^{*}$. To study the stability of this homogeneous flow solution, we linearize the system of equations for small perturbations of the homogeneous flow solution $\delta v_x(y,t)$ and of the constant kinetic temperature field $\delta\tilde{T}(y,t)$:

$$v_x(y,t) = \dot{\gamma}y + \delta v_x(y,t) \tag{3.7}$$

$$\tilde{T}(y,t) = T_0 + \delta\tilde{T}(y,t) \tag{3.8}$$

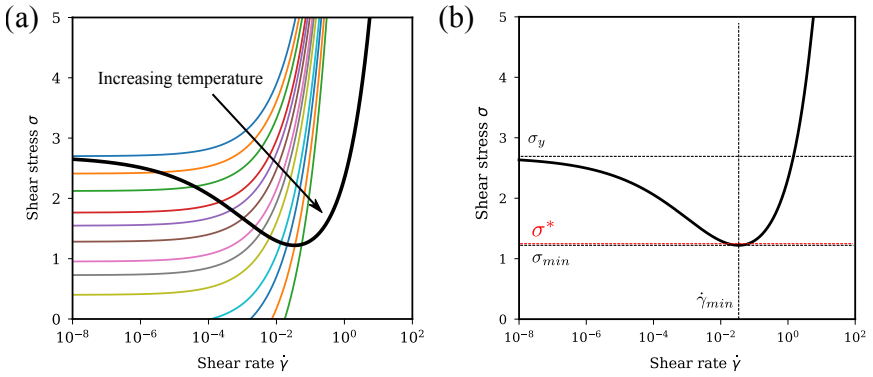

FIGURE 3.4: **Constitutive flow curve (shear stress as a function of shear rate) used to study the continuum model** (black solid line). (a) By showing the monotonic flow curves obtained for various values of temperature (colored lines). (b) The black solid line is obtained numerically using the implicit equation (Eq. 3.6).

using the ansatz:

$$\delta v_x(y,t) = v_x \exp\{\lambda t\} \exp\{-iky\} \tag{3.9}$$
$$\delta\tilde{T}(y,t) = \tilde{T} \exp\{\lambda t\} \exp\{-iky\} \tag{3.10}$$

We get the linearized equations:

$$\begin{bmatrix} \delta\dot{v}_x \\ \delta\dot{\tilde{T}} \end{bmatrix} = J \begin{bmatrix} \delta v_x \\ \delta\tilde{T} \end{bmatrix} \tag{3.11}$$

with J:

$$J = \begin{bmatrix} -k^2 \frac{1}{\rho}\frac{\partial\sigma}{\partial\dot{\gamma}} & -\frac{ik}{\rho}\frac{\partial\sigma}{\partial T} \\ -\frac{ik\sigma}{c_v} - \frac{ik\dot{\gamma}}{c_v}\frac{\partial\sigma}{\partial\dot{\gamma}} & \frac{-\lambda_T k^2}{c_v} - \frac{1}{\tau} + \frac{\dot{\gamma}}{c_v}\frac{\partial\sigma}{\partial T} \end{bmatrix} \tag{3.12}$$

The trace of the Jacobian matrix is equal to the sum of the eigenvalues:

$$\mathrm{Tr}\, J = \lambda_1 + \lambda_2 = -k^2\left(\frac{1}{\rho}\frac{\partial\sigma}{\partial\dot{\gamma}} + \frac{\lambda_T}{c_v}\right) - \frac{1}{\tau} + \frac{\dot{\gamma}}{c_v}\frac{\partial\sigma}{\partial T} \tag{3.13}$$

and the determinant (product of eigenvalues) reads:

$$\det J = \lambda_1\lambda_2 = k^4\left(\frac{\lambda_T}{\rho c_v}\frac{\partial\sigma}{\partial\dot{\gamma}}\right) + k^2\left(\frac{1}{\rho\tau}\frac{\partial\sigma}{\partial\dot{\gamma}} + \frac{\sigma}{\rho c_v}\frac{\partial\sigma}{\partial T}\right) \tag{3.14}$$

The expression in Eq. 3.13 for the sum of the eigenvalues is negative (because $\frac{\partial\sigma}{\partial\dot{\gamma}} < 0$), meaning that at least one eigenvalue is negative. For the homogeneous flow to be stable we need both eigenvalues to be negative and thus the expression for their product (Eq. 3.14) to be positive. The first term on the right hand side of Eq. 3.14 is positive and thus stabilizing, since we started from a monotonic flow curve assumption in the overdamped limit ($\frac{\partial\sigma}{\partial\dot{\gamma}} > 0$). The sign of the second term however depends on the competition of two contributions, a stabilizing one related to the efficiency of the thermostat and a destabilizing one related to the sensitivity of the flow curve to the increase in kinetic temperature. When this last term becomes predominant in the case of weakly damped systems, we expect the homogeneous flow solution to become unstable for large wavelength perturbations. We can thus estimate the critical

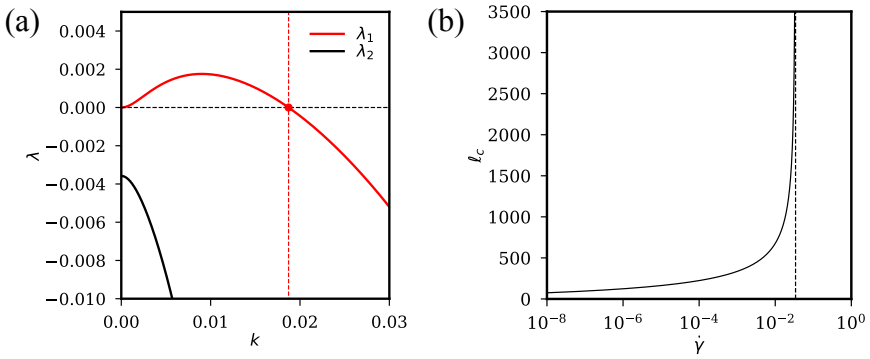

FIGURE 3.5: **Linear stability analysis of the homogeneous flow solution in the continuum model**. (a) Eigenvalues λ_1 and λ_2 obtained from Eq. 3.13 and 3.14 computed for a shear rate $\dot{\gamma} = 10^{-3}$ using our simple constitutive curve given by Eq. 3.6. The red dashed line indicates the change of sign of λ_1 for a wavevector $k = k_c$. (b) Critical length for the instability ℓ_c as a function of shear rate using the same other parameters as in (a). The vertical dashed line indicates the value of $\dot{\gamma}_{\min} = 3.42 \cdot 10^{-2}$, the minimum of the flow curve.

wavevector k_c for which the product of eigenvalues changes sign. We find:

$$k_c^2 = \frac{1}{\lambda_T}\left(-\frac{c_v}{\tau} - \sigma\frac{\partial\sigma/\partial T}{\partial\sigma/\partial\dot{\gamma}}\right) \tag{3.15}$$

System size dependence: comparison with particle-based simulations

From the expression of the critical wavevector k_c, we get a critical wavelength $\ell_c = 2\pi/k_c$ for the instability:

$$\ell_c = 2\pi\sqrt{\lambda_T}\left(-\frac{c_\mathrm{v}}{\tau} - \sigma\frac{\partial\sigma/\partial\tilde{T}}{\partial\sigma/\partial\dot{\gamma}}\right)^{-\frac{1}{2}} = 2\pi\sqrt{\lambda_T}\left(-\frac{c_\mathrm{v}}{\tau} + \sigma\frac{1}{\partial\tilde{T}/\partial\dot{\gamma}}\right)^{-\frac{1}{2}} \tag{3.16}$$

The instability of the homogeneous flow arises for small wavevectors and hence large wavelengths. Therefore, for system sizes smaller than this critical wavelength, $L < \ell_c$, no instability is expected even if the constitutive flow curve is nonmonotonic.

The eigenvalues obtained using the flow curve of Eq. 3.6 with a shear rate $\dot{\gamma} = 10^{-3}$ and the parameters given above are shown in Fig. 3.5(a). One finds in this case a value of k_c (wave vector at which λ_1 changes sign), corresponding to a critical length $\ell_c = 2\pi/k_c \approx 336$ (model size units). The evolution of the critical length ℓ_c with the shear rate is depicted in Fig. 3.5(b), exhibiting a divergence for a shear rate corresponding to the minimum of the flow curve.

From the expression in Eq. 3.16 one can clearly identify the reason for the linear instability that arises from a competition of a stabilizing term related to the thermostatting at zero temperature and a destabilizing local heating effect, quantified through the kinetic temperature change caused by the change of the local shear rate. In the case where this heating effect becomes negligible, as it is the case for overdamped dynamics, the value of ℓ_c becomes infinite and the flow remains stable for any system size as expected.

In the following we test this scenario in the particle-based simulations. We compute ℓ_c using Eq. 3.16 inputting the values of numerically measured parameters: λ_T, c_v and τ. To compare with simulations, we do not assume any form for the constitutive flow

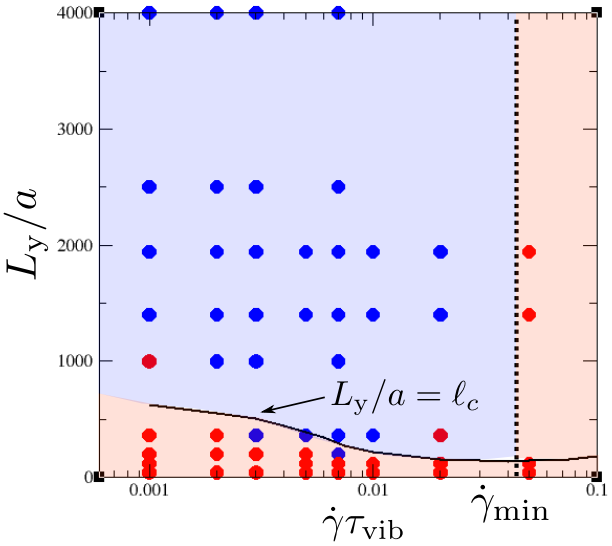

FIGURE 3.6: **Parametric plot (system size - shear rate) for the emergence of shear bands.** System size (represented by the length of the gradient dimension L_y) as a function of shear rate $\dot{\gamma}$. The symbols depict the state points at which simulations were performed. Red symbols represent the state points where we find homogeneous flow and blue symbols represent the state points where we find a steady-state shear instability. The value of $L_y = \ell_c$ computed from Eq. 3.16 is used to define the area coloring (and depicted by the dashed line), with the red region representing the stable homogeneous flow and the blue region representing the flow instability. The method used to estimate ℓ_c is discussed in Appendix B. The vertical dotted line represents the shear rate at the minimum of the flow curve for small systems (solid black line in Fig. 3.1).

curve, but perform a numerical estimate of $\partial\tilde{T}/\partial\dot{\gamma}$ (see Appendix B). In the parametric plot of Fig. 3.6, we show the simulated system size along the gradient direction L_y as a function of $\dot{\gamma}$. The black solid line represents ℓ_c computed from Eq. 3.16 and the vertical dotted line represents the minimum of the flow curve ($\dot{\gamma} < \dot{\gamma}_{min}$), beyond which the flow curve has a positive slope. The homogeneous flow solution is expected to be stable (red shaded area) either (i) in the case of an increasing flow curve ($\dot{\gamma} > \dot{\gamma}_{min}$, right of the vertical dotted line in Fig. 3.6) or (ii) in the case of a decreasing flow curve but for system sizes smaller than the critical wavelength for the instability ($L_y < \ell_c$, below the dashed line in Fig. 3.6). Outside of these two regimes, the homogeneous flow is expected to be unstable (blue shaded area). The symbols represent numerical simulations data where we find either a homogeneous flow (red symbols) or a localized flow (blue symbols). We find a good match between the prediction from the continuum model and numerical simulations at intermediate shear rates. These results indicate that our model can predict quantitatively the onset of the flow instability observed in microscopic simulations, at least for intermediate shear rates (where there is a clear negative slope in the flow curve). For small shear rates, it is difficult to estimate the numerical derivative of the kinetic temperature with respect to the shear rate.

In order to investigate the dynamics in the case of an unstable homogeneous steady state, we integrate numerically the continuum model in the next section.

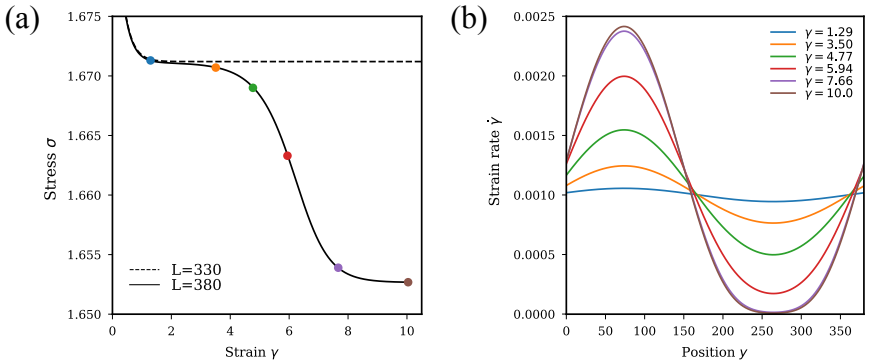

FIGURE 3.7: **Stress dynamics and flow profiles in the continuum model**. (a) Stress as a function of strain for an imposed shear rate $\dot{\gamma} = 10^{-3}$ and system sizes $L = 330$ (dashed line) and $L = 380$ (solid line). (b) Shear rate profiles for $L = 380$ at various strain values indicated by colored dots in panel (a). $L = 330$ would correspond to homogeneous flow profiles ($L < \ell_c$).

3.2.6 Non linear dynamics

To go beyond the linear stability analysis, we can integrate the full non-linear continuum model (Eq. 3.1 and 3.2) using an Euler explicit scheme. We use boundary conditions such that the shear rate and the temperature profiles obey periodic boundary conditions, as in the particle-based simulations: $\frac{\partial \dot{\gamma}}{\partial y}(y = 0) = \frac{\partial \dot{\gamma}}{\partial y}(y = L)$ and $\frac{\partial T}{\partial y}(y = 0) = \frac{\partial T}{\partial y}(y = L)$. As initial configurations, we use shear rate and temperature profiles with average values equal to the imposed shear rate (and corresponding temperature in steady state using Eq. 3.6) and with a small amplitude white noise.

As pointed out by Gross et al. (2018), the stability criterion of the explicit numerical scheme depends directly on the local shear rate $\dot{\gamma}$: $\Delta t < \Delta x^2 \rho \dot{\gamma}^{1-n}/2An$ (with Δt and Δx the time and spatial discretization steps, $\dot{\gamma}$ the local shear rate, A the constant in the Herschel-Bulkley fit and $n < 1$ the Herschel-Bulkley exponent). For an infinite system size, the shear rate in the non-flowing band is equal to 0, and the steady state of the system cannot be reached using an explicit integration scheme. For finite systems, due to the interface width between the non flowing and the flowing regions, the minimum shear rate remains finite but tends towards increasingly small values as the system size is increased, thus requiring an increasingly small integration timestep. The study is thus limited to rather small systems, near the instability threshold, $L \approx \ell_c$.

In the following, we will thus discuss the dynamics of the model in the regime $L \approx \ell_c$, in terms of evolution of the macroscopic stress and of the flow profile. We integrate the above model imposing a macroscopic shear rate $\dot{\gamma} = 10^{-3}$, yielding a value for the critical system size $\ell_c = 336$.

Evolution of the average stress

For $L < \ell_c$ (dashed line in Fig. 3.7(a) for $L = 330$), the steady-state stress is simply given by the constitutive relationship that can be implicitly solved using the unique $T = f(\dot{\gamma})$ relationship valid in the homogeneous case. For $L > \ell_c$ (solid line in Fig. 3.7(a) for $L = 380$), the steady-state stress takes a value lower than the homogeneous solution. The system first relaxes to the homogeneous solution state, before the instability sets in and the stress relaxes to another steady-state stress value (that depends upon the system size, and this point will be further discussed in the next

section). Note that the same type of dynamics is also observed in particle-based simulations (see Appendix B, Fig. B.4).

Evolution of flow profiles

Fig. 3.7(b) depicts shear rate profiles associated with various strain values for a system size $L = 380$. As the average stress decreases, the shear rate profile becomes increasingly heterogeneous and eventually reaches a steady state. The corresponding temperature and stress profiles are shown in Appendix B (Fig. B.5). At large strains, the average shear stress reaches a plateau and the stress becomes uniform in the system, indicating that the system has reached a steady-state heterogeneous flow regime.

This study enables us to evidence that once the state of the system has departed from the homogeneous flow state, it evolves towards a new steady state corresponding to a phase-separated profile, as in particle-based simulations. As mentioned above, integrating the time-dependent equations until steady state is reached is restricted to small systems due to numerical stability limitations of our explicit numerical scheme. In the following, we study the properties of the steady state profiles by integrating directly the continuum model equations in steady state to avoid numerical issues.

3.2.7 Steady-state flow profiles

Steady-state flow profiles obtained using the shooting method

We integrate the continuum model in steady state (Eq. 3.2 with the left-hand-side term equal to 0) using the shooting method for single-banded profiles. This is equivalent to solving the non-linear second order ordinary differential equation (ODE):

$$\lambda \frac{\partial^2 \tilde{T}}{\partial y^2} = -\sigma\dot{\gamma} + \frac{c_V \tilde{T}}{\tau} \tag{3.17}$$

We invert the constitutive relation (Eq. 3.5) to get the shear rate $\dot{\gamma}$ as a function of the stress σ:

$$\dot{\gamma}(\sigma, \tilde{T}) = A^{-1/n}(\sigma - \sigma_y + B\tilde{T}^{\alpha})^{1/n} \text{ if } \sigma > \sigma_y - B\tilde{T}^{\alpha}; \tag{3.18}$$

$$\dot{\gamma}(\sigma, \tilde{T}) = 0 \text{ otherwise} \tag{3.19}$$

Inserting Eq. 3.19 into Eq. 3.17, we get an ODE that we numerically solve using the shooting method. To do so, one needs to choose initial conditions for the temperature $\tilde{T}(y = 0)$ and for the temperature gradient $\tilde{T}'(y = 0)$. We set $\tilde{T}'(y = 0) = 0$, and try iteratively different values of $\tilde{T}(y = 0)$ such that $\tilde{T}(y = L) = \tilde{T}(y = 0)$ and $\tilde{T}'(y = L) = 0$ to satisfy the periodic boundary conditions. Additionally, we only look for solutions with a single band (as it is the expected state in the long time limit), i.e., solutions for which the period exactly matches the system size L. In practice, we look for periodic steady-state solutions of Eq. 3.2 for a given value of stress σ, with a period equal to the system size L. We set a criterion : $|\tilde{T}(y = 0) - \tilde{T}(y = L)| < \varepsilon$ with $\varepsilon = 10^{-4}$ to stop the iterative procedure. From the temperature profile, we can then reconstruct the shear rate profile using the relationship:

$$\dot{\gamma} = \frac{1}{\sigma}\left(\frac{c_V \tilde{T}}{\tau} - \lambda \frac{\partial^2 \tilde{T}}{\partial y^2}\right) \tag{3.20}$$

The macroscopic shear rate in the system can then be computed *a posteriori* by integrating the shear rate profile.

Comparison with particle-based simulations: lack of lever rule

Fig. 3.8 depicts examples of flow profiles obtained both in particle-based simulations (a) and using the continuum model (b) for a system size $L_y = 2000a$ and for different stress values (corresponding to different shear rates). As the shear rate is increased in the system, both the width and the maximum of the flow profiles increase. This

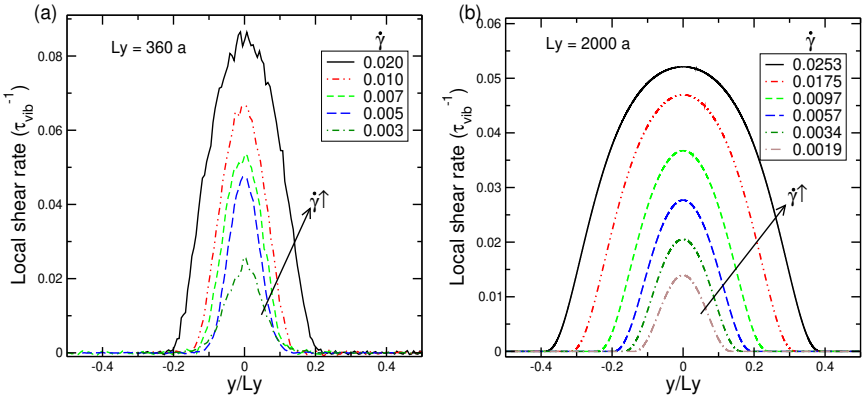

FIGURE 3.8: **Profiles of local shear rate** obtained from (a) particle-based simulations for different applied shear rates (for a system dimension $L_x = L_y = 22a$ and $L_y = 360a$ and (b) continuum model (for a system size $L_y = 2000a$), for different stresses using the shooting method.

contrasts with usual shear banding scenarios (Divoux et al., 2016), where the maximum shear rate in the system is generally expected to be independent of the applied shear rate (if the average stress is homogeneous). In this scenario, an increase of the applied shear rate yields an increase of the shear band width so as to conserve the global shear rate (so-called "lever rule").

In Fig. 3.8(a), we show the local shear rate profiles obtained from the particle-based simulations for different applied shear rates for a given system size (with $L_y > \ell_c(\dot{\gamma})$). The profiles show that, even though the width of the band increases with an increase in shear rate, there is a clear absence of one chosen maximum shear rate. Instead, the profiles exhibit a continuous interface, without a clear plateau associated with the flowing region. Similar features are observed in the flow profiles computed from the model (Fig. 3.8(b)). In the next part, we explain, using a mechanical analogy, the shape of these flow profiles in the context of our continuum model.

Rationalizing the flow profiles

A stationary localized flow corresponds to a situation of coexistence between flowing and nearly immobile regions, with a homogeneous stress profile. The determination of the flow profile is analogous to the determination of interfacial profiles in phase coexistence problems, and can be described using a classical mechanical analogy (Rowlinson et al., 1982; Oxtoby et al., 1982).

The steady-state temperature $\tilde{T}(y)$ obeys equation 3.2 with $\partial\tilde{T}/\partial t = 0$, and this equation can be interpreted as describing the trajectory $\tilde{T}(y)$ of a fictitious particle

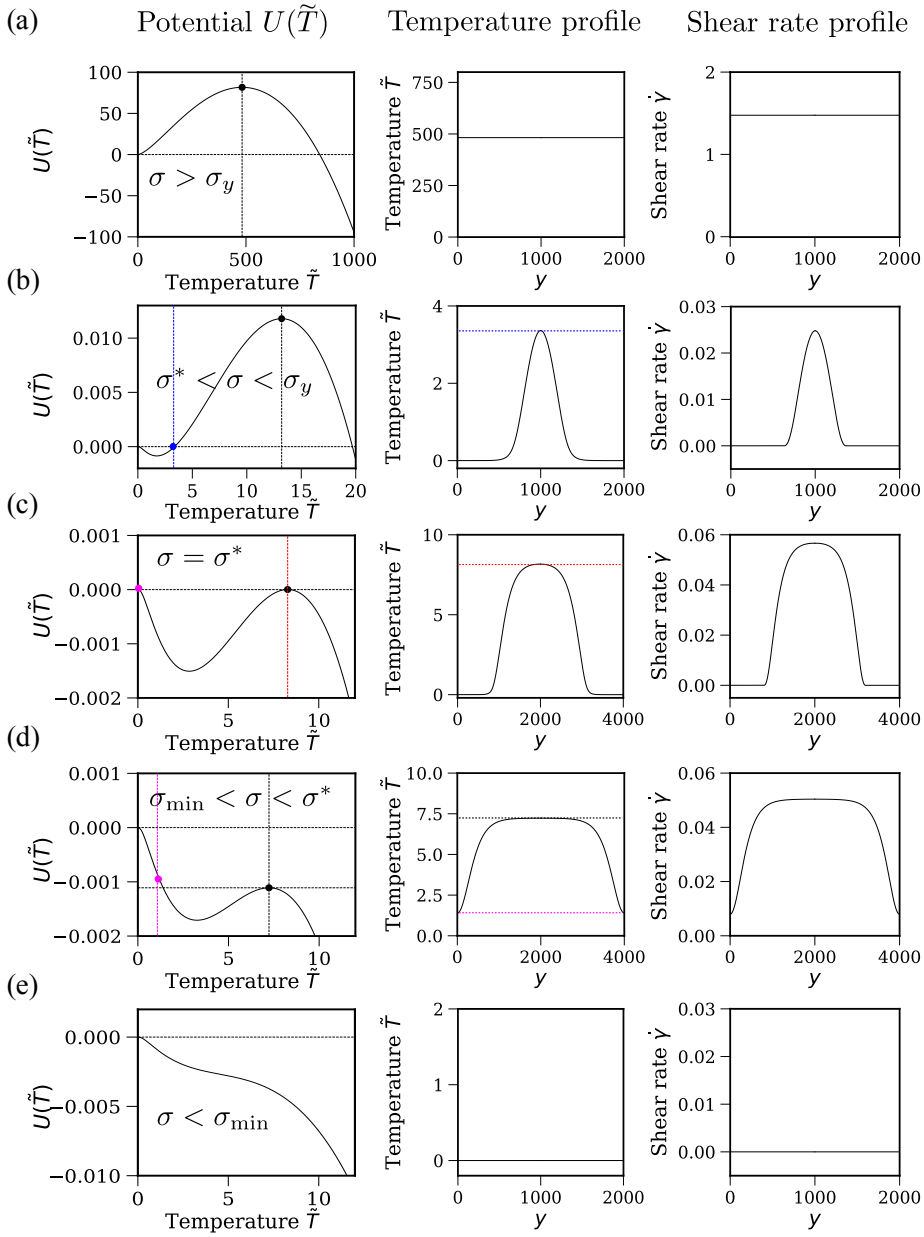

FIGURE 3.9: **Mechanical analogy to rationalize the shear rate profiles**. Potential $U(\tilde{T})$ (left), temperature (middle) and shear rate profiles (right) for various stress values (from top to bottom), for system sizes ($L = 2000$ or 4000) large enough to see a clear plateau in the profiles. (a) For $\sigma > \sigma_y$ ($\sigma = 2.8$): $U(\tilde{T})$ has a single extremum (at finite temperature) corresponding to homogeneous temperature and shear rate profiles. (b) For $\sigma^* < \sigma < \sigma_y$ ($\sigma = 1.28$): $U(\tilde{T})$ has three extrema and the shear banded solutions correspond to oscillations around the minimum of $U(\tilde{T})$, where the temperature oscillates between 0 and $\tilde{T}^{\max}_{flow}$ (blue line), leading to a plateau of shear rate close to 0 in the profile. (c) For $\sigma = \sigma^*$ ($\sigma = 1.2374$): the temperature oscillates between two equal extrema of $U(\tilde{T})$, between 0 and $\tilde{T}^{\max}_{flow}$ (red line), leading to two coexisting plateaus in the profiles. (d) For $\sigma_{min} < \sigma < \sigma^*$ ($\sigma = 1.23$): the temperature oscillates between $\tilde{T}^{\min}_{flow}$ (magenta line) and the temperature corresponding to the second maximum of $U(\tilde{T})$ (black line), leading to a plateau at large temperature in the profiles. (e) For $\sigma < \sigma_{min}$ ($\sigma = 1.21$), $U(\tilde{T})$ has a single extremum at $\tilde{T} = 0$, no flow is possible.

in an external potential $U(\tilde{T})$, in one dimension:

$$\lambda_T \frac{d^2\tilde{T}}{dy^2} = -\frac{dU(\tilde{T})}{d\tilde{T}}. \tag{3.21}$$

In this mechanical analogy, $\tilde{T}$ corresponds to the position of the particle and y to time. The effective potential is computed by integrating Eq. 3.2 in steady state with respect to $\tilde{T}$ at a fixed value of the stress σ:

$$U(\tilde{T}) = \sigma \int_0^{\tilde{T}} \dot{\gamma}(\sigma, \tilde{T}')d\tilde{T}' - c_V\tilde{T}^2/2\tau \tag{3.22}$$

where the function $\dot{\gamma}$ is expressed using equations 3.18 and 3.19. The resulting potential is displayed in Fig. 3.9(left) for various values of the stress, and will define five different regimes for the possible trajectories. We first note that, by construction, extrema of the effective potential correspond to temperatures (and shear rates) that are solutions of the set of equations 3.3 and 3.6, which describe homogeneous flow. The different regimes observed depending upon the value of stress in steady state are explained below and illustrated in Fig. 3.9. Note that, as in the particle-based simulations, we are only interested in periodic solutions with a period equal to the system size, L.

No flow regime: The case $\sigma < \sigma_{\min}$ is depicted in Fig. 3.9(e). Below a minimum stress $\sigma < \sigma_{\min}$, where $\sigma_{\min}$ corresponds to the minimum of the actual flow curve, the only extremum of $U(\tilde{T})$ is obtained for $\tilde{T} = 0$, which implies $\dot{\gamma} = 0$. For $\sigma < \sigma_{\min}$, no flow is possible.

Stable homogeneous flow: For large stresses, $\sigma > \sigma_y$, the potential $U(\tilde{T})$ exhibits a single extremum at a large value of temperature and $U(\tilde{T})$ has a finite, positive slope at $\tilde{T} = 0$. This maximum corresponds to homogeneous flow in the high shear rate, high stress regime, as shown by the corresponding flat profiles of temperature and shear rate in Fig. 3.9(a). The location of the maximum coincides with the stable part of the constitutive flow curve in Fig. 3.10.

Phase separated flow regimes: For stress values $\sigma_{\min} < \sigma < \sigma_y$, $U(\tilde{T})$ has three extrema: a maximum at $\tilde{T} = 0$, a second maximum at $\tilde{T}_{\max}$, and an intermediate minimum at $0 < \tilde{T}_{\min} < \tilde{T}_{\max}$. Possible interfacial profiles correspond to oscillations of $\tilde{T}$ around the minimum, with the "period" of the oscillation being equal to the size of the system. Here, two cases must be distinguished, and we focus first on the one that corresponds to the profiles effectively observed in simulations, with $U(\tilde{T}_{\max}) > U(0)$, as illustrated in Fig. 3.9(b).

- In this case (Fig. 3.9(b)), an oscillation can be obtained for values of the potential energy U between $U(T_{\min})$ and $U(0)$. The period of the oscillation has a value that starts from a minimum, nonzero value for the smallest energies in the vicinity of $U(T_{\min})$, where the oscillation is harmonic. This minimal period defines the critical system size, below which no interface can be observed and the system remains in a homogeneous state. We have checked that the corresponding value of ℓ_c obtained from this analysis coincides with the one obtained from the linear stability analysis in Eq. 3.16. As the value of the energy increases towards $U(0)$, the period of oscillation increases and becomes infinite at $U(0)$, where the trajectory spends a short "time" (i.e., space y in our system) at a finite

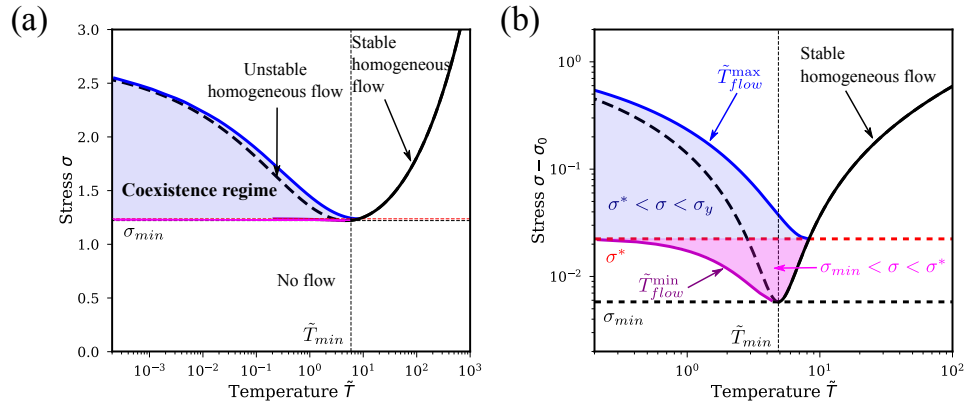

FIGURE 3.10: **Temperature-stress diagram**. (a) The black line corresponds to the constitutive temperature-stress curve (flow curve expressed using the temperature $\tilde{T} = \tau\sigma\dot{\gamma}/c_v$). The solid black line corresponds to a stable homogeneous flow while the dashed line corresponds to a regime of unstable homogeneous flow where various temperatures coexist in the system if $L > L_c$. The solid blue line indicates the maximum temperature of the profile T^{max}_{flow} in the regime $\sigma^* < \sigma < \sigma_y$ and the solid magenta line indicates the minimum temperature in the system T^{min}_{flow} in the regime $\sigma_{min} < \sigma < \sigma^*$. The blue and magenta shaded area represent the coexisting temperatures in the two regimes allowing for shear instabilities. (b) Same figure with the x-axis shown as $\sigma - \sigma_0$, σ_0 being a value close to σ_{min} for a better display of the narrow region near the minimum of the flow curve.

temperature and most of the time near $\tilde{T} = 0$. This corresponds to a narrow sheared layer coexisting within a broad non-flowing part, as illustrated by the horizontal dashed blue line in the figure, where the point marks the maximum temperature $\tilde{T}_{flow}$ inside the destabilized region. The above described regime, which accounts well for the observations made in the particle-based simulations, is observed for values of the stress $\sigma^* < \sigma < \sigma_y$.

- At σ^*, $U(\tilde{T}_{flow}) = U(0)$ (Fig. 3.9(c)), and for $\sigma_{min} < \sigma < \sigma^*$, $U(\tilde{T}_{flow}) < U(0)$ (Fig. 3.9(d)). As a result, for $\sigma_{min} < \sigma < \sigma^*$, oscillating trajectories exist between a small temperature (magenta dashed line in Fig. 3.9(d)) and T_{flow} (black dashed line in Fig. 3.9(d)), with most of the "time" being spent in the vicinity of T_{flow}. This situation is illustrated in the profiles of Fig. 3.9(d), where there is a wide plateau of temperature or shear rate at T_{flow} coexisting with a narrow region at lower temperature/shear rate. We have not observed this situation in the particle-based simulations: this is not surprising, as it corresponds to a very narrow range of stresses (see the locations of σ_{min} and σ^* in Fig. 3.4), approaching the minimum of the flow curve, where the critical size for the flow instability to develop becomes increasingly large (see Fig. 3.6). Note that in the special case where the two maxima have equal heights, $U(\tilde{T}_{flow}) = U(0)$ (Fig. 3.9(c)), two bands are coexisting in the system, as in a usual shear banding scenario.

These different regimes are summarized in Fig. 3.10. Fig. 3.10(a) and (b) depict the stress as a function of temperature in steady state. The black line represents the constitutive temperature-stress curve (which is directly related to the constitutive stress-strain rate curve for a homogeneous flow using Eq. 3.3). The solid part of the

black line corresponds to a stable homogeneous flow and is constructed from the loci of the high temperature maxima of $U(\tilde{T})$ when varying σ. The dashed part of the black line, constructed from the loci of the minima of $U(\tilde{T})$, corresponds to unstable homogeneous flow leading to coexistence of various temperatures in the system if the system size L exceeds the critical size L_c. In Fig. 3.10(a), the stress is represented using a linear scale to make a direct link with the constitutive flow curve of Fig. 3.4. Fig. 3.10(b) depicts the same data by zooming onto the region near the minimum of the flow curve, by plotting the stress in a log scale as $\sigma - \sigma_0$ (with σ_0 close to σ_{min}).

The blue solid line in Fig. 3.10 represents the maximum temperature that can coexist in the system (in the limit of an infinite system), and corresponds to the solution of $U(\tilde{T}_{\text{flow}}) = 0$ with $\tilde{T}_{\text{flow}} \neq 0$ (blue dot in Fig. 3.9(b)). The shaded blue region thus corresponds to the values of temperatures that can exist within the profile. Clearly the value of $\tilde{T}_{\text{flow}}$, which can be defined by $U(\tilde{T}_{\text{flow}}) = U(0)$, depends on the applied stress. As a result, no lever rule is expected: the total shear rate increases as stress increases not only by broadening the sheared region, but also by increasing temperature and strain rate inside the flowing region.

The magenta solid line in Fig. 3.10 represents the minimum temperature that can coexist in the system (in the limit of an infinite system) in the regime $\sigma_{\text{min}} < \sigma < \sigma^*$. In this regime, the temperature in the profile oscillates between this magenta line (constructed the from magenta dot in Fig. 3.9(d)) and the solid black line, as depicted by the magenta shaded area in Fig. 3.10(b).

To sum up, this mechanical analogy enables us to understand the different steady-state flow profiles obtained in the continuum model. Unsurprisingly, the phase separation scenario observed in particle-based simulations (Fig. 3.8(a)) corresponds to the case observed for the largest range of stresses in the model (Fig. 3.9(b)). In our model, the scenario of two bands coexisting (and obeying a possible lever rule) appears as a special case when $\sigma = \sigma^*$. One could speculate that in some systems, an additional stress-selection mechanism would lead to a selection of this special stress value in steady state. This is not the case in the particle-based simulations, where the steady-state stress depends on the applied shear rate and system size as shown in the flow curves in Fig. 3.1, and does not reach a single-valued plateau.

3.3 Discussion

In this work, we have shown how small changes in the microscopic dynamics of soft amorphous solids can lead to the emergence of permanent shear bands.

In general, the linear instabilities in the steady state rheology of complex fluids can be induced by spatial fluctuations of a field coupled to the flow (e.g., local concentration (Dhont, 1999; Dhont et al., 2008; Olmsted, 2008), local temperature (Dafermos et al., 1983; Katsaounis et al., 2017) or local microstructure (Dhont, 1999; Dhont et al., 2008)). Although this picture appears very general, there is still a lack of quantitative models especially in the framework of yield-stress materials, that could be directly compared to experiments or simulations. In this work we single out a specific destabilizing field that couples with the stress dynamics to produce permanent shear bands. In this context, our description allows for a quantitative comparison with particle based simulations by inferring all parameters of our proposed continuum model in simulations.

We show that a small change in the dynamics induced by microscopic inertia can lead to a local increase of kinetic temperature which promotes local shear-weakening. We identify this process as the leading cause for the phenomenon of shear localization.

Hence in the continuum model, we define a destabilizing field in terms of a local kinetic temperature. Contrary to effective fields, or parameters that enter former continuum descriptions (Shi et al., 2007; Manning et al., 2007; Fielding, 2014; Hinkle et al., 2017), the kinetic temperature has the advantage of having a clear microscopic definition, and is thus easily measurable in particle based simulations (as shown in Fig. 3.1(d)) and has been measured in some granular experiments (Losert et al., 2000). One could think of other possible destabilizing mechanisms at play in the microscopic simulations, such as shear-concentration coupling effects. We checked that, although there is a slight change in density between the flowing and non-flowing regions in our system, the concentration inhomogeneities are not sufficient to induce a local fluidization (see Appendix B).

Effective temperatures have been discussed in a large amount of papers in the context of sheared amorphous materials. For instance, in the context of the Shear Transformation Zone (STZ) theory (Langer, 2004), an internal variable χ, called "effective disorder temperature", governs the density of structural rearrangements and thus the plastic flow. This provides a mechanism for strain localization as a region with higher disorder has more chances to flow under stress, and flowing regions become more disordered. Within this framework, Manning et al. (2007) reported transient shear bands as those observed in athermal particle-based simulations (Shi et al., 2007). Similarly to the model we proposed in this work, they consider the dynamics of the local strain rate coupled to the dynamics of the local effective temperature χ, as well as a heat equation to describe the dynamics of χ (including a relaxation towards its steady-state value χ_∞ and a diffusion term). At long times, the effective temperature reaches its steady-state value χ_∞ everywhere in the system, so this model accounts for transient shear banding, as expected from their monotonic (Herschel-Bulkley type) constitutive flow curve. They could compare qualitatively their model to the simulations of Shi et al. (2007) under the assumption that the effective temperature χ is linearly related to the potential energy per atom. In this sense, the effective temperature is a hidden variable that has no explicit microscopic meaning. In our case, the kinetic temperature introduced in our model can be explicitly measured in particle-based simulations from velocity data; there is no hidden variable. This allows for quantitative comparisons between model and simulations, as we are able to predict the appearance of a linear flow instability for systems larger than a critical size $L_y > \ell_c$ using parameter inputs from the simulation.

To go beyond the linear stability analysis, we showed that the qualitative features in the stationary profiles match well between particle simulations and the continuum model. Notably, our description allows us to understand why the stationary profiles do not exhibit a simple band but a more complex continuous profile, leading to a lack of lever rule. The mechanical analogy highlights a variety of possible heterogeneous flow scenarios, with either flowing or immobile bands depending upon the stress value. Only one of these scenarii was observed in particle-based simulations, possibly due to the similarity between the values of $\sigma_{\min}$ and σ^* and the divergence of ℓ_c for $\sigma = \sigma_{\min}$. It could be of interest to tune the parameters in microscopic simulations to attempt to access these different shear banding regimes and further test our continuum model.

In many inertial systems the role of the kinetic temperature and its shear weakening effect is often ignored. This is, for example true in the case of granular materials where flow instabilities have been attributed to lubrication of frictional contacts (Dijksman et al., 2011; DeGiuli et al., 2017). The emergence of hysteresis and shear bands in these systems could result from a complex interplay between the different mechanisms involved in the dynamics. Following a similar approach as the one suggested in this work, a complete continuum description should couple the stress dynamics to

several destabilizing fields, including the local kinetic temperature.

From phase separation to a critical point?

Many systems exhibit nonmonotonic flow curves associated with flow instabilities. In the case of granular materials for instance, flow instabilities have been attributed to lubrication of frictional contacts (Dijksman et al., 2011; DeGiuli et al., 2017). Friction is thus at the origin of an endogenous mechanical noise that induce self-fluidization, and hence nonmonotonic flow curves. On the other hand, external mechanical noise (mechanical vibrations for instance) can induce a fluidization of a granular packing (Wortel et al., 2014; Wortel et al., 2016) at small imposed stress. Interesting flow features arise when fluctuations result from an interplay between a self-fluidizing and an external source of noise. When the external noise dominates over the self-fluidizing noise, this induces a transition from a nonmonotonic to a monotonic constitutive flow curve, due to the fluidizing effect of the external noise. This transition has been evidenced in granular media by Wortel et al. (2016), and studied in the context of nonequilibrium phase transitions.

In the next chapter, we study the effect of competing self-fluidizing and external noise within a generic mesoscale elasto-plastic model for the flow of soft glassy materials that account for a shear banding instability (Martens et al., 2012). Our work suggests the existence of a generic critical point when self-fluidization competes with an external fluidizing noise.

It would be of interest to test this scenario by adding an external source of noise in the case where self-fluidization emerges due to inertial dynamics, as studied in this chapter. Is the critical point restricted to "usual" shear banding scenarios obeying a lever rule (reminiscent of equilibrium phase separation scenarios), or is it more general?

Chapter 4

Fluidization, giant fluctuations and critical point in the flow of soft glassy materials

Résumé : Fluidisation et fluctuations critiques dans l'écoulement de solides désordonnés

Dans ce chapitre, nous nous intéressons à la rhéologie de fluides à seuils dont l'écoulement peut être hétérogène dans l'état stationnaire (bandes de cisaillement) en présence d'une source additionnelle de bruit mécanique.

Le rôle du bruit mécanique dans la rhéologie de systèmes denses désordonnés ainsi que différents scénarios de fluidisation étudiés dans la littérature ont été introduit dans le Chapitre 1 (section 1.2) et certains aspects sont rappelés en introduction de ce chapitre. Nous insistons en particulier sur les études abordant la compétition entre sources de bruit endogènes (résultant de l'écoulement) et sources de bruit externes, ou indépendantes de l'écoulement. Cette compétition peut être à l'origine de fluctuations géantes du taux de cisaillement dans l'écoulement de granulaires cisaillés et vibrés, associées à l'existence d'un point critique tel que proposé par Wortel et al. (2016).

La question centrale de ce chapitre concerne les conséquences sur l'écoulement de fluides à seuil d'une compétition entre sources de bruit mécanique endogène et externe. En particulier, l'existence d'un point critique (et ses caractéristiques) est-elle une propriété générique de ces systèmes ou dépend-elle de détails microscopiques tels que le frottement dans les systèmes granulaires?

Nous modélisons l'écoulement de fluides à seuil en utilisant un modèle élasto-plastique sur réseau comme décrit dans le Chapitre 2, ce qui permet d'aborder de façon générique la question de la compétition entre diverses sources de bruit mécaniques (endogène et externe), sans modéliser de façon détaillée la dynamique de particules. Les modèles utilisés (décrits en détail dans le chapitre 2) sont présentés brièvement dans la section 4.1 et les résultats sont organisés en quatre parties.

Dans une première partie (section 4.2), nous montrons comment une source de bruit mécanique indépendante de l'écoulement peut fluidiser un fluide à seuil, en faisant disparaître la contrainte seuil. En particulier, ce nouveau régime d'écoulement dépend du modèle de bruit considéré, et nous discutons plusieurs arguments théoriques qui permettent de prédire le comportement rhéologique dans le régime fluidisé.

Dans une deuxième partie (section 4.3), nous montrons comment le fait de varier l'amplitude du bruit mécanique externe (dans deux modèles de bruit différents) peut induire une transition entre une rhéologie non monotone associée à une instabilité de l'écoulement homogène et une rhéologie monotone où le système s'écoule de façon homogène. Cette transition s'accompagne, dans le cas d'un forçage à contrainte imposée,

de fluctuations géantes du taux de cisaillement macroscopique dans le système, que nous discutons dans une troisième partie (section 4.4). Cette phénoménologie peut s'expliquer par l'existence d'un point critique séparant les régimes dominé par le bruit endogène et dominé par le bruit extérieur.

Dans la dernière partie (section 4.5), nous menons une étude détaillée de ce point critique afin d'estimer les exposants critiques décrivant l'évolution de grandeurs macroscopiques moyennes et de leur fluctuations au voisinage de la transition. Nous montrons que ces exposants ne dépendent pas du modèle de bruit considéré (et sont compatibles avec ceux mesurés dans des expériences sur des granulaires par Wortel et al. (2016)).

Le travail présenté dans ce chapitre suggère donc un scénario générique pour l'émergence d'un point critique lors de la compétition de sources de bruit endogènes (auto-fluidization sous cisaillement) et exogènes (indépendantes de l'écoulement) dans l'écoulement de solides désordonnés.

Introduction

Understanding the mechanisms of fluidization of soft glassy materials by sources of noise independent of the flow is a question concerning a large class of materials, ranging from fluidization of yield stress materials due to an external noise (vibrations) (Wortel et al., 2014; Gibaud et al., 2020) to the nature of the transitions to dynamical arrest in active or biological systems (Janssen, 2019; Berthier et al., 2019).

In the absence of fluidizing noise, soft glassy materials behave as yield stress fluids (YSFs), and can be described at the continuum level using empirical laws such as the Herschel-Bulkley relationship (Herschel et al., 1926), or continuum descriptions, such as visco-elasto-plastic (Marmottant et al., 2007; Saramito, 2007) and fluidity models (Bocquet et al., 2009; Fielding, 2014). While such descriptions account well for the average flow behaviour at a coarse-grained scale, it has appeared that some flow features of YSFs are dominated by giant fluctuations of the macroscopic stress or shear rate (Coussot et al., 2002a; Lootens et al., 2003; Cantat et al., 2006; Pastore et al., 2011; Barés et al., 2017; Srivastava et al., 2019). This can for example lead to non-local, strongly system-size dependent, transport coefficients for the material dynamics (Lemaître et al., 2009; Martens et al., 2011; Tyukodi et al., 2018). Accordingly, understanding the role of mechanical noise and its spatio-temporal features has not only attracted a strong fundamental interest (Nicolas et al., 2018a) but is also of direct importance in rheological applications (Bonn et al., 2017).

Part of the mechanical fluctuations in driven disordered materials are usually generated by the flow itself, for example resulting from the elastic response of the material to localized plastic events as described in the first two chapters (Argon et al., 1979; Schall et al., 2007). They are therefore very different in nature from thermally generated fluctuations (Nicolas et al., 2014a) and must be incorporated into modeling approaches in a self-consistent manner (Hébraud et al., 1998; Agoritsas et al., 2015).

Interestingly, flow-induced fluctuations can be associated in some cases with a self-fluidization of the material, i.e., a decrease in shear stress with increasing shear rate. This leads to nonmonotonic rheological constitutive curves (Schall et al., 2010; Mansard et al., 2011; Fielding, 2014), that can be associated with flow instabilities, potentially leading to shear localization, metastability and hysteresis (Wortel et al., 2014). In the case of granular materials, this self-fluidization process finds its origin in sliding frictional contacts (Wortel et al., 2014; Wortel et al., 2016; DeGiuli et al., 2017). In non-frictional YSFs, nonmonotonic flow curves can be explained by

mechanisms such as inertia (Nicolas et al., 2016; Karimi et al., 2016; Vasisht et al., 2018) or local softening following structural rearrangements (Coussot et al., 2010; Martens et al., 2012; Cloitre, 2018).

Besides this self-generated mechanical noise, additional sources of noise can induce a softening or even a fluidization of YSFs at small imposed external stresses. These "external" sources of noise (in the sense that they are supposed to be independent of the shear-induced one) can be for instance of thermal origin (Chattoraj et al., 2010; Ikeda et al., 2012), due to an external vibration (D'anna et al., 2003; Caballero-Robledo et al., 2009; Jia et al., 2011; Hanotin et al., 2012; Gibaud et al., 2020), or result from local processes such as coarsening in foams (Cohen-Addad et al., 2004), or internal activity (Mandal et al., 2016; Tjhung et al., 2017; Matoz-Fernandez et al., 2017a).

An even more interesting case is the scenario where fluctuations result from the interplay of a self-fluidizing and an external source of noise. Upon an increase of the external noise magnitude, the fluidization induced by the external noise will dominate at some critical value over the self-fluidization. This scenario can induce a change from a nonmonotonic constitutive behavior to a simple monotonic one, due to the fluidization effect of the external noise. This scenario has been confirmed in a recent experimental work on sheared and vibrated granular media by Wortel et al. (2016). In this experiment (described in Chapter 1, Fig. 1.13), mechanical vibrations fluidize the granular packing at low shear stress and, upon a critical vibration magnitude, induce a transition from a nonmonotonic to a monotonic flow curve. This transition is accompanied by giant fluctuations of the macroscopic strain rate, which, in the context of non-equilibrium phase transitions, can indicate the presence of a critical point.

Beyond the specific case of granular materials, one can expect critical dynamics to appear as soon as soft glassy systems exhibit both a nonmonotonic flow curve and a fluidization mechanism. In this chapter, we explore this generic scenario for the emergence of a critical point in the framework of elasto-plastic models for the flow of frictionless soft glassy materials which can be tuned to exhibit a nonmonotonic rheology (as shown in Chapter 2). We consider two different models for an external fluidizing noise, and show that although they lead to distinct rheological behaviors at low stress, both induce a transition from a nonmonotonic to a monotonic flow curve, associated with the transition from shear-banded to homogeneous flow. We evidence that the competition between the endogenous noise and an external fluidizing noise leads to giant fluctuations in the flow of soft glassy materials, that become relevant on the macroscopic scale. When interpreting the transition between the self-fluidized and the externally fluidized regimes upon increasing the noise magnitude as a critical phenomenon as done by Wortel et al. (2016), we find that critical exponents do not depend on the model of external noise. This suggests that this type of transition might be very generic, independent of the microscopic details in the underlying dynamics.

This chapter is organized as follows: the elasto-plastic models used in this work (introduced in detail in Chapter 2) are briefly presented in section 4.1. Section 4.2 is dedicated to the rheology of yield stress materials in presence of an external source of noise. Section 4.3 concerns the effect of competing self-fluidizing and external sources of noise on the flow, and we show evidences for a transition from a shear-banded or hysteretic flow to homogeneous or stable flow upon increasing the external noise magnitude. In section 4.4, we show that this transition is associated with increased fluctuations of the macroscopic shear rate, supporting the scenario for the existence of a critical point. Section 4.5 finally deals with the characterization of this critical point for the two models of noise, leading to critical exponents that appear to be generic.

4.1 Elasto-plastic models

For this study we chose to use coarse-grained elasto-plastic models (EPMs), which provide a generic framework to describe the flow of soft glassy materials. An overview of EPMs as well as a detailed derivation were provided in Chapters 1 and 2 of this thesis (more details can also be found in the recent review by Nicolas et al. (2018a)) and we will only present here the specific models used in this chapter.

4.1.1 Numerical model

The spatially-resolved models considered in this work are extended from previous versions used to describe both steady-state flows of YSFs using a shear-imposed protocol model (Picard et al., 2005; Martens et al., 2012; Nicolas et al., 2014a; Liu et al., 2016), and transient (creep) flow using a stress-imposed protocol model (Liu et al., 2018).

We model an amorphous medium as a collection of mesoscopic blocks, each block being represented as a node (i,j) of a square lattice of size $L \cdot L$ (the lattice indices i,j represent the discretized coordinates along x and y directions respectively). The mesh size corresponds to the typical cluster size of rearranging particles undergoing a plastic rearrangement. These local plastic transformations are assumed to have the same geometry as the globally applied simple shear, i.e., we consider a scalar model. We decompose the total deformation of each node (i,j) into a local plastic strain $\gamma^{\mathrm{pl}}_{ij}$, which is, in general, heterogeneous, and an elastic strain $\gamma^{\mathrm{el}}_{ij}$.

Stress-imposed model

When controlling the global stress in the system as done by Liu et al. (2018), we also decompose the local stress into two parts, $\sigma_{ij} = \sigma^{\mathrm{ext}} + \sigma^{\mathrm{int}}_{ij}$, where σ^{ext} is the externally applied uniform stress, and $\sigma^{\mathrm{int}}_{ij}$ describes the stress fluctuations resulting from the elastic interactions between regions undergoing plastic deformation (i.e., particle rearrangements), as described by:

$$\sigma^{\mathrm{int}}_{ij} = \mu \sum_{i'j'} G^{*}_{ij,i'j'} \gamma^{\mathrm{pl}}_{i'j'} \tag{4.1}$$

The interaction kernel, G^{*}, is of Eshelby's type and is expressed, in Fourier space, as: $\tilde{G^{*}}(\mathbf{q}) = -4\frac{q_x^2 q_y^2}{q^4}$ for $\mathbf{q} \neq 0$ and $\tilde{G^{*}}(\mathbf{0}) = 0$ so that $\sigma^{\mathrm{int}}_{ij}$ describes the local stress fluctuations in a macroscopically stress-free state. Applying a macroscopic driving stress σ^{ext} induces a uniform shift of the local stresses without altering internal fluctuations. The local dynamics is expressed as:

$$\frac{d}{dt}\gamma^{\mathrm{pl}}_{ij} = n_{ij}\frac{\sigma_{ij}}{\mu\tau} = n_{ij}\frac{\sigma^{\mathrm{ext}} + \sigma^{\mathrm{int}}_{ij}}{\mu\tau} \tag{4.2}$$

with μ the elastic modulus, τ a mechanical relaxation time setting the time units of the model and $\frac{d}{dt}\gamma^{\mathrm{pl}}_{ij} = \frac{n_{ij}\sigma_{ij}}{\mu\tau}$ the shear rate produced by a plastic rearrangement occurring at a site (i,j). The state variable n_{ij}, indicates whether the site deforms plastically ($n_{ij} = 1$) or elastically ($n_{ij} = 0$), and has its own stochastic dynamics that will be described below.

Strain-imposed model

Another widely used model consists in imposing the strain rate to the system, as done by Picard et al. (2005), Martens et al. (2012), Nicolas et al. (2014a), and Liu et al.

(2016). In this model, $\dot{\gamma}$ is the externally applied shear rate and we compute the local stress σ_{ij}, evolving with the overdamped dynamics:

$$\frac{d}{dt}\sigma_{ij} = \mu\dot{\gamma} + \mu\sum_{i'j'} G_{ij,i'j'}\frac{d}{dt}\gamma^{\mathrm{pl}}_{i'j'} \tag{4.3}$$

with $d\gamma^{\mathrm{pl}}_{ij}/dt = n_{ij}\sigma_{ij}/\mu\tau$. The interaction kernel G is also of Eshelby's type (Eshelby, 1957), and its Fourier transform $\tilde{G}(\mathbf{q})$ is such that $\tilde{G}(\mathbf{0}) \neq 0$ is determined by the integral over the whole system of the elastic response. It is related to G^* by: $G = G^* - 1/L^2$, because unlike G^*, G does not describe the stress fluctuations in a macroscopically stress-free state, but the full stress field instead.

Stochastic dynamics for the plastic activity

Besides the dynamics described in either Eq. (4.2) or Eq. (4.3) depending upon the driving protocol, each node alternates between a local plastic state ($n_{ij} = 1$) and a local elastic state ($n_{ij} = 0$). The stochastic rules, as introduced by Picard et al. (2005), involve a rate of plastic activation $1/\tau_{\mathrm{pl}}$ when the local stress exceeds a barrier $|\sigma_{ij}| > \sigma_{\mathrm{y}}$ ($n_{ij} : 0 \to 1$) and a rate $1/\tau_{\mathrm{el}}$ for a plastic node turning elastic again ($n_{ij} : 1 \to 0$). We consider in this work that a fluidizing noise induces additional plastic events ($n_{ij} : 0 \to 1$) with a "vibration rate" k_{vib}. The three different types of transitions between elastic and plastic states are illustrated in Fig. 4.1 and summarised below:

$$\begin{cases} n_{ij}(t) : 0 \overset{1/\tau_{\mathrm{pl}}}{\to} 1 & \text{if } \sigma_i > \sigma_{\mathrm{y}} \\ n_{ij}(t) : 0 \overset{k_{\mathrm{vib}}}{\to} 1 & \forall\sigma_i \\ n_{ij}(t) : 1 \overset{1/\tau_{\mathrm{el}}}{\to} 0 & \end{cases} \tag{4.4}$$

We study two different models for the activation of plastic events by an external noise:

1. Model 1: Constant activation rate: $k_{\mathrm{vib}} = 1/\tau_{\mathrm{vib}}$ for any value of the local stress σ_{ij}
2. Model 2: Arrhenius-like activation: $k_{\mathrm{vib}} = k_0 e^{\lambda_{\mathrm{vib}}(\sigma_{ij}-\sigma_{\mathrm{y}})}$ with k_0 a prefactor kept constant in our study and λ_{vib} controlling the magnitude of the noise.

These activated events have the same properties as the ones induced by shear, i.e., they lead to a redistribution of stress in the system through the Eshelby propagator.

In the following, the values of stress, strain rate and time are respectively given in units of σ_{y}, $\sigma_{\mathrm{y}}/\mu\tau$ and τ. We set $\tau_{\mathrm{pl}} = 1$ and the restructuring time τ_{el} can be set either to 1 when studying only the effect of a fluidizing noise on a monotonic flow curve, or using $\tau_{\mathrm{el}} = 10$ in order to induce local softening. Long restructuring times lead to nonmonotonic flow curves (Coussot et al., 2010) and are associated with permanent shear bands when imposing the shear rate in the system, as described by Martens et al. (2012).

We study the influence of an external noise by varying the value of the vibration rate k_{vib}, either varying $\tau_{\mathrm{vib}} = k_{\mathrm{vib}}^{-1}$ for model 1 (random activation), or λ_{vib} for model 2 (Arrhenius-type activation) using both shear rate and stress controlled driving protocols, as they give access to different flow features in the case of nonmonotonic flow curves.

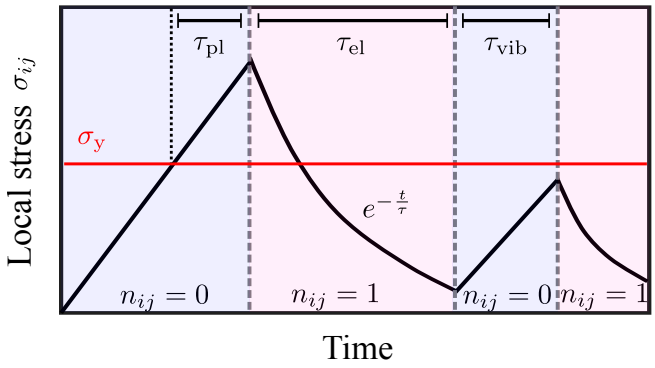

FIGURE 4.1: **Typical local stress dynamics in an elasto-plastic model with a fluidizing noise**: local stress σ_{ij} as a function of time t for a site initially in an elastic state ($n_{ij} = 0$, blue shaded area) undergoing first a plastic rearrangement due to loading after a time $\tau_{\rm pl}$ once $\sigma_i > \sigma_{\rm y}$, leading to plastic state ($n_{ij} = 1$, red shaded area) with a viscoelastic relaxation $e^{-\frac{t}{\tau}}$ and recovering an elastic behavior after a typical time $\tau_{\rm el}$ ($n_{ij} = 0$). Another plastic event is triggered by the fluidizing noise, with a rate $k_{\rm vib} = 1/\tau_{\rm vib}$ (leading to $n_{ij} = 1$ and the same relaxation dynamics as for shear induced plastic events).

.

4.1.2 Simulation methods

As we are interested in bulk quantities, we simulate the above elasto-plastic model using periodic boundary conditions in all directions. Large scale simulations of the elasto-plastic model are performed using a GPU-based parallel implementation as done by Liu et al. (2016).

We perform simulations of the 2d elasto-plastic model using shear- and stress-controlled protocols. Using a shear-imposed protocol, we measure the average steady-state stress in the system to compute the flow curve, by averaging over a strain window $\gamma = 50$. To compute the shear rate profiles in the shear banding regime, we average the profiles along the direction in which the flow is homogeneous and over a strain window $\gamma = 1000$. Using a stress-controlled protocol, we analyse time-series of the average shear rate in the system (of average duration $T = 2 \cdot 10^6$ for $L = 128$ and $L = 256$, $T = 6 \cdot 10^5$ for $L = 512$ and $T = 10^5$ for $L = 1024$, corresponding to strains ranging from $\gamma = 2000$ to $4 \cdot 10^4$).

4.2 Fluidization by a flow-independent mechanical noise

In this section, we study how including an additional timescale in Picard's model to account for the random activation of plastic events, $\tau_{\rm vib}$, affects the rheology.

We first consider a single site version of the model to study the rheology in the same spirit as Martens et al. (2012). We simulate the effective single site dynamics with an additional timescale $\tau_{\rm vib}$, and find that (i) this additional timescale induces a fluidization (vanishing yield stress) and that (ii) upon increasing noise magnitude (decreasing $\tau_{\rm vib}$), the flow curve goes from a nonmonotonic to a monotonic behavior. We further find that using a simplified version of the single site model (Martens et al., 2012) enables to predict a linear rheology at low shear rate, as observed in simulations. We then solve numerically the spatially-resolved Picard model with an additional timescale $\tau_{\rm vib}$ and find the same phenomenology. Last, we show that various

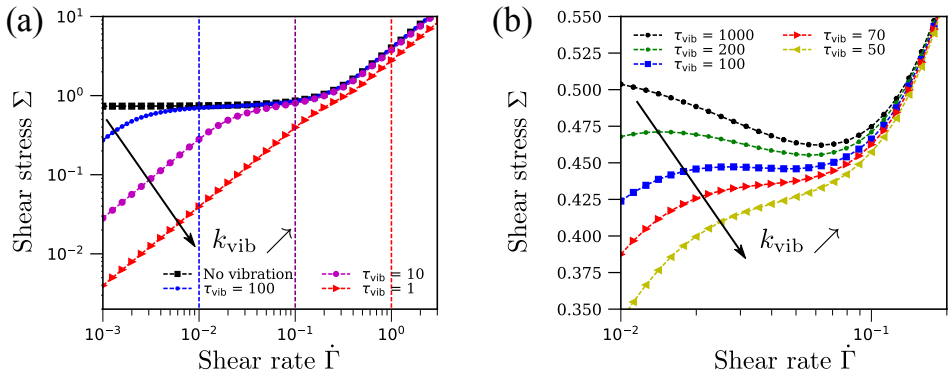

FIGURE 4.2: **Numerical flow curve in the effective single site dynamics version of Picard's model** (shear stress Σ as a function of the shear rate $\dot{\Gamma}$) for various values of τ_{vib}. (a) In a log-log representation for a restructuring time $\tau_{el} = 1$ (monotonic flow curve) and increasing values of $k_{vib} = \tau_{vib}^{-1}$. The vertical dashed lines correspond to $\dot{\gamma} = \tau_{vib}^{-1}$ for each value of τ_{vib}. (b) In a lin-log representation for a restructuring time $\tau_{el} = 10$ (nonmonotonic flow curve).

.

activation rules for the external noise can lead to distinct rheological behaviors at low stress, and rationalize these findings using a simple theoretical argument.

4.2.1 Fluidization in a single site elasto-plastic model

Following the work of Martens et al. (2012), we first investigate the rheology with an additional source of noise by considering the effective single site dynamics of the elasto-plastic model introduced above. The advantage of such single site elasto-plastic model is to obtain a proxy for the underlying constitutive flow curve in different regimes. In particular, nonmonotonic flow curves are usually not seen in spatial simulations (for sufficiently large systems at least, see Chapter 3) due to flow instabilities. This single site model for the rheology in the absence of fluidizing noise was introduced in Chapter 2 and we recall the main points below.

Single site elasto-plastic model

In the model for the effective single site dynamics (see Chapter 2), the stress dynamics is described by:

$$\frac{\partial \sigma(t)}{\partial t} = \dot{\Gamma} - g n(t) \sigma(t) \tag{4.5}$$

with $\dot{\Gamma}$ the effective shear rate and $g = |G(0,0)|$ the absolute value of the stress propagator at the origin ($g \simeq 0.57$ for large systems) (Martens et al., 2012). The dynamics of the activity $n(t)$ remains unchanged with respect to the spatial model: the activation of plastic events ($n : 0 \to 1$) results both from an activation rate $1/\tau_{pl}$ when the stress exceeds a barrier $|\sigma| > \sigma_y$ and from a random activation with a rate $k_{vib} = 1/\tau_{vib}$ independently of the stress value. The transition from a plastic to an elastic state ($n : 1 \to 0$) occurs with a rate $1/\tau_{el}$.

We perform simulations of this stochastic model for the one-site dynamics with both shear- and noise-induced (with a rate $k_{vib} = \tau_{vib}^{-1}$) plastic events in order to obtain the time evolution of stress $\sigma(t)$ for an imposed effective shear rate $\dot{\Gamma}$.

Rheology in the single site elasto-plastic model

In order to compute the steady-state flow curve in this single site elasto-plastic model, we compute the time averaged stress $\langle\sigma\rangle_t$ as a function of $\dot{\Gamma}$. Fig. 4.2(a) depicts the flow curves obtained for a restructuring time $\tau_{\rm el} = \tau_{\rm pl} = \tau = 1$, leading to a monotonic rheology (Martens et al., 2012). The random activation of additional plastic events leads to a fluidization at low stress (vanishing yield stress), while the rheology remains unchanged at high shear rates (the flow curves collapse with the flow curve in absence of fluidizing noise, represented by the black squares). This enables us to define two regimes: "noise dominated" and "shear dominated", determined by the competition of shear and noise associated timescales, $\dot{\gamma}^{-1}$ and $\tau_{\rm vib}$, as indicated by the vertical dashed lines in Fig. 4.2(a) (corresponding to $\dot{\gamma} = \tau_{\rm vib}^{-1}$). In the noise dominated regime, the plasticity is mainly induced by the external noise, leading to a linear fluid-like regime in the flow curve of Fig. 4.2(a). Using the same approach as Martens et al. (2012), we can compute analytically the stress in this regime, under the assumption that all the plasticity is induced by the external noise at a rate $k_{\rm vib}$. The details of the computation are shown in Appendix C.1.1. We find a linear rheological behavior $\Sigma = c(\tau_{\rm el}, \tau_{\rm vib})\dot{\Gamma}$ ($c(\tau_{\rm el}, \tau_{\rm vib})$ given in Eq. C.8), in agreement with simulations of the complete model.

In Fig. 4.2(b), a large value for the restructuring time ($\tau_{\rm el} = 10$) is responsible for a self-fluidization of the system (decreasing flow curve for $\dot{\gamma} < \dot{\gamma}_c \simeq 0.06$). Upon an increase of the external noise ($k_{\rm vib} = \tau_{\rm vib}^{-1}$), a transition from a flow curve exhibiting a negative slope (nonmonotonic) to a monotonically increasing flow curve is observed. This is similar to what was reported in experiments on sheared and vibrated granular media (Wortel et al., 2016) (see Introduction, Fig. 1.13).

Conclusion

We see through simulations of this simple single site elasto-plastic model that random activation of plastic events due to an external noise induces a fluidization of yield stress materials at low stress. Within this model of activation at constant rate $k_{\rm vib}$, this results in a linear rheology regime at low shear rate, that can be rationalized under several simplifying assumptions (neglecting for instance the mechanical noise due to elastic interactions). Note that in the regime where plasticity is dominated by the random activation of plastic events, the internal mechanical noise due to elastic interactions has only little effect on the rheology, as demonstrated for instance by comparing scalar and tensorial elasto-plastic models using different rules for the orientation of randomly activated events (see section 4.6). We will see further in this chapter that the low shear rate rheology depends on the particular rules of activation.

As mentioned in introduction, another widely used model to describe the rheology of yield stress fluids is the model introduced by Hébraud et al. (1998) (HL). This model was further extended by Matoz-Fernandez et al. (2017a) to account for fluidization by a flow-independent noise term in the dynamics. The corresponding rheological curves are shown in Fig. 1.16(c) and resemble that of Fig. 4.2(a), with a linear "noise dominated" regime. In the work of Matoz-Fernandez et al. (2017a), the external noise takes the form of an additional constant contribution to the diffusion coefficient that describes stress diffusion in the HL model and aims at describing the mechanical noise induced by cell divisions and death events occurring at rates d_0 and a respectively. The comparison between particle-based simulations and the theoretical model reveal that the additional stress diffusion constant in the HL model appears to be proportional to the rate of apoptosis events a, leading to a viscosity $\eta \sim 1/a$. This suggests that the random activation model proposed here could also be interpreted

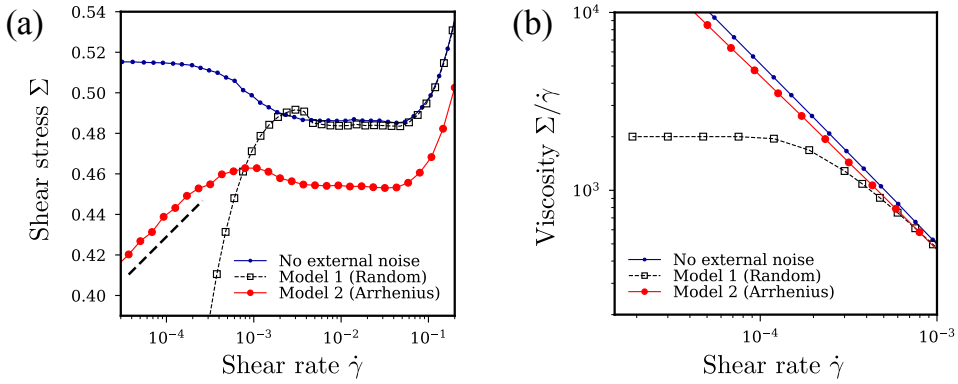

FIGURE 4.3: **Flow curves and viscosity for two models of noise**. (a) Shear stress Σ as a function of the imposed shear rate $\dot{\gamma}$ in the absence of external noise (small dark blue dots) and for the two models of agitation with $k_{\text{vib}} = 3.3 \cdot 10^{-4}$ (model 1, black square symbols) and $\lambda_{\text{vib}}^{-1} = 3.3 \cdot 10^{-2}$ (model 2, red dots), for a system size $L = 256$. The dashed line is a guide-to-the-eye indicating a logarithmic behaviour. (b) Log-log plot of the viscosity $\Sigma/\dot{\gamma}$ as a function of the shear rate (for $\dot{\gamma} < 10^{-3}$) showing the linear rheology regime (constant viscosity) at small shear rates for model 1.

in a Hebraud-Lequeux framework as an additional constant contribution D_0 to the diffusion coefficient for the stress, with $D_0 \sim 1/\tau_{\text{vib}}$.

Another important outcome of this section concerns the nonmonotonic rheology obtained in this simple single site elasto-plastic model for large values of the restructuring time τ_{el}. This regime, characterized in detail by Martens et al. (2012) in absence of external noise, is associated with a flow instability in the corresponding spatial model. We show in this section that the flow curve can be tuned by introducing an external noise and a monotonic rheological behavior can be obtained for sufficiently large magnitudes of the noise. This is qualitatively similar to the transition reported in sheared and vibrated granular media by Wortel et al. (2016) and shown to be associated with critical dynamics.

In the following, we explore a spatial (2d) version of this elasto-plastic model using two different models of external noise to further investigate the flow behavior induced by an external noise. Using a spatial model enables us to study how the flow instability is affected by an external noise and test the possible existence of a generic critical point.

4.2.2 Fluidization in the spatial (2d) elasto-plastic model

We now consider the spatial elasto-plastic model introduced in Chapter 2 and at the beginning of this chapter, with two different models of fluidizing noise: a random activation model (model 1, as studied above in the single site model) and an Arrhenius-like activation model (model 2). We compare two different models of noise in order to understand how the specific details of the activation mechanisms due to an external noise influence the low shear rate rheology, and, whether these details affect the nature of the transition from a nonmonotonic to a monotonic flow curve.

In the absence of fluidizing noise ($k_{\text{vib}} = 0$) the elasto-plastic model exhibits a yield-stress fluid behavior (Picard et al., 2005), as shown by the finite stress plateau at low shear rate in the upper dark blue curve in Fig. 4.3(a). With the value of restructuring time $\tau_{\text{el}} = 10$ used in this work, the rheology in the absence of fluidizing

noise is nonmonotonic, i.e., the underlying constitutive (single site) flow curve has a minimum which is set by the choice of $\tau_{\rm el}$, as discussed by Martens et al. (2012) and in Chapter 2. The minimum of the constitutive flow curve for $\tau_{\rm pl} = \tau = 1$ and $\tau_{\rm el} = 10$ corresponds to a shear rate of about $\dot{\gamma}_c \simeq 0.06$.

For finite dimensions and sufficiently large systems, this (unstable) nonmonotonic flow curve cannot be observed in simulations, due to the existence of shear bands (leading to a stress plateau, as shown for intermediate shear rates in the top curve of Fig. 4.3(a)). This is the main qualitative difference between the rheology obtained within the single site model and the 2d spatial model. Note that negative slopes can still be observed in the flow curve of finite systems (around $\dot{\gamma} = 10^{-3}$) due to finite-size effects.

Flow curves obtained for the two models of noise are shown in Fig. 4.3(a), with magnitudes $k_{\rm vib} = 3.3 \cdot 10^{-4}$ for model 1 (random activation) and $\lambda_{\rm vib}^{-1} = 3.3 \cdot 10^{-2}$ for model 2 (Arrhenius) respectively. First, the system exhibits a fluid-like behavior at low stress (and $\dot{\gamma} < 10^{-3}$), as shown by the absence of stress plateau at low shear rate. This regime is followed by a stress-plateau ($10^{-3} < \dot{\gamma} < 10^{-1}$), associated with a shear banding instability (see Fig. 4.5), analogous to the case when the fluidizing noise is absent. Shear-banded profiles will be further discussed in section 4.3.1. The last regime ($\dot{\gamma} > 10^{-1}$) corresponds to a stable homogeneous flow.

Low shear rate rheology

While the global shape of the flow curve is the same, the rheological behavior in the low stress regime differs between the two models of activation. The random activation rule (model 1) leads to a Newtonian behavior at low shear rates, with a constant viscosity $\eta = \Sigma/\dot{\gamma}$ as shown in Fig. 4.4(b), whereas the Arrhenius-like rule (model 2) leads to a logarithmic-like flow behavior, reminiscent of experiments on vibrated granular media (see Fig. 1.12(b) or Fig. 1.13(a) from the work of Dijksman et al. (2011) and Wortel et al. (2016)). This can be understood from the activation rule, using a simplified argument in the low shear-rate regime, as detailed in Appendix C.1.2. This calculation is based on two simplifying assumptions: (i) that the internal mechanical noise is negligible, in this regime, with respect to the external noise, and (ii) that the plastic relaxation fully relaxes the local stress and that its duration is negligible with respect to the duration of the elastic phase. Within this simplified dynamics, we obtain for model 1 the linear behavior $\Sigma = \mu\dot{\gamma}/k_{\rm vib}$, and for model 2 the logarithmic behavior

$$\Sigma = \frac{\sigma_c}{2} + \frac{1}{2\lambda} \ln\left(\frac{\lambda\mu}{k_0}\dot{\gamma}\right). \tag{4.6}$$

Note that this simplified argument enables us to get the right rheological behavior (and the scaling with $k_{\rm vib}$ for model 1) but the dependence of the low shear rate viscosity with the restructuring time $\tau_{\rm el}$ cannot be obtained under the assumption of full stress relaxation.

Flow curves for various noise magnitudes

Flow curves for various noise magnitudes are depicted in Fig. 4.4 for the two models of activation (by varying either $k_{\rm vib} = 1/\tau_{\rm vib}$ in model 1 or $\lambda_{\rm vib}$ in model 2). For the two models, the effect of noise is (i) a fluidization (vanishing yield stress) at any value of the noise magnitude and (ii) a transition from a nonmonotonic to a monotonic flow curve at a noise magnitude, $k_{\rm vib}^c = (1.3 \pm 0.2) \cdot 10^{-3}$ or $\lambda_{\rm vib}^c = 20 \pm 2$ (the thick black lines in Fig. 4.4 correspond to $k_{\rm vib}^c = 1.25 \cdot 10^{-3}$ and $\lambda_{\rm vib}^c = 20$).

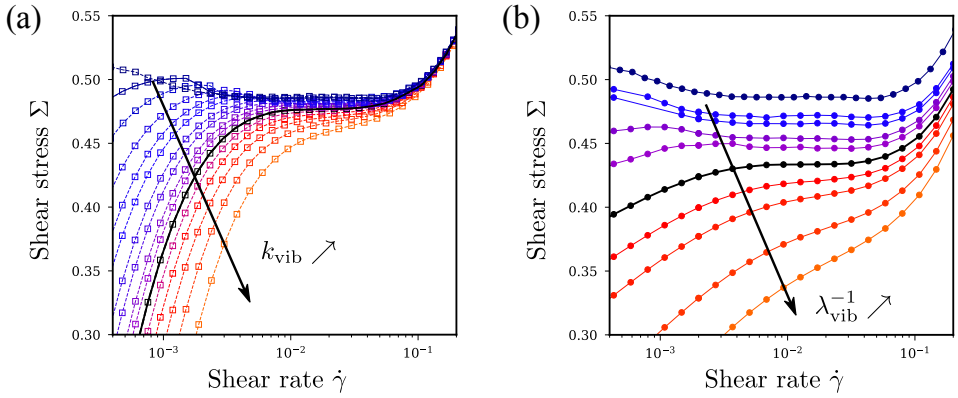

FIGURE 4.4: **Shear stress Σ as a function of the imposed shear rate $\dot{\gamma}$ for various noise magnitude** for (a) the random activation model (model 1, $k_{\rm vib}$ ranging from 10^{-5} to $3.3 \cdot 10^{-3}$) and (b) the Arrhenius activation model (model 2, $\lambda_{\rm vib}^{-1}$ ranging from $2 \cdot 10^{-2}$ to 10^{-1}), for a system size $L = 256$. The upper curve in (a) and (b) is obtained in absence of noise.

4.3 Competing self-fluidization and external fluidization

In this part, we investigate how the competition of self-fluidization and external fluidization affects the flow properties of soft glassy materials in a spatial elasto-plastic model. While self-fluidization is known to induce mechanical instabilities in the form of shear bands or hysteretic flow, we study how external sources of noise affect these features.

4.3.1 Shear rate profiles

Fig. 4.5 depicts profiles of shear rate in steady state averaged over a strain window of 1000, for the two models of noise. In the low noise regime (nonmonotonic flow curves) the system separates into two flowing regions (blue curves in Fig. 4.5), where the minimum and the maximum of the shear rate profile are determined by the boundaries of the stress plateau in Fig. 4.4. This is similar to the shear bands reported by Martens et al. (2012) within a mesoscale elasto-plastic model in the absence of fluidizing noise, leading to the coexistence of a flowing and an arrested region instead. In our model, the difference in shear rate between the two bands decreases as the magnitude of the noise is increased, until reaching a stable homogeneous flow regime as shown by the flat profiles (light purple curves in Fig. 4.5) corresponding to a monotonic flow curve.

The transition from a phase separated flow to a homogeneous flow can thus be characterized using the difference in shear rate between the two flowing bands. We define the order parameter of this transition as the logarithm of the ratio of shear rates in the two flowing bands:

$$\text{Order parameter} = \log\left(\frac{\dot{\gamma}_{\rm fast}}{\dot{\gamma}_{\rm slow}}\right) = S_{\rm fast} - S_{\rm slow} \tag{4.7}$$

with $S = \log(\dot{\gamma})$.

Shear banding occurs as a result of a multi-valued relation between the stress and shear rate in the material as it is the case for nonmonotonic flow curves (Olmsted, 2008). In the case of gradient banding, two different shear rates coexist for a given stress value. The selected stress value corresponds to the stress plateau value $\Sigma_{\rm p}$

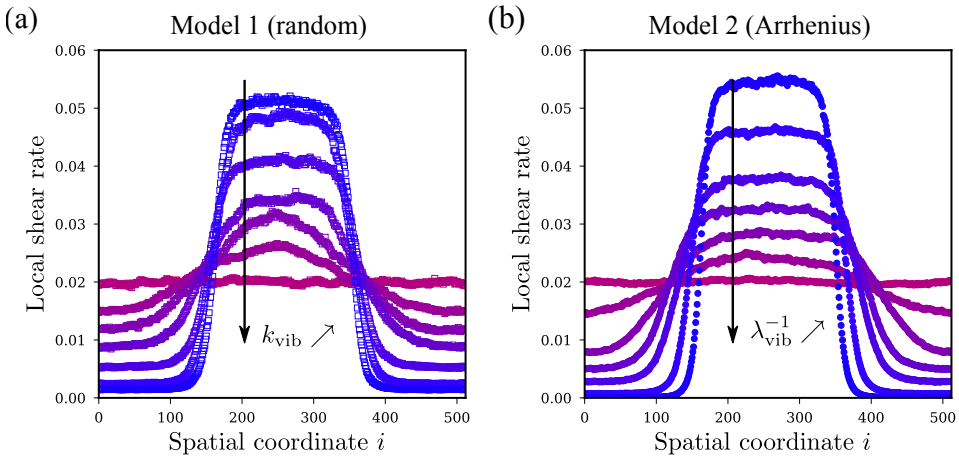

FIGURE 4.5: **Steady-state shear rate profiles** (computed over a strain window of 1000) for various values of the noise (for a system size $L = 512$) for (a) the random activation model ($k_{\rm vib}$ ranging from $3.3 \cdot 10^{-4}$ to $1.4 \cdot 10^{-3}$) and (b) for the Arrhenius activation model ($\lambda_{\rm vib}^{-1}$ ranging from $2.5 \cdot 10^{-2}$ to $5 \cdot 10^{-2}$).

.

measured using a shear-controlled protocol. When controlling the stress Σ in the system, shear banding would thus occur only if the applied stress coincides precisely with the stress-plateau value $\Sigma = \Sigma_{\rm p}$. In practice, the flow remains homogeneous in stress-controlled protocol. The extent of the plateau (and hence the order parameter defined above) can however be probed as the lower stable shear rate branch will be reached if the applied stress $\Sigma < \Sigma_{\rm p}$ and the upper shear rate branch will be reached if $\Sigma > \Sigma_{\rm p}$.

4.3.2 Metastable flow regime (model 1)

In this section, we characterize the phase coexistence regime using a stress-controlled protocol in the case of model 1. With this protocol, the shear rates within the unstable part (negative slope) of the constitutive flow curve becomes inaccessible. By varying the initial conditions for the flow, the width of this unstable region can thus be characterized, giving access to the extent of the stress plateau, as done indirectly by studying the shear rate profiles.

Protocol: We impose a stress $\sigma_{\rm ext} = \Sigma$, and examine the flow features starting from either flowing or arrested initial states. Flowing states are prepared by shearing the system at $\Sigma_{\rm prep} = 100\sigma_y$ during 50 time units, and then setting the stress to the value of interest Σ and letting the shear rate relax to its steady-state value. Arrested states are prepared by setting the initial values of local stresses σ_{ij}, activities n_{ij} and local deformations γ_{ij} to 0. Fig. 4.6(a-b) depict two examples of $S = \log(\dot{\gamma})$ as a function of time starting from either flowing or arrested states, in the hysteretic region (panel (a)) and near the transition to a monotonic flow curve (panel (b)), for strain values up to 800. We are interested in the values of S at large strain in the two flowing branches: $S_{\rm fast}$ and $S_{\rm slow}$. The value of stress Σ selected to measure $S_{\rm fast}$ and $S_{\rm slow}$ is chosen such that it is the lowest value of stress for which the fast flowing branch remains stable within the time of our simulation (corresponding to strain values $\gamma > 700$). The value of the minimum stress is determined with an accuracy of about 10^{-5} to 10^{-4} (relative error of about 10^{-4}), leading to the errorbars for S displayed in Fig. 4.6(c). This

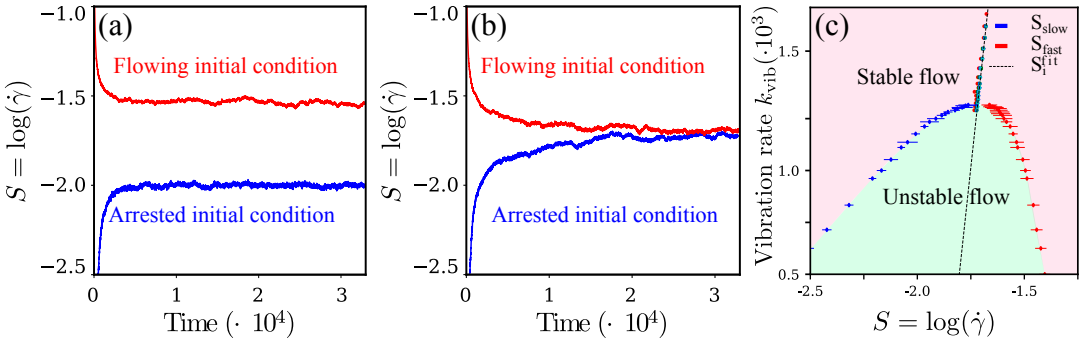

FIGURE 4.6: **Stable and hysteretic flow regimes**. (a) and (b): $S = \log(\dot{\gamma})$ as a function of time starting from either a flowing (red) or an arrested state (blue) (system size $L = 1024$): (a) Phase separated regime with $k_{\text{vib}} = 1.177 \cdot 10^{-3}$ and $\Sigma = 0.47715$ and (b) near the critical point with $k_{\text{vib}} = 1.324 \cdot 10^{-3}$ and $\Sigma = 0.47595$. (c) Stable and hysteretic flow regimes: (pink and green shaded regions respectively) determined with a stress-controlled protocol ($L = 1024$) from the limits of stability of the stable slow (blue dots) and fast (red dots) flowing branches. Black dashed line: linear fit of the inflection point of the flow curves in the stable flow regime for various system sizes.

method gives a robust measurement of the scaling of the order parameter in the phase separation regime, although it can seem somehow arbitrary because it does not give a direct access to the exact binodal or spinodal lines of the system.

Phase diagram: Using this protocol for various noise magnitudes, we report the values of S_{fast} and S_{slow} in the $(S - k_{\text{vib}})$ plane in Fig. 4.6(c), which delimit the coexistence regime in the phase diagram. The difference between the two flow solutions depicted in Fig. 4.6(c), $S_{\text{fast}} - S_{\text{slow}}$, then quantifies the ratio of shear rates $\log_{10}(\dot{\gamma}_{\text{fast}}/\dot{\gamma}_{\text{slow}})$ in the two branches. It decreases as vibration is increased, up to the point where it vanishes, consistent with the transition to a stable homogeneous flow in a shear-rate-controlled driving protocol.

This is reminiscent of equilibrium phase transitions, where the distance between the two flow solutions $S_{\text{fast}} - S_{\text{slow}}$ can be seen as the analogue of the density difference (order parameter) in the liquid-gas critical point. As a consistency check, we will see in section 4.5 that the scaling of the order parameter $S_{\text{fast}} - S_{\text{flow}}$ near the transition is independent of the protocol used.

4.4 Giant shear-rate fluctuations

We now investigate in more details the noise dominated regime corresponding to $k_{\text{vib}} > k_{\text{vib}}^c$ (model 1) or $\lambda_{\text{vib}}^{-1} > {\lambda_{\text{vib}}^c}^{-1}$ (model 2), where the flow curve is monotonously increasing, so that the homogeneous flow is stable. In this regime, using shear- or stress-controlled protocols leads to the same average rheological behavior. Interesting properties are rather to be found in shear-rate fluctuations (using a stress-controlled protocol), that we first describe qualitatively.

In Fig. 4.7, we measure the macroscopic shear rate in the system as a function of time in steady state, for two different values of k_{vib} (for model 1), choosing stress values corresponding to the inflection point of the flow curve. For large values of the noise magnitude ($k_{\text{vib}} = 5 \cdot 10^{-3}$, lower red curve in Fig. 4.7), the fluctuations of shear rate $\dot{\gamma}$ are relatively small (variations of about 10 % of the mean value for a system size

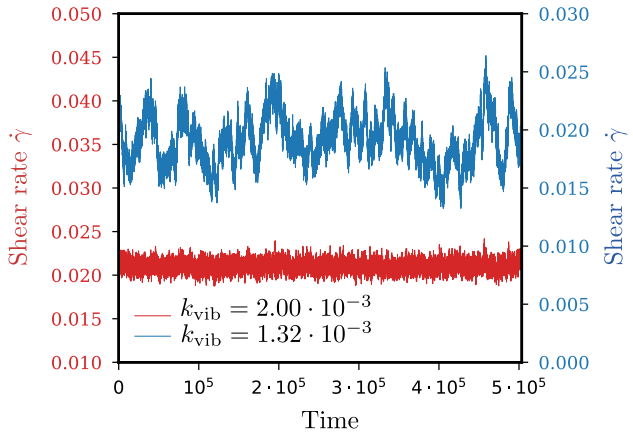

FIGURE 4.7: **Macroscopic shear rate $\dot{\gamma}$ as a function of time** for model 1 (random activation) for $k_{\mathrm{vib}} = 1.325 \cdot 10^{-3}$ (top, blue curve) and $k_{\mathrm{vib}} = 5 \cdot 10^{-3}$ (bottom, red curve) for a system size $L = 512$ (the y-axes of the two curves are shifted for readability).

$N = 512^2$) and not correlated in time. When decreasing the noise towards its value at the transition between monotonic and nonmonotonic flow curves ($k_{\mathrm{vib}} = 1.32 \cdot 10^{-3}$, see Fig. 4.4), the fluctuations of $\dot{\gamma}$ increase (50 %) and become correlated in time, as it can be seen on the upper (blue) curve of Fig. 4.7.

4.4.1 Rescaled shear-rate distributions

To perform a quantitative analysis, we compute the distributions of macroscopic shear rate in steady state for various system sizes N and noise magnitudes k_{vib}, again for a stress value corresponding to the inflection point of the flow curves. From the central limit theorem, one expects relative fluctuations of the shear rate to scale as $1/\sqrt{N}$ for large system size. Fig. 4.8 depicts the centered distributions of $\dot{\gamma}$ rescaled by $\sqrt{N}$ for different system sizes N. In this representation, curves collapse if relative fluctuations scale like $1/\sqrt{N}$. For large noise magnitudes (Fig. 4.8(a), $k_{\mathrm{vib}} = 5 \cdot 10^{-3}$), the data for all system sizes collapse onto the same curve, indicating that the shear rate fluctuations obey the central limit theorem. Unsurprisingly, the shear rate fluctuations in this regime follow a Gaussian distribution as shown by the fit in the inset of Fig. 4.8(a). As the noise magnitude is decreased (Fig. 4.8(b-d)), the rescaled distributions widen and a systematic dependence with the system size appears. This indicates a deviation from the central limit theorem at the approach of the transition, associated with growing spatial correlations of the macroscopic shear rate. Moreover, the maximum system sizes for which finite size effects are observed in Fig. 4.8 give an estimate of the correlation length ξ in the system as the noise is varied (in Fig. 4.8(b) $32 < \xi < 64$ for $k_{\mathrm{vib}} = 2 \cdot 10^{-3}$, (c) $64 < \xi < 128$ for $k_{\mathrm{vib}} = 1.35 \cdot 10^{-3}$ and (d) $\xi > 512$ for $k_{\mathrm{vib}} = 1.32 \cdot 10^{-3}$). The increase of the correlation length when decreasing the noise indicates a possibly diverging length scale in the system at the transition, which is consistent with the existence of a critical point (Wortel et al., 2016). We show in the inset of Fig. 4.8(d) that the distribution for $k_{\mathrm{vib}} = 1.32 \cdot 10^{-3}$ can be approximately collapsed by rescaling the shear rate by N^x with $x \simeq 0.275$ (instead of $1/2$ far from the transition). This shows that relative fluctuations of the shear rate decay approximately as $1/N^{0.275}$ with system size, that is, much more slowly than the standard $1/\sqrt{N}$ scaling corresponding to the central limit theorem. This slower decay of relative fluctuations with system size can be described as the presence of giant shear-rate

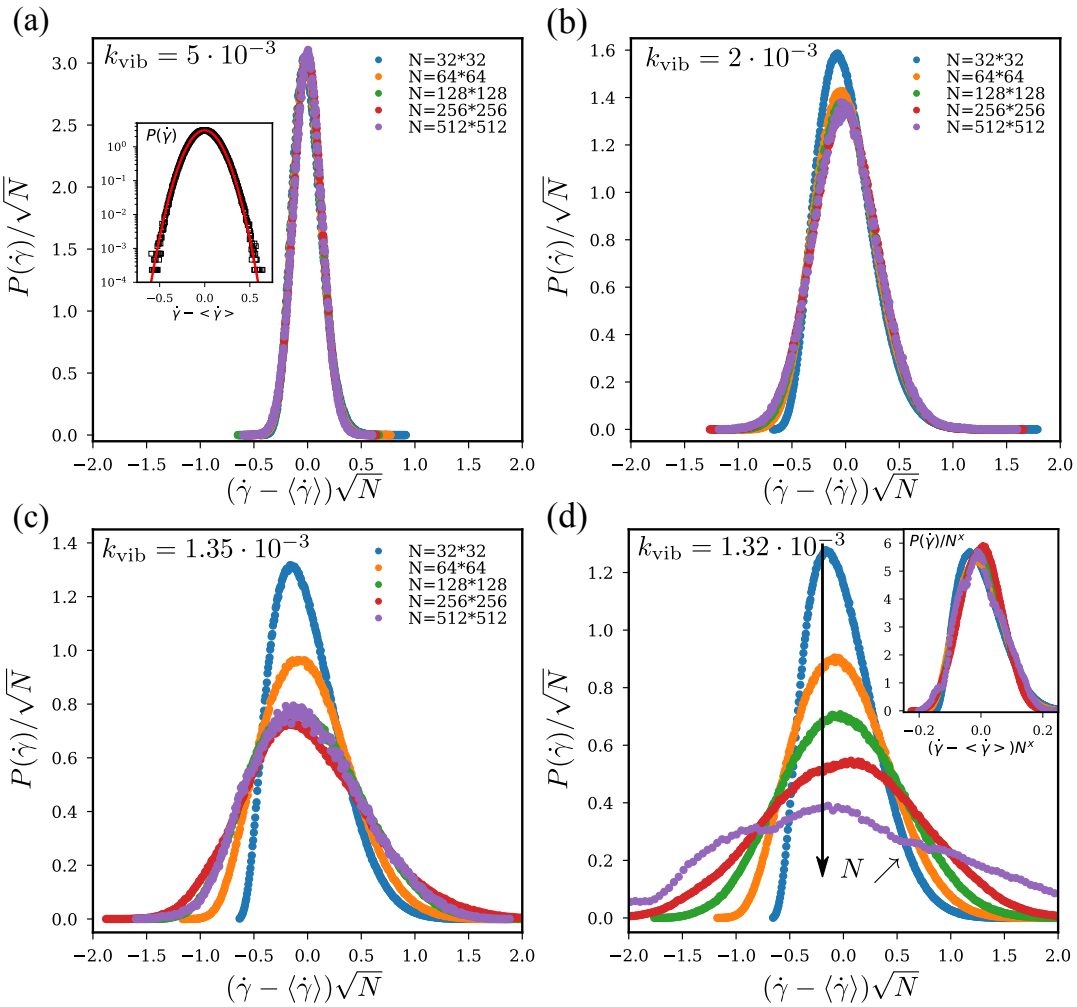

FIGURE 4.8: **Centered distributions of macroscopic shear rate** $\dot\gamma$ computed for model 1 (random activation) at the inflection point of the flow curve for various system sizes (from $L = 32$ to $L = 512$), with the x-axis rescaled by multiplying $\dot\gamma$ by the linear system size $L = \sqrt{N}$ and the y-axis by dividing $P(\dot\gamma)$ by $\sqrt{N}$, in the stable flow phase (monotonic flow curve), for decreasing values of the noise magnitude: (a) $k_{\mathrm{vib}} = 5 \cdot 10^{-3}$, (b) $k_{\mathrm{vib}} = 2 \cdot 10^{-3}$, (c) $k_{\mathrm{vib}} = 1.35 \cdot 10^{-3}$ and (d) $k_{\mathrm{vib}} = 1.32 \cdot 10^{-3}$. Inset of (a): Lin-log plot of the distribution for $L = 256$ with Gaussian fit (red). Inset of (d): Finite size data collapse of the shear rate distributions using an exponent $x = 0.275$.

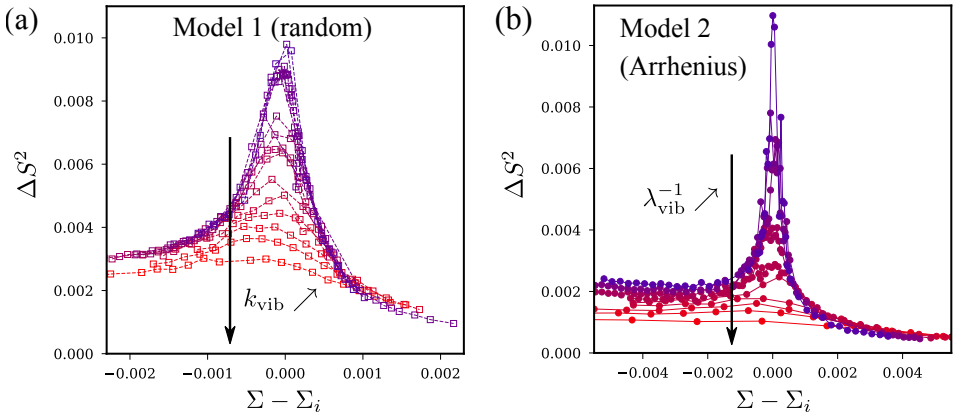

FIGURE 4.9: **Variance of $S = \log(\dot{\gamma})$, ΔS^2, as a function of the distance (in stress) to the inflection point of the flow curve**, $\Sigma - \Sigma_i$ for various noise magnitudes and for a system size $L = 128$. (a) Model 1, for values of k_{vib} ranging from $1.29 \cdot 10^{-3}$ (upper purple curve) to $1.75 \cdot 10^{-3}$ (lower red curve). (b) Model 2, for values of $\lambda_{\mathrm{vib}}^{-1}$ ranging from $5.12 \cdot 10^{-2}$ to $6.6 \cdot 10^{-1}$.

fluctuations. These giant shear-rate fluctuations are directly visible in an experimental context (work by Wortel et al. (2016)), and their characterization is thus of interest.

Note that for a linear system size L ($= \sqrt{N}$) much larger than the correlation length of the system, the standard $1/\sqrt{N}$ scaling is recovered, together with a Gaussian shape of the distribution. This crossover is visible on Fig. 4.8(b) and (c).

4.4.2 Shear-rate fluctuations varying the applied stress

Instead of looking at the dependence of fluctuations on system size, one may also look at their dependence on stress. In Fig. 4.9, we depict the variance of S as a function of the distance (in stress) to the inflection point of the flow curve for various noise magnitudes (for a single system size, $L = 128$). It can be clearly seen that the variance at the inflection point is maximal (for $\Sigma = \Sigma_i$) and increases monotonously as the noise magnitude is decreased towards its value at the transition. The same phenomenology is observed for model 2 (Fig. 4.9(b)). Enhanced fluctuations are thus observed close to the inflection point, even for a fixed, intermediate system size. A similar behavior is observed for the correlation time of the fluctuations (extracted from an exponential fit of the temporal autocorrelation data), as shown in Fig. 4.16(a). Wortel et al. (2016) report similar results in experiments on vibrated and sheared granular media, as shown in Fig. 1.12(b,d).

4.4.3 Origin of non-standard fluctuations

The emergence of fluctuations with non-trivial statistics is actually consistent with the presence of a critical point, around which the system becomes correlated over a large lengthscale. This flow transition can be characterized using the distance between the two flowing branches $S_{\mathrm{fast}} - S_{\mathrm{slow}}$ as an order parameter. The parameter controlling the noise magnitude (k_{vib} or λ_{vib}) is used as a control parameter (analogous to temperature) while the stress Σ plays the role of an external field (or pressure) in equilibrium phase transitions.

Both average quantities and fluctuations are expected to exhibit power-law scalings at the transition, so the critical point is described by a set of critical exponents, which

are supposed not to depend on details of the system, but rather only on generic properties shared by a broad class of systems. For instance, one may expect that both model 1 and model 2 share the same critical properties. This statement, though, does not rest on any firm theoretical consideration, and should be tested numerically. This is one of the goals of the next section.

The next section contains both a detailed analysis of the critical point in model 1 (random activation) and a comparison of some of the results to model 2 (Arrhenius like activation). We show that the scaling of both average quantities and fluctuations does not depend on the model of noise in the critical regime, and are also consistent with experimental values (Wortel et al., 2016). We find in particular that while some of the critical exponents resemble simple mean-field values, the exponents characterizing the divergence of correlation length and time display non-trivial values.

4.5 Generic critical point at finite shear and vibration rates

In this section, we first study the evolution of average steady-state quantities as the noise magnitude is varied in the critical regime by studying the scaling of the flow curves and of the order parameter. We then investigate the scaling of shear rate fluctuations.

In the following, the noise magnitude is designated by the relative distance to the critical point, which reads, for the two models of noise:

$$\varepsilon = \frac{k_{\text{vib}} - k^c_{\text{vib}}}{k^c_{\text{vib}}} \qquad \text{(Model 1)} \tag{4.8}$$

$$\varepsilon = \frac{\lambda^{-1}_{\text{vib}} - {\lambda^c_{\text{vib}}}^{-1}}{{\lambda^c_{\text{vib}}}^{-1}} \qquad \text{(Model 2)} \tag{4.9}$$

The stable flow (noise dominated) regime thus corresponds to $\varepsilon > 0$ and the phase separated regime to $\varepsilon < 0$. We summarise below the list of scalings expected at the transition.

In the regime $\varepsilon < 0$, the order parameter $S_{\text{fast}} - S_{\text{slow}}$ vanishes as the noise magnitude is increased towards its critical value as a power law with an exponent β:

$$S_{\text{fast}} - S_{\text{slow}} \sim |\varepsilon|^{\beta} \text{ for } \varepsilon < 0 \tag{4.10}$$

The critical point corresponds to the transition from a monotonic to a nonmonotonic flow curve, and hence the slope of the flow curve at the inflection point vanishes at the critical point. It can be interpreted as an inverse susceptibility χ, expected to scale as a power law of the distance to the critical point ε with an exponent γ:

$$\chi \sim \varepsilon^{-\gamma} \text{ for } \varepsilon > 0 \tag{4.11}$$

At the critical point ($\varepsilon = 0$), the flow curve exhibits a zero slope and S is expected to vary as a power law of the imposed shear stress (after centering the flow curve using the coordinates of the critical point (S_c, Σ_c)) with an exponent $1/\delta$:

$$|S - S_c| \sim |\Sigma - \Sigma_c|^{1/\delta} \text{ for } \varepsilon = 0 \tag{4.12}$$

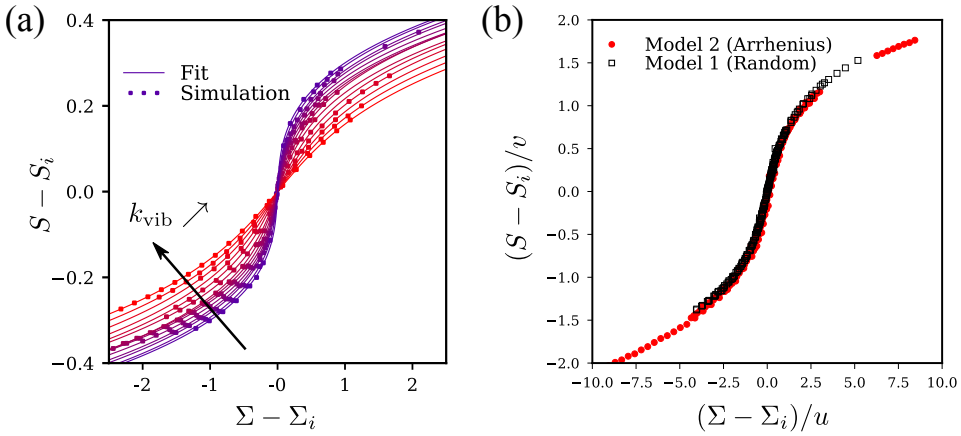

FIGURE 4.10: **Landau expansion fit in the stable flow regime**. (a) Example of data for model 1 (random activation): $S - S_i$ as a function of $\Sigma - \Sigma_i$, with S_i and Σ_i the coordinates of each flow curve inflection point. Simulation points for $L = 256$ (averaged over $\gamma > 2 \cdot 10^4$) (dots) and fits to Eq. 4.16 (solid lines). (b) Data collapse for the two models using the fitting parameters from the fit to Eq. 4.16 ($a(\varepsilon)$, $b(\varepsilon)$, $S_i(\varepsilon)$ and $\Sigma_i(\varepsilon)$) with $u = \sqrt{b/a}$ and $v = \sqrt{b^3/a}$. Data shown for a system size $L = 128$.

The variance of S diverges at the critical point when varying the imposed stress:

$$\Delta S^2 \sim |\Sigma - \Sigma_c|^{-\kappa} \text{ for } \varepsilon = 0 \tag{4.13}$$

The variance and the correlation time of S diverge as the critical point is approached from the high noise regime:

$$\Delta S^2 \sim \varepsilon^{-\gamma^*} \text{ for } \varepsilon > 0 \tag{4.14}$$

$$\tau_{\text{corr}} \sim \varepsilon^{-\mu} \text{ for } \varepsilon > 0 \tag{4.15}$$

4.5.1 Scaling of the flow curves and susceptibility

Using a stress-controlled protocol, we compute the steady-state flow curve in the stable flow regime ($\varepsilon > 0$), for the two models of fluidizing noise and investigate the scaling of the stress Σ as a function of $S = \log(\dot{\gamma})$. The data for the two models can be well fitted to a Landau type expansion in the critical regime:

$$\Sigma = \Sigma_i + a\,(S - S_i)^3 + b\,(S - S_i) \tag{4.16}$$

where a, b, S_i and Σ_i are fitting parameters shown in Fig. 4.11 for various values of ε and system sizes L. Examples of fits are shown for model 1 for a system size $L = 256$ in Fig. 4.10(a). Using the fitting parameters obtained for the two models (see (Fig. 4.11), all the data can be collapsed onto the same master curve, as shown in Fig. 4.10(b). $a(\varepsilon)$ is roughly constant (Fig. 4.11(a)). The coordinates of the inflection point ($S_i(\varepsilon)$,$\Sigma_i(\varepsilon)$) evolve monotonously as the noise is varied, and describe the analogous of the super-critical liquid-gas boundary in equilibrium phase transitions (Fig. 4.11(c-d)). The prefactor b of the linear term in Eq. (4.16), (Fig. 4.11(b)), decreases linearly as ε is increased and vanishes at the critical point. As it describes the slope of the flow curve at the inflection point, it is interpreted as the inverse susceptibility $b = 1/\chi$, which diverges at the critical point with an exponent $\gamma \simeq 1$ [Eq. (4.11)] (see Fig. 4.17). At

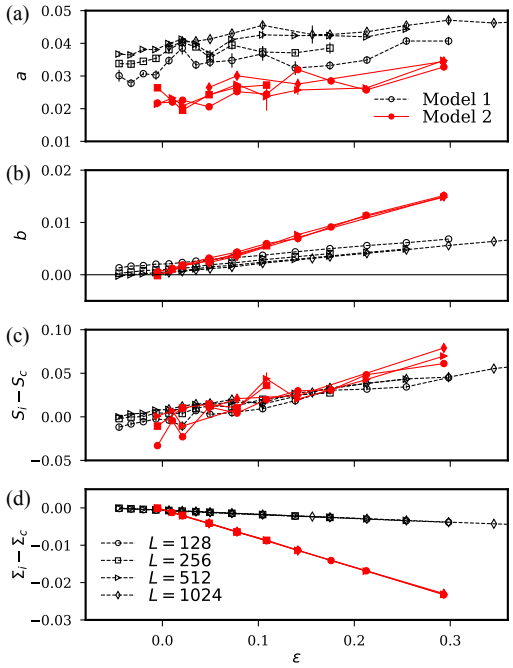

FIGURE 4.11: **Parameters from the Landau-like expansion fit** for various values of the noise ε and various system sizes L, for model 1 (black empty squares, dashed line) and model 2 (red dot, solid line). (a) Prefactor a; (b) inverse susceptibility b; (c) and (d) coordinates of the inflection point shifted by the critical point location, respectively $S_i - S_c$ (c) and $\Sigma_i - \Sigma_c$ (d).

the critical point, $b = 0$ and hence the flow curve ("critical isotherm") is well described by Eq. (4.12), with $\delta = 3$.

Critical point location

To locate the critical value of noise, we fit the data of Fig. 4.11(b) to extract the value of k^c_{vib} and λ^c_{vib} for which $b = 0$ (diverging susceptibility). While significant finite size effects are observed for model 1 (random) (and discussed in section 4.5.3), the finite size effects on the value of b remain within the error bars for model 2. We find $k^c_{\text{vib}} = (1.35 \pm 0.01)10^{-3}$ for model 1 (see section 4.5.3) and ${\lambda^c_{\text{vib}}}^{-1} = (5.1 \pm 0.2)10^{-2}$ for model 2.

4.5.2 Scaling of the order parameter

Shear-imposed protocol

In Fig. 4.12(a), we investigate the scaling of the order parameter $S_{\text{fast}} - S_{\text{slow}}$ extracted from the shear rate profiles (Fig. 4.5) at the approach of the transition, in the regime $\varepsilon < 0$. The order parameter decreases as ε is decreased, and scales as a power law of the distance to the critical point (fit of the form $S_{\text{fast}} - S_{\text{slow}} = A|\varepsilon|^{\beta}$). In the fit of Fig. 4.12(a), $\varepsilon = (k_{\text{vib}} - k^c_{\text{vib}})/k^c_{\text{vib}}$ for model 1, $\varepsilon = (\lambda_{\text{vib}} - \lambda^c_{\text{vib}})/\lambda^c_{\text{vib}}$ for model 2 and k^c_{vib}, λ^c_{vib}, β and A are free fitting parameters. We get $\beta_1 = 0.58 \pm 0.07$ (model 1) and $\beta_2 = 0.49 \pm 0.04$ (model 2), with $k^c_{\text{vib}} = (1.21 \pm 0.05) \cdot 10^{-3}$ and $({\lambda^c_{\text{vib}}}^{-1} = 4.95 \pm 0.05) \cdot 10^{-2}$. For the two models, the critical exponent β is close to 0.5, which is consistent with the Landau-type scaling in the regime $\varepsilon > 0$.

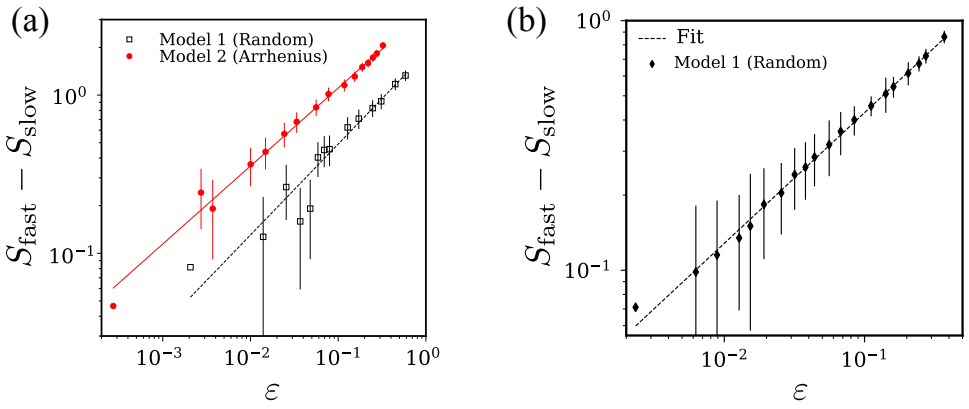

FIGURE 4.12: **Order parameter $S_{\rm fast} - S_{\rm slow}$ as a function of the scaled distance to the critical noise magnitude** ε, $\lambda^c_{\rm vib}$ and $k^c_{\rm vib}$ being fitting parameters of the fit $S_{\rm fast} - S_{\rm slow} = A|\varepsilon|^\beta$ (see text). (a) From shear rate profiles data, Model 1: lower black square symbols (with dashed line fit). Model 2: Upper solid circles (with solid line fit). Error bars are estimated from the standard deviation of S in the bands. (b) From stress-controlled protocol data for model 1.

The critical noise magnitudes ($k^c_{\rm vib}$, ${\lambda^c_{\rm vib}}^{-1}$) obtained from the fit for a system size $L = 512$, although they are not far from the previous estimate, are slightly underestimated. In fact, extracting the order parameter from the flow profiles is a difficult task near the critical point, as the coarsening time of the shear bands increases (and is expected to diverge for $\varepsilon = 0$). As a consequence, we cannot access steady-state profiles in the critical regime. The configurations associated with the closest data points to the critical point in Fig. 4.12 are not coarsened yet, thus leading to large error bars and possibly explaining the slight underestimate of ΔS and hence an underestimate of the critical noise magnitudes.

Stress-imposed protocol (model 1)

Using the stress-controlled protocol described in section 4.3.2 (to get the phase diagram), we also examine the scaling of the order parameter $S_{\rm fast} - S_{\rm slow}$ with the distance to the critical point, by performing a power-law fit of the form: $S_{\rm fast} - S_{\rm slow}(L) = A((k^c_{\rm vib}(L) - k_{\rm vib})/k^c_{\rm vib}(L))^\beta$.

In Fig. 4.12(b), we find a good agreement with a power law with the following parameters for $L = 1024$: $k^c_{\rm vib}(L) = (1.324 \pm 0.005)10^{-3}$, $A = 1.43 \pm 0.03$ and $\beta = 0.52 \pm 0.02$. Note that the value of $k^c_{\rm vib}(L)$ is consistent with the value obtained from the divergence of the susceptibility ($1/\chi = b(k_{\rm vib}) = 0$) in Fig. 4.13(b) (where we had, for $L = 1024$, $k^c_{\rm vib}(L) = (1.33 \pm 0.02)10^{-3}$).

4.5.3 Finite size effects

In Fig. 4.8, we evidenced the existence of finite size effects on the distributions of macroscopic shear rate. In this section, we study in detail these finite size effects in the case of model 1 (random activation). Let us recall that at the critical point, the correlation length of the system diverges as:

$$\zeta \sim \varepsilon^{-\nu} \text{ for } \varepsilon > 0 \tag{4.17}$$

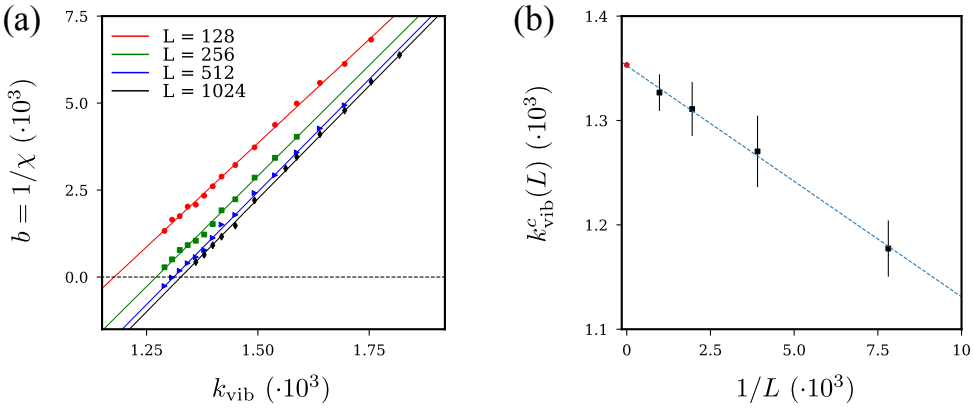

FIGURE 4.13: **Susceptibility and critical point location.** (a) Inverse susceptibility b as a function of $k_{\rm vib}$ for $L = 128, 256, 512, 1024$ and linear fits to estimate $k^c_{\rm vib}(L)$ for which $b(k^c_{\rm vib}, L) = 0$. (b) $k^c_{\rm vib}(L)$ as a function of L^{-1} and linear extrapolation (dashed line) to get $k^c_{\rm vib}(\infty)$ (red dot)

We first study how the transition point in model 1 (as determined from susceptibility measurements) is shifted when changing the system size, which provides a first estimate of the critical exponent ν. We then confirm this scaling by performing direct measurements of correlations in the system. We finally test this exponent by performing finite size data collapse of the susceptibility data for the two models, and find a good agreement of the two models with $\nu \simeq 1$.

Finite size shift of the transition (model 1)

To get the critical random activation rate $k^c_{\rm vib}$, we estimate the value of $k_{\rm vib}$ corresponding to a diverging susceptibility χ, or equivalently, $b(k_{\rm vib}) = 1/\chi(k_{\rm vib}) = 0$. In Fig. 4.13(a), we show linear fits of $b(k_{\rm vib})$ for system sizes up to $L = 1024$, from which we extract the values $k^c_{\rm vib}(L)$ corresponding to $b(k_{\rm vib}) = 0$ depicted in Fig. 4.13(b). By performing a linear extrapolation of $k^c_{\rm vib}(L)$, we get the critical value in the limit of an infinite system size (red dot in Fig. 4.13(b)), leading to $k^c_{\rm vib} = (1.35 \pm 0.01)10^{-3}$. The linear scaling of the transition shift in Fig. 4.13(b) suggests that the value of the exponent ν related to the correlation length ξ should be close to 1, as one would expect a scaling for the shift of the critical rate of the form $|k^c_{\rm vib}(L) - k^c_{\rm vib}(\infty)| \sim L^{-1/\nu}$ (see for instance Binder et al. (2010)).

Correlation length measurements (model 1)

In order to determine how spatial correlations evolve in the system as $k_{\rm vib}$ is varied, we compute the squared modulus of the Fourier transform of the instantaneous local shear rate configuration, averaged over at least 10^4 configurations, $\tilde{C}(q)$. $\tilde{C}(q)$ is depicted in Fig. 4.14 for various values of $k_{\rm vib}$. Note that the data look noisier as approaching $k^c_{\rm vib}$, due to growing time correlations in the system near the critical point, i.e., due to finite-time limitations of our simulations. In the vicinity of the critical point, we expect a scaling of the form $\tilde{C}(q) \sim q^\alpha$ (see for instance Le Bellac (1992)). We estimate the value of α from data where $k_{\rm vib} \simeq k^c_{\rm vib}$ (thick solid line in Fig. 4.14(a)) and find $\alpha \simeq 0.75$. We show, in Fig. 4.14(b), $\tilde{C}(q)q^\alpha$ as a function of $q\xi$, with $\xi = \left((k_{\rm vib} - k^c_{\rm vib})/k^c_{\rm vib}\right)^{-\nu}$. The best collapses are found for $\nu = 0.95 \pm 0.05$, consistent with the linear scaling of Fig. 4.13(b).

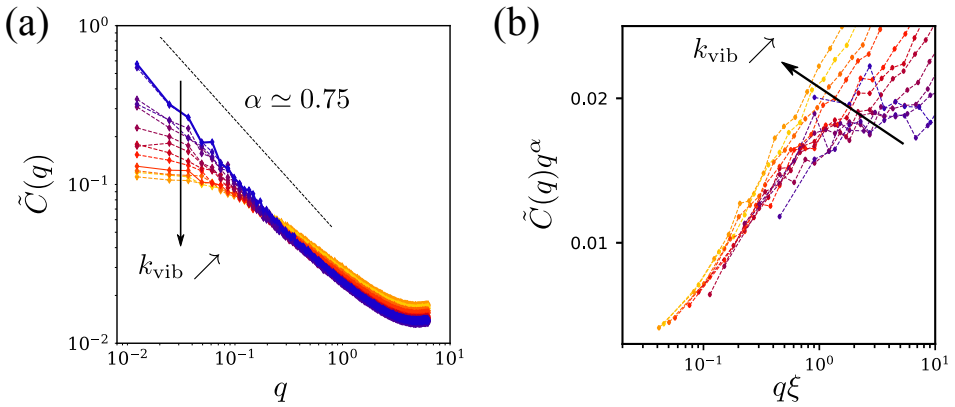

FIGURE 4.14: **Spatial correlations**: (a) Fourier transform of the autocorrelation of local shear rate $\tilde{C}(q)$ as a function of q for a system size $L = 1024$ and various values of $k_{\rm vib}$ ranging from $k^c_{\rm vib} = 1.35 \cdot 10^{-3}$ (solid blue line) to $k_{\rm vib} = 1.81 \cdot 10^{-3}$ (yellow dashed line) (b) Same data normalized by a power-law dependence $\tilde{C}(q)q^{\alpha}$ as a function of $q\xi$ with $\xi = \left((k_{\rm vib} - k^c_{\rm vib})/k^c_{\rm vib}\right)^{\nu}$ with $\nu = 0.95$ enabling data collapse for small values of q.

Finite size data collapse for the two models

Using $\nu = 1$, we show in Fig. 4.17(a) the data for the susceptibility $\chi = 1/b$ rescaled by a factor $L^{-\gamma/\nu}$ as a function of the scaled distance to the critical point $\varepsilon L^{1/\nu}$. ε is expressed using the above value $k^c_{\rm vib} = (1.35 \pm 0.01)10^{-3}$ and refining the value of ${\lambda^c_{\rm vib}}^{-1}$ to get the best data collapse (${\lambda^c_{\rm vib}}^{-1} = 5.15 \cdot 10^{-2}$). The ability to collapse the data for all system sizes for the two models of noise suggests that they share similar critical exponents for the susceptibility and the correlation length ($\gamma \simeq 1$ and $\nu \simeq 1$).

In the next section, we will also see that using this value of ν enables us to perform finite size data collapse for the fluctuations data for the two models of noise.

4.5.4 Scaling of fluctuations

In equilibrium systems, fluctuations are related to average quantities like the susceptibility, and at a critical point, the divergences of both quantities are related. In this part we study the evolution of the fluctuations of S when varying the imposed stress and the noise magnitude in the critical regime.

Varying the imposed stress in the critical regime:

As shown in Fig. 4.9, the variance of the order parameter increases as the stress approaches its value at the inflection point of the flow curve, where it is maximal. In Fig. 4.15, we report, in a log-log plot, for the value of the noise closest to the critical point ($\varepsilon \simeq 0$), the value of the variance of S as a function of the distance to the inflection point, for various system sizes. Let us point out that the scattering of data near the maximum is due to finite size effects, where the smallest values correspond to the smallest systems. We find that the variance of S varies as a power law of the distance to the critical stress, with exponents $\kappa_1 = 0.82 \pm 0.12$ (model 1) and $\kappa_2 = 0.73 \pm 0.15$ (model 2), that do not depend significantly on the noise model. From the Landau fit of Eq. (4.16), the susceptibility ($\chi = \partial S/\partial \Sigma$ for $\varepsilon = 0$) varies as $(|\Sigma - \Sigma_c|^{2/3})$, which is within the error bars of our estimate of κ.

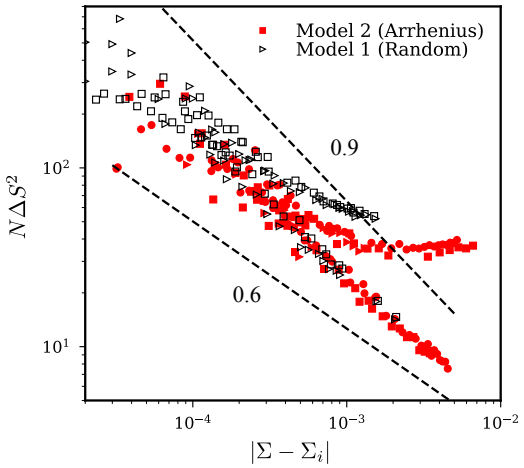

FIGURE 4.15: **Variance of S multiplied by the number of sites, $N\Delta S^2$ as a function of $|\Sigma - \Sigma_i|$** for values of the noise magnitude close to the critical value ($\varepsilon \simeq 0$). Data for model 1 (black empty data points) and model 2 (red solid points) and various system sizes (circles: $L = 128$, squares: $L = 256$, triangles: $L = 512$). Dashed lines: power-law guides to the eye with exponents 0.6 and 0.9.

While the extent of the power law spans two decades in the "shear dominated" regime (for $\Sigma > \Sigma_i$, lower data points in Fig. 4.15(c)), the range is reduced in the "noise dominated" regime ($\Sigma < \Sigma_i$, upper data points in Fig. 4.15(c)). This asymmetry is likely to be due to the different origins of mechanical noise in these two regimes, where it arises mainly due to activated events in the "noise dominated" regime.

Temporal autocorrelation To extract the correlation time τ_{corr}, we fit the autocorrelation function $C(\tau) = \langle \Delta S(t+\tau)\Delta S(t) \rangle$ to an exponential and extract the characteristic time τ_{corr} from the fit. We report in Fig. 4.16(a) the correlation time as a function of the distance (in stress) to the inflection point of the flow curve for various values of λ_{vib} (model 2), which exhibits a sharp peak at the critical point. We report in a log-log plot the correlation time as a function of the absolute distance to the inflection point $|\Sigma - \Sigma_i|$, for a noise magnitude close to the critical point ($\varepsilon \simeq 0$), for the two models of noise. Although the data is more noisy than for the variance of the fluctuations (Fig. 4.15), we can see there is a power-law scaling of the correlation time as well, with an exponent close to that of the variance.

Varying the noise magnitude ε:

We now investigate the scaling of fluctuations at the inflection point of the flow curve ($\Sigma = \Sigma_i$) when varying the noise magnitude ε. We compute the variance of the fluctuations and extract their correlation time from an exponential fit of the autocorrelation of S. A finite size data collapse is performed using $\nu = 1$. We find, for the two models of noise, a power law increase of both the variance (Fig. 4.17(b)) and the correlation time (Fig. 4.17(c)) of the fluctuations when approaching the critical point, with the exponents $\gamma^* \simeq 0.9$ and $\mu \simeq 1$ respectively.

Let us now discuss the scaling of shear rate distributions depicted in Fig. 4.8(d) in the light of the critical exponents estimated in this section. In Fig. 4.8(d), the shear rate distributions at the transition could be approximately collapsed by rescaling the shear rate with a factor N^x ($N = L^2$) and the best collapse was found with an

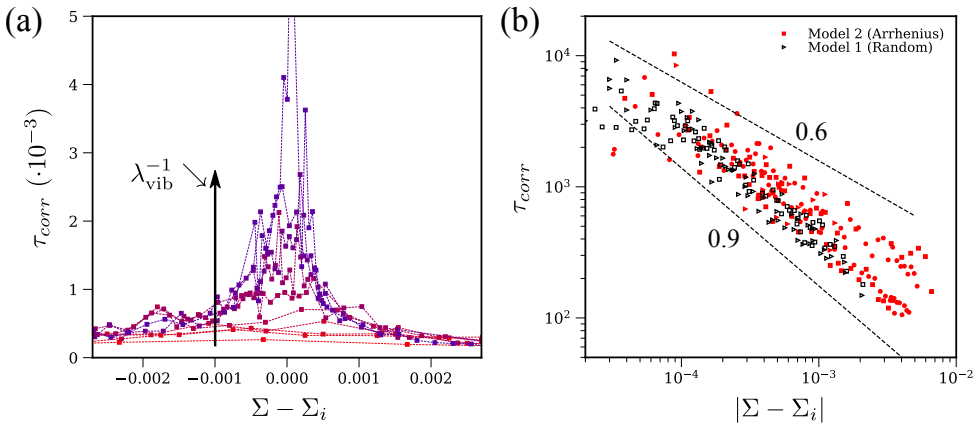

FIGURE 4.16: **Correlation time of shear rate fluctuations.** (a) Auto-correlation timescale τ_{corr} as a function of $\Sigma - \Sigma_i$ for various values of noise magnitude λ_{vib} (model 2). (b) Log-log plot of the correlation time τ_{corr} as a function of $|\Sigma - \Sigma_c|$ for $\varepsilon \simeq 0$ ("critical isotherm") for the two models of noise.

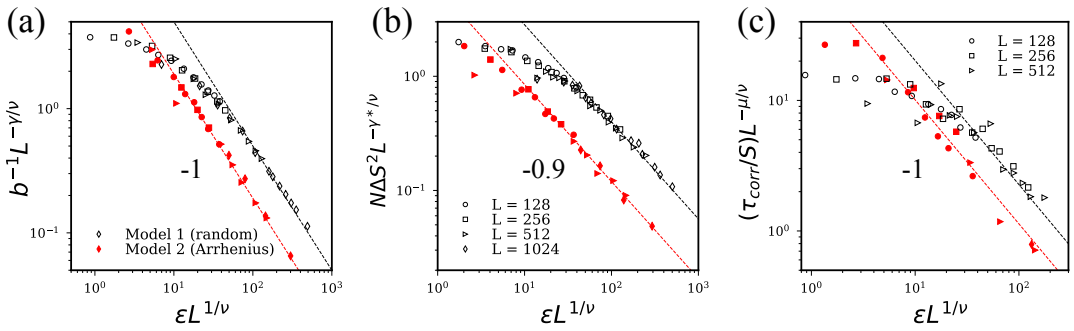

FIGURE 4.17: **Critical scaling of the susceptibility and fluctuations** (a) Susceptibility $\chi = 1/b$ rescaled by $L^{-\gamma/\nu}$ as a function of the scaled distance to the critical point $\varepsilon L^{1/\nu}$ for model 1 (unfilled black symbols) and model 2 (solid red symbols). (b) Rescaled variance ΔS^2 vs. $\varepsilon L^{1/\nu}$. (c) Rescaled correlation time vs. $\varepsilon L^{1/\nu}$

exponent $x = 0.275$. In other words, the width of the distribution of shear rate scales as: $\Delta\dot{\gamma} \sim L^{-2x} \sim L^{-0.55}$. For sufficiently small fluctuations of the shear rate, the fluctuations of $S = \log(\dot{\gamma})$, ΔS, correspond approximately to relative fluctuations of $\dot{\gamma}$, $\Delta\dot{\gamma}/\dot{\gamma}_c$, with $\dot{\gamma}_c$ the critical shear rate (approximately independent of system size, see Appendix C). Hence similar scalings for ΔS and $\Delta\dot{\gamma}$ with the system size would be expected. From the data collapse of Fig. 4.8(d), the scaling for the shear rate variance is $L^2\Delta\dot{\gamma}^2 \sim L^{0.9}$. This is consistent with the scaling of Fig. 4.17(b), where data collapse for the variance of S suggests a scaling form: $L^2\Delta S^2 \sim L^{\gamma^*/\nu}$, with $\gamma^*/\nu = 0.9$.

Note that, due to finite time limitations of our simulations in the critical regime, the data for the correlation time of the fluctuations (Fig. 4.17(c)) is restricted to intermediate system sizes ($L \leq 512$) and exhibit strong scattering (see Fig. 4.16(a)). An approximate collapse can still be performed with an exponent $\mu = 1.0 \pm 0.2$ and seems to be independent of the model of noise. This value would correspond to a dynamic scaling exponent $z = \mu/\nu \approx 1$, far from the equilibrium mean-field value $z = 2$ obtained for non-conserved scalar order parameters (Hohenberg et al., 1977).

4.6 Discussion

In this chapter, we studied the effect of a fluidizing noise on the rheology of soft glassy materials using a mesoscale elasto-plastic modeling approach.

We consider two distinct models of fluidizing noise, both leading to a transition between a self-fluidized regime and an externally fluidized regime in the flow of soft glassy materials. Upon an increase of the external noise amplitude, we evidence the vanishing of shear bands (shear imposed protocol) and the transition from a metastable to a stable flow regime near the inflection point of the flow curve (stress-imposed protocol). This is an indication of a transition from an unstable shear-localized flow to a stable homogeneous flow with the noise magnitude as a control parameter. We also find that a decrease of the fluidizing noise amplitude in the homogeneous flow regime yields increasingly large and long lived fluctuations of the macroscopically measurable shear rate.

These findings can be rationalized in the context of out-of equilibrium phase transitions, in which the transition between the flow regimes described above is associated with a critical point. This critical point is characterized by the scaling exponents summarized in Table 4.1. While the rheology at low stress differs between the two models (and can be rationalized with simple theoretical arguments), we find a generic scaling of the flow curves in the critical regime, that is well fitted by a Landau-type expansion, as found by Wortel et al. (2016). The scaling of the order parameter (power law scaling with an exponent $\beta \simeq 0.5$), as determined either from the flow profiles in the phase coexistence regime or from the boundaries of the metastable regime using a stress-controlled protocol, is consistent with the scaling of the flow curves in the stable flow regime. We also find power law scalings of the susceptibility and the shear rate fluctuations, with exponents being independent of the model of noise. The critical exponent of the susceptibility, obtained from an average quantity S ($\gamma \simeq 1$) is close to that of the fluctuations ΔS^2 ($\gamma^* \simeq 0.9$) but not identical. This may be due to the fact that fluctuations were slightly underestimated in our analysis (because one could not access exactly the inflection point of the flow curve, where the fluctuations are maximal). Note that the values of some critical exponents (β, γ, γ^*), indicate that the scaling of average quantities is close to a standard mean-field scaling for equilibrium phase transitions, as observed by Wortel et al. (2016). However, the scaling of correlations departs from standard exponent values (Le Bellac, 1992; Hohenberg et al., 1977) (even with long-range interactions, see Appendix C.2) and are consistent with experimental values (Wortel et al., 2016). To summarize, the finite shear-rate critical point studied here in two minimal elasto-plastic models suggests that a generic critical behavior arises in systems combining a nonmonotonic flow curve with a fluidization process, irrespective of the detailed physical mechanisms at play. The out-of-equilibrium character of the transition leads to non-trivial scalings.

The existence of such critical point at finite shear rate can have important consequences in the study of the flow of soft glassy materials in the presence of an additional source of noise. In this scenario, a single trajectory of the system can strongly differ from its average behavior as given by the constitutive flow curve, thus leading to several difficulties for experimental characterizations of the flow behavior. Since the correlation time of the fluctuations becomes increasingly large at the transition point, averaging values in the steady state becomes tedious and care has to be taken in the data interpretation. This is a situation where conventional continuum descriptions of the flow tend to break down and call for more sophisticated modeling approaches that allow for incorporating the spatio-temporal features of the fluctuations in the

Scaling relation	Exponent	Model 1	Model 2	Wortel et al.	Mean field
$\Sigma - \Sigma_c \sim (S - S_c)^\delta$	δ	3	3	3	3
$\xi \sim \varepsilon^{-\nu}$	ν	1.0 ± 0.1	-	-	0.5
$\Delta S \sim \varepsilon^\beta$	β	0.52 ± 0.02	0.49 ± 0.04	0.5	0.5
$\chi \sim \varepsilon^{-\gamma}$	γ	1.0 ± 0.05	1.0 ± 0.05	1	1
$\Delta S^2 \sim \varepsilon^{-\gamma^*}$	γ^*	0.9 ± 0.05	0.9 ± 0.05	1	1
$\tau_{\text{corr}} \sim \varepsilon^{-\mu}$	μ	1.0 ± 0.2	1.0 ± 0.2	$[0.5; 1]$	0.5
$\Delta S^2 \sim \lvert\Sigma - \Sigma_c\rvert^{-\kappa}$	κ	0.82 ± 0.12	0.73 ± 0.15	-	2/3
$\tau_{\text{corr}} \sim \lvert\Sigma - \Sigma_c\rvert^{-\kappa *}$	$\kappa *$	0.75 ± 0.2	0.75 ± 0.2	-	2/3

TABLE 4.1: **Critical exponents measured in our model**, compared with the values obtained by Wortel et al. (2016) and with standard equilibrium Ising mean-field values for the static exponents, and with model A of critical dynamics for the dynamic exponent μ.

rheologically relevant quantities. Another important message regarding experimental and numerical studies is that, when using shear-imposed protocols, the flow can be heterogeneous due to the nonmonotonicity of the constitutive flow curve. In the vicinity of the transition, the time for the shear bands to coarsen becomes increasingly large, and the steady state of the system may be out of reach on any experimentally relevant timescale.

We discussed the consequences of competing self-fluidization and external fluidization mechanisms on the rheology of soft glassy materials and in the following we would like to suggest situations where this phenomenon might be of importance. As shown experimentally, this transition can easily arise in frictional granular materials (Wortel et al., 2016). But one could also speculate about other systems where such mechanisms could be at play. The minimal ingredients for the emergence of this critical point in systems sheared at a finite strain rate are: (i) a microscopic mechanism at the origin of self-fluidization (such as an intrinsic timescale for restructuration in the material (Coussot et al., 2010)), and (ii) a source of mechanical noise independent of the flow. An example for a class of materials, that provides naturally various sources of additional mechanical noise with a fluidization effect, are dense active systems, such as biological tissues (Matoz-Fernandez et al., 2017a; Mandal et al., 2016; Tjhung et al., 2017). Depending on the details of microscopic interactions, self-fluidization could arise from a competition between intrinsic timescales in the system and shear; hence such systems would be good candidates for the emergence of critical dynamics accompanied by giant fluctuations as described in this work.

In this chapter, we considered phenomenological models for the (rate-independent) mechanical noise, simply assuming that some source of noise could activate additional plastic events contributing to the flow. In active systems, various types of activity could contribute to this mechanical noise, such as cell division and apoptosis, self-propulsion, shape or volume fluctuations, etc. The mechanism by which additional sources of mechanical noise arise is related to the disturbance of stress and strain fields by these local active events.

In the following chapter, we will explicitly consider local active events such as volume or shape fluctuations and study how they affect the dynamics and the rheology of the system, using both microscopic models and elasto-plastic modeling. In the case of a (local) driving of active origin and not due to an externally imposed shear, a tensorial description of the amorphous materials is required since there is no preferred orientation for the plastic rearrangements of particles. Let us first discuss

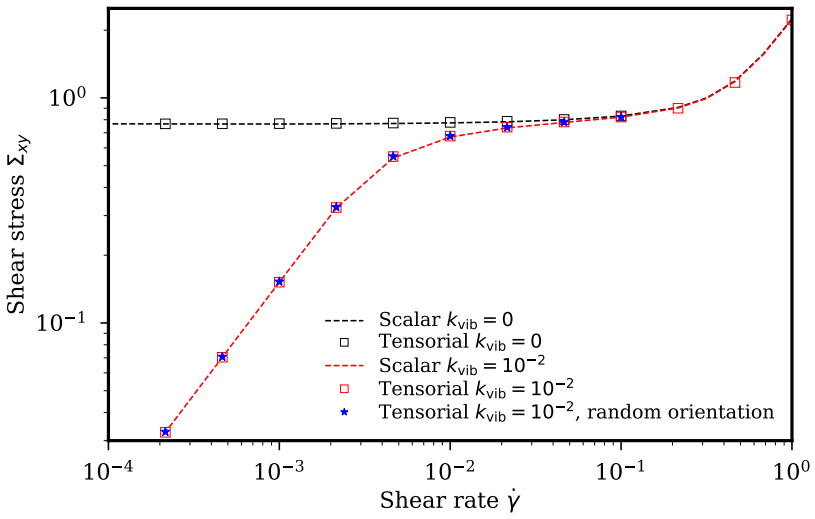

FIGURE 4.18: **Fluidization in scalar and tensorial elasto-plastic models**. Flow curves in the absence (black) and presence of an external noise (red) with $k_{\text{vib}} = 10^{-2}$ for a scalar version of the elasto-plastic model (dashed line), a tensorial version (square symbols) and for a tensorial version with a random orientation of the events activated by the external noise (blue star symbols).

how the fluidization discussed in this chapter is affected by a tensorial description of the medium and by the orientation of the plastic rearrangements induced by the external noise.

Scalar versus tensorial description of the fluidization

In this work, we considered a simplified scalar model to study the role of an external source of noise on the rheology. In the experiment of Wortel et al. (2016) however, the driving due to shear and to the external vibrations have different geometries (orthoradial flow with a velocity gradient along the radial direction and vertical mechanical vibrations). We now discuss how the direction of the plastic events induced by an external noise may affect the rheology in the elasto-plastic model.

We consider (i) the scalar model considered in this chapter, (ii) a tensorial model with the direction of noise-activated events determined by the relative components of the stress tensor and (iii) a tensorial model with events activated in a random direction. The tensorial implementation of the model is discussed in Chapter 2.

We show the flow curves obtained for these models in Fig. 4.18. We find that the rheology is only slightly affected by the tensoriality of the model (as shown by Nicolas et al. (2014b)) and by the orientation of the randomly activated events. These findings indicate that the fluidization is mainly explained by the stress relaxation induced by the additional plastic events, and that correlations between events play only a little role in this regime. This also supports the hypothesis of neglecting the internal mechanical noise in the "noise dominated" regime, as we did in order to compute the low shear rate rheological behavior in this regime.

Although the correlations between events seem to play a negligible role in the fluidized regime, a further study in the critical regime would be required to conclude on how the tensoriality and the orientation of plastic events impact the critical features

of the model. In this regime, important spatial correlations develop in the system and may be affected by the details of spatial interactions.

Chapter 5

Building an active elasto-plastic model

Résumé : Construction d'un modèle élasto-plastique actif

La dynamique de systèmes actifs denses tels que les tissus biologiques résulte de processus actifs à l'échelle des particules, comme l'autopropulsion des cellules, la division cellulaire, la mort ou extrusion des cellules, ou encore la déformation (active) des cellules. Ces processus, pouvant être responsables de la fluidisation du tissu, ont été principalement étudiés dans des modèles microscopiques (simulations de particules) (Mandal et al., 2016; Tjhung et al., 2017; Matoz-Fernandez et al., 2017b) ou dans des modèles continus (Ranft et al., 2010).

Dans ce chapitre, nous proposons de construire un modèle spatial élasto-plastique à l'échelle mésoscopique pour modéliser la dynamique d'un système dense de particules se déformant sous la forme d'oscillations de leur rayon, tel qu'étudié par Tjhung et al. (2017). Dans cette étude, Tjhung et al. (2017) considèrent un système dense de particules molles (en 2d) dont le rayon oscille périodiquement avec une amplitude d'oscillation a au cours du temps et avec un déphasage tel qu'il n'y a pas d'oscillation macroscopique du volume du système. Ils mettent en évidence une transition entre un état solide pour de faibles amplitudes d'oscillations ($a < a_c$) et un état fluide pour $a > a_c$ dans lequel le déplacement des particules au cours du temps suit un comportement diffusif. La dynamique du système change de façon abrupte lorsque $a = a_c$, suggérant une transition discontinue entre ces deux états. Tjhung et al. (2017) proposent par ailleurs que cette transition est analogue à la transition de mise en écoulement observée dans les verres soumis à un cisaillement oscillatoire macroscopique (voir Chapitre 1, section 1.2). Lorsque la dynamique du rayon ne suit pas des oscillations périodiques mais un processus stochastique de type Ornstein-Uhlenbeck, la transition devient alors continue et ressemble à une transition vitreuse pour $a \to 0$.

Pour construire notre modèle élasto-plastique actif, nous caractérisons tout d'abord la réponse élastique d'un système dense de particules à la variation de rayon d'une seule particule à l'aide de simulations microscopiques. La caractérisation de ce propagateur élastique permet de construire un modèle mésoscopique où le forçage résulte de particules actives, qui, en se déformant, redistribuent de la contrainte au reste du système. Notre modèle élasto-plastique est basé sur le scénario suivant : des sites actifs se déforment de façon périodique en propageant de la contrainte au reste du système. Lorsque la contrainte locale totale dépasse une valeur seuil locale, alors le site devient plastique, relaxe localement de la contrainte, et redistribue de la contrainte au reste du système via un propagateur élastique de type Eshelby.

Des simulations de ce modèle élasto-plastique permettent de mettre en évidence une transition entre un état stationnaire fluide et un état arrêté (sans activité plastique) pour une valeur finie de l'amplitude de déformation, tel que décrit par Tjhung

et al. (2017). La dynamique pour atteindre l'état stationnaire au voisinage de la transition est très lente, et il est difficile de déterminer la nature de la transition d'après les données de plasticité moyenne ou les trajectoires de particules traceurs. Cette dynamique lente pour la plasticité est accompagnée d'une déplétion progressive des petites barrières dans la distribution de barrières d'énergie locales à franchir pour produire un évènement plastique et dont la valeur moyenne augmente avec le nombre de cycle aux abords de la transition. Ce phénomène rappelle les effets observés dans les verres soumis à un cisaillement oscillatoire où de petites amplitudes de déformation contribuent à augmenter la stabilité du verre ("mechanical annealing" en anglais) (Leishangthem et al., 2017).

Un autre point commun avec les verres cisaillés suivant un protocole oscillatoire concerne la contrainte macroscopique, qui présente un dépassement ("overshoot") pour une valeur critique de l'amplitude d'oscillation a_c, ce qui constitue une signature de transition discontinue.

Nous montrons par ailleurs que la coopérativité entre évènements plastiques est maximale une fois le dépassement de contrainte franchi, avec une organisation spatiale pouvant indiquer une forme de localisation dans un système actif. A la différence des verres cisaillés où la localisation se fait sous formes de bandes dues à la symétrie imposée par le forçage macroscopique, nous observons ici des groupes de sites plastiques coexistant avec des groupes de sites immobiles.

Pour résumer, ces premiers résultats concernant le modèle élasto-plastique actif semblent suggérer une transition de fluidisation discontinue lorsque la dynamique de déformation est sinusoïdale, similaire aux observations faites dans les simulations de particules. Dans le cas où la dynamique de la déformation active est simplement décrite par un processus stochastique (bruit corrélé en temps), alors la transition devient continue et se produit dans la limite $a \to 0$, sans aucune forme de localisation de la plasticité, comme observé par Tjhung et al. (2017).

Nous étudions dans une dernière partie la rhéologie du système. Nous montrons que pour $a < a_c$, le comportement rhéologique est celui d'un fluide à seuil dont la contrainte seuil (dynamique) dépend de a. Au contraire, pour $a > a_c$, la contrainte seuil disparait et on observe un comportement fluide. Pour de grandes valeurs de a, la rhéologie à faible taux de cisaillement devient linéaire. Ces résultats sont en bon accord qualitatif avec les simulations du modèle de particules.

Le chapitre est organisé de la façon suivante : dans la section 5.1.1, nous rappelons certains résultats de la littérature concernant (i) l'étude de systèmes de particules se déformant en se dilatant ou se contractant ainsi que (ii) la théorie de l'élasticité linéaire décrivant la réponse à une inclusion ponctuelle se contractant ou se dilatant dans un milieu élastique homogène. Dans la section 5.2, nous décrivons le modèle de particules introduit par Tjhung et al. (2017) que nous utilisons ensuite pour caractériser la réponse à une particule se déformant activement dans un milieu constitué de particules passives. Nous construisons ensuite notre modèle élasto-plastique actif dans la section 5.3. Les résultats numériques obtenus avec le modèle mésoscopique concernant la transition de fluidisation sont exposés dans la section 5.4, et les aspects de rhéologie sont étudiés dans la section 5.5.

Introduction

The dynamics of dense active systems such as biological tissues results from distinct active processes at the microscopic scale, which can lead to rich collective behaviors. Active cellular-scale processes include for instance self-propulsion of particles, cell

division, cell death or extrusion, active cell deformation, etc. All these processes influence the large scale dynamics and the fluidization of the material (Ranft et al., 2010; Mandal et al., 2016; Bi et al., 2016; Tjhung et al., 2017; Matoz-Fernandez et al., 2017b; Czajkowski et al., 2019; Tjhung et al., 2020; Krajnc et al., 2018). The mechanisms by which biological activity fluidizes a dense system are not yet fully understood, and the link between the microscopic dynamics and the large scale behaviors remains an open question.

Continuum mechanical models have been built to relate cellular scale events and the mechanics of biological tissues. Etournay et al. (2015) developed a theoretical model accounting for the deformation induced by individual events in a tissue (cell rearrangements, cell division, cell deformation) and for the forces exerted on the tissue, able to capture the total tissue scale deformation during morphogenesis of the *Drosophila* pupal wing. Ranft et al. (2010) studied the fluidization induced by cell division and cell death by describing the source stress due to cell division and apoptosis in a tissue described as an elastic medium. As a main result, they find that cell division and apoptosis lead to a dynamic reorganization of the elastic tissue, leading to a liquid-like relaxation at long time, with a viscosity depending upon the rate of division. The role of cell division and apoptosis was further investigated by Matoz-Fernandez et al. (2017a) using particle-based simulations, and it was shown to lead to a fluidization (Newtonian regime) at shear rates small compared to the apoptosis rate, and to a shear-thinning behavior at larger shear rates. These findings were rationalized using a mean-field elasto-plastic model (Hébraud-Lequeux model with an external noise). This study provides an example of description of an active system as a yield stress fluid with an additional source of noise.

In the recent years, there has been an increasing interest in drawing analogies between the dynamics of dense amorphous systems where the dynamics is enabled by thermal fluctuations or by external driving forces (e.g., shear) and the dynamics of dense active systems, where the dynamics results from particle-scale active processes (Bi et al., 2014; Tjhung et al., 2017; Tjhung et al., 2020; Mandal et al., 2020a; Morse et al., 2020; Henkes et al., 2020). Although this question can be very difficult to tackle experimentally, a lot of effort has been made in understanding the effect of different sources of activity in microscopic simulations (see Chapter 1 for a review of the literature). It has been shown that biological activity can induce various types of fluidization transitions (from an arrested or glassy state to a fluid-like state), but the nature of this transition may strongly differ depending on the type of activity and the parameter range considered. In particular, active volume fluctuations, cell division and death events as well as (infinitely persistent) self-propulsion have been proposed to act as local shear forces in the material (Tjhung et al., 2017; Tjhung et al., 2020; Morse et al., 2020), opening the route to extend tools from the sheared amorphous systems community to the study of active systems. Among the different sources of activity in epithelial tissues, fluctuations of the cell volume have been shown to occur periodically and to induce large scale velocity fields in the system (Zehnder et al., 2015b; Zehnder et al., 2015a). This type of activity has been studied numerically by Tjhung et al. (2017) in a minimal particle-based model accounting for periodic oscillations of the particle radius. In this work, the authors have proposed an analogy between the solid-to-fluid transition induced by actively (and periodically) deforming particles and the yielding transition of amorphous materials subjected to an oscillatory shear protocol.

Elasto-Plastic Models (EPMs) have enabled a qualitative understanding of many features of the dynamics of sheared amorphous materials (Nicolas et al., 2018a), including, very recently, under quasi-static oscillatory shear (Liu et al., 2020b). In

this chapter, we propose to build a mesoscale EPM for a system of actively deforming particles to further study the analogy with driven systems proposed by Tjhung et al. (2017). This could constitute a first step towards the development of active elasto-plastic models accounting for more complex types of biological activity (e.g., self-propulsion, cell division and death).

Our aim is to model local active deformation as stress sources in an elastic medium, as done by Ranft et al. (2010) in the context of cell division and death. In our active elasto-plastic model (AEPM), the local driving is implemented under the form of the elastic response to point-like isotropically deforming particles (so called "breathing particles" in the following), as predicted by linear elasticity and measured from molecular simulations. Simulations of our elasto-plastic model suggest the existence of a discontinuous fluidization transition between an arrested state and a fluid-like state, as reported by Tjhung et al. (2017). We discuss similarities and differences with the case of sheared glasses with an oscillatory shear protocol. We then study how changing the dynamics of active deformation affects the transition and study the response to an applied shear.

The chapter is organized as follows: in section 5.1.1, we present a quick review of the state of the art regarding the role of volume fluctuations in dense assemblies of cells or particles as well as the response to dilating or contracting point-defects in elastic media. In section 5.2, we introduce the microscopic model first proposed by Tjhung et al. (2017). We recall their results regarding the solid-to-fluid transition and study the response to a single actively deforming particle. In section 5.3, we propose a mesoscale EPM to describe such an active system, based on the response to a single contracting/dilating event and numerically study this model in section 5.4 (fluidization transition) and 5.5 (rheology).

5.1 Contracting or dilating inclusions in disordered passive and active systems

In this section, we first present some results from the literature regarding the effect of deforming particles in disordered materials (granular materials, biological tissues, numerical models of amorphous materials) and then compute the elastic response to a point-like contracting (or dilating) particle.

5.1.1 Breathing particles in the literature

Deforming cells in biological tissues

Zehnder et al. (2015a) have evidenced fluctuations of the cell volume in epithelial tissues, as illustrated in Fig. 5.1(a). They find that cell volumes oscillate with a timescale of 4h and an amplitude of 20%, with the timescale and amplitude of oscillations depending on the cytoskeletal activity. They also find groups of cells fluctuating together in time, giving rise to regions of low and high cell number density (Fig. 5.1(b)). These volume fluctuations are thought to play an important role in epithelial dynamics since they influence cell motion inside the epithelial layer by inducing divergent velocity fields (Zehnder et al., 2015b) (Fig. 5.1(c)). The mechanisms for such volume fluctuations have not been fully elucidated yet but seem to involve water transport between cells (Zehnder et al., 2015a).

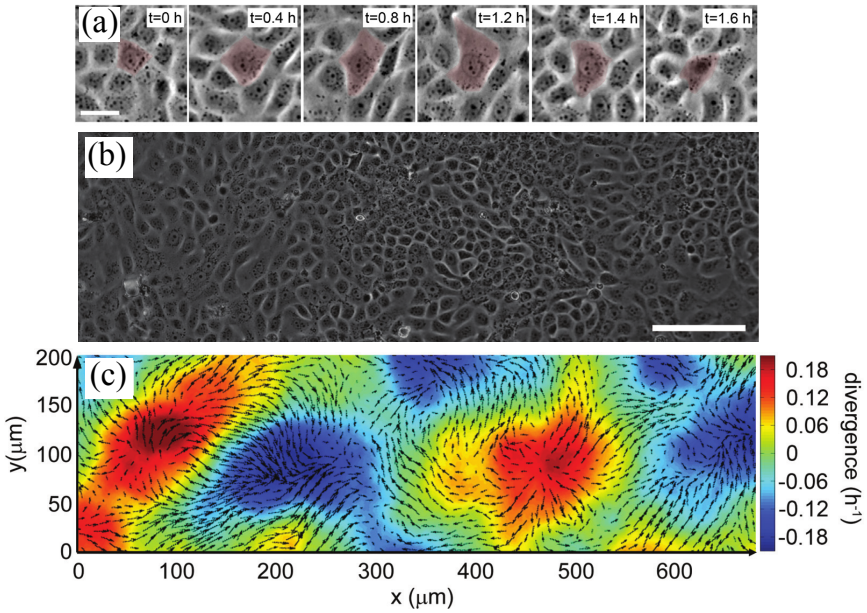

FIGURE 5.1: **From Zehnder et al. (2015a) and Zehnder et al. (2015b): Cell volume fluctuations in an epithelial monolayer**. (a) Example of a single cell fluctuating by $\sim 200\%$ relative to its minimum area. (b) Epithelial monolayer exhibiting large variations in projected cell area (scale bar: 150 mm).(c) Velocity fields of cell motion superimposed on top of divergence fields show coherent patterns of spreading (positive) and contracting (negative) regions spanning hundreds of microns.

.

Inflated particles in granular experiments and soft disks simulations

The response to a dilating particle in a dense disordered assembly of particles was studied experimentally in granular media by Coulais et al. (2014) and in numerical simulations of harmonic disks by Ellenbroek et al. (2009). The purpose of these studies was mainly to study the dynamics of amorphous systems near the jamming transition.

Coulais et al. (2014) induce a shear by inflating an intruder in the center of a monolayer of bidisperse frictional grains. They find that linear elasticity does not generally apply, mainly due to dilatancy effects and shear softening. They also find that elasticity is effectively recovered only for strains larger than a critical strain which depends on the distance to jamming.

The applicability of linear elasticity near the jamming transition has also been discussed in details by Ellenbroek et al. (2009) in a study of disordered packing of soft frictionless particles. They find that by averaging the stress response over a large number of realizations, linear elastic responses can be fitted. In single packings however, a lengthscale ℓ^* is identified as the length up to which the response is dominated by local disorder. This lengthscale diverges at the jamming transition and the elasticity breaks down. The authors also show that this lengthscale corresponds to the coarse-graining scale needed to obtain a smooth stress response tensor in a single globally deformed packing.

Concluding remarks

The response of a disordered medium to locally contracting or dilating particles has been considered in the context of the jamming transition as a test of the applicability of

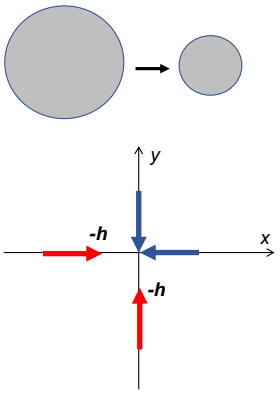

FIGURE 5.2: **Schematic of two force dipoles to model a dilating or contracting inclusion**

.

linear elasticity. Linear elasticity is found to apply in average for soft particles systems above jamming (Ellenbroek et al., 2009), although dilatancy effects may dominate in hard frictional particles systems (Coulais et al., 2014). Let us mention that beside the studies mentioned above, studies of the deformation induced by crystal defects such as interstitial or vacancies have also evidenced a good agreement with the elastic response to local point-like contracting or dilating inclusions (Lechner et al., 2009). Let us now present a possible linear elasticity computation of the response to a point-like contracting particle.

5.1.2 Point-force model of dilating inclusion

In Chapter 2, we discussed the response of an elastic medium to a local shear transformation, as studied by Eshelby (1957). The case of local contracting or dilating inclusions was also discussed by Eshelby (1954), to account for instance for dilation induced by local heating in crystals. We recall here the results of linear elasticity regarding the response of a homogeneous isotropic medium to a local isotropic deformation. We follow the approach of Lechner et al. (2009), who use a point-defect model to describe the contraction or dilation of an inclusion in a linear elastic medium.

The dilation (or contraction) of the active particle is modeled by two orthogonal pairs of forces. Each pair consists of two forces of equal magnitude f_0 but opposite directions acting at two points separated by a distance h, as illustrated in figure 5.2. Such a pair of force exerts no net force on the material. We assume that one force pair acts in the x-direction and the other one in the y-direction and that the defect is centered at the origin. The total force density is given by:

$$\vec{f}(\vec{r}) = -f_0\delta(\vec{r})\vec{e_x} + f_0\delta(\vec{r} - h\vec{e_x})\vec{e_x} - f_0\delta(\vec{r})\vec{e_y} + f_0\delta(\vec{r} - h\vec{e_y})\vec{e_y} \tag{5.1}$$

where $\vec{e_x}$ and $\vec{e_x}$ are unit vectors in the x- and y-direction and $\delta(\vec{r})$ is the delta Dirac function in two dimensions. By taking the limit $h \to 0$ (ensuring that $f_0 \to \infty$ so $f_0 h$ remains finite), we get:

$$\vec{f}(\vec{r}) = -f_0 h\vec{\nabla}\delta(\vec{r}) \tag{5.2}$$

The Navier equation describing the static state of a material reads

$$(\lambda + \mu)\vec{\nabla}(\vec{\nabla} \cdot \vec{u}) + \mu\Delta\vec{u} = -\vec{f} \tag{5.3}$$

Taking the divergence on both sides of the above equation and using the expression for $\vec{f}$ yields

$$\Delta(\lambda + 2\mu)(\vec{\nabla} \cdot \vec{u}) = Fh\Delta\delta(\vec{r}) \tag{5.4}$$

To find the displacement field obeying the above equation, one can then write the displacement field as deriving from a scalar potential ϕ: $\vec{u} = \vec{\nabla}\phi$ (see e.g., Lechner et al. (2009) for a detailed derivation). This is analogous to the Poisson equation for a punctual charge in electrostatics. A possible solution of the equation $\Delta K = \delta(r)$ is $K(r) = \log(r)/2\pi$ thus leading to : $\phi(\vec{r}) = \alpha \log(\vec{r})$ with $\alpha = \frac{Fh}{(\lambda+2\mu)}$ (for a vanishing displacement field at infinity). We finally get for an isotropic response for the displacement field:

$$\vec{u}(\vec{r}) = \alpha \frac{\vec{r}}{r^2} \tag{5.5}$$

We re-write the two components of the displacement field in polar coordinates (r, θ):

$$u_x(r,\theta) = \alpha \frac{\cos\theta}{r} \quad , \quad u_y(r,\theta) = \alpha \frac{\sin\theta}{r} \tag{5.6}$$

The stress field in response to a dilating inclusion then reads:

$$\sigma_{ij} = 2\mu\varepsilon_{ij} = \mu\left(\frac{\partial u_i}{\partial x_j} + \frac{\partial u_j}{\partial x_i}\right) \tag{5.7}$$

And we get for the two shear components:

$$\sigma_{xy}(r,\theta) = -\alpha\mu\frac{\sin 2\theta}{r^2} \quad , \quad \frac{\sigma_{xx} - \sigma_{yy}}{2}(r,\theta) = -\alpha\mu\frac{\cos 2\theta}{r^2} \tag{5.8}$$

while the pressure response is null: $-\frac{\sigma_{xx}+\sigma_{yy}}{2}(r,\theta) = 0$. The linear elastic stress response to a dilating inclusion is depicted in Fig. 5.6(b,d,f). In the next section, we will compare the displacement and stress fields induced by a single deforming particle in soft disks simulations to the response computed using linear elasticity theory.

5.2 Microscopic model for breathing-like particles

We consider in this section a slightly modified version of the model introduced by Tjhung et al. (2017), who considered a dense assembly of athermal particles interacting via a repulsive potential, among which some (or all) of the particles are active, i.e., they change size periodically. We first present the model, then recall the results of Tjhung et al. (2017) regarding the fluidization transition induced by activity when all the particles are active (Fig. 5.3) and last we study the response of the medium to a single actively deforming particle.

5.2.1 Particle-based model

We consider a two-dimensional system of N athermal particles modeled as disks in a squared box of linear dimension L, with periodic boundary conditions. The dynamics of the ith disk is described by the position of its center $\vec{x}_i(t)$. The dynamics is governed by the equation:

$$m\ddot{\vec{x}}_i = -\gamma\dot{\vec{x}} + \sum_{i\neq j}^{N} \vec{f}_{ij} \tag{5.9}$$

with m the mass of the particle, γ a friction coefficient and $\vec{f}_{ij}$ the (conservative) force deriving from an interaction potential: $\vec{f}_{ij} = -\frac{\partial V(r_{ij})}{\partial \vec{x}_j}$. Here, we consider a binary mixture of particles with average diameters σ_0 and $0.71\sigma_0$ with 40:60 proportion to avoid crystallization. We use σ_0 as unit length.

We have considered two types of repulsive interaction potentials, depicted in Fig. D.1. We consider a truncated and shifted Lennard-Jones interaction potential as in Chapter 3 to study the response to single breathing particles: $V(r_{ij}) = 4\varepsilon\left[(\sigma_{ij}/r_{ij})^{12} - (\sigma_{ij}/r_{ij})^{6}\right] + \varepsilon$ if $r_{ij} < r_c$ (with a cutoff $r_c = 2^{1/6}$ to have a purely repulsive potential) and $V(r_{ij}) = 0$ if $r_{ij} > r_c$. where $r_{ij} = |\vec{x}_i - \vec{x}_j|$ and $\sigma_{ij} = (\sigma_i + \sigma_j)/2$ and $\varepsilon = 1$ the energy scale of the potential. We also consider, as Tjhung et al. (2017), a short-ranged repulsive harmonic potential to study the fluidization transition: $V(r_{ij}) = \epsilon/2(1 - r_{ij}/\sigma_{ij})^2\Theta(\sigma_{ij} - r_{ij})$.

The particle radius $r_i(t)$ also has its own dynamics. Tjhung et al. (2017) have considered several types of dynamics such as periodic deformation or random fluctuations. In the case of oscillatory deformation, the radius dynamics is described by:

$$r_i(t) = r_i^0(1 + a\sin(\omega t + \psi_i)) \tag{5.10}$$

where r_i^0 is the radius of the passive particle, a is the amplitude and ϕ_i the phase of the active deformation. The phase of each particle is shifted by an amount $\psi_i = i\frac{2\pi}{N}$, in order to maintain a constant volume fraction throughout the simulation.[1]

Numerical implementation and simulations

This model is implemented by modifying the LAMMPS source code (Plimpton, 1995) to account for the dynamics of the particle radii in time. This was done in collaboration with P. Chaudhuri, S. Ghosh and V. Vasisht within the Indo-French CEFIPRA collaboration project.

We generate configurations of the system by randomly placing the centers of the N particles in a squared box of area L^2 (where the value of L is chosen depending upon the volume fraction) and setting the initial velocity to zero for all the particles. We then run a few thousand simulations timesteps at finite temperature without any activity before minimizing the energy of the system using a FIRE algorithm.

We then turn on the breathing activity (for all or only a fraction of particles). The above dynamics is solved using Langevin dynamics at zero temperature, using either a truncated and shifted Lennard-Jones potential or a harmonic potential (the type of potential will be specified in the following), where the conservative force is computed using the dynamically evolving particle radius. Unlike Tjhung et al. (2017), we do not consider a strictly overdamped dynamics but set $m/\gamma = 1$ in LAMMPS simulations to be in the damping regime where viscous effects are comparable to inertial effects.

5.2.2 Discontinuous fluidization transition

Discontinuous fluidization

We show in Fig. 5.3 numerical results obtained by Tjhung et al. (2017) using overdamped simulations and a harmonic interaction potential between particles that deform periodically with a fixed frequency (with a period $T = 820\tau_0$, τ_0 being the dissipation timescale). In Fig. 5.3(a), snapshots of particle configurations are depicted during one cycle at $t = 0$, $t = T/2$ and $t = T$. The trajectory of the highlighted

[1] The compensation of volume changes in order to preserve the volume fraction of the system is possible in groups made of at least four particles.

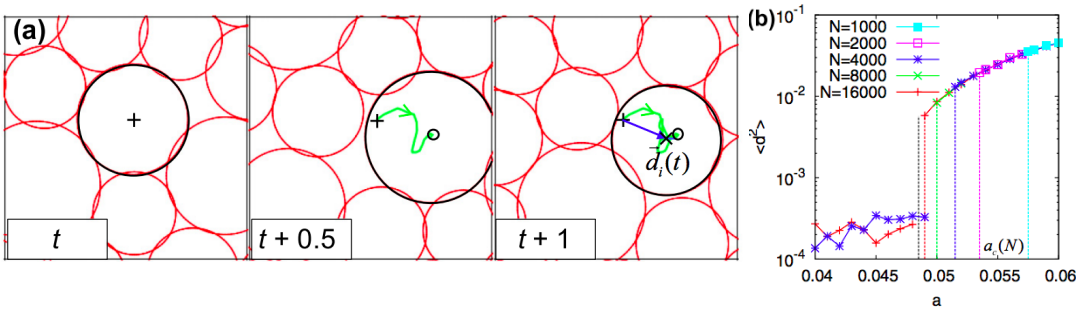

FIGURE 5.3: **From Tjhung et al. (2017): Fluidization transition in a system of actively deforming particles**. (a) Snapshots of a system during one-cycle of deformation, at $t = 0$, $t = T/2$ and $t = T$, with $T = 1$, the period of oscillation. The trajectory of the particle center is depicted in green and the total displacement during the cycle is depicted by the blue line. (b) Mean squared one cycle displacement as a function of the radius oscillation amplitude a exhibiting a sharp transition between an arrested or slow state and a fluid-like state for different system sizes.

particle during one cycle is depicted in green, and the total displacement undergone by the center of the particle $\vec{d}_i(t) = \vec{r}_i(t+T) - \vec{r}_i(t)$ is depicted in blue.

The average one-cycle squared displacement is depicted in Fig. 5.3(a) as a function of the amplitude of the periodic active driving a. The authors evidence a sharp transition between an arrested solid-like state where the particles remain essentially localized and a fluid-like state where particle displacements are large. The different symbols correspond to different system sizes, thus evidencing finite-size effects at the transition. The discontinuous character of the transition is also confirmed by hysteresis effects. They further show in their study that particle trajectories in the fluid-like phase are diffusive.

Diffusive behavior in the fluid phase

We reproduce similar results using our LAMMPS-based simulation code with a harmonic interaction potential (work done in collaboration with S. Ghosh and P. Chaudhuri, IMSC Chennai, India). We show for instance in Fig. 5.4 the mean squared displacement of particles as a function of time, which displays a sharp transition between an arrested state (with oscillations of the MSD) and a long-time diffusive behavior for $a \simeq 0.50$ (for a system size $N = 16000$), consistent with the results of Tjhung et al. (2017) (although no detailed analysis to localize the transition was performed).

5.2.3 Response to a single breathing particle

We now study the response of the system to a single actively deforming particle, using the above defined model with a truncated and shifted Lennard-Jones interaction potential. We choose a single particle in the system whose radius deforms following Eq. 5.10. We measure the displacement field and the stress field change in response to a small change in radius ΔR_0.

Protocol

We generate configurations and prepare the system as described above. We turn on the breathing activity for a single particle in the system and let the system evolve for

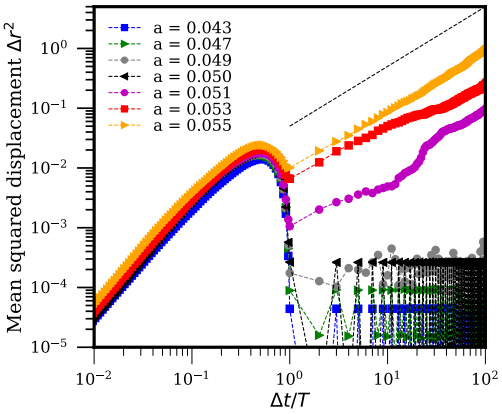

FIGURE 5.4: **Mean squared displacement of actively deforming particles**. Δr^2 as a function of $\Delta t/T$, T being the period of oscillation. The dashed line indicates a diffusive behavior $\Delta r^2 \propto \Delta t$ (simulations performed by S. Ghosh and P. Chaudhuri within our CEFIPRA collaboration).

5×10^4 LAMMPS time steps, which corresponds to half a period of oscillation and output configurations every 500 time-steps. We choose the values of volume fraction (ϕ comprised between 0.85 and 1.25 in 2d), amplitude (a between 0.05 and 0.3) and frequency ($f = 10^{-2}$) in order to ensure that the response of the system remains essentially elastic. In practice, with this choice of parameters, plastic rearrangements induced by the deformation of the active particle are rare, and the configurations with plastic activity (that can be spotted through abrupt changes in the stress or energy of the system and by looking at the displacement maps (see Fig. 5.5(b))) are removed from our analysis.

We compute the difference in displacement and stress between two consecutive configurations (spaced by a time interval $\Delta t = 500$ time-steps) corresponding to a radius change of the active particle of about $\Delta R = 7 \times 10^{-4}$ or a deformation of $\varepsilon_{\text{act}} \simeq 0.00035$. We compute the change in the three components of the stress tensor (2d system): σ_{xy}, σ_{xx} and σ_{yy}, using the "compute stress/atom" command in LAMMPS which returns both a contribution from the potential (Virial stress) as well as a kinetic energy contribution (Subramaniyan et al., 2008). The stress and displacement fields are then coarse-grained in squared boxes of area $d\ell \times d\ell$ using $d\ell = 1.5$.

Displacement field

An example of displacement between two configurations of the system spaced by a time interval Δt (with a radius increment of the central dilating particle of 7×10^{-4}) is shown in Fig. 5.5(a). The displacement of particles is most clearly visible in the vicinity of the breathing particle and decays away from the active particle. The resulting displacement field is however highly anisotropic, and we do not observe the isotropic response expected from linear elasticity when looking at a single realization. In Fig. 5.5(b), we show an example where a plastic rearrangement has been triggered in the vicinity of the actively deforming particle due to the active driving. We recognize the Eshelby-like quadrupolar response (see in Introduction, Fig. 1.18(a) for a response averaged over 50 plastic events).

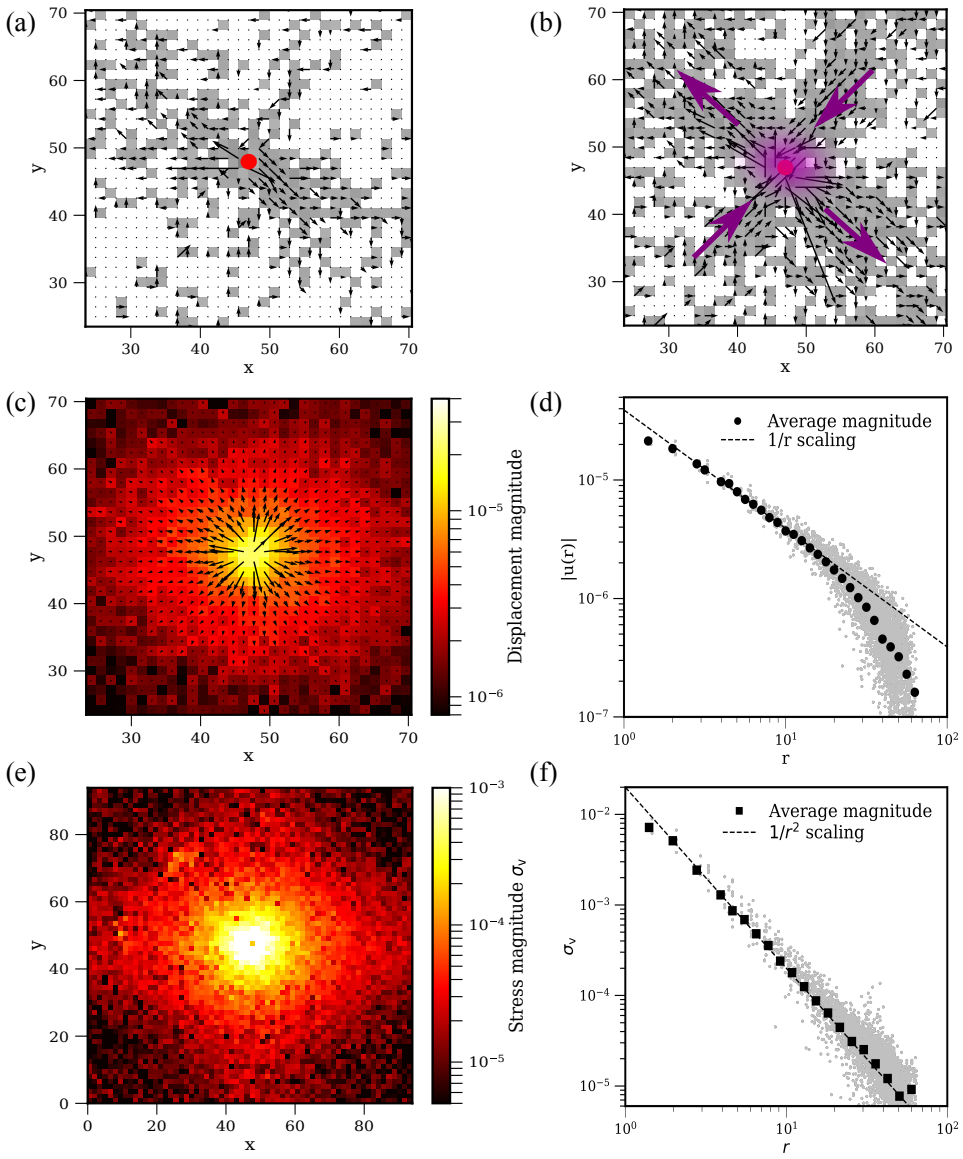

FIGURE 5.5: **Displacement and stress fields in response to a single actively deforming particle in particle-based simulations** (the displacement vectors are up-scaled for visualization purpose). (a) Example of displacement field in response to a single dilating particle (red dot) located in the center of the system. (b) Example of configuration where a plastic rearrangement of particles is induced by the active driving in the vicinity of the actively deforming particle (red dot), as it can be seen from the Eshelby-like quadrupolar response. (c) Elastic displacement field in response to a single dilating particle located in the center of the system averaged over 500 realizations. (d) Displacement magnitude averaged over the angle as a function of the distance to the active particle r following a power law decay $|u(r)| \sim 1/r$. (e) Von Mises stress map $\sigma_v = \sqrt{\sigma_{xy}^2 + (\sigma_{xx} - \sigma_{yy})^2/4}$. (f) Von Mises stress averaged over the angle as a function of the distance to the active particle r following a power law decay $\sigma_v \sim 1/r^2$.

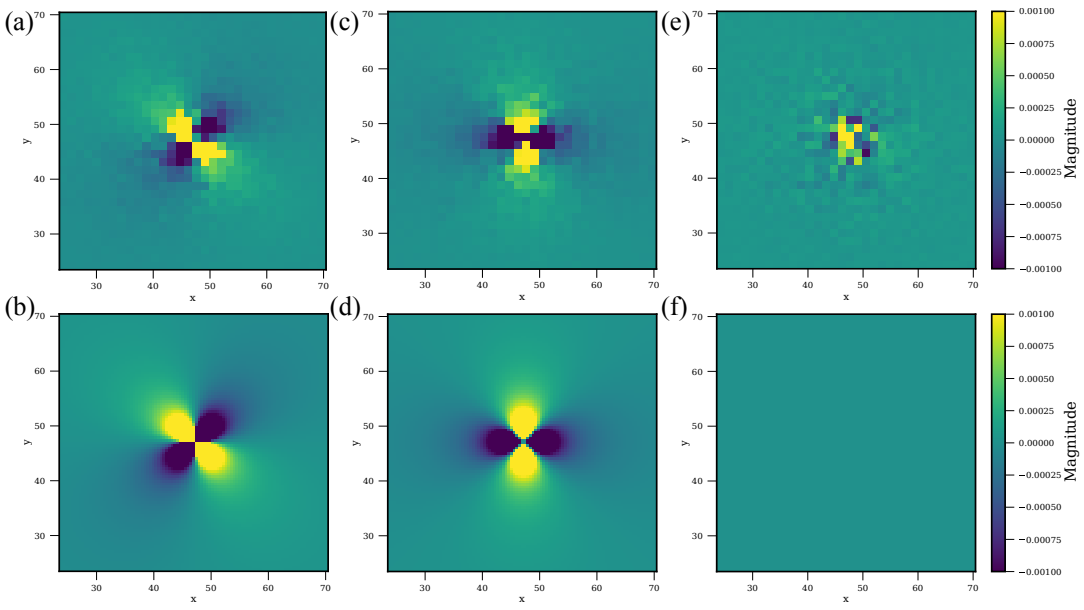

FIGURE 5.6: **Stress response to a dilating inclusion: microscopic simulations (top row) and linear elasticity (bottom row).** (a) and (b) σ_{xy}, (c) and (d) $(\sigma_{xx} - \sigma_{yy})/2$, (e) and (f) $p = -(\sigma_{xx} + \sigma_{yy})/2$. Results from microscopic simulations (with $\phi = 1.15$ and $a = 0.15$) are obtained by averaging over 1000 realizations.

.

We show in Fig. 5.5(c) the displacement field in response to a dilating particle averaged over 500 independent samples. In this case, the response is isotropic and the decrease of the displacement magnitude follows a power law $\sim 1/r$ as expected from linear elasticity (Fig. 5.5(d)). We note however that we need to average over a large number of configurations (a few hundreds) to recover linear elasticity theory, while the response to plastic rearrangements is found to match elasticity theory when averaging over ~ 50 configurations only (Puosi et al., 2014). This may be due to the fact that a single plastic event involves already a few particles, thus leading to some local averaging on the disorder. On the other hand, the elastic response to an isotropically deforming particle might be more sensitive to the configuration of the first neighboring particles, thus inducing a more anisotropic response in the system.

Stress field

We compute the coarse-grained stress field averaged over 500 independent realizations. We show in Fig. 5.5(e) a map of the Von Mises (VM) stress $\sigma_{\mathrm{v}} = \sqrt{\sigma_{xy}^2 + (\sigma_{xx} - \sigma_{yy})^2/4}$ (with the VM yielding criterion being $\sigma_{\mathrm{v}} > \sigma_{\mathrm{y}}$ with σ_{y} a threshold for plasticity). The averaged VM stress response to a dilating particle follows an isotropic power-law radial decay in $\sim 1/r^2$, as expected from linear elasticity.

We show in Fig. 5.6 the two shear components σ_{xy} and $(\sigma_{xx} - \sigma_{yy})/2$ and the pressure $-(\sigma_{xx} + \sigma_{yy})/2$ for both the microscopic simulations and the linear elasticity theory. Although we see that the shear components agree well between the microscopic simulations and the theory, we note that the pressure response, expected to be zero for an isotropically dilating inclusion in a uniform linear elastic medium, is fluctuating in the simulations.

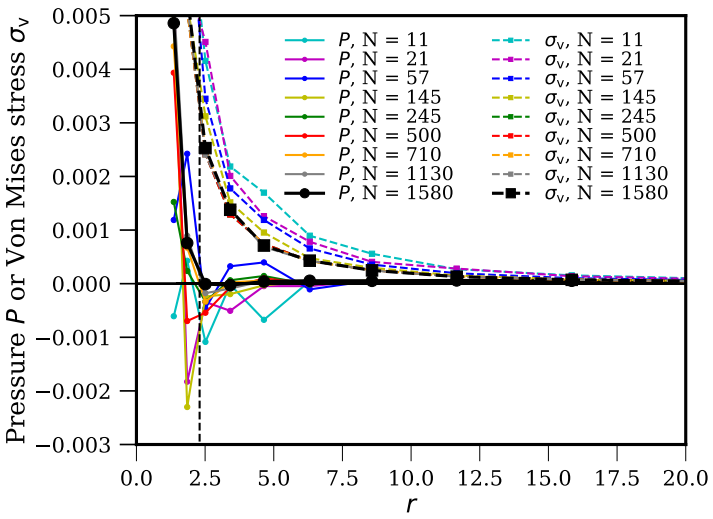

FIGURE 5.7: **Pressure and Von Mises stress as a function of the distance to the active particle** when averaging over a varying number of configurations. The VM stress curves from $N = 245$ to the maximum number of configurations ($N = 1580$) collapse. The pressure fluctuations away from the first two layers of particles become increasingly small when increasing the number of configurations.

.

We measure the mean pressure and VM stress by averaging over a varying number of configurations in Fig. 5.7. We see that the VM stress reaches an average radial evolution when averaging over 245 independent configurations, and remains unchanged when increasing the statistics. The pressure fluctuations away from the active particle become smaller and smaller when increasing the number of averaged configurations, as shown in Fig. 5.7. We expect that when averaging over a large number of configurations, the pressure field will be disturbed in the first layer of surrounding particles (due to the increase of radius of the active particle), but pressure fluctuations should vanish further away, as shown by the thick solid black line in Fig. 5.7.

Next, we perform VM stress measurements by varying the breathing amplitude a. We see in Fig 5.8(a) that all data can be collapsed by rescaling the displacement field with the amplitude a, supporting the fact that the stress response is linear with the deformation of the active particle.

We also see in Fig 5.8(b) that the power law radial decay of the VM stress holds for a large range of volume fractions in the jammed phase (from $\phi = 0.94$ to $\phi = 1.20$), but the agreement is not as good for $\phi = 0.85$, probably due to the proximity to the jamming point. To get a more quantitative understanding, one should perform these measurements using a harmonic potential where the jamming transition has been investigated in details (van Hecke, 2009).

Moreover, the prefactor of the power law decay is expected to depend on the elastic moduli (bulk and shear) that themselves depend upon the volume fraction. Measurements of elastic moduli in microscopic simulations should thus be performed in the future to get a quantitative understanding of the response to a single dilating particle in the dense regime.

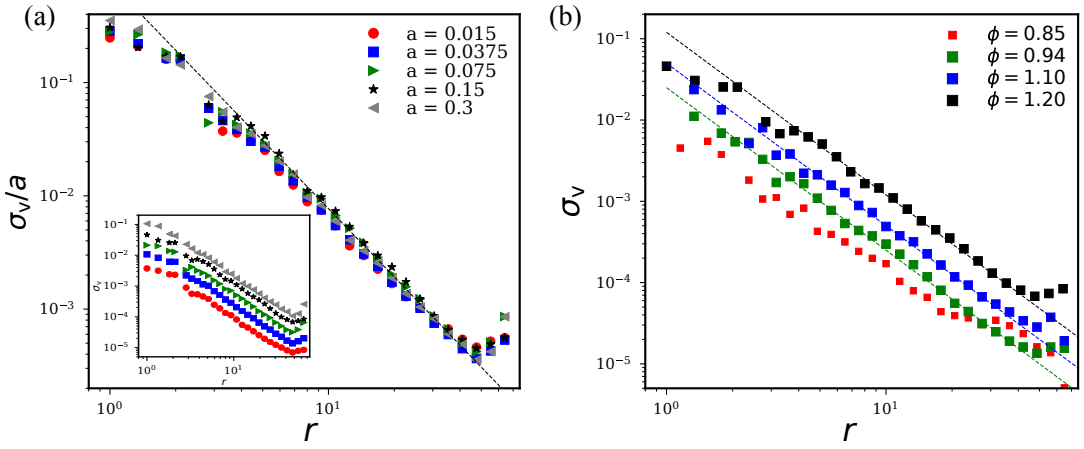

FIGURE 5.8: **Stress response for various deformation amplitudes and volume fractions**. (a) Von Mises stress σ_v rescaled by the deformation amplitude a as a function of the distance r to the active particle for various deformation amplitudes a. Inset: σ_v as a function of r without rescaling. (b) VM stress as a function of r for a deformation $a = 0.15$ and different volume fractions (data averaged over 200 independent realizations).

Concluding remarks

We evidenced in this section that the average response to a single actively dilating particle can be reasonably well described by linear elasticity, thus opening the way to build a coarse-grained elasto-plastic model accounting for this kind of active particle dynamics, as schematically shown in Fig. 5.9(a).

However, we did not discuss the relevant coarse-graining scale that should be considered in particle-based simulations in order to build such a mesoscale elasto-plastic model. As pointed out by Liu et al. (2020a), the choice of a correct coarse-graining scale is critical when trying to get a quantitative agreement between particle-based and mesoscale simulations. In our case, we do not aim for a quantitative comparison yet, but rather at building an active mesoscale model that reproduces the same phenomenology as the particle-based model. It is however important to clarify the scale at which coarse-graining is performed, i.e., to understand which aspects of the microscopic dynamics remain relevant at the mesoscopic scale.

According to Ellenbroek et al. (2009), a possible criterion for coarse-graining would be to find, on a single realization, from which distance to the active particle the elastic response looks isotropic (thus fulfilling linear elasticity) in order to base our mesoscale approach on a linear elasticity assumption, as commonly done in EPMs (see Chapter 2) (Nicolas et al., 2018a). In practice however, the response is highly anisotropic (see Fig. 5.5(a)) and such length would be larger than the system size considered in our study. We will thus consider in the following a mesoscale model describing the average behavior of a dense active system.

The lengthscale at which the fluctuations of the pressure averaged over a large number of configurations vanish provides another lengthscale to build a coarse-grained model. The linear elastic response to a contracting inclusion in an infinite medium predicts a pure azimuthal invariant shear response, and no change in pressure. It appears in Fig. 5.7 that the pressure change in response to a dilating particle becomes very small for $r > r_c$ with $r_c \simeq 2$. Considering a coarse-graining scale larger than r_c thus enables us to neglect the pressure contribution to the stress response in the

surrounding material. Local pressure changes remain present, and we will discuss further how they could be included in the modeling.

The elementary length in elasto-plastic models built for sheared passive amorphous systems corresponds to the typical size of a cluster of rearranging particles. As we aim at building a mesoscale model describing systems where plastic rearrangements of particles are induced by a local active driving, our unit length should thus also match the requirement of being of the order of the typical size of a plastic rearrangement. The number of particles involved in a plastic rearrangement depends on several parameters such as the type of interaction potential, the spatial dimension, the volume fraction, etc. The coarse-graining length for the pressure being of the order of 2 particle diameters (corresponding to a region of about 12 particles), it is likely to be of the order or smaller than the typical radius of a rearranging region, at least for some regimes of volume fraction/ pressure.

To sum up, a single dilating particle induces a displacement field and a stress field in the material that are well described by linear elasticity (i) when averaging over a few hundreds of realization and (ii) when looking at the far-field response (beyond 2 particle diameters). In the following, we propose a mesoscale model to describe a system of actively deforming particles, where we describe the activity as mesoscale regions redistributing stress to the surrounding material through elastic interactions. As in standard EPMs, the size of these mesoscale regions correspond to the typical size of a cluster of rearranging particles, and is larger than the typical size of local pressure variations induced by the active deformation.

There is one remaining point to clarify before introducing our mesoscale model: how many active particles does a mesoscale region contain? The mesoscale picture that we introduce can actually describe two different microscopic scenarios: (i) either we consider a single actively deforming particle surrounded by a few passive particles, or (ii) we consider a group of active particles with coordinated deformation dynamics. The second scenario was evidenced in experiments on epithelial tissues (Zehnder et al., 2015a; Zehnder et al., 2015b), where patches of cells of about 250 μm were shown to exhibit collective periodic contraction or dilation dynamics with a period of 3-4h. In the following, we do not specify a particular microscopic scenario, but study the properties of a generic mesoscale model with a source of local driving resulting from actively contracting and dilating regions, as depicted schematically in Fig. 5.9(a).

5.3 Active mesoscale elasto-plastic model

We consider a two-dimensional elasto-plastic tensorial model with a local driving. The driving is implemented under the form of an imposed local stress that depends upon the distribution of actively deforming sites (red sites in Fig. 5.9(b)).

The spirit of this model is the same as the model developed for simple shear (e.g., using a stress-controlled protocol), except that instead of considering a homogeneous drive and applying the same value σ^{ext} to all sites, we define a new stress field, σ^{act}, that results from the local contraction or dilation of particles. This stress field σ^{act} is computed as the convolution of an active deformation field γ^{act} with an elastic propagator F, as depicted in Fig. 5.9(b). We consider here only the case of purely dilating or contracting inclusions.

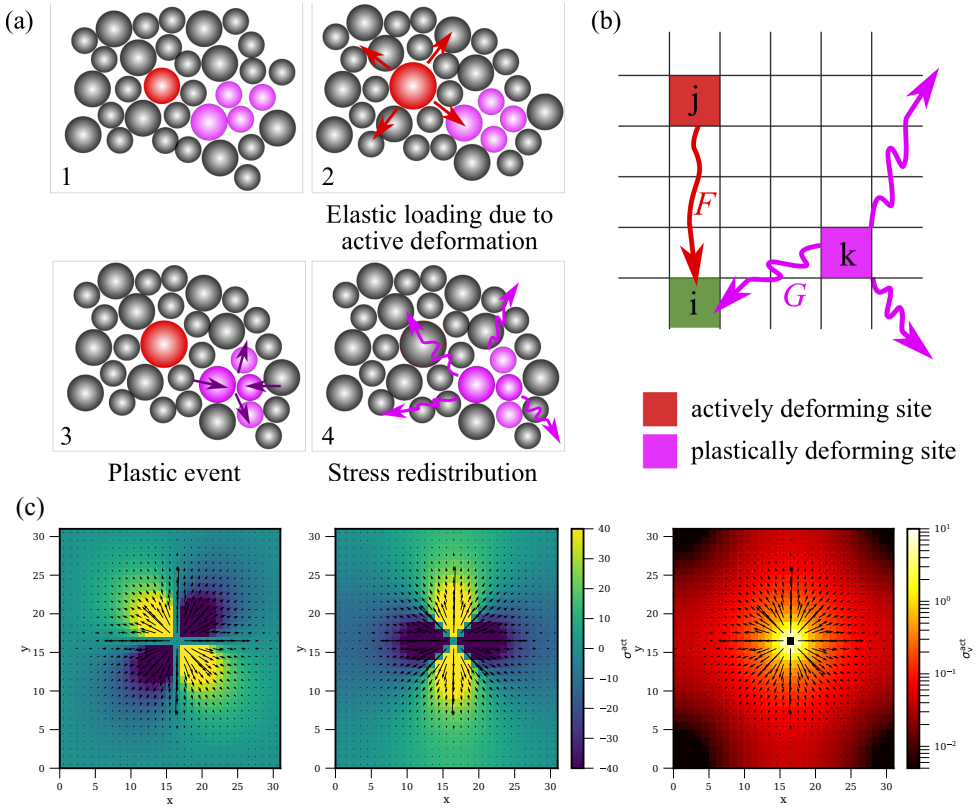

FIGURE 5.9: **Principle of the mesoscale active elasto-plastic model**. (a) Sketch of plastic deformation induced by an internal activity. 1 and 2: a particle (in red) undergoing an active deformation induces a displacement of the surrounding particles and elastic stress in the surrounding material. 3: This increase in stress induces a plastic rearrangement of particles (magenta particles). 4: This plastic rearrangement leads to a stress redistribution in the system. (b) **Lattice model describing the active elasto-plastic scenario**: the stress state at site i (green) results from the contribution of the actively deforming sites (red), described with an elastic propagator F and from the plastically deforming sites (magenta), described with an Eshelby-like elastic propagator G. (c) **Snapshots of stress and displacement fields in the AEPM** for a single actively deforming site in the center of the system without enabling for relaxation by plastic events (the stress scale and the displacement vectors scale are chosen for visualization purpose). Left: $\sigma_{xy}^{\mathrm{act}}$ component. Middle: $\sigma_{xx}^{\mathrm{act}}$ component. Right: Von Mises stress $\sigma_{\mathrm{v}}^{\mathrm{act}}$

.

5.3.1 Elastic propagator

As shown in the previous section, the elastic response derived using a point-defect model of contracting/dilating inclusion describes well the response to a single deforming particle in microscopic simulations (up to some prefactors). In our mesoscale model, we further assume that the medium is incompressible, and the stress response reads, in Fourier space (see Appendix D):

$$\tilde{\sigma}^{\text{act}}_{xy}(q_x, q_y) = \mu \frac{2q_x q_y}{q^2} \tilde{\gamma}^{\text{act}} \tag{5.11}$$

$$\tilde{\sigma}^{\text{act}}_{xx}(q_x, q_y) = -\tilde{\sigma}^{\text{act}}_{yy} = \mu \frac{q_x^2 - q_y^2}{q^2} \tilde{\gamma}^{\text{act}} \tag{5.12}$$

for $q_x \neq 0$, $q_y \neq 0$ and- $\tilde{\sigma}^{\text{act}}_{xy}(0,0) = \tilde{\sigma}^{\text{act}}_{xy}(0,0) = 0$, with μ the shear modulus and $\tilde{\gamma}^{\text{act}}$ the Fourier transform of the active deformation field. We show the stress components $\tilde{\sigma}^{\text{act}}_{xy}$ and $\tilde{\sigma}^{\text{act}}_{xx}$ in response to a single actively deforming (dilating) site located in the center of the system in Fig. 5.9(c, left and middle panels). When looking at the Von Mises stress σ_{v} redistributed to the system depicted in Fig. 5.9(c, right panel), it appears that the stress response is similar to what is measured on average in particle-based simulations (see Fig. 5.5(e), apart from the locally redistributed value (i.e., in the active site), that we set to 0 in the elasto-plastic model (and is thus close to 0 for finite lattice sizes). This assumption is not very realistic due to the fact that a mesoscale active block includes in reality several neighboring particles in addition to the active particle and is thus subjected to stress redistribution. This points again towards the question of the meaning of the coarse-graining length in the AEPM. Testing more realistic rules for the local stress response should be addressed in future work. In this chapter, we will focus on this first simple version of the AEPM and test whether it gives the same qualitative behavior as particle-based simulations.

5.3.2 Elasto-plastic dynamics

The local stress results from three contributions:

$$\sigma_{\alpha\beta}(\vec{x}, t) = \sigma^{\text{ext}}_{\alpha\beta}(t) + \sigma^{\text{act}}_{\alpha\beta}(\vec{x}, t) + \sigma^{\text{int}}_{\alpha\beta}(\vec{x}, t) \tag{5.13}$$

where $\sigma^{\text{ext}}_{\alpha\beta}$ is an externally imposed stress (e.g., applied shear), $\sigma^{\text{act}}_{\alpha\beta}$ results from the internal active driving and $\sigma^{\text{int}}_{\alpha\beta}$ describes the stress redistribution due to localized plastic events. Using a shear-rate-controlled protocol, the dynamics of the stress reads:

$$\frac{\partial \sigma_{\alpha\beta}(\vec{x}, t)}{\partial t} = \mu\dot{\gamma}(t) + \mu \int d^d\vec{x'} G_{\alpha\beta,\gamma\delta}(\vec{x}-\vec{x'}) \frac{\partial \gamma^{\text{pl}}_{\gamma\delta}(\vec{x'}, t)}{\partial t} + \mu \int d^d\vec{x'} F_{\alpha\beta}(\vec{x}-\vec{x'}) \frac{\partial \gamma^{\text{act}}(\vec{x'}, t)}{\partial t} \tag{5.14}$$

with G an Eshelby kernel, F an elastic kernel describing the response to a dilating or contracting inclusion, $\dot{\gamma}(t)$ an externally imposed shear rate, γ^{pl} the plastic deformation field and γ^{act} the active deformation field. The dynamics of the plastic deformation $\gamma^{\text{pl}}_{\alpha\beta}$ remains the same as in the standard EPM as presented in Chapter 2:

$$\frac{\partial \gamma^{\text{pl}}_{\alpha\beta}(\vec{x}, t)}{\partial t} = \frac{n(\vec{x}, t)\sigma_{\alpha\beta}(\vec{x}, t)}{\mu\tau} \tag{5.15}$$

with $n(\vec{x}, t)$ the local plastic state which has its own dynamics, determined by a yielding rule based on a yield stress distribution and a recovery rule with a fixed

rate, as described in Chapter 2 (and that we recall in the next section for our specific implementation).

5.3.3 Implementation

We rewrite the above expression with discretized spatial coordinates (i, j).

$$\frac{d}{dt}\sigma_{\alpha\beta}(i,j) = \mu\dot{\gamma} + \mu\sum_{i'j'} G_{\alpha\beta,\gamma\delta}\frac{d}{dt}\gamma^{\mathrm{pl}}_{\gamma\delta}(i',j') + \mu\sum_{i'j'} F_{\alpha\beta}\frac{d}{dt}\gamma^{\mathrm{act}}(i',j') \tag{5.16}$$

with $\gamma^{\mathrm{act}}(i', j')$ the active deformation undergone by the site (i', j'), related to radius change of an active particle: $\gamma^{\mathrm{act}} \sim \Delta r/r_0$. The plastic deformation $\gamma^{\mathrm{pl}}_{\alpha\beta}$ obeys the same dynamics as previously introduced in Chapter 2:

$$\frac{d\gamma^{\mathrm{pl}}_{\alpha\beta}(i,j)}{dt} = n(i,j)\frac{\sigma_{\alpha\beta}(i,j)}{\mu\tau} \tag{5.17}$$

with τ a relaxation timescale and $n(i, j)$ the plastic activity at site (i, j). We use the set of rules termed as "model 2" in Chapter 2 for the dynamical evolution of $n(i, j)$, i.e., based on a yield stress distribution and a fixed recovery time. A site becomes plastic when the local yielding criterion is met, using a Von Mises criterion $\sigma_{\mathrm{v}}(i, j) > \sigma_{\mathrm{y}}$, with the local threshold σ_{y} drawn from a distribution and renewed after each yielding event. When a site has yielded, it becomes elastic again after a typical time τ_{el}.

We use in the following a 2d tensorial description using an incompressibility assumption, as introduced in Chapter 2, considering two components of the stress tensor: $\sigma_{xx} = -\sigma_{yy} = (\sigma_{xx} - \sigma_{yy})/2$ and σ_{xy}. In this case, the local yielding criterion is $\sigma_{\mathrm{v}}(i, j) = \sqrt{\sigma^2_{xx}(i, j) + \sigma^2_{xy}(i, j)} > \sigma_{\mathrm{y}}$. The propagators G and F thus read, in Fourier space:

$$\tilde{G} = \frac{1}{q^4}\begin{bmatrix} -(q_x^2 - q_y^2)^2 & -2q_xq_y(q_x^2 - q_y^2) \\ -2q_xq_y(q_x^2 - q_y^2) & -4q_x^2q_y^2 \end{bmatrix} \tag{5.18}$$

$$\tilde{F} = \frac{1}{q^2}\begin{bmatrix} 2q_xq_y \\ q_x^2 - q_y^2 \end{bmatrix} \tag{5.19}$$

The details of the numerical implementation have been presented in Chapter 2 and Appendix A. We simply extend the standard 2d tensorial elasto-plastic model to account for this source of active driving γ^{act} by introducing a new propagator F. This can be done using either a shear-rate controlled protocol (as presented here) or a stress-controlled protocol. We use a mesh refinement (as done by Nicolas et al. (2013a)) to compute the convolution in Fourier space both for the Eshelby contribution and for the active contribution to the stress.

Active driving dynamics

Different types of dynamics for the active deformation $\gamma^{\mathrm{act}}(i, j)$ at site (i, j) are considered in the following, as in the work of Tjhung et al. (2017).

Periodic driving: We first consider sinusoidal oscillations of the active deformation:

$$\gamma^{\mathrm{act}}(i,j) = a\cos(\omega(i,j)t + \psi(i,j)) \tag{5.20}$$

with a frequency $f(i,j) = f = \omega/2\pi$ that we take identical for all the sites. The oscillation phases $\psi(i,j)$ are set such that, for a homogeneous frequency $f(i,j) = f$, there is not net active drive in the system, i.e., $\sum_{i,j} \gamma^{\mathrm{act}}(i,j) = 0$ at all times.

Random driving: We also consider another type of activity dynamics in the AEPM as in the work of Tjhung et al. (2017), by considering random fluctuations of the local active deformation:

$$\gamma^{\mathrm{act}}(i,j;t) = f(i,j;t) \tag{5.21}$$

where $f(i,j;t)$ in an Ornstein-Uhlenbeck process

$$\frac{\partial f(i,j;t)}{\partial t} = -\frac{1}{\tau} f(i,j;t) + \sqrt{\frac{2}{\tau}} a\eta(i,j;t) \tag{5.22}$$

with τ the relaxation time and a the noise magnitude. $\eta(i,j;t)$ is delta-correlated (white noise). $f(i,j;t)$ is thus a colored noise with zero mean and a variance

$$\langle f(i,j;t) f(i',j';t') \rangle = \delta_{ii'} \delta_{jj'} a^2 \exp\left(-|t-t'|/\tau\right) \tag{5.23}$$

We solve the above equation numerically

$$f(i,j;t+\Delta t) = f(i,j;t) - \frac{\Delta t}{\tau} f(i,j;t) + \sqrt{\frac{2\Delta t}{\tau}} a\xi(i,j;t) \tag{5.24}$$

with $\xi(i,j;t)$ a Gaussian noise of unit variance.

Let us remind that in the case of a random driving, Tjhung et al. (2017) find that the discontinuous transition between an arrested and a fluid-like state reported for monochromatic oscillations is transformed into a glass-like continuous transition between an arrested state and a fluid-like state for vanishing active deformation magnitudes ($a = 0$).

Simulation details

We perform simulations of the active elasto-plastic model (AEPM) using a GPU-based parallel implementation as described in Appendix A. We use the following simulation parameters: we choose a yield stress distribution with the following parameters: $E_{\mathrm{y}}^{\mathrm{min}} = 2.5 \cdot 10^{-4}$, $E_{\mathrm{y}}^{\mathrm{max}} = 1.8225 \cdot 10^{-2}$ and $\lambda = 701.67$ (Nicolas et al., 2014a), and an elastic recovery time $\tau_{\mathrm{el}} = \tau = 1$. The elastic modulus is set to $\mu = 1$. We use a simulation timestep $dt = 0.01$.

We run simulations fixing the values the amplitude and frequency of oscillations of the local active driving. The initial stress and activity are set to zero and the initial yield stress values are drawn from the same distribution. We measure spatially resolved fields during the simulation such that the components of the local stress, the local threshold, the accumulated plasticity (induced by activity, by other plastic events, both), as well as the displacement of fictitious particles induced by the far field response to activity and local plastic rearrangements (computed using the Oseen tensor (Martens et al., 2011)). We present in the following the results obtained with a first set of simulations of the AEPM for a linear system size $L = 64$ (simulations running for a maximum number of 24000 cycles of oscillation[2] for each independent simulation in the fluidization transition regime). Numerical simulations as well as the analysis of these results are still an ongoing work. When performing simulations with

[2]Simulations performed using a parallel GPU-based implementation and running for about 200h for each independent simulation point on Tesla K20 GPUs on the university cluster.

an external shear (in addition to the internal activity), the shear is applied along the xy direction: $\dot{\gamma} = \dot{\gamma}_{xy}$ and $\dot{\gamma}_{xx} = 0$ (and the steady state stress is averaged over a window of 200% strain for the lowest shear rates).

5.4 Fluidization in the active elasto-plastic model

5.4.1 Plastic deformation and stress in the AEPM with periodic driving

In this section, we perform simulations of the AEPM with a periodic driving protocol using a fixed frequency $f = 10^{-3}$ and varying the oscillation amplitude a. We want (i) to investigate the existence of a transition from a solid-like to a fluid-like state at finite activity amplitude a and (ii) to characterize this transition.

We show in Fig. 5.10(a) the cumulated plasticity (number of plastic events divided by the number of lattice sites) occurring in the system during one cycle of oscillation, $\langle n \rangle_{\text{cycle}}$ (averaged over windows of 100 cycles of oscillation), as a function of the number of cycles n_{cycle}. $\langle n \rangle_{\text{cycle}}$ quickly decreases to 0 for $a \lesssim 0.14$, while it reaches a finite steady-state value for $a \gtrsim 0.30$. For activity amplitudes comprised between 0.14 and 0.30, $\langle n \rangle_{\text{cycle}}$ decreases with the number of cycles, and the system undergoes a transition between a solid-like state (no plasticity) and a fluid-like state (finite level of plasticity) as the amplitude a is varied. This is a first indication that the active elasto-plastic model undergoes a solid-to-fluid transition for a finite value of the active driving amplitude a, as observed in the particle-based model of Tjhung et al. (2017).

In Fig. 5.10(b), we plot the spatially averaged (instantaneous) plasticity in the system $\langle n \rangle$ (averaged over a time window $\Delta t = 20T$ after N_{cycles} of oscillation, see caption) as a function of the active driving amplitude a. There is no clear sign of a sharp transition between a plastic fluid-like state and an arrested solid-like state (one could argue about a slight inflection for $a \simeq 0.19$), although all simulation data points have not reached steady state yet. Beside macroscopic observables such as the average number of plastic events, one can also look at the dynamics of tracer particles following the displacement field of the AEPM. We show in Appendix D examples of data for the one-cycle displacement distributions as well as the mean squared displacement of tracer particles. There is however no sign of a sharp transition in particle trajectories in our data (in contrast to the particle-based simulations (Tjhung et al., 2017)), and this discrepancy will be further investigated in the future.

Next, we plot in Fig. 5.10(c) the average Von Mises (VM) stress $\Sigma_{\text{v}} = \frac{1}{L^2} \sum_{i,j} \sigma_{\text{v}}(i,j)$ as a function of the amplitude a. We see a clear stress overshoot with a maximum for $a = a_c \simeq 0.19$, similar to what is observed in oscillatory shear driving protocols of glasses (see Chapter 1, Fig. 1.7). This stress overshoot thus suggests that the fluidization transition may be discontinuous, although no clear sign of discontinuity was found in particles trajectories. Moreover, unlike in the oscillatory shear case where no plasticity is expected before the stress overshoot, we see in Fig. 5.10(a) that there is a finite level of plasticity for $a < a_c$. If this plasticity actually persists in steady state, it can be explained by an important difference between the active driving and the oscillatory shear case. In the oscillatory shear case, the maximum driving amplitude, often termed as γ_{max}, is the same everywhere in the system. On the other hand, the maximum driving amplitude received by a given site in the active oscillatory model depends upon the phases of oscillations of the neighboring sites, and is thus heterogeneous. There is actually a distribution of the driving amplitude in the system, as depicted in Appendix D (Fig. D.4). This means that locally, isolated sites can undergo yielding due to a strong local driving. We see in Appendix D (Fig. D.2(c))

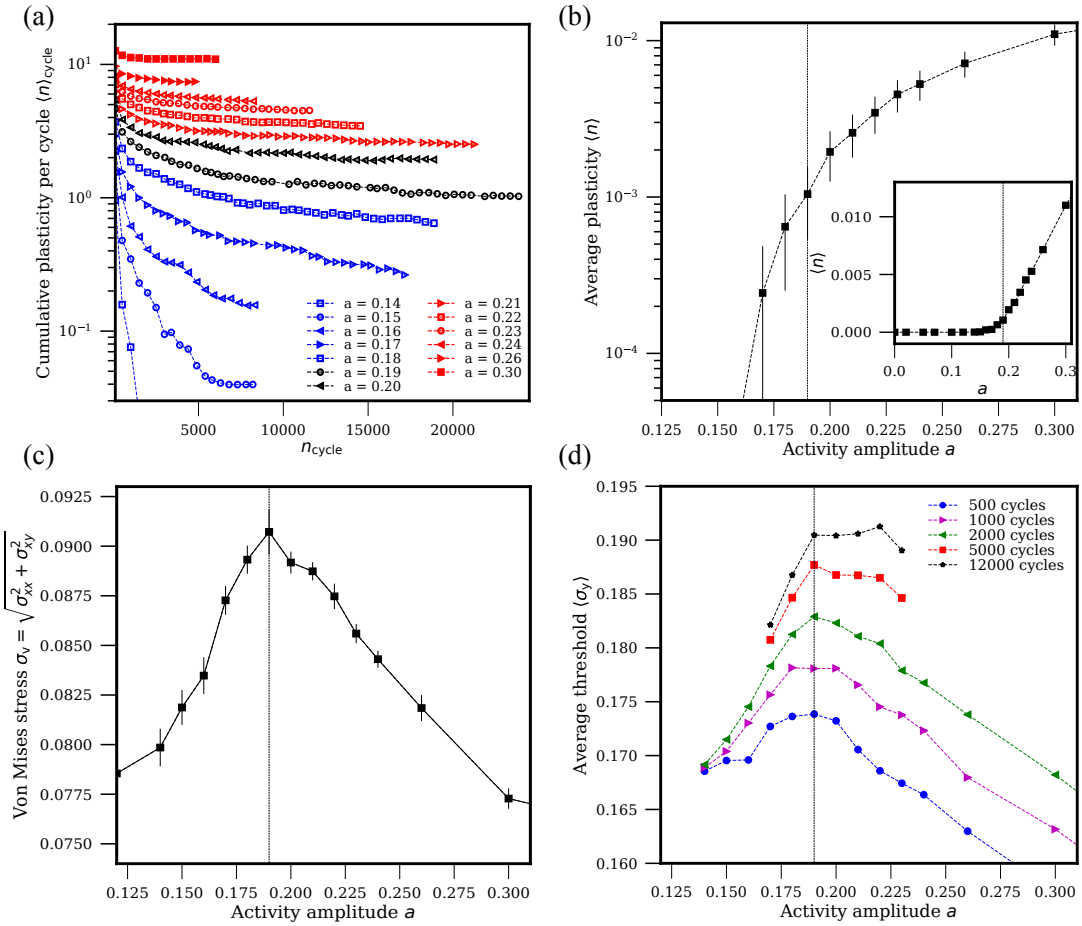

FIGURE 5.10: **Plastic activity, stress and stress threshold in the active elasto-plastic model**. (a) Cumulated plasticity (number of plastic events divided by the system size $N = L^2$) occurring in the system during one cycle of oscillation $\langle n \rangle_{\text{cycle}}$ (averaged over windows of 100 cycles of oscillation) as a function of the number of cycles n_{cycle} for a system linear size $L = 64$. (b) Average instantaneous plasticity (measured after N_{cycles} of oscillation, N_{cycles} being the maximum number of cycles displayed for each value of a in panel (a) (e.g., $N_{\text{cycles}} = 8000$ for $a = 0.15$ and $N_{\text{cycles}} = 24000$ for $a = 0.19$) and averaged over a time window $\Delta t = 20T$ with errobars corresponding to the standard deviation) as a function of the activity amplitude a. Inset: plot in a linear scale. (c) Von Mises stress as a function of the active deformation magnitude a (averaged over $\Delta t = 20T$ after N_{cycles}) exhibiting an overshoot for an activity amplitude $a_c \simeq 0.19$ (the value of a_c is indicated by the dashed line in the different plots). (d) Spatially averaged yield stress $\langle \sigma_y \rangle = 1/L^2 \sum_{i,j} \sigma_{\text{y}}(i,j)$ as a function of a after various number of cycles.

that the plastic events in the regime $a < a_c$ are induced mainly due to the active driving (and not due to stress redistribution following plastic events), hence leading to a small cooperativity between plastic events in the system. Moreover, as the spatial distribution of phases remains fixed throughout the simulation (and the distribution of local thresholds has an upper bound), we expect an isolated site to be continuously yielding in steady state (in particular if the magnitude of the local driving exceeds the upper bound of the yield stress distribution).

Interestingly, the slow decrease of the plasticity with the number of cycles observed in the regime $0.14 < a < 0.30$ (Fig. 5.10(a)) is accompanied by an increase of the average barrier to yield, as shown in Fig. 5.10(d) and Fig. D.2(b).

Moreover, the larger values of the average yield stress are reported for driving amplitudes close to the amplitude corresponding to the stress overshoot ($a \simeq 0.19$), as depicted in Fig. 5.10(d). This effect is reminiscent of "mechanical annealing" observed in glasses sheared with an oscillatory shear protocol (Leishangthem et al., 2017; Yeh et al., 2020).

The following features: (i) increase of the time needed to reach steady state, (ii) stress overshoot when increasing the amplitude of the active oscillatory driving and (iii) increased stability (higher thresholds) near the transition, thus suggest that the phenomenology of the AEPM may be similar to that of oscillatory sheared glasses.

5.4.2 Spatial organization of the plastic deformation in the AEPM

Next, we study the organization of the plastic deformation in the vicinity of the fluidization transition. We show in Fig. 5.11(a) snapshots of the plastic activity accumulated during 10 cycles (after 6000 cycles of oscillation) for different values of the amplitude of active deformation a in the case of a periodic driving (below and above the stress overshoot of Fig. 5.10(c)). We see that for $a < a_c$ (stress overshoot for $a_c \simeq 0.19$), the plastic events are localized and a macroscopic fraction of them is due only to breathing (see Fig. D.2(c)). For $a > a_c$, we see that some sites will be continuously yielding (with a finite plastic activity set by the value of the plateau in Fig. 5.11(d)) while clusters of plastically inactive sites appear (see the regions of zero plasticity for $a = 0.23$ in Fig. 5.11(a)). In this regime, the fraction of sites undergoing plastic deformation increases with a (Fig. 5.11(d)) while the number of plastic events per plastic site remains stable, as illustrated by the plateau in Fig. 5.11(e), reminiscent of the "lever rule" often associated with shear banding in sheared glasses.

These preliminary findings suggest that cooperative structures of plasticity can form upon heterogeneous drive, analogous to the formation of shear bands in sheared systems. A more detailed study of correlations between plastic events for values of the active driving close to the stress overshoot should be conducted in the future to further characterize these structures.

5.4.3 Fluidization in the AEPM with a random driving

We then consider the case of a random active driving protocol, by considering random fluctuations of the active deformation following an Ornstein-Uhlenbeck process, as described above and studied by Tjhung et al. (2017). We fix the value of $\tau = T = 10^3$ in order to compare the results to the oscillatory driving (with a period $T = 10^3$) and perform simulations for various values of the magnitude a.

We show in Fig. 5.11(c) the evolution of the plasticity cumulated during $\Delta t = 10T$ as a function of the noise magnitude a for the random active driving model (and also display the results of the periodic model for comparison), We see, as reported by

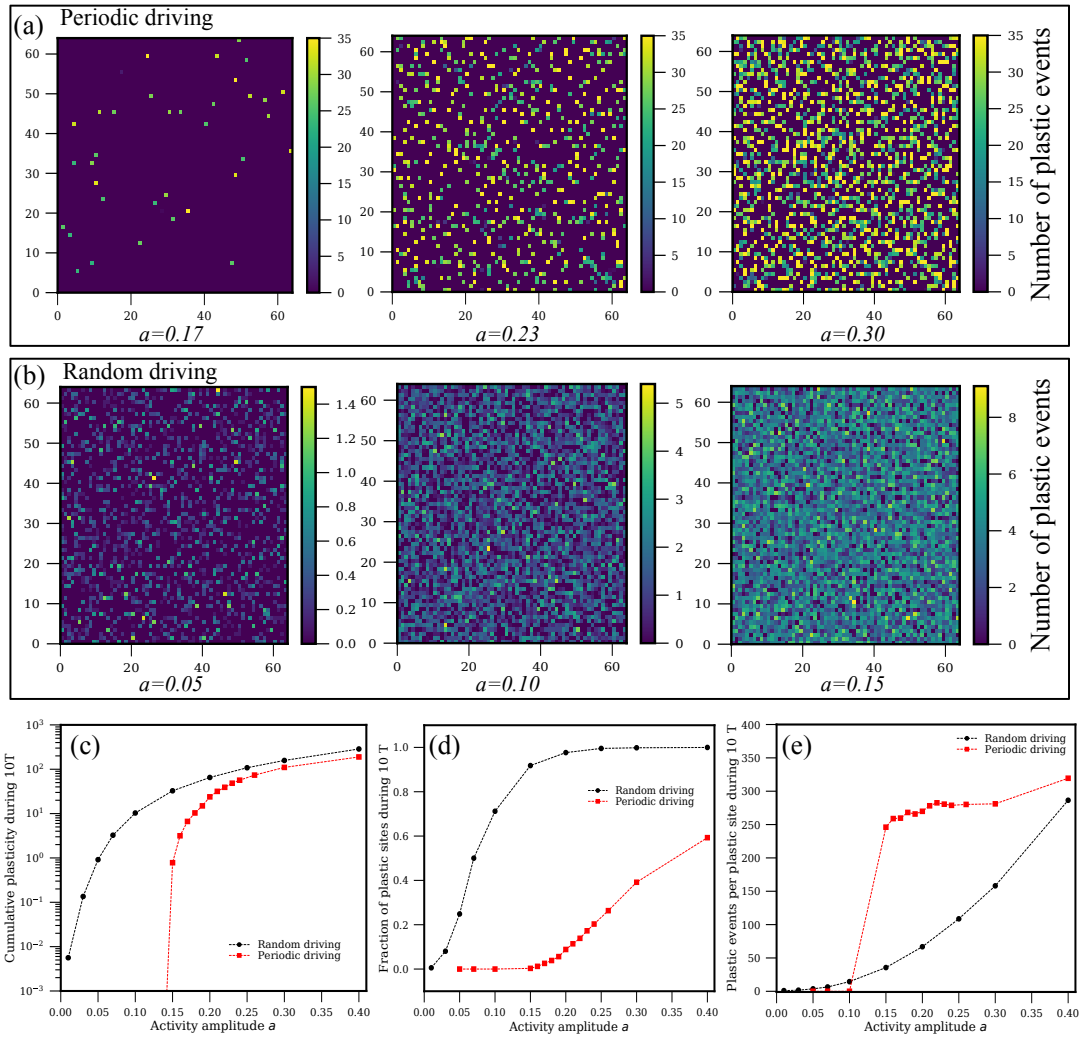

FIGURE 5.11: **Organization of the plastic deformation in an active elasto-plastic model.** (a) Snapshots of plastic events accumulated during $\Delta t = 10T$ (10 cycles) in the periodic driving model for various values of the activity amplitude a: $a = 0.17$ (after $N_{\text{cycles}} = 15000$ (left), $a = 0.23$ (middle) and $a = 0.30$ (right). (b) Snapshots of plastic events accumulated during $\Delta t = 10T$ in the random driving model for various values of the activity amplitude a: $a = 0.05$ (left), $a = 0.10$ (middle) and $a = 0.15$ (right). (c) Cumulated plasticity during $\Delta t = 10T$ as a function of a for the periodic driving model (red square symbols) and for the random driving model (black circles). (d) Fraction of sites undergoing plastic deformation (during $\Delta t = 10T$) as a function of a for the two models. (e) Number of plastic events in plastically deforming sites (average number of events accumulated in sites undergoing plastic deformation during $\Delta t = 10T$) as a function of a for the two models.

Tjhung et al. (2017), that switching from a periodic active drive to random fluctuations destroys the transition at finite activity a. In the case of random driving, the fluidization transition occurs continuously for $a \to 0$.

We show in Fig. 5.11(b) typical snapshots of the plastic activity (accumulated during $\Delta t = 10T$) for various values of the noise magnitude a. Unlike in the oscillatory case, we do not observe a spatial localization of the plasticity. This is confirmed by measurements of the number of plastic events occurring in plastic sites, that does not exhibit a plateau but increases monotonously with a (Fig. 5.11(e)).

These results support the hypothesis of an active yielding transition for periodic oscillations of the local active drive, that holds as long as there is a characteristic frequency for the driving. This could be further tested in the AEPM by implementing the other active driving dynamics considered by Tjhung et al. (2017) (e.g., periodic drive with a distribution of frequencies, or by prescribing a frequency spectrum to each oscillating site).

5.4.4 Concluding remarks

The first results of our AEPM suggest the existence of a transition between a solid-like and a fluid-like state in the case of a periodic active drive, occurring for a finite value of the oscillation amplitude of the active drive $a_c \simeq 0.19$, similar to what was observed in particle-based simulations (Tjhung et al., 2017). Although the nature of the transition is not clear from particle trajectories (due to the long time needed to reach steady state and the absence of reversible events in our model), a number of features resembling the discontinuous yielding transition in oscillatory sheared glasses have been reported. We can mention in particular: a stress overshoot for $a = a_c$, a minimum value of the plastic activity in plastically active sites, a spatial organization of the flow near the transition, as well as an increase of the material's stability (higher yielding barriers) close to the transition. The fluidization observed in the case of a random driving protocol exhibits quite different features, resembling a continuous transition for $a \to 0$ without any particular spatial organization of the plastic deformation.

These results are a first step in the analysis of our AEPM and there are still several aspects that we did not discuss, such as e.g., correlations between events, finite-size effects, hysteresis dynamics, etc., that we leave to future studies. In order to further test our model in comparison to particle-based simulations, we study in the last section the response of the AEPM to an externally-imposed shear.

5.5 Rheology of a system of actively deforming particles

We show in this part the first results regarding the response of the active system to an externally imposed shear, both in mesoscopic and microscopic simulations, using oscillatory dynamics for the active deformation (ongoing work in collaboration with S. Ghosh and P. Chaudhuri from IMSC, Chennai, India). We impose a fixed shear rate along the xy direction $\dot{\gamma} = \dot{\gamma}_{xy}$ and measure the shear stress σ_{xy}.

We show the flow curves obtained for various values of the oscillation amplitude a in Fig. 5.12(a) and (b). While the rheology is not affected by the activity at high shear rate (all the curves collapse), we see a decrease in shear stress as the activity amplitude is increased. The same qualitative behavior is observed in mesoscopic and microscopic simulations. We further observe in Fig. 5.12(c) that, in particle-based simulations, the dynamic yield stress vanishes for breathing amplitudes $a > a_c$ (with $a_c \simeq 0.0493$), which is consistent with the results on the fluidization transition of Tjhung et al. (2017), which predict a fluid-like behavior for $a > 0.49$. Studying the

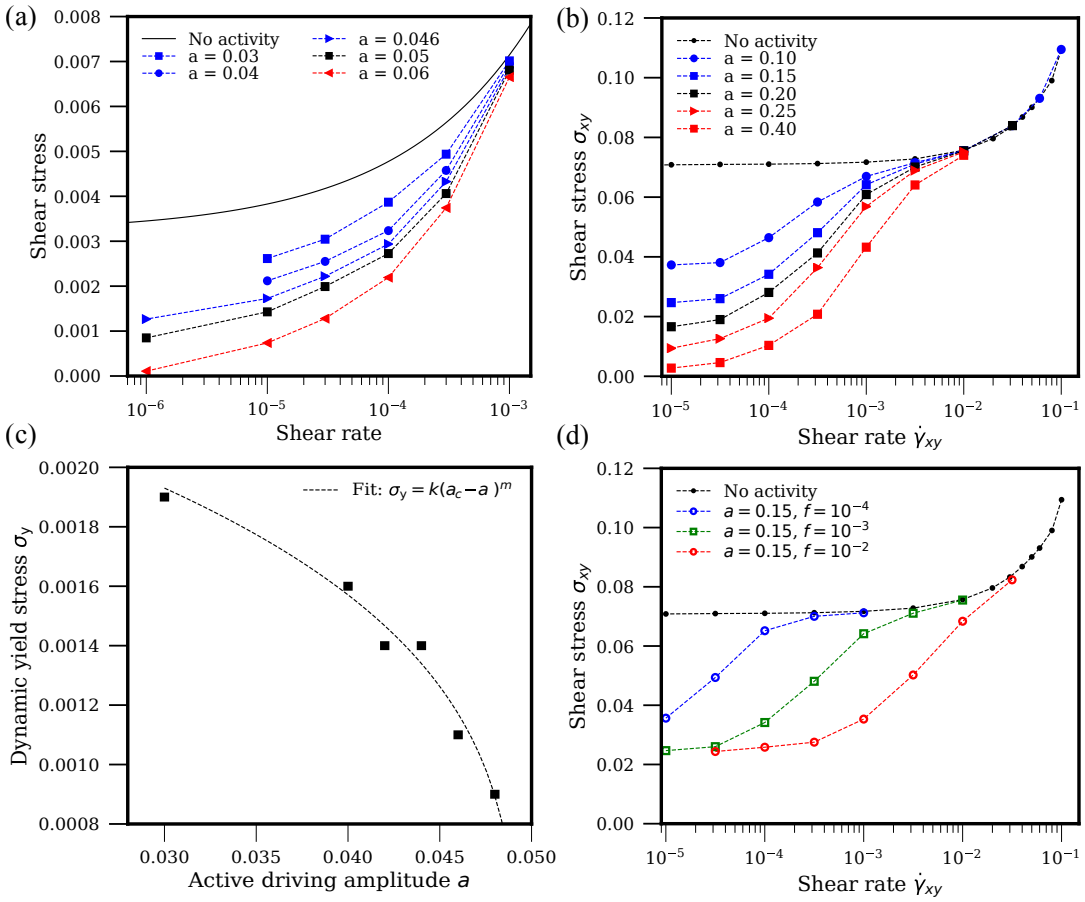

FIGURE 5.12: **Rheology in microscopic simulations and in the active EPM**. (a) Shear stress as a function of shear rate for various values of the breathing amplitude a in particle-based simulations (numerical simulations performed by S. Ghosh and P. Chaudhuri within our CEFIPRA collaboration). (b) Rheological curves obtained with the AEPM for a system size $L = 64$. (c) Dynamic yield stress (obtained by fitting the rheological curves from particle-based simulations with a Herschel-Bulkley fitting form) as a function of the active drive amplitude a with a fitting form: $\sigma_y = k(a_c - a)^n$ with $a_c = 0.493$, $k = 0.0059$ and $n = 0.281$. (d) Rheological curves obtained in the AEPM for $L = 64$ and $a = 0.15$ for different frequencies: $f = 10^{-4}$ (blue), $f = 10^{-3}$ (green) and $f = 10^{-2}$ (red).

response to an external shear thus constitutes another manner to probe the mechanical behavior of an assembly of actively deforming particles, and yields results consistent with what is obtained from particle trajectories. The evolution of the yield stress close to the transition should also be studied in the mesoscale model in future work.

The effect of the breathing frequency in the mesoscale model is shown in Fig. 5.12(d). While the shear rate at which fluidization effects are observed seem to depend directly on the frequency of oscillation (thus delimiting a shear-dominated and an activity-dominated regime as discussed in Chapter 4), the low shear rate rheology and the yield stress value seem to be independent of the frequency of the active drive. The role of the frequency on the rheology should also be investigated in particle-based simulations. Another interesting perspective would be to adapt our model to include an active quasi-static driving protocol, both in particle-based and in mesoscopic simulations in order to study the limit of small frequencies / small shear rates (Liu et al., 2020b).

5.6 Discussion

In this chapter, we proposed a generalization of the mesoscale elasto-plastic model accounting for a heterogeneous drive in order to test the applicability of the mesoscopic elasto-plastic approach to dense active systems. We considered the case of an active drive generated by the active isotropic deformation of particles embedded in an overall elastic medium. This model of activity, inspired by the particle-based model of Tjhung et al. (2017), has the advantage to be simple since it has only two control parameters: the amplitude and timescale of the active deformation, and does not require to introduce phenomenological ingredients (in addition to that of standard EPMs). Moreover, the results of Tjhung et al. (2017) regarding the type of fluidization transition observed depending upon the type of dynamics for the active deformation (oscillatory, random fluctuations, etc.) constitute a benchmark to test our model.

We studied in particular the case of oscillatory active deformations, shown by Tjhung et al. (2017) to induce an active yielding transition between an arrested state and a flowing state for a finite amplitude of deformation a.

We evidenced a transition between an arrested solid-like state where only little plasticity is observed and a fluid-like phase where irreversible rearrangements take place, consistent with the particle-based model of Tjhung et al. (2017). The data amount obtained so far does not yet allow for the in depth characterization of the transition. Close to the transition, the time to reach stationary state is expected to diverge and prevents so far to obtain reliables observables. Also, observables computed from tracer particle trajectories (e.g., one cycle displacement, mean square displacement) could not enable us yet to determine the nature of this transition. Let us also mention that one should be careful when comparing the displacement fields computed in the mesoscale EPM to the actual displacement field as measured in, e.g., particle-based simulations. In the mesoscale EPM, we only account for the non-affine displacement field induced in the material (in the far field) in response to a local shear transformation and we do not account for the local particle displacements occurring in the shear transformation zone itself (Martens et al., 2011). On the other hand, both the displacement of particles in the rearranging zone and the far field response are measured in particle-based simulations. Whether these quantities evolve at the transition between the solid-like to the fluid-like state is not known, and this difference could also contribute to the discrepancy between particle-based and mesoscale models.

As future perspectives, we should first consider running longer simulations in order to determine the nature of the transition, and then possibly find an alternative way to reach steady state (e.g., by changing the rules for renewing the local yielding barriers and/or by including reversible plastic rearrangements). In fact, we expect that even running longer simulations, the solid-like phase of the AEPM would remain different from that of particle-based simulations (probably more fluid-like). In particle-based simulations, plasticity is observed in the solid-like phase but the average one-cycle displacement remains very small due to the fact that particles go back to their position after one cycle (due to the reversibility of the drive), hence leading to reversible plastic rearrangements (Tjhung et al., 2017). Reversible plastic rearrangements are however not implemented in the AEPM. Although the two stress components $\sigma_{xy}^{\mathrm{act}}$ and $\sigma_{xx}^{\mathrm{act}}$ evolve periodically, the Von Mises stress determining the local yielding criterion ($\sigma_{\mathrm{v}} = \sqrt{\sigma_{xy} + \sigma_{xx}} > \sigma_{\mathrm{y}}$) is not periodic, even in the absence of plastic rearrangements in the system (see Appendix D, Fig. D.4). Considering another yielding criterion based on maximum stress (e.g., Tresca criterion) may thus enable to account for reversible plasticity in the AEPM.

Accounting for reversible plasticity in mesoscale EPMs could thus constitute an interesting perspective, since Tjhung et al. (2017) have emphasized the role of microscopic reversibility in the discontinuous character of the transition, enabled by the periodicity of the drive with a characteristic frequency. Note that even using a yielding criterion based on maximum stress rather than a Von Mises criterion, steady state reversible rearrangements would only be observed if the local drive due to activity is larger than the upper bound of the yield stress distribution (because a new yielding barrier is drawn after each plastic event). We could thus imagine also changing the stochastic rules for plasticity in such a way that when a plastic event is induced only due to the active deformation (and not due to other plastic rearrangements), then the energy barrier for local yielding remains unchanged such that the exact reverse plastic event can occur after half a period of oscillation. Energy-based elasto-plastic models may however be more suited to include reversible plasticity, by considering a hierarchical energy landscape for instance, as suggested in the recent work of Liu et al. (2020b). Moreover, considering an energy-based mesoscopic model as done by Liu et al. (2020b) to study quasistatic oscillatory shear driving would enable us to study the evolution of the system's energy across the transition, known to exhibit either a sharp minimum or at least an inflection point (depending upon glass stability) in the case of oscillatory sheared glasses (Leishangthem et al., 2017; Yeh et al., 2020; Liu et al., 2020b).

Beside average plasticity and particle trajectories, we measured the average Von Mises stress in the system as a function of the activity amplitude a and evidenced a clear stress overshoot, reminiscent of what can be observed in oscillatory sheared glasses (Leishangthem et al., 2017; Yeh et al., 2020), and supporting the scenario of a discontinuous transition. However, the stress drop following the overshoot is not very sharp. This could be explained by the fact that we considered finite deformation rates and a rather small system size (compared to, e.g., the system sizes considered in Chapter 4). It would be of interest in the future to adapt our model to account for a quasi-static active driving protocol and see how this affects the stress overshoot, as well as running simulations for other system sizes.

The plastic events occurring for activity amplitudes well below the stress overshoot are mainly due to the active driving (see Fig. D.2(c)) and stress redistribution due to plastic events in the system becomes more important as a is increased. There also seems to be indications of a spatial organization of the plasticity in regions undergoing plastic flow and immobile regions. This feature seems to be absent in the case of the

active drive with random fluctuations of the active deformation, emphasizing the role of the periodic drive to induce such spatial organization. In the future, the existence of a stress overshoot as well as the organization of the flow in correlated plastic region in the fluid-like phase just above the transition should be studied in particle-based simulations.

To sum up, we propose four main possible explanations to explain why we do not observe a sharp discontinuity in particle trajectories in the AEPM: (i) the data points close to the transition have not reached steady state yet (and are expected to reach a state with lower plastic deformation in the long time limit), (ii) we do not account for reversible plastic events (which do not contribute to the one-cycle displacement in the solid-like phase), (iii) we do not account for the particle displacement in the shear transformation zone (which does not contribute to the one-cycle displacement in the reversible solid-like phase but may contribute importantly in the fluid-like phase) and (iv) the driving rate is too high (far from the quasi-static limit) and prevents the observation of a clear stress drop that would be associated with a clear discontinuity in particle trajectories.

Last, we showed preliminary results regarding the rheology of this dense system of actively deforming particles. Interestingly, the fluidization induced by the breathing activity resembles that of sheared colloidal gels subjected to ultrasonic vibrations as studied by Gibaud et al. (2020), where the yield stress is found to decrease with the vibration magnitude. This fluidization scenario is very different from that of, e.g., vibrated frictional granular media (Dijksman et al., 2011) or induced by cell division and apoptosis (Matoz-Fernandez et al., 2017a), where the yield stress is found to vanish for any finite rate of vibration or activity (although at low activity a plateau reminiscent of the yield stress appears in the flow curve). These first results regarding the rheology are also consistent with the results of Ovarlez et al. (2010) on the three-dimensional flow behavior of yield stress fluids, showing that soft glassy materials are always unjammed simultaneously in all directions of space (i.e., when a flow is imposed in one direction of space, there is no resistance to a secondary flow along another direction). In the case of the active system studied here, the flow induced by the activity for $a > a_c$ thus yields a vanishing yield stress for an externally imposed shear flow.

There are still several points that we did not address in this first preliminary study, such as, e.g., correlations between plastic events, finite-size effects or the importance of sample-to-sample variations. We show preliminary data for two independent sample in Fig. D.2(d), suggesting that sample-to-sample variations may be relatively small. These aspects should be investigated in future work in order to characterize in more details the fluidization transition induced by activity in the AEPM.

Let us now discuss the assumptions of our active elasto-plastic model, which is based on several simplifications of the underlying microscopic dynamics. A strong hypothesis of our model is for instance to neglect the effect of density fluctuations. Although the total density in the system is fixed (through the phase-shift of radius oscillations), local density fluctuations can still occur and lead to a local softening of the system, increasing the propensity of the region to yield. The effect of local density changes should thus be assessed in particle-based simulations in future work.

Moreover, we considered only the shear response to the active deformation of particles (as expected from linear elasticity), although we saw in particle-based simulations that a pressure change is induced in the neighborhood of the active particle. Although this would not affect the response of a perfectly incompressible material,

the soft disks systems considered in particle-based simulations are actually quite compressible and pressure variations may indeed affect the dynamics of the system. The incompressibility assumption usually made in EPMs is thus a simplification, and one could in principle derive elastic propagators (both for the Eshelby stress response and for active isotropic deformations) for compressible linear elastic material (Cao et al., 2018).

Despite these important simplifications, our minimal elasto-plastic model suggests that local shear driving due to the active deformation of particles is able to fluidize a dense packing for a finite activity magnitude. However, although we showed in this chapter, following the work of Tjhung et al. (2017) that cell volume fluctuations themselves can fluidize a tissue, the tissue dynamics studied for instance by Zehnder et al. (2015a) and Zehnder et al. (2015b) probably results from multiple sources of activity, including the ability of cells to migrate. In their study, Zehnder et al. (2015b) suggest that density fluctuations induced by the active volume fluctuations play an important role since they induce divergent velocity fields. The velocity field measured in tissues may however result from an interplay of the self-propulsion of cells, of the elastic response to contracting/dilating cells and of the (plastic) cell rearrangements induced by active forces. The coupling of these different mechanisms remains an open question.

Finally, let us mention how the AEPM could be extended to account for other types of biological activity. The elastic responses to local active events in particle-based simulations shown in the introduction of the thesis (Fig. 1.18) suggest that the above mesoscale elasto-plastic approach could be extended to other kind of activities, such as cell division, cell death and self-propulsion.

Modeling cell growth, cell division and apoptosis in a EPM would follow the same lines as for actively deforming particles. These active events generate strain and stress fields in the material that can be described using elastic propagators. Cell division events are usually preceded by a slow process of cell growth, that could be described (assuming isotropic growth) using the same elastic propagator as the one describing active radius changes in the first part of this chapter. The division itself generates an anisotropic displacement field and could be modeled using either an Eshelby-like propagator or perhaps the superimposition of an isotropic dilation with an Eshelby shear transformation (without any stress relaxation). Cell death can be seen as a cell shrinkage event with an amplitude of deformation set by the initial size of the cell. In summary, one could imagine describing all these active events using force dipoles (assembled in a geometry that depends upon the type of event) and describing the elastic response of the medium as we did here in the case of isotropic particle deformation. The dynamics of these events would then be set by stochastic rules (that could possibly depend on the local stress field) including e.g., division and apoptosis rates.

The dynamics of self-propelled particles systems can resemble, in the case of a large persistence time for the direction of self-propulsion, that of a sheared system with localized rearrangements of particles, triggering avalanches (Mandal et al., 2020a). One could then imagine to describe self-propulsion in a simplified manner by activating rearrangements with a random orientation, as done e.g., in Chapter 4. It is however not clear how the activation rules for the random plastic events should be chosen, and how an activation rate could be related to (microscopic) parameters controlling the self-propulsion magnitude (e.g., the self-propulsion force f_0). Recent works have suggested that self-propelled particles systems in the infinite persistence time limit could be described as sheared systems with a random force field (Morse et al., 2020;

Mandal et al., 2020b). These recent advances will be further discussed in the general discussion of Chapter 7.

Moreover, in biological systems such as epithelial sheets, self-propulsion mechanisms are often thought to be coupled to the forces applied onto the cell. It has been proposed for instance that coupling the direction of the self-propulsion force to the direction of the cell velocity (resulting from the forces exerted onto the cell) could lead to collective cell migration, such as flocks or velocity oscillations. The next chapter is dedicated to study the emergence of oscillations of the cell velocity in epithelial monolayers confined to elongated patterns, using a Self-Propelled Voronoi model.

Chapter 6

Velocity oscillations in confined epithelial monolayers

Résumé : Oscillations collectives de la vitesse de migration cellulaire dans un épithelium confiné

L'émergence de mouvements collectifs dans des systèmes actifs denses tels que des tissus biologiques a suscité un intérêt croissant ces dernières années[1]. De nombreux travaux ont abordé le lien entre le ralentissement de la dynamique dans des régimes très denses (parfois sous le nom de "active jamming") et les propriétés des mouvements collectifs observés dans ce régime, par analogie avec les systèmes désordonnés denses non actifs. Plus récemment, plusieurs travaux sur les tissus épithéliaux ont rapporté l'existence de mouvement collectifs sous la forme d'oscillations de vitesse des cellules, soit lors de la croissance d'épithéliums, soit lorsque le tissu est soumis à un confinement.

Des expériences récentes menées au laboratoire ont mis en évidence de telles oscillations de la vitesse de déplacement des cellules dans des tissus épithéliaux soumis à un confinement quasi-unidimensionnel, caractérisé par une longueur L_X. Ces expériences révèlent l'existence de deux types d'oscillations suivant la longueur de confinement : pour de petits systèmes $L_X < L_X^c$, les vitesses de migration de la majorité des cellules sont en phase et le tissu oscille de façon globale (toutes les cellules se déplacent vers la gauche, puis vers la droite, en alternance) avec une période temporelle d'oscillation variant linéairement avec la taille du système L_X. Pour un confinement $L_X > L_X^c$, les oscillations sont multi-nodales, i.e., des groupes de cellules se déplacent de façon cohérente et la direction de migration des cellules est modulée spatialement, faisant apparaître une longueur d'onde caractéristique $\lambda \simeq L_X^c$. De plus, la vitesse de propagation de ces ondes semblent indépendante de la longueur de confinement et intrinsèque au tissu.

Ces expériences ont motivé le travail de modélisation présenté dans ce chapitre. Notre approche de modélisation est basée sur un modèle de Voronoi, proche des modèles de vertex couramment utilisés pour modéliser des tissus épithéliaux (voir Chapitre 1). Nous considérons un modèle de type "Voronoi auto-propulsé" ("Self-Propelled Voronoi", SPV en anglais) dont la dynamique résulte d'une énergie calculée d'après la position des vertex des cellules, et d'un mécanisme d'autopropulsion sur les centres des cellules de Voronoi. L'autopropulsion se fait suivant la direction de la polarisation de la cellule, dont la direction diffuse au cours du temps. Ce type de modèle, étudié auparavant dans la littérature, a un diagramme de phase connu, et en particulier, présente une transition entre un état "fluide" et un état "solide" en

[1] et la notion de confinement aussi, surtout ces derniers mois

fonction de deux paramètres de contrôle : le paramètre de forme de repos des cellules (rapport entre le périmètre et la racine carrée de l'aire de repos des cellules), et l'amplitude de la force d'autopropulsion exercée sur les centres de Voronoi. Nous montrons dans ce chapitre que pour reproduire des oscillations dans un système confiné à l'aide de ce modèle, il est nécessaire d'introduire un mécanisme d'alignement de la direction d'autopropulsion de la cellule avec la direction de sa vitesse, avec un délai τ_{al}. Ceci semble cohérent avec les travaux de Giavazzi et al. (2018), également basés sur un modèle SPV, concernant l'émergence de mouvements collectifs dans le cas d'épitheliums non confinés. Si le temps typique d'alignement est inférieur au temps typique de diffusion de la polarisation, alors le mouvement des cellules est coordonné sur des distances pouvant aller jusqu'à une dizaine de diamètre cellulaires, reproduisant les mouvements collectifs observés expérimentalement.

Avec ce mécanisme d'alignement, nous observons dans le modèle SPV des oscillations dont les propriétés sont similaires à celles des oscillations mesurées expérimentalement au laboratoire. Pour une longueur de confinement inférieure à une longueur critique (qui dépend du délai pour l'alignement), $L_X^c(\tau_{\mathrm{al}})$, les vitesses de l'ensemble des cellules sont coordonnées, et la période temporelle des oscillations évolue linéairement avec le confinement L_X. Pour $L_X > L_X^c(\tau_{\mathrm{al}})$, seules des régions de taille finie coordonnent leur vitesse, qui oscille périodiquement au cours du temps. La période temporelle des oscillations reste alors inchangée lorsque L_X augmente, tel que rapporté dans les expériences. La vitesse de propagation de ces ondes dans le système ne dépend pas du confinement, également en accord avec les résultats expérimentaux. Elle semble par contre dépendre de plusieurs paramètres du modèle, tels que ceux décrivant l'élasticité du système, ainsi que du temps de délai τ_{al}. Ces résultats préliminaires suggèrent qu'un modèle continu basé sur une description élastique avec une inertie effective induite par le délai τ_{al} pourrait prédire le même type d'oscillations.

Il est important de noter que ce travail résulte de multiples collaborations: avec l'équipe de biophysique MicroTiss au LIPhy (V. Pettrolli, M. Tadrous, M. Balland, T. Boudou, G. Cappello) qui a réalisé les expériences sur les tissus épithéliaux en collaboration avec une équipe du CEA-LETI (Grenoble) pour la microscopie (C. Allier, O. Mandula, L. Hervé). Le travail de modélisation et simulation présenté ici a été réalisé en collaboration avec S. Henkes (Université de Bristol) et R. Sknepnek (Université de Dundee), qui ont développé le code pour le modèle de Voronoi de tissu épithélial (Barton et al., 2017). Ce travail est publié dans *Physical Review Letters 122, 168101* (Petrolli et al., 2019).

Le chapitre est organisé de la façon suivante : dans la section 6.1, nous présentons quelques approches de modélisation décrivant des oscillations de vitesse dans des monocouches épithéliales, en particulier dans le cas de systèmes confinés. Les principaux résultats expérimentaux de la thèse de Petrolli (2019) sont ensuite synthétisés dans la section 6.2. Le modèle et les méthodes utilisés sont ensuite présentés dans la section 6.3. Enfin, les résultats numériques sont présentés dans la section 6.4: dans une première partie, nous décrivons les oscillations observées dans le modèle, en comparaison avec les expérience et dans une deuxième partie, les rôles respectifs du mécanisme d'alignement et des propriétés élastiques du système sont discutés.

Introduction

A remarkable feature of dense active systems such as epithelial monolayers is the ability of their constituents (i.e., epithelial cells) to move collectively, exhibiting a rich dynamics such as swirls, flocks and mechanical waves. By mechanical waves, we

mean the periodic fluctuations of mechanical parameters, such as the cell displacement or velocity, the associated strain (or strain rate), traction forces (as measured in the substrate), and stresses (Petrolli et al., 2020; Pajic-Lijakovic et al., 2020). In particular, several recent works have reported that wave-like patterns of the local cell velocity spontaneously appear in colonies of epithelial cells. Propagative velocity waves have been observed in spreading epithelial sheets (Serra-Picamal et al., 2012; Rodríguez-Franco et al., 2017; Ladoux et al., 2017; Hakim et al., 2017), regardless of cell proliferation (Tlili et al., 2018), and are correlated to oscillations of the forces exerted by the cells on the substrate (Trepat et al., 2009). Such long wavelength patterns also appear in confined geometries, in the form of standing waves, where the extent of cell migration is limited to the substrate size (; Deforet et al., 2014; Notbohm et al., 2016; Duclos et al., 2018b; Peyret et al., 2019).

When confined to two-dimensional substrates, cells proliferate until they fill the available space, reaching a so-called "confluent state"[2]. Cell movement in the monolayer slows down as density increases. This observation, classically associated with the so-called "density mediated contact inhibition of locomotion" (Stoker et al., 1967) has also been attributed to the maturation of adhesive junction between cells and between the cells and the substrate in time (Garcia et al., 2015). The dynamical arrest occurring in biological and active systems has attracted an increasing interest, both experimentally and theoretically. Various works have emphasized the analogy between cell monolayers and dense systems of soft spheres, where the motion of particles is restricted to cages leading to an overall solid-like behavior (Szabo et al., 2006; Henkes et al., 2011; Angelini et al., 2011; Garcia et al., 2015; Bi et al., 2015). This dense regime where glassy or arrested dynamics is observed was described in more details in Chapter 1, and was also the focus of the previous chapter (Chapter 5).

We focus in this chapter on confluent monolayers that are not yet arrested, where cells are able to move over large distances (compared to their size) with cell displacements (and velocities) that can be correlated over long distances (Hakim et al., 2017; Alert et al., 2019). Confining the cells in micro-patterns whose size is typically the size of this correlation length (around 150 to 200 microns) or smaller gives an extra control parameter on the behavior of these cells. Collective oscillations of the velocity field in confined monolayers of epithelial cells *in vitro* have been reported in various experimental setups (Deforet et al., 2014; Notbohm et al., 2016; Peyret et al., 2019). Periodic oscillations of the velocity have been evidenced in Epithelial sheets of Madin-Darby Canine Kidney (MDCK) cells confined to circular adhesive patterns by Deforet et al. (2014), where the oscillations were propagating along the radial direction. Such oscillations were further investigated by Notbohm et al. (2016), who modeled the monolayer as an active elastic medium with active coupling terms between cell displacement, polarization and contractility. A recent study by Peyret et al. (2019) also evidenced velocity oscillations using anisotropic confinement.

Although mechanical waves seems to be ubiquitous in confined epithelia, their origin remains debated. As mentioned in Chapter 1, epithelial monolayers have been shown to exhibit elastic, plastic and viscous flow behavior depending on the forces applied and the observation timescale. Various studies have evidenced elastic properties (that can be of active origin) (Serra-Picamal et al., 2012; Harris et al., 2012) and it is well known that elastic materials have the ability to propagate mechanical perturbations. In passive mechanical systems, oscillatory perturbations such as sound waves result from an exchange of elastic potential energy and inertial kinetic energy.

[2]The division rate and the overall density will be kept approximately constant, achieving an homeostatic state in the monolayer (process known as "contact inhibition of proliferation" (Martz et al., 1972))

In cell monolayers however, inertia is thought to play a negligible role in the dynamics, considered as overdamped. Hence, the emergence of collective oscillations in cell monolayers must be of active origin, different from the mechanism known in passive elastic systems.

Tissue-level oscillations in confined epithelia have been modeled using approaches either at the particle level (Deforet et al., 2014) or using continuum approaches (Notbohm et al., 2016) including active cellular forces. There is however no consensus on the biophysical nature of these forces and on the mechanism by which mechanical oscillations are generated. Experiments have revealed that mechanical oscillations depend on cell–cell junctions and cell contractility, suggesting that the ability of the monolayer to transmit forces is crucial. Various models have been developed based on a delayed coupling between cell motility and intercellular forces, playing the role of an effective inertia. Note that other approaches based on the visco-elastic properties of epithelial monolayers have thought of these mechanical waves in terms of "elastic turbulence" (Pajic-Lijakovic et al., 2020).

While various models have been shown to exhibit oscillations that qualitatively match the experimental observations, various questions regarding the oscillations remain open, e.g., how does the confinement size affect the oscillations patterns? What sets the waves propagation velocity? In this work, combining modeling and experimental approaches, we study the wave-like patterns generated in confined epithelial monolayers. The experiments consist in confining Madin-Darby Canine Kidney (MDCK) cells to quasi-unidimensional patterns where we vary a single parameter (the pattern length) controlling the confinement. These experiments reveal that tuning the length of the confining channel induces a transition between a state of global oscillations (where the motion of all cells is coordinated) and a multi-nodal wave state. In order to understand what could be the minimal ingredients to observe such collective oscillations in a simple model of epithelial monolayer, we use a numerical model based on a self-propelled Voronoi model (SPV) (Bi et al., 2016; Barton et al., 2017; Giavazzi et al., 2018), adapted to take into account the confining geometry. We find that a delayed polarity-velocity alignment mechanism with a delay time τ_{al} as studied in the physics of dense active matter systems (Henkes et al., 2011) is required to observe oscillations. We also find that below a critical confining length $L_x < L_X^c(\tau_{\mathrm{al}})$, all cells coordinate their motion and the tissue exhibits global oscillations while multi-nodal oscillations are observed for $L_x > L_X^c(\tau_{\mathrm{al}})$, consistent with experimental results.

This work was conducted in collaboration with experimentalists in the lab (V. Petrolli, M. Tadrous, M. Balland, T. Boudou, G. Cappello from the MicroTiss in LIPhy) and in the CEA-LETI research unit in Grenoble (C. Allier, O. Mandula, L. Hervé). We conducted the numerical modeling in collaboration with S. Henkes (Bristol University) and R. Sknepnek (Dundee University), who developed the SAMoS code for simulations of a Voronoi model for epithelial dynamics (Barton et al., 2017).

The chapter is organized as follows: in section 6.1 we review different theoretical approaches used to model collective oscillations in confluent monolayers. In section 6.2, we present the experimental setup used in the lab and the experimental results. In section 6.3 we present the Self-Propelled Voronoi (SPV) model used in our study and the numerical results are shown in section 6.4.

6.1 Models of collective cell oscillations in epithelial layers

In this section, we present a few theoretical and numerical approaches used to describe collective cell migration, in particular in confined environment.

Collective cell migration is defined as the coordinated movement of multiple cells that retain cell–cell junctions while coordinating their dynamics (Hakim et al., 2017). The mechanical properties of single cells, as determined mainly from their cytoskeleton, allow them to interact mechanically with their extracellular environment and with other cells. Forces are mainly transmitted via focal adhesions (protein complexes bridging the actin network to the extra-cellular matrix) and through cell-cell junctions that connect the cytoskeleton of adjacent cells. The mechanisms by which individual cells propel on a substrate are diverse and depend upon the cell type. Key processes involve cell polarization (i.e., determination of the front and the back of the cell), actin assembly and treadmilling as well as formation of new adhesion sites at the front, together with actin contraction and de-adhesion at the cell back. Understanding these processes at the bio-molecular level constitutes an extended research field, and is far beyond the scope of the work presented in this chapter. In epithelial monolayers, cell motion can, depending upon the cell type, either (i) be driven mainly by the mechanisms at play in single cell migration (as described above) or (ii) by adhesion between cells and cortical contractions inducing cell rearrangements (Hakim et al., 2017).

Particle-based models for collective cell migration, inspired from Vicsek-like models (Vicsek et al., 1995), have been developed to model the case where cell movements are mainly due to the propulsion of individual cells (i). On the other hand, the need to include a description of cell shapes and cell-cell interfaces emerges when cell motion in the monolayer is mainly controlled by interactions between neighbors rather than by locomotion on a substrate. This has motivated the development of cellular Potts and vertex models (that have been generalized to describe motile cells). Voronoi-based models, lie somehow at the interface between particle-based and vertex-based models since the degrees of freedoms are the cell centres, but the role of adhesion and contractility is described through a vertex energy computed from the tessellation of the cell centres.

6.1.1 Collective oscillations in microscopic models of epithelial dynamics

The general features of microscopic models have been presented in Chapter 1, section 1.4. We summarize here the main results regarding collective oscillations obtained within these models.

Particle-based models: In particle-based models, cell migration is modeled by introducing a self-propulsion force acting on the cell center of the particle. Various models inspired by the Vicsek model (Vicsek et al., 1995) exhibit steady state oscillations in the dense regime of confined assemblies of self-propelled particles. The general finding is that an alignment mechanism is required to observe oscillations.

Henkes et al. (2011) have proposed a model of self-propelled soft repulsive disks with a polar alignment mechanism. In this model, each cell propels along the direction of a polarity vector and its velocity arises both from the self-propulsion and from repulsive contact forces between particles. The cell's polarity aligns with the actual velocity with a lag time $\tau_{\rm al}$, leading to a positive feedback mechanism. In the dense regime and in a confined geometry (circular box of radius R with soft repulsive boundary conditions), particles are trapped by their neighbors, and their displacement oscillates around a mean position, resulting in an oscillatory behavior of the mean square displacement of the particles, leading to large scale oscillations in the

system. Henkes et al. (2011) further find that these oscillations are controlled by the low-frequency modes of the jammed packing.

Deforet et al. (2014) model radial oscillations using another particle-based model, where cells are modeled as persistent random walkers interacting with their neighbors, in a "Vicsek" fashion. The model exhibits breathing radial oscillations as in the experiments. The authors conclude that no specific mechanism is required for these oscillations to emerge, but are the natural consequence of oscillatory modes in a confined domain excited by the spontaneous stochastic motion of cells.

Voronoi model: Although oscillations were not yet reported in vertex or Voronoi models for epithelial tissues (which is the aim of the work presented in this chapter), such models were used to study collective cell migration. In a recent work, Giavazzi et al. (2018) evidenced both fluid and solid-like collective behavior in the form of "flocks" in the bulk of a monolayer (using periodic boundary conditions) using a Self-Propelled Voronoi (SPV) model with a similar coupling mechanism as the one introduced by Henkes et al. (2011). The coupling consists of a positive feedback that tends to align the self-propulsion direction to the velocity direction and is controlled by a parameter $J = 1/\tau_{\mathrm{al}}$, with τ_{al} the lag time for the feedback. The dynamical phases obtained when varying the values of the target shape index p_0 and the magnitude of the coupling J are shown in Fig. 6.1. Collective motion (in form of flocks) is reported for large values of the coupling magnitude J, and can be observed either in solid-like (Fig. 6.1(a)) or fluid-like systems (b), although flocking tends to promote solidification, as shown by the shift of the solid-like transition for increasing values of J in Fig. 6.1(e). For small coupling (low J), the system doesn't exhibit coordinated motion and can be either a stationary solid or a stationary fluid (Fig. 6.1(c)-(d)

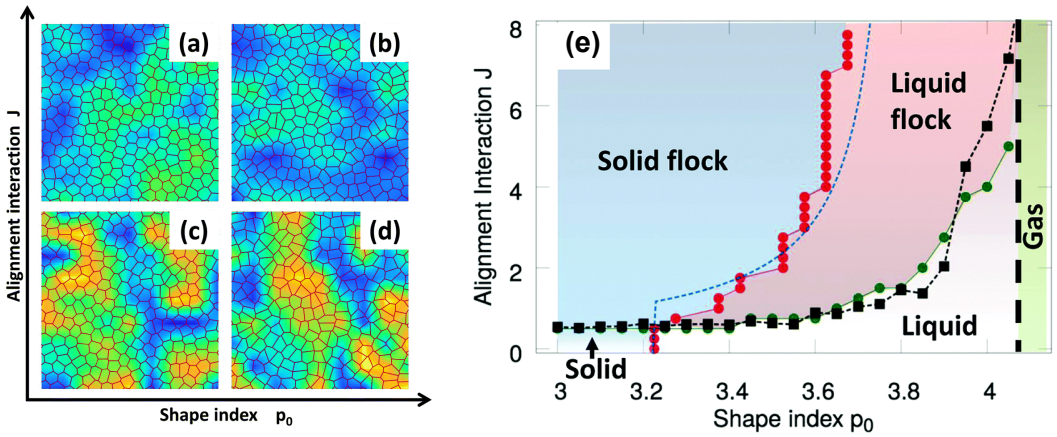

FIGURE 6.1: Adapted from Giavazzi et al. (2018): **Phase diagram of a Self-Propelled Voronoi model endowed with a positive feedback mechanism between the self-propulsion direction and the velocity direction** with a lag time $1/J$. In panels (a)-(d) the color code represents the angle of velocity with respect to the horizontal so a uniform color indicates coherent migration in a given direction. For strong coupling (large J) collective motion is observed: (a) liquid like flocking state and (b) solid-like flocking state. For weak coupling, the system is either a (c) stationary solid or (d) liquid. (e) Phase diagram summarizing the different dynamical phases. (see the article for details about how transitions lines were obtained (Giavazzi et al., 2018).)

Phase-field models: Apart from particle-based and vertex-based models, phase-field descriptions, where each cell is modeled as a highly-deformable self-propelled object have also been used to model the dynamics of confluent tissues (Palmieri et al., 2015). The main difference with the previously cited models is that it enables to model larger cell deformations that can be relevant in the dynamics of epithelial layers. This approach has been used to model confined epithelial monolayers in a parallel study in the work by Peyret et al. (2019). Using a dynamics for the polarity (direction of self propulsion) similar to that of Henkes et al. (2011) and Giavazzi et al. (2018), the authors have evidenced velocity oscillations in anisotropic confinement conditions. The characteristic of these oscillations are very similar to what we report in this study and will be further discussed at the end of this chapter.

6.1.2 Continuum models

Notbohm et al. (2016) have developed a continuum model of epithelial tissue based on an active elastic medium description, where the mechanical variables are coupled to internal fields related to the biological activity. Unlike in the previous models, multiple coupling terms are introduced in the model, due to the fact that two internal fields are considered: a dimensionless vector polarization field (direction of cell propulsion on the substrate) and a scalar field describing the concentration of a chemical controlling cell contractility (e.g., concentration of molecular motors). The displacement field is coupled to the chemical concentration (which obeys a reaction-advection dynamics) such that a local increase in cell area generates a local increase in the contractile stress. The polarization field also has its own dynamics: it relaxes to an homogeneous state with a characteristic time, and tends to align to its nearest neighbors. There is also an active coupling between the polarization and the gradient of chemicals, so polarization is favored in regions of higher contractility.

The motivation to introduce two independent internal fields comes from the fact that the authors aim at capturing a specific experimental observation in their model: the misalignment between traction force and cell velocity. This model enables to reproduce the spontaneous oscillations of the velocity field in epithelial tissues confined to a circular pattern, alternating between inward and outward motion, as reported in the experiments of Deforet et al. (2014) and Notbohm et al. (2016). This model suggests that a feedback between mechanical strain and cellular contraction is required to generate collective oscillations. This is consistent with their experiments, where oscillations are eliminated when contractility is inhibited. Moreover, this work suggests that most of the elasticity in the tissue is of active origin due to the coupling between strain and contractility, with a decrease in effective modulus and oscillation frequency when contractility is inhibited.

Pajic-Lijakovic et al. (2020) proposed another modeling approach to describe oscillations in epithelia, where a viscoelastic resistive force caused by a residual stress accumulation during cell migration is capable of inducing apparent inertial effects, by analogy with elastic turbulence effects observed in the flow of complex fluids at low Reynolds number.

6.1.3 Related models

Waves in spreading epithelia: The model studied by Notbohm et al. (2016) is actually an extension of the model of Banerjee et al. (2015) first used to describe propagating waves in a spreading epithelium, as observed in the experiments of Serra-Picamal et al. (2012). In these experiments, waves arise at the front of the expanding

layer and propagate backwards, with the wave velocity direction opposed to the cell velocity direction. The model of Banerjee et al. (2015) predicts a wave velocity depending upon the effective elasticity of the monolayer, with an effective mass density (inertia) of the form $\zeta\tau_c$ with ζ the friction coefficient for viscous friction with the underlying substrate and τ_c the timescale for myosin turnover. Note that the viscoelastic model of Pajic-Lijakovic et al. (2020) was also used to describe waves in spreading epithelia. There were also other continuum models developed to describe oscillations in spreading epithelial tissues, in absence of confinement. The work by Blanch-Mercader et al. (2017b) for instance, also motivated by the experiments of Serra-Picamal et al. (2012) is based on an active viscous fluid description. This theory describes a 2d compressible active polar fluid with nematic elasticity. It appears that for sufficiently high active stresses, the homogeneously polarized state becomes unstable, and the model predicts the emergence of traveling waves. Interestingly, this model also exhibits an effective elastic-like behavior of active origin while the model is based on an active fluid description. The continuum model of Tlili et al. (2018), based on a delayed coupling between strain and polarity and assuming a Maxwell-like viscoelastic behavior of the monolayer also predicts waves in a migrating epithelium. The cell velocity is in phase opposition with the cell density, and similarly, the wave propagation velocity decreases with an increase in cell density.

Mechanical excitability models: We would like to mention here another class of models, which, by accounting for "mechanical excitability" of epithelia, can also lead to oscillatory dynamics. The general idea behind these models is to couple rapid threshold phenomena to slow refractory phenomena as in action potential propagation. Serra-Picamal et al. (2012) model oscillations of the stress field in an expanding epithelium using a model in which cells can migrate only if the density is sufficiently small coupled to a non-monotonic time evolution of the cytoskeleton stiffness. In their model, reinforcement and fluidization of the cytoskeleton act over disparate timescales, and hence lead to a propagating mechanical wave.

Other studies investigate oscillatory dynamics in tissue using threshold-based activation dynamics models, such as the study of Idema et al. (2013) reporting mitotic waves in the *Drosophila* embryonic development and proposing a bio-mechanical model for signal propagation. Finally, recent works have studied propagative waves of the extracellular signal-related kinase (ERK) protein, involved in biological processes such as cell proliferation, differentiation and cell motility (Aoki et al., 2017; Ogura et al., 2018), for which models based on switch-like activation dynamics have been proposed (Ogura et al., 2018).

6.1.4 Concluding remarks

All the microscopic modeling approaches used to model velocity oscillations in confined tissues rely on a delayed velocity alignment mechanism. This mechanism is most often encoded in the dynamics for the polarity of the cell (i.e., the direction of self-propulsion), which tends to align to the direction of the cell velocity (Henkes et al., 2011; Giavazzi et al., 2018), or to the direction of the force exerted onto the cell (Peyret et al., 2019), with a lag time τ_{al}. In the case of the particle-based model introduced by Deforet et al. (2014), cells explicitly adapt their velocity to that of their first neighbors.

The continuum approach of Notbohm et al. (2016) relies on a chemo-mechanical feedback between mechanical strain, contractility (described by a myosin concentration field), and polarization. This modeling approach seems to be versatile since a

similar model accounts for oscillations in a spreading epithelia (Banerjee et al., 2015). A strain-polarization coupling approach has also been used by Tlili et al., 2018 to describe oscillations emerging in a migrating monolayer without cell proliferation. On the other hand, mechanical excitability models offer an alternative way to model collective oscillations in epithelial tissues (in the non-confined case).

Although delayed feedback mechanisms seem to be generic ingredients in both microscopic and continuum approaches describing oscillations in models of epithelial layers, their bio-molecular origin often remains unclear. It is in general difficult to measure experimentally the values of model parameters such as the lag time involved in feedback mechanisms.

What determines the waves characteristics in a confined geometry also remains a largely open question. As proposed by Henkes et al. (2011) and Deforet et al. (2014), the motion of cells with an intrinsic timescale for alignment playing the role of an effective inertia might be sufficient to excite the oscillatory modes of the confined domain. In the (bulk) Voronoi model studied by Giavazzi et al. (2018), such a mechanism for alignment has been shown to induce collective migration in the form of flocks. The typical size of flocks or swirls in epithelial tissues, as determined from the cell velocity correlation ("Velocity fields in a collectively migrating epithelium"), has been shown to be around 150 to 200 μm. Coordinated motion of the monolayer is thus expected when confining the cells in patterns whose size is smaller than this correlation length, as evidenced in small circular patterns by Deforet et al. (2014). Further, the confinement size is thought to play an important role in oscillation dynamics since the period of radial (breathing) oscillations increases with the radius of the confining disk. The geometry of the confining setup can actually be simplified in order to disentangle the effect of various parameters, such as anisotropy and size for instance[3]. In particular, using a very strong confinement along one spatial dimension enables one to get directed migration along the other dimension, thus simplifying the analysis of the velocity fields in experiments.

In order to characterize the waves appearing due to the effect of confinement, we use in our study simple rectangular confining patterns, with a fixed width of size 40 μm) smaller than the typical velocity correlation length in unconfined tissues (about 150 μm ("Velocity fields in a collectively migrating epithelium")). We are thus left with a single control parameter, the length of the pattern (L_X), to tune the oscillations in our system. We detail in the following the experimental approach used in this work.

6.2 Experiments on confluent epithelial monolayers

The experimental work summarized in this section is part of the PhD thesis work of Vanni Petrolli (Petrolli, 2019).

6.2.1 Experimental methods

The experimental methods are described briefly here and more details can be found in Petrolli (2019) and Petrolli et al. (2019). Epithelial Madin-Darby Canine Kidney (MDCK) cells are confined to a quasi one-dimensional pattern, by preparing adherent stripes on soft polyacrylamide gels (of stifness E $\simeq$ 40 kPa), as described by Vignaud et al. (). Stripes of different length (L_X = 100 to 2000 μm), but of the same width (L_Y = 40 μm), are patterned on the same substrate. MDCK cells are then seeded

[3] A study conduced in parallel to ours by Peyret et al. (2019) is also based on rectangular patterns and yields a similar phenomenology.

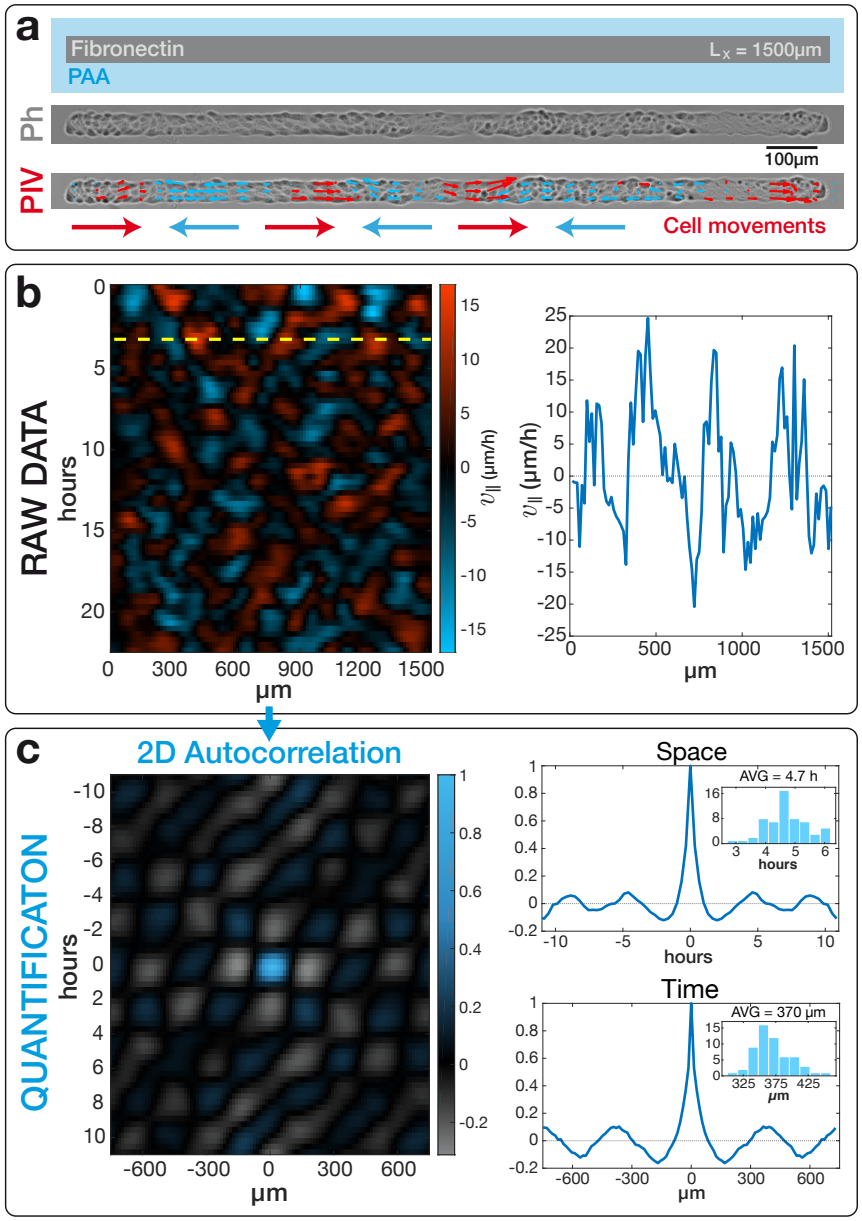

FIGURE 6.2: From Petrolli et al. (2019). **Velocity oscillations in MDCK epithelial monolayers**. (a) *Top*: MDCK cells seeded onto a polyacrylamide (PA) gel patterned with fibronectin stripes (width: $L_Y = 40$ μm, length: $L_X = 1500$ μm). *Middle*: phase-contrast image of a confluent monolayer. *Bottom*: velocity field measured by PIV. Velocities pointing in the positive (negative) x-axis direction are shown in red (blue), in agreement with the arrows reported under the image.(b) *Left*: kymograph representing the average horizontal velocity $v_\parallel(x;t)$ in time. *Right*: an example of velocity profile along the dashed line. The low frequency drifts are removed using a Gaussian high-pass filter. (c) The spatio-temporal autocorrelation of the kymograph is computed to quantify the periodicity of oscillations (*left*) and measure peak spacing along the spatial (*top-right*) and temporal (*bottom-right*) coordinates (insets: distribution of peak periodicity for n=59 independent stripes). Images in panels (*b - left*) and (*c - left*) were smoothed for visualization purposes with a low-pass Gaussian filter (σ_x=15 μm, σ_t=30 min).

on the patterned substrates with initial concentration of $2.5 \pm 0.5{\cdot}10^4$ cells/cm^2. The samples are washed with fresh medium 1h after seeding, then placed in the incubator (37° C and 5% CO_2) until the end of the experiments. Cells are imaged *in situ* using in-line holographic (defocus) microscope (see Supplementary Information of Petrolli et al., 2019 and references therein) for $\simeq$ 48 hours after confluence, gathering one image every 10 minutes.

Cell velocities are computed with a custom-made Particle Image Velocimetry (PIV) algorithm with a final resolution of 20 min and 14 μm (see an example of velocity field in Fig. 6.2(a), bottom). To generate the space-time kymographs, videos are cropped in time to consider only confluent monolayers, in an interval where the average speed is higher than 4 μm/h ("Velocity fields in a collectively migrating epithelium").

While cells confined to a square surface have a ratio of mean velocities $\langle|v_x|\rangle/\langle|v_y|\rangle \simeq 1$, the ratio increases up to 4 for rectangular confinement with $L_x = 500\mu m$ and $L_y = 40\mu m$ ($L_x/L_y = 12.5$). In the following, only the horizontal (x) component of the velocity will be considered, and averaged along the transverse direction (of width L_y) of the confining area: $v_\parallel(x;t) = \langle v_x(x,y;t)\rangle_y$. Low frequency drifts are then removed using a Gaussian high-pass filter cropping 50% of the signal at 700 μm and 10 h.

6.2.2 Experimental results

Velocity oscillations in confined epithelial monolayers

The kymograph in Fig. 6.2(b)-*left* represents the spatio-temporal evolution of the velocity field over 22 hours and over the whole stripe. A typical instantaneous velocity profile (Fig. 6.2(c)-*right*) displays periodic oscillations in space. To quantify the period and the wavelength of these oscillations, the autocorrelation function of the kymograph is computed $g(\delta x, \delta t) = \langle v_\parallel(x,t)\ v_\parallel(x+\delta x, t+\delta t)\rangle_{x,t}$ and displayed in Fig. 6.2(c)-*left*. An oscillating pattern can be observed in the autocorrelation function, both along the spatial and the temporal directions (Fig. 6.2(c)-*right*). This pattern indicates the establishment of an extended multi-nodal standing wave, with wavelength and period equal to $\lambda = 370 \pm 30$ μm and $T = 4.7 \pm 0.7$ h, respectively (errors represent the standard deviation, with $n = 59$ samples) (see histograms in Fig. 6.2(c)-*right*).

Transition between wave-like migration modes

In approximately 95% of the experiments, two types of behaviors are observed: (i) a global movement of all cells alternating between rightward and leftward motion (as seen from the autocorrelation function of the kymograph in Fig. 6.3(a)) and (ii) the establishment of a multi-nodal standing wave with cells moving back and forth and cells at the nodes being alternately compressed and dilated (Fig. 6.3(b)).

The length of the pattern L_X is varied between 100 μm and 2000 μm (examples between 200 μm and 1000 μm are shown in Fig. 6.3), in order to assess the influence of the confining length on the oscillatory behavior. The incidence of the two behaviors strongly depends on L_X, with a transition for $L_X \simeq \lambda$. Fig. 6.3(c) quantifies the transition, with on average 39 monolayers per point, obtained from three independent experiments. In the experiments with $L_X < 200$ μm, the global oscillation statistically dominates. In this case, the period scales approximately linearly with the monolayer size (Fig. 6.3(d), blue area), while the wavelength is imposed by the confinement. In large structures ($L_X > 500$ μm), only multi-nodal waves are observed, with the period and wavelength independent of L_X (Fig. 6.3(d), red area).

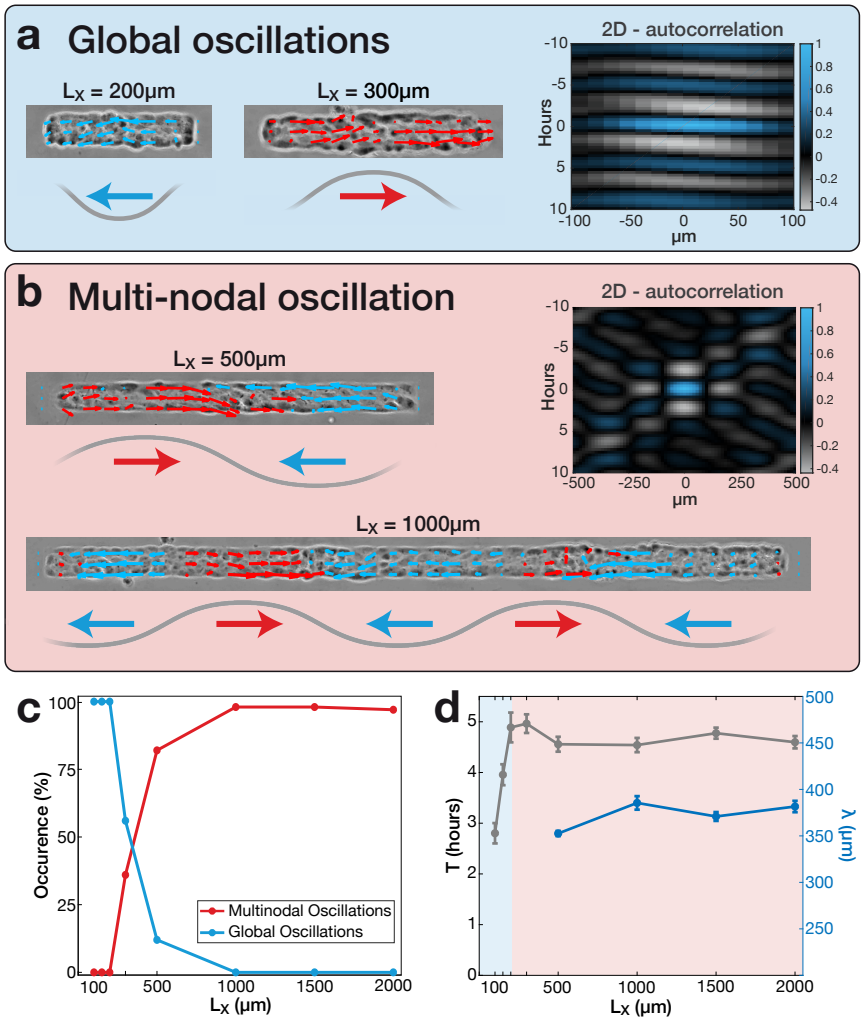

FIGURE 6.3: From Petrolli et al. (2019). **Dependence of oscillatory behavior on the stripe length**. (a) The velocity field superimposed on phase contrast images for short stripes of length 200 μm and 300 μm displays global oscillations, generating a characteristic two-dimensional autocorrelation (*right*). (b) Longer lines (500 μm and 1000 μm) display multi-nodal oscillations which give rise to a different pattern in the autocorrelation image (*right*). Velocities pointing in the positive x-axis direction are represented in blue, those pointing in the negative x-axis direction are represented in red, in agreement with the arrows reported in the schemes under each image. For each length, we display (c) the frequency of each phenotype and (d) the characteristic time and space periodicity calculated. Bars represent the standard error of the mean.

The wave velocity does not depend on monolayer length

Using the typical period and wavelength, an effective velocity $u_\phi = L_X/T \simeq 78 \pm 13$ μm/h can be defined, which is independent of the pattern size. Even for small patterns (L_X <500 μm), this velocity is preserved as the period scales linearly with the pattern length. We also note that u_ϕ is approximately ten times larger than the average speed of individual cells within the epithelial layer (between 4 and 12 μm/h, depending on cell density ("Velocity fields in a collectively migrating epithelium"; Puliafito et al., 2012)). This value of wave velocity is in the same range as other

results from the literature, finding velocities between 10 and 60 μm/h (Pajic-Lijakovic et al., 2020).

6.2.3 Concluding remarks

The experiments performed by V. Petrolli during his PhD (Petrolli, 2019; Petrolli et al., 2019) reveal the following features: (i) epithelial monolayers confined to quasi 1d substrates exhibit velocity oscillations. (ii) Upon increasing the confining length L_X there is a transition between two different types of velocity oscillations: global oscillations for small patterns and multi-nodal oscillations for large patterns. (ii) For small patterns, the time period of oscillations scales approximately linearly with the confining length. (iv) The wave propagation velocity is independent of the confining length.

In the following section, we study a numerical model based on a Voronoi description of epithelial monolayers, the self-propelled Voronoi model (Bi et al., 2016; Barton et al., 2017; Giavazzi et al., 2018) to study the dynamics induced by confining boundary conditions. We will investigate what are the necessary ingredients in the dynamics to observe velocity oscillations, and test the above listed features.

6.3 Numerical model

We consider a computational framework based on a recently introduced self-propelled Voronoi model (SPV) (Bi et al., 2016; Barton et al., 2017; Giavazzi et al., 2018).

6.3.1 Description of the model

The model used in this study is similar to that used by Giavazzi et al. (2018) to describe flocking transitions in confluent monolayers, but rather than using periodic boundary conditions, we imposed confinement through a repulsive rectangular wall of size (L_X, L_Y) to reproduce the experimental geometry. The confluent cell monolayer is modeled as a two-dimensional network of Voronoi polygons covering the plane (Voronoi tessellation of all cell centre positions, see Fig. 6.4). Each configuration of the monolayer is described by the positions of cell centroids with an energy given by the commonly used Vertex Model (Farhadifar et al., 2007),

$$E = \sum_{i=1}^{N_{\text{cells}}} \frac{K}{2} (A_i - A_0)^2 + \sum_{i=1}^{N_{\text{cells}}} \frac{\Gamma}{2} (P_i - P_0)^2 \tag{6.1}$$

N_{cells} is the total number of cells, A_i and P_i are the area and perimeter of the i-th cell, K and Γ are the area and perimeter stiffness respectively, and A_0 and P_0 are the target area and perimeter, identical for all cells. In most of the simulations, these parameters were chosen to describe a monolayer rather in a solid-like regime (with a shape factor $p_0 = P_0/\sqrt{A_0} = 2.5$ - 3.4) (Bi et al., 2014; Bi et al., 2016), to avoid shear flows induced by the boundaries.

As in the works of Bi et al. (2016), Barton et al. (2017), and Giavazzi et al. (2018), we consider an overdamped dynamics, i.e., a force balance between frictional force with the substrate, self-propulsion at a constant velocity v_0 along the direction of cell polarity, $\vec{n}_i$, and mechanical forces between the cells determined as a negative gradient with respect to cell position of the SPV model energy functional $\vec{F}_i$. $\vec{F}_i = -\nabla_{\vec{r}_i} E$ is the force arising from the monolayer energy and from a soft-core repulsion introduced to stabilize the simulations (described as a quadratic potential of stiffness k_{cc} with an

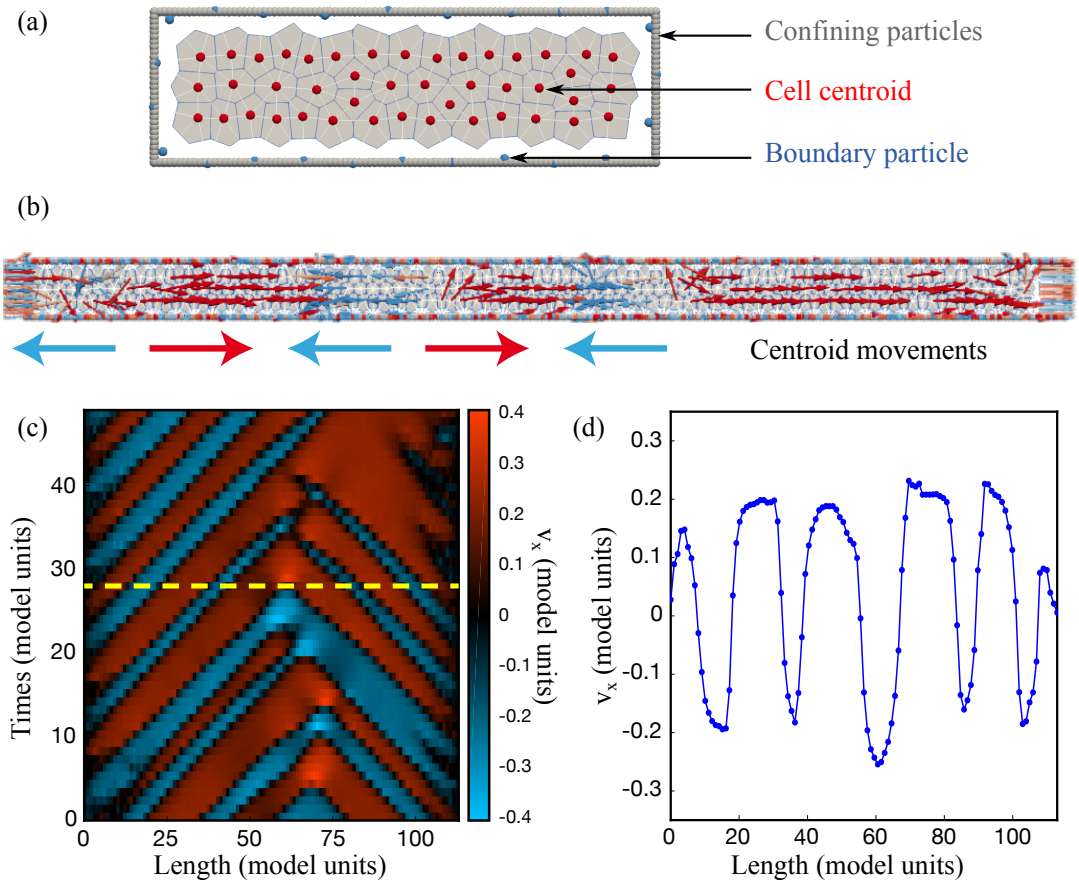

FIGURE 6.4: **Example of simulation data for the SPV model with confining boundary conditions.**. (a) SPV configuration for a system size $L_X = 25$ where cell centroids are colored in red, boundary particles in blue and confining repulsive particles in grey. (b) SPV configuration for a system size $L_X = 113$. Velocity field superimposed to the monolayer configuration with positive x-velocities in red and negative x-velocities in blue. (c) Space-time kymograph of the x-component of the cell velocity (averaged over the transverse dimension, y). (b) Instantaneous velocity profile plotted along the x-direction exhibiting spatial oscillations (for parameters $v_0 = 0.2$, $p_0 = 2.5$ and $\tau_{\text{al}} = 0.3$)

interaction radius of half the typical distance between cell centers a_c) Barton et al., 2017.

$$\gamma \frac{\partial \vec{r}_i}{\partial t} = f_a \vec{n}_i + \vec{F}_i + \vec{\nu}_i(t) \tag{6.2}$$

$\vec{\nu}_i(t)$ is an uncorrelated stochastic force and $f_a \vec{n}_i$ models the self-propulsion force.

The value of v_0 can be set to match the experimental observations, but does not affect the general oscillatory behavior (see Appendix E, Fig. E.3). The dynamics of the cell polarity $\vec{n}_i$, described by the angle θ_i with the x-axis of the laboratory reference frame (i.e., $\vec{n}_i = (\cos\theta_i, \sin\theta_i)$) are

$$\frac{\partial \theta_i}{\partial t} = \frac{1}{\tau_{\text{al}}} \sin(\theta_i - \phi_i) + \nu_i^r(t), \tag{6.3}$$

with ϕ_i being the angle between the velocity of cell i and the x-axis, and $\nu_i^r(t)$ being an orientational Gaussian noise. The angular dynamics is thus controlled by the interplay

of rotational diffusion (kept constant in this study) and the polarity-velocity alignment with rate τ_{al}^{-1}, with τ_{al} being the time required by the cell to reorient its polarization in the direction of its velocity. This feedback mechanism leads to oscillations in confinement, where the lag time τ_{al} introduces an effective inertia into the system, and the oscillations are along the lowest-energy elastic modes of the material (Henkes et al., 2011). This feedback mechanism is also at the origin of flocks in unconfined monolayers (Giavazzi et al., 2018). Cell division can also be included in this model (and is used in our simulations to prepare monolayer configurations, see Appendix E.1) but does not affect the oscillations, as reported in previous works (Deforet et al., 2014; Tlili et al., 2018).

6.3.2 Methods and data analysis

We use the SAMoS implementation of the SPV model as described in detail by Barton et al. (2017) for which the source code can be found at https://github.com/sknepneklab/SAMoS. This implementation enables for open flexible boundaries which is convenient to model systems with a small number of cells as it is the case in the confined monolayers experiments. Details regarding the numerical implementation of confining boundary conditions are given in Appendix E.1. All the simulation parameters are also provided in Appendix E.1. An example of monolayer configuration obtained with the SPV model with confining boundary conditions is shown in Fig. 6.4(a).

6.4 Simulation results

We first present the results obtained using the SPV model choosing parameters describing a monolayer in a rather solid-like state ($p_0 \leq 3.1$) with a fixed value of the lag time $\tau_{\text{al}} = 0.3$, and show that this model exhibits steady state oscillations of the cell velocity. We further show that when increasing the confining length, the system undergoes a transition from global to multi-nodal oscillations, as observed in experiments. We then discuss the role of the lag time τ_{al}. Preliminary results regarding how waves are affected by changes in the monolayer properties such as, e.g., its target shape index p_0 or its elastic properties are discussed in the last section.

6.4.1 Oscillations in a Self-Propelled Voronoi model

We first consider the case of long confining channels, where multi-nodal oscillations were observed experimentally (Fig. 6.2). The simulation results displayed in Fig. 6.4(b-d) are obtained for a system with the same transverse confining length L_Y (about 3 cells in $y-$direction) and aspect ratio as in the experiments of Fig. 6.2 (and a value $\tau_{\text{al}} = 0.3$). We observe a pattern in the x-component of the velocity, v_x, and using the same analysis tools as in Fig. 6.2, we extract the wavelength $\lambda_{\text{SPV}} \approx 22$ model length units and the period $T_{\text{SPV}} \approx 8$ model time units. Note that by approximately matching the timescale of the model to the experiments (through the self-propulsion velocity v_0[4]), one would get from these simulation data $\lambda \approx 300$ μm and for the period $T \approx 2$ hours. This indicates that this model is able to reproduce the features observed in the experiments, although some fine tuning of parameters (τ_{al}, v_0) is required for a quantitative match. Note that although the instantaneous velocity profiles Fig. 6.4(b)) appear to be similar to the experiments, the full spatio-temporal

[4]Changing the self-propulsion velocity v_0 only affects the amplitude but leaves the period of oscillations unchanged, as shown in Appendix E.

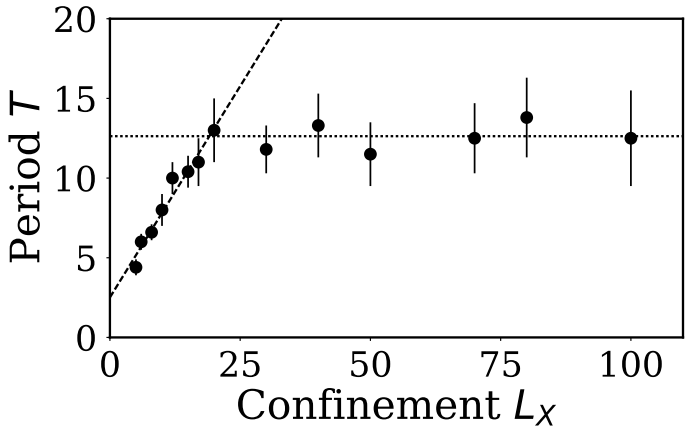

FIGURE 6.5: **Temporal period of velocity oscillations as a function of confining length** L_X (for parameters $v_0 = 0.2$, $p_0 = 3.1$ and $\tau_{\rm al} = 0.3$). Dashed line: linear fit $T = aL_X + b$ with $a = 0.53$ and $b = 2.51$. Dotted line: average period $T_{\rm max} = 12.6$ model time units in the large system regime.

dynamics of the model (Fig. 6.4(a)) does not correspond to standing wave oscillations, but rather to propagating waves. The precise mechanisms by which standing waves could appear in experiments thus remain to be understood.

6.4.2 Evolution of oscillations with the confinement

If the system size L_X is decreased (keeping the value of $\tau_{\rm al}$ constant), the number of nodes also decreases down to a point where the system size can only accommodate a single spatial period of oscillation, reaching a regime of global oscillation, where the direction of motion of all cells is coordinated. In the small system regime (when the oscillation wavelength is bounded by the system size), the oscillation period increases linearly with the system size, as shown in Fig. 6.5 and previously reported by Deforet et al. (2014) and Notbohm et al. (2016). When the system size exceeds a critical length L_X^c, the time period saturates to a value T^*, as observed in experiments (see Fig. 6.3). The increase of the period with the length L_X is reminiscent of elastic waves (vibrating string for instance). The role of elasticity will be further investigated in the next section.

6.4.3 Role of the delayed feedback mechanism

A delayed feedback mechanism is required to observe oscillations

The transition from global to multi-nodal oscillations upon increasing the system size is shown in the $\tau_{\rm al} - L_X$ plane in Fig. 6.6. The feedback timescale plays an important role since no oscillations are observed if $\tau_{\rm al}$ is too large (i.e., the noise dominates over the coupling) and the critical length L_X^c at which one observes multi-nodal oscillations increases with $\tau_{\rm al}$. The phase diagram of Fig. 6.6, was constructed using a timescale for the decorrelation of the orientation equal to $\tau_r = 10$, thus explaining the transition from the "global oscillations" regime to the absence of oscillations when the feedback timescale becomes larger than τ_r.

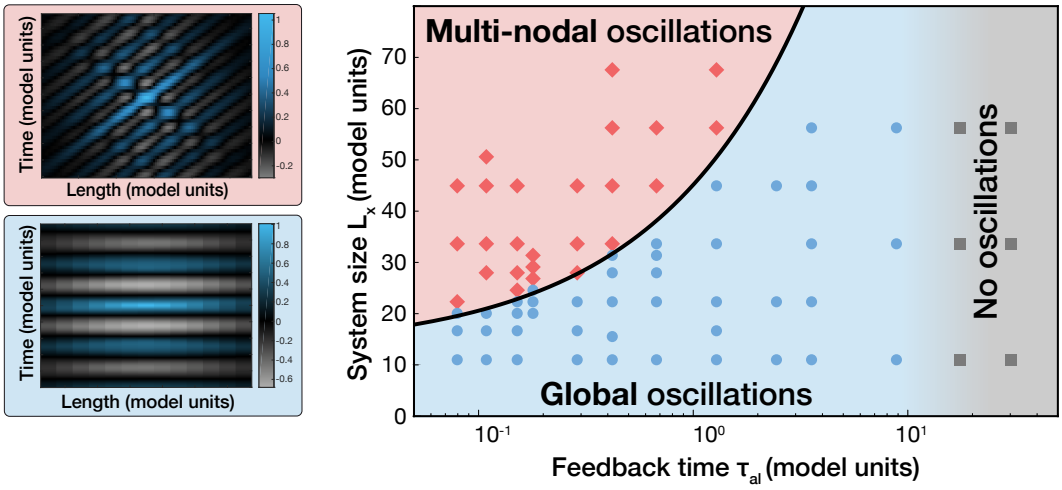

FIGURE 6.6: **Phase diagram of oscillation patterns in the SPV model in the $(\tau_{\mathrm{al}} - L_X)$ plane.** Two types of oscillations are observed depending upon the system size L_X: *Top left*: For large systems where $L_X > L_X^c(\tau_{al})$ the autocorrelation of the kymograph shows multi-nodal oscillations whereas for small systems (*bottom left*) where $L_X < L_X^c(\tau_{al})$ the autocorrelation exhibits global oscillations. *Right*: Simulation data points indicating whether the system exhibits global (blue disks), multi-nodal (red diamond), or no oscillations (grey squares symbols) for large values of the feedback timescale ($\tau_{al} > \tau_{al}^c \approx 17$ model time units). The solid line delimiting the global and multi-nodal oscillation phases is a power law fit of the transition data points ($L_X^c(\tau_{al}) = a\tau_{al}^b + c$ with $a \simeq 32$, $b \simeq 0.62$, $c \simeq 13$).

The feedback mechanism induces a delay between the velocity and the polarity, as illustrated in Fig. 6.7. This effect was confirmed in experiments by Peyret et al. (2019) who measured a time delay between the cell velocity and the traction force exerted onto the substrate, with a typical realignment time of the order of 30 min.

Evolution of the wave velocity with the feedback timescale

We measure the propagation velocity in simulations of a long monolayer ($L_X = 100$) for various values of the feedback timescale τ_{al} and target shape index p_0, with $v_0 = 0.2$, $K = \Gamma = 1$. Propagation velocity measurements are performed using the Hough transform of the autocorrelation of kymographs (see Appendix E.1.3), and the results are depicted in Fig. 6.8(a). The propagation velocity c decreases as the alignment timescale τ_{al} is increased and scales as a power law: $c \sim \tau_{\mathrm{al}}^{-\alpha}$, with $\alpha = 0.51 \pm 0.12$. The value of the exponent close to 0.5 supports the hypothesis of the feedback timescale playing a role of effective inertia at the origin of oscillations.

We also note in Fig. 6.8(a) that the wave velocity decreases monotonously as p_0 is increased. This is not surprising since the elastic constants of the material depend on p_0 (Sussman et al., 2018), and this is a first indication that the elastic properties of the monolayer influence the oscillations.

We also measure the period of oscillations for a small system ($L_X = 15$) exhibiting global oscillations in Fig. 6.8(b). The period T increases with the alignment timescale τ_{al}, as reported by Peyret et al. (2019). The data fit suggests a scaling form: $T \sim \tau_{\mathrm{al}}^{\beta}$ with an average exponent $\beta = 0.55 \pm 0.15$. Note that Peyret et al. (2019) found a linear increase, although they fitted the data over a smaller range of values of $\tau_{\mathrm{al}} = 10 - 50$.

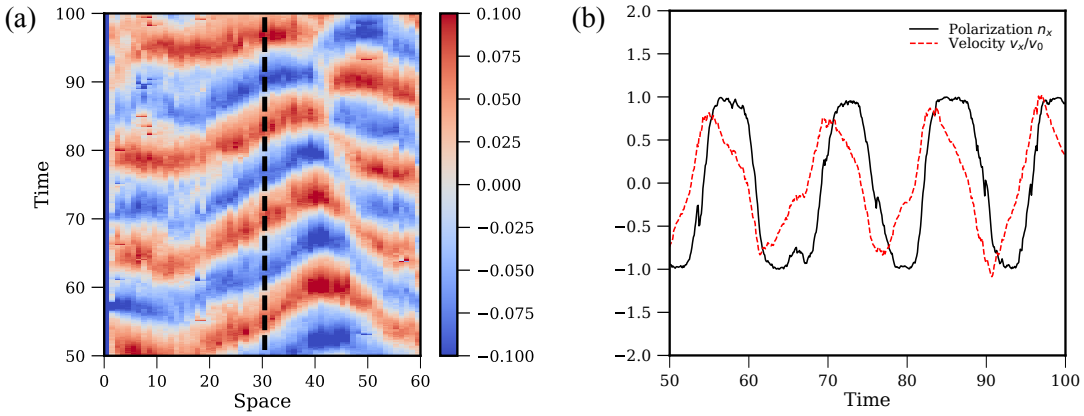

FIGURE 6.7: **Time delay between velocity and polarity**. (a) Space-time kymograph of v_x (averaged over the y dimension) and (b) Time evolution of v_x and of the polarity n_x (averaged over y) at a location indicated by the dashed line in (a) exhibiting a time delay between the polarization and the velocity due to the delayed feedback mechanism.

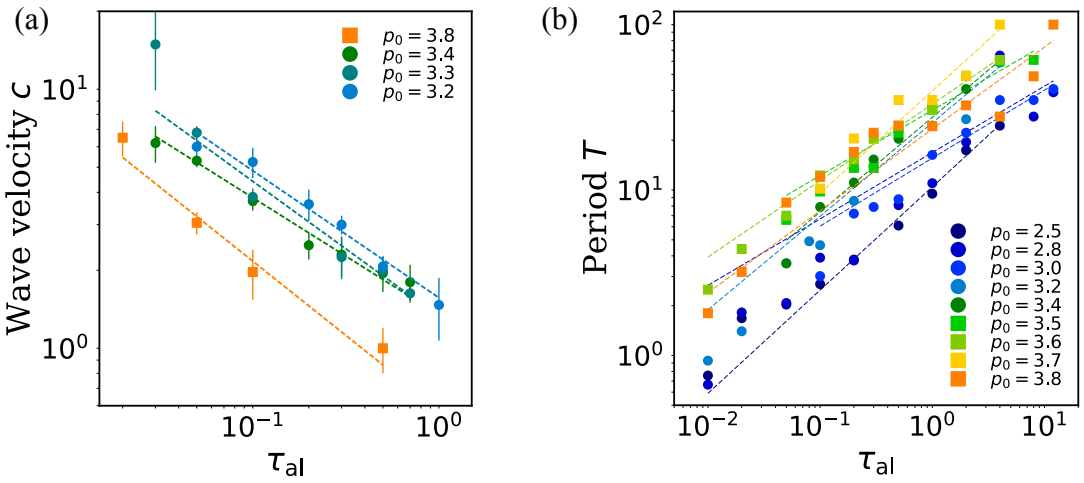

FIGURE 6.8: **Evolution of wave propagation velocity and period with τ_{al}**. (a) Wave propagation velocity c as a function of τ_{al} for a system of length $L_X = 100$ (multi-nodal regime), with $v_0 = 0.2$, $K = \Gamma = 1$ for various values of the target shape index p_0. Dashed lines are power law fits with exponents: -0.49 ± 0.05 (black), -0.52 ± 0.05 (blue), -0.45 ± 0.04 (green), -0.57 ± 0.09 (red). (b) Oscillation period T as a function of τ_{al} for a system of length $L_X = 15$ (global oscillations regime). Dashed lines are power law fits (see text).

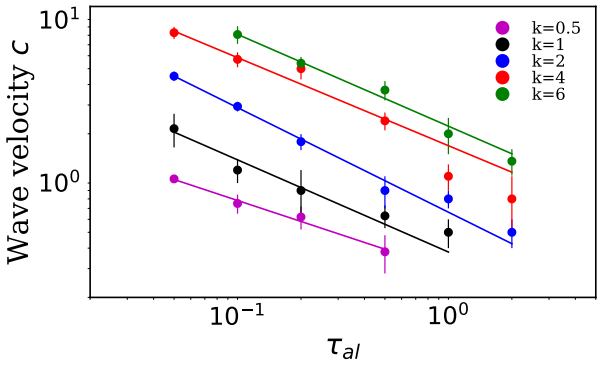

FIGURE 6.9: **Evolution of wave propagation velocity with τ_{al} in a system of repulsive particles** for a system of length $L_X = 100$, with $v_0 = 0.2$, for various values of the interaction potential stiffness k. Dashed lines are power law fits with exponents: -0.43 ± 0.04 (magenta) -0.57 ± 0.08 (black), -0.63 ± 0.04 (blue), -0.54 ± 0.07 (red), -0.56 ± 0.04 (green).

As shown in Fig. 6.5, the period T increases linearly with the system size for small system regimes, $T \sim L_X$, so we expect that the maximum period $T_{\max} \sim L_X^c \sim \tau_{\rm al}^\beta$. The fit of Fig. 6.6 yields $L_X^c(\tau_{al}) = a\tau_{al}^b + c$ with $b \simeq 0.62$, consistent with our estimate $\beta = 0.55 \pm 0.15$.

To test the robustness of this scaling, we also performed simulations without the vertex energy and by only considering repulsive interactions between the centroids of the Voronoi tessellation. This change in the model does not affect significantly the waves. The wave velocity as a function of $\tau_{\rm al}$ for various values of the stiffness k are shown in Fig. 6.9. We find a similar scaling, with an average exponent $\alpha = 0.54 \pm 0.13$.

6.5 Discussion and preliminary results

In this chapter, we characterized the oscillations emerging in a Self-Propelled Voronoi model due to a coupling mechanism between the direction of self-propulsion and the forces exerted on a cell. Our results suggest that oscillations arise in a generic manner when a feedback mechanism with a lag time leads to the alignment of cell velocity and self-propulsion force with no strong dependence on the details of interactions, as the same phenomenology is observed when considering the full vertex interactions or only repulsive interactions between cell centroids. We also find that the waves properties (wave velocity, period) do not depend on v_0, the magnitude of the self-propulsion velocity (see Appendix E, Fig. E.3).

We studied the oscillations by focusing on a rather solid-like regime (choosing values of p_0 comprised between 2.5 and 3.1). In section 6.5.1, we show preliminary results regarding the oscillations when the target shape index p_0 is varied, and propose the (preliminary) phase diagram of Fig. 6.10, suggesting an analogy between flocks in the unconfined SPV and oscillations in the confined SPV model.

We evidenced that the wave velocity is affected by the lag time for alignment, with a scaling $c \sim 1/\sqrt{\tau_{\rm al}}$. This points towards the description of elastic waves with an effective inertia, where we would expect a scaling of the wave velocity of type $c \sim \sqrt{\mu/\zeta\tau_{\rm al}}$ or $c \sim \sqrt{(\mu + B)/\zeta\tau_{\rm al}}$ with μ and B being respectively the shear and bulk moduli of the monolayer and ζ the friction coefficient with the substrate. Relating (macroscopic) elastic moduli to microscopic parameters is however not an easy task

and has been addressed in the unconfined SPV model in a recent work by Sussman et al. (2018). It is however not clear yet how the results of Sussman et al. (2018) could be used in our case since the confinement adds geometrical constraints to the system, impacting, e.g., the average area. Using the values of bulk and shear moduli measured by Sussman et al. (2018) and assuming a relation of type $c \sim \sqrt{(\mu + B)/\zeta\tau_{\mathrm{al}}}$ yields the right order of magnitude for the wave velocity in the solid-like regime, although slightly overestimated. A careful characterization of the elastic properties of the monolayer in the confined case should thus be performed. In section 6.5.2, we show preliminary results regarding the evolution of the wave velocity as a function of Γ, the (microscopic) parameter describing perimeter elasticity, suggesting that the elastic properties of the monolayer indeed affect the wave velocity.

Testing these scalings in experiments is however not an easy task. Experiments commonly performed to modify the mechanical properties of an epithelium include for instance inhibition of myosin contractility, disruption of cell-cell junctions, etc., which have been shown to affect the oscillations (Deforet et al., 2014; Notbohm et al., 2016; Peyret et al., 2019). Tuning the cell's ability to coordinate their motion (without changing the mechanical properties of the layer) is more challenging. It was recently proposed that the RAB5 protein promotes large-scale directed migratory patterns in epithelial layers (Malinverno et al., 2017). Tuning the expression of RAB5 could thus potentially enable to tune the magnitude of the velocity-polarity coupling (Giavazzi et al., 2018), which is expected to affect the oscillations. Let us also mention a very recent work by Boocock et al. (2020), that proposes that mechanical waves in epithelial tissues are related to spatio-temporal waves of cellular density and ERK activity, due to delayed mutual feedbacks between tissue mechanics and mechanosensitive ERK activity. Interestingly, the model of Boocock et al. (2020) is able to account (quantitatively) for the experimental data presented in this chapter (Petrolli et al., 2019). These recent results thus provide a possible biochemical explanation for the delayed feedback mechanisms leading to oscillatory dynamics in epithelial tissues.

In the confined SPV, an arbitrary choice has to be made for the cell number density. In our work, we chose the cell number density such that the tissue would remain confluent (and not detaching from the boundary) for a sufficiently large range of simulation parameters. Indeed, for large values of τ_{al} (but in the regime where collective oscillations are still observed, i.e., $\tau_{\mathrm{al}} < \tau_r$), the direction of the collective motion persists for so long that we observe a detachment of the monolayer from the extremity of the confining box. Choosing a large number density thus prevents this effect for a sufficiently large range of τ_{al} values. The cell number density sets the value of the average cell area, $\langle A_i \rangle$, which can be in practice very different from the target value $\langle A_0 \rangle$. According to Sussman et al. (2018), such a difference between $\langle A_i \rangle$ and $\langle A_0 \rangle$ should just act as an offset in the overall pressure of the system. The way the cell number density affects the wave features in the SPV model remains an open issue. It turns out that it is important to address this question, since it was shown in spreading epithelia experiments that the propagative wave velocity depends on the cell density (Tlili et al., 2018).

From a broader perspective, let us point out that although it is now well known that self-propulsion induces a solid-to-fluid transition in dense systems of active particles, the details of the dynamics (such as the alignment mechanisms studied here) may impact this transition. Giavazzi et al. (2018) have for instance shown that alignment mechanisms leading to flocks promote solidification by limiting the number of cellular rearrangements. How does the interplay of this mechanism and confining boundary conditions affect the solid-to-fluid transition of the SPV should also be investigated carefully. The proposed phase diagram of Fig. 6.10 is indeed schematic and

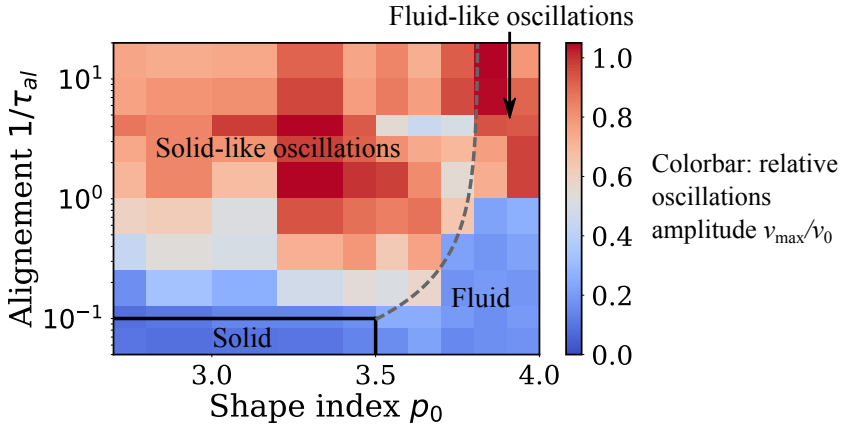

FIGURE 6.10: Phase diagram of the confined SPV model in the $1/\tau_{\mathrm{al}} - p_0$ plane (alignment, target shape index plane).

the different transitions mentioned should be investigated in details in the future.

In our study, we considered quasi-unidimensional confining boundary conditions, and did not discuss the effect of varying the lateral confinement. In their study, Peyret et al. (2019) propose that the wave period and amplitude are set by the smallest confinement dimension (i.e., lateral confinement size). We perform some numerical tests to probe this hypothesis in section 6.5.3, and find that the period of oscillations increases when the lateral confining dimension is increased, in agreement with Peyret et al. (2019).

A final important question concerns the nature of the oscillations observed in anisotropic confining conditions. For short patterns ($L_X < L_X^c$), there is a good agreement between the phenomenology observed in experiments and in simulations (global oscillations). For larger patterns ($L_X > L_X^c$), although the waves observed in experiments resemble standing waves, the waves observed in simulations of the SPV model resemble in general superimposed propagative waves (see the kymographs of Fig. 6.4(c) and Fig. 6.7(a)). Peyret et al. (2019), using large patterns, report standing waves along the short confining dimension and a mix of multi-nodal and traveling waves along the long confining dimension. Under which conditions standing waves are observed remains an open question. Is a specific confining length required? Is there an adapatative or self-tuning mechanism in epithelial tissues at play that would explain the fact that standing waves are easily observed in experiments but not in simulations?

6.5.1 Phase diagram of the confined SPV model in the $p_0 - \tau_{\mathrm{al}}$ plane

Let us discuss in more details the preliminary phase diagram for the SPV model (in the $1/\tau_{\mathrm{al}} - p_0$ plane) shown in Fig. 6.10. The colormap represents the relative amplitude of the oscillations $v_{\max}/v_0$ (measured mean amplitude of the x-component of the velocity normalized by the self-propulsion velocity v_0). Red colored regions indicate the existence of wave-like dynamics while blue colored regions rather indicate a stationary state.

This phase diagram was obtained for values of the self-propulsion velocity $v_0 = 0.2$ and rotational diffusion rate $\tau_r^{-1} = 0.1$. According to Bi et al. (2016), these parameters lead to a solid-to-fluid transition for a value of the shape index $p_0 \simeq 3.5$ in the absence of alignment mechanisms, as depicted by the solid vertical line in Fig. 6.10. The transition between a solid-like state and solid-like oscillations occurs

when the timescale for alignment equals the timescale for rotational diffusion, and is depicted by the solid horizontal line in Fig. 6.10. As shown by the color code of Fig. 6.10, there exist oscillations for $p_0 > 3.5$, in a regime expected to be fluid-like. We checked in the simulations that these oscillations indeed corresponded to states where rearrangements of particles could be seen. We did however not determine the solid-to-fluid transition line in this oscillatory regime (this can be done by measuring the effective diffusion coefficient of cells, as done by Giavazzi et al. (2018)), and leave it for future work. The grey line corresponds to the analytical expression derived by Giavazzi et al. (2018) to approximate the transition between solid-like and fluid-like flocking states: $J_c(p_0) = (v_0^2 D_r)/(k\mu^2(p_0^* - p_0))$, with $p_0^* = 3.813$ (Bi et al., 2014) and $k = 0.13$ a fitting parameter chosen such that this expression matches the solid lines (for $p_0 = 3.5$) in the phase diagram. We neither determined the transition line delimiting the fluid-like oscillations and the fluid-like stationary regime. This could be done by calculating numerically the cage lifetime (typical time to escape from a cage, infinite in the solid phase and finite in the fluid phase) as done by Giavazzi et al. (2018) and setting it equal to the timescale for alignment τ_{al}, and could also be done in future research.

Note that all the transitions lines discussed above were obtained in simulations of unconfined SPV models, and we do not expect to have a quantitative match with the results of Bi et al. (2016) and Giavazzi et al. (2018).

To summarize, this preliminary diagram suggests the existence of four distinct phases by varying the alignment rate $1/\tau_{\mathrm{al}}$ and the target shape index p_0. For small values of $1/\tau_{\mathrm{al}}$ (low alignment) and p_0, the monolayer behaves essentially as a solid, with no collective oscillations nor cellular rearrangements. For low alignment but higher values of p_0, no collective oscillations are observed, but increased cell motion enabled by cellular rearrangements leads to a fluid-like phase. When increasing the alignment rate $1/\tau_{\mathrm{al}}$, collective oscillations are observed, with (fluid-like) or without (solid-like) cellular rearrangements. In the solid-like regime, the only condition for the oscillations to be visible is that alignment dominates over rotational diffusion (horizontal solid line separating the solid and solid oscillations regimes). In the fluid-like regime, however, a higher alignment rate is required for collective oscillations to appear because alignment competes with the timescale for cage breaking. This phase diagram is very similar to that of flocks in a SPV model for unconfined monolayers (see Fig. 6.1) (Giavazzi et al., 2018). In this work, they also evidence four different phases depending on the alignment rate and target shape index: a solid, a fluid, a solid flock and a fluid flock phase. They conduct a detailed study of these different phases and show that alignment promotes solidification by limiting the number of cellular rearrangements, thus inducing a shift of the solid-fluid transition in the flocking regime (when alignment is increased). Our study was mainly qualitative, and this aspect remains to be tested. Determining the transitions lines as described above would give further insights into the analogy between flocks in unconfined monolayers and velocity oscillations in confined monolayers.

6.5.2 Role of elasticity

Although oscillations can be seen in both solid-like and fluid-like regimes, they are more pronounced in the solid-like elastic regime. In Fig. 6.11(a), we observe in preliminary data a change of wave velocity c when varying the microscopic elastic modulus relating to perimeter changes in Eq. 6.1 of the form $c = a\Gamma^b$ with $b \simeq 0.65 \pm 0.1$, not

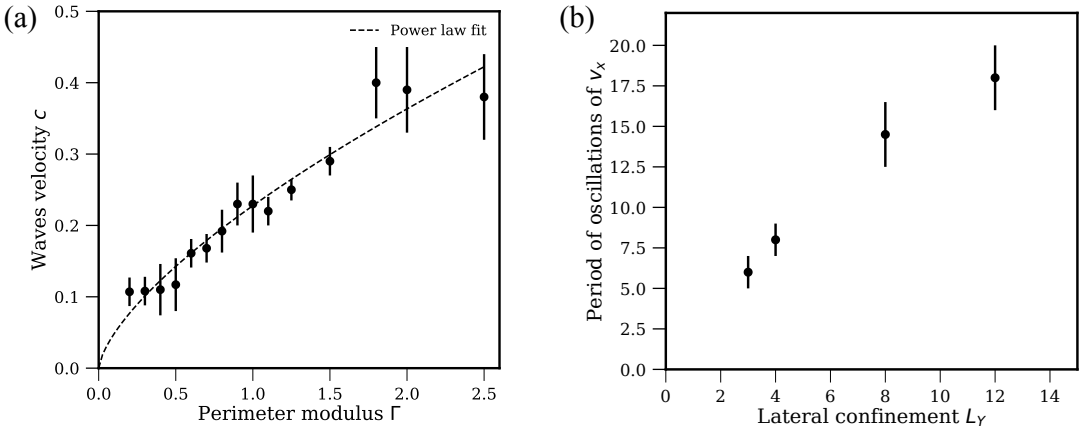

FIGURE 6.11: **Role of the perimeter elasticity constant and lateral confinement on the waves.** (a) Wave velocity as a function of the perimeter elastic constant Γ for $L_X = 60$, $p_0 = 3.1$ and $\tau_{\text{al}} = 1$. The errorbars correspond to the error on the estimated velocity (using the Hough transform method) and the dashed line is a power law fit of the form ax^b with $a = 0.23$ and an exponent $b = 0.65$. (b) Period of oscillations of the x-component of the cell velocity (averaged over the y dimension) as a function of lateral confining size L_Y for a system with $L_X = 12$, $p_0 = 2.3$ and $\tau_{\text{al}} = 1$.

far from a scaling form $c \sim \sqrt{\Gamma/\tau_{\text{al}}}$. The respective role of perimeter and area elasticity in confined conditions (and for different p_0 values) should however be studied carefully in order to rationalize the wave velocity.

To sum up, although we saw qualitatively that the elastic properties of the system affect the wave velocity (increasing velocity with increasing stiffness), a full study of the macroscopic elastic properties of the confined SPV with self-propulsion should be performed.

6.5.3 Effect of the lateral confinement

In Fig. 6.11(b), we test the effect of changing the lateral confining length L_Y in the SPV model on the period of oscillations of the x-component of the velocity for small systems size (where global oscillations are observed). We find an increase of the period of oscillations with L_Y.

As proposed by Peyret et al. (2019), this points towards a mechanism by which the smallest confinement length sets the period and hence the lengthscale of coordinated motion of the confined tissue (and beyond a critical confining length, the intrinsic lengthscale is that provided by the velocity correlation length in non-confined epithelial layers). We thus expect that the lengthscale of coordinated motion in the multi-nodal regime will be affected by the lateral confinement L_Y. This hypothesis remains to be tested in future work.

Chapter 7

Conclusion and perspectives

7.1 Conclusion et perspectives de la thèse (en français)

Nous avons étudié dans cette thèse différents aspects de la dynamique et de la rhéologie des matériaux amorphes et des systèmes actifs denses. Nous avons considéré deux classes principales de systèmes : des matériaux amorphes athermiques, soumis à un cisaillement et dont la dynamique était affectée par des sources de bruit mécanique supplémentaires ainsi que des matériaux amorphes actifs où l'activité (d'origine biologique par exemple) pouvait aussi générer un bruit mécanique additionnel. La motivation pour étudier ces deux classes de système dans un cadre (au moins en partie) commun provient des multiples analogies proposées récemment entre la physique des systèmes denses thermiques ou forcés et la physique de systèmes actifs denses comme les tissus biologiques (Janssen, 2019; Berthier et al., 2019). Plusieurs travaux récents ont par exemple proposé de décrire les tissus biologiques comme des fluides à seuil fluidisés sous l'effet d'une activité locale, agissant comme une source de bruit mécanique (Matoz-Fernandez et al., 2017a; Popović et al., 2018; Mongera et al., 2018). Certains travaux ont en outre proposé que l'activité biologique elle-même agissait comme un cisaillement local, suggérant une forte analogie entre les matériaux denses actifs et les matériaux amorphes athermiques cisaillés (Tjhung et al., 2017; Tjhung et al., 2020; Morse et al., 2020). Nous nous sommes donc intéressés dans cette thèse à la manière dont la dynamique de solides amorphes était affectée par diverses sources de bruit mécanique et à comment une activité biologique pouvait être décrite à l'échelle mésoscopique, par analogie avec les systèmes cisaillés.

Concernant la première classe de systèmes, nous avons étudié dans le chapitre 3 l'effet d'une dynamique inertielle sur l'écoulement de solides amorphes. D'après Salerno et al. (2012), l'inertie permet de passer des barrières d'énergies successives lors d'un réarrangement plastique, facilitant alors l'échantillonnage des états de basse énergie du système et induisant donc une relaxation de contrainte plus importante que dans un système sur-amorti. En d'autres termes, les oscillations persistantes induites par l'inertie vont induire de nouveaux réarrangements plastiques dans le voisinage d'un évènement plastique, de façon plus efficace que dans le cas sur-amorti (Karimi et al., 2016). Ce mécanisme d'autofluidisation se traduit par une courbe d'écoulement non monotone, telle qu'observée dans des simulations de particules et dans un modèle élasto-plastique continu pour la déformation de solides amorphes (Nicolas et al., 2016; Karimi et al., 2016). Des bandes de cisaillement avaient été observées dans le modèle continu avec inertie (Karimi et al., 2016) et les auteurs, remarquant que ces bandes ne respectaient pas de loi du levier, avaient attribué cet effet aux petites tailles de système considérées dans leur étude. Dans le chapitre 3, nous avons suivi l'approche proposée par Nicolas et al. (2016) consistant à décrire le bruit mécanique induit par l'inertie en introduisant une température cinétique responsable d'un mécanisme de fluidisation.

Nos résultats montrent d'une part que, dans des simulations de particules inertielles employant de grandes tailles de systèmes, des bandes de cisaillement permanentes sont observées, et ne respectent pas de loi du levier. D'autre part, le modèle continu basé sur une température cinétique permet de prédire la taille de système nécessaire pour observer des bandes de cisaillement et prédit des profils d'écoulement stationnaires ne satisfaisant pas non plus une loi du levier (que nous rationalisons à l'aide d'une analogie mécanique). Ces résultats permettent d'éclaircir la question de l'écoulement hétérogène associée aux courbes rhéologiques non monotones dans le cas d'une dynamique inertielle soulevée par Nicolas et al. (2016) and Karimi et al. (2016) ainsi que de conforter la description de l'inertie par une température cinétique dépendant du taux de cisaillement proposée par Nicolas et al. (2016). Certains points restent cependant à éclaircir. Nous n'avons par exemple pas étudié le régime transitoire de formation des bandes de cisaillement. Il apparaît dans les simulations de particules que plusieurs bandes se forment initialement et évoluent jusqu'à ce qu'une unique bande reste présente dans l'état stationnaire. Étudier la dynamique transitoire pour de grands systèmes (pour voir initialement plusieurs bandes) dans le modèle continu requièrerait cependant de faire appel à d'autres méthodes numériques dû aux limites de stabilité du schéma explicite utilisé.

Les études concernant un système modèle de particules molles, non frictionnelles, avec une dynamique inertielle, telle que la nôtre ou celles de Salerno et al. (2012), Nicolas et al. (2016), Karimi et al. (2016), and Karimi et al. (2017) restent à un niveau très fondamental où il est assez difficile de faire le lien avec des systèmes expérimentaux. En effet, des matériaux typiques où l'inertie est supposée jouer un rôle dans la dynamique sont les matériaux granulaires (voir par exemple Chapitre 1, Fig. 1.1). Cependant, ces matériaux sont constitués de grains durs frictionnels, et des études récentes ont montré que le frottement seul aussi pouvait induire une instabilité de l'écoulement (DeGiuli et al., 2017). Une étude complète devrait donc tenir compte de ces différentes sources d'instabilité (frottement, inertie, etc.). Une autre perspective à ce travail serait d'étudier l'effet d'une source de bruit externe (comme une vibration) dans les simulations de particules inertielles, afin de tester le scénario de point critique étudié dans le chapitre 4 dans ce système.

Le chapitre 4 de cette thèse était en effet dédié à l'étude de la fluidisation d'un fluide à seuil par une source de bruit externe, indépendante de l'écoulement. Les systèmes dans lesquels ces mécanismes de fluidisation peuvent être mis en jeu sont divers, et appartiennent aux deux classes de matériaux évoqués plus haut (systèmes cisaillés ou actifs). On peut penser aux solides amorphes cisaillés qui sont en plus soumis à un bruit mécanique externe de type vibration (Dijksman et al., 2011; Gibaud et al., 2020). On peut évoquer les mousses ou les émulsions où des processus internes comme de la coalescence ont également un effet fluidisant (Cohen-Addad et al., 2004). Les systèmes actifs ou biologiques offrent également une multitude d'exemple où des processus locaux, indépendants (au moins dans une certaine mesure) de l'écoulement, induisent un bruit mécanique additionnel dans le matériau.

Le travail mené dans le chapitre 4 s'est réduit à l'étude générique d'un processus de fluidisation, où, sans spécifier l'origine physique du bruit mécanique, on considère que celui-ci induit des réarrangements plastiques aléatoires (indépendamment de ceux induits par le cisaillement) dans un modèle élasto-plastique sur réseau. Ce type de bruit induit, par construction, une disparition de la contrainte seuil (puisque de la plasticité, même très faible, est introduite dans le modèle quelque soit la valeur de la contrainte). La rhéologie à petit taux de cisaillement dépend par contre du modèle d'activation considéré. Alors qu'une rhéologie linéaire est observée pour un taux

d'activation constant τ_{vib}, une loi d'activation dépendant de la contrainte locale de type Arrhenius, conduit à une rhéologie où la contrainte augmente linéairement avec le logarithme du taux de cisaillement. Lorsque ce type de bruit externe est appliqué à un système avec une instabilité de l'écoulement sous forme de bandes de cisaillement (induites dans le modèle élasto-plastique par un long temps de restructuration locale lorsqu'un évènement plastique se produit (Coussot et al., 2010)), alors, pour de faibles amplitudes de bruit, la rhéologie est non monotone. A faible taux de cisaillement, on observe le régime fluidisé discuté précédemment, où la contrainte augmente de façon monotone avec le taux de cisaillement et où l'écoulement homogène est stable. Pour des taux de cisaillement intermédiaires, la courbe constitutive est décroissante et on observe, suivant le protocole employé, des bandes de cisaillement ou un écoulement instable avec de l'hystérèse. Enfin, pour des taux de cisaillement plus importants, on retrouve un écoulement homogène et le même comportement rhéologique (croissant) qu'en l'absence de bruit. En augmentant l'amplitude du bruit, la région instable à taux de cisaillement intermédiaire devient de plus en plus réduite, jusqu'à laisser la place à une courbe d'écoulement monotone croissante au delà d'une valeur critique du bruit. Nous avons caractérisé cette transition en étudiant l'évolution des grandeurs rhéologiques macroscopiques et de leur fluctuations, et montrons que celle-ci peut être interprétée comme un point critique. De plus, le comportement critique, caractérisé par un ensemble d'exposants critiques, semble être similaire dans les deux modèles de bruit considérés. Nous trouvons en outre que les exposants critiques décrivant la transition dans le modèle élasto-plastique scalaire considéré sont compatibles avec ceux déterminés expérimentalement dans une expérience de granulaires cisaillés et vibrés (Wortel et al., 2016). Ces résultats suggèrent donc un possible scénario générique pour l'émergence d'un point critique lorsqu'un processus d'auto-fluidisation entre en compétition avec une source de fluidisation externe, distinct du point critique dans la limite des petits taux de cisaillement $\dot{\gamma} \to 0$. Il n'existe cependant pas d'approche théorique, même de type champ moyen, prédisant la valeur des exposants critiques. Notons que, comme remarqué par Wortel et al. (2016), certaines valeurs d'exposants sont compatibles avec une théorie de champ moyen d'équilibre standard, mais les exposants décrivant l'évolution des corrélations spatiales et temporelles diffèrent d'une telle théorie. Enfin, il est intéressant de noter que la rhéologie du modèle élasto-plastique fluidisé par un bruit externe ne dépend ni du choix d'un modèle scalaire ou tensoriel, ni de l'orientation des évènements plastiques (aléatoire ou dans la direction du cisaillement) activés par le bruit. Ceci suggère que c'est principalement la relaxation de contrainte supplémentaire due aux évènements plastiques induits par le bruit qui explique la fluidisation observée sur la courbe d'écoulement, et que les corrélations entre évènements jouent un rôle moindre. Ceci explique aussi pourquoi la rhéologie à faible taux de cisaillement prédite dans le modèle simplifié à un site décrit bien les simulations spatiales dans ce régime fluidisé. Nous n'avons cependant pas exploré la dépendance des exposants critiques avec la tensorialité du modèle, la dimension spatiale ou encore l'orientation des évènements plastiques dus au bruit. Une telle étude pourrait permettre de comprendre plus en détail le rôle joué par les corrélations spatiales dans les propriétés critiques du modèle à taux de cisaillement fini. Enfin, il serait souhaitable de tester l'existence de ce point critique ainsi que, le cas échéant, la valeur des exposants dans d'autres systèmes expérimentaux ou modèles numériques de solides désordonnés, comme par exemple en ajoutant une source de bruit mécanique externe dans les simulations de particules inertielles décrites dans le chapitre 3.

Dans le chapitre 5, nous avons cherché à étudier la fluidisation d'un fluide à seuil en

spécifiant cette fois-ci un type de bruit mécanique particulier, induit par des fluctuations actives du volume des particules. Les fluctuations du volume cellulaire, pouvant suivre une dynamique oscillatoire, constituent un exemple de processus actif mis en jeu dans les tissus épithéliaux, et affectant la dynamique (e.g., champs de vitesse par exemple) à grande échelle (Zehnder et al., 2015a; Zehnder et al., 2015b). En se basant sur le modèle microscopique proposé par Tjhung et al. (2017), nous avons construit un modèle élasto-plastique tensoriel actif, dans lequel nous décrivons l'effet moyen d'une particule se dilatant ou se contractant comme étant à l'origine d'une redistribution de contrainte dans le système via un propagateur élastique. Nous étudions la dynamique de ce modèle avec comme source de forçage des oscillations périodiques du rayon des particules telles qu'étudiées par Tjhung et al. (2017), que nous modélisons comme une déformation active locale oscillante.

Nous montrons tout d'abord que, sous l'effet de la déformation active seule (sans cisaillement), ce modèle élasto-plastique actif présente une transition entre un état solide (sans réarrangement plastique) et un état fluide pour une valeur finie de l'amplitude d'oscillation de la déformation active. La nature de cette transition est cependant difficile à déterminer d'après les valeurs de plasticité moyenne ou les trajectoires de particules traceurs. En effet, au voisinage de la transition, le système évolue très lentement vers l'état stationnaire (qui n'est pas atteint dans nos simulations pour les points à proximité de la transition) et les barrières pour la plasticité locale (renouvelées à chaque évènement plastique) deviennent de plus en plus hautes au fur et à mesure des cycles de déformation active locale. Ces phénomènes évoquent la transition vers l'écoulement observée dans certains verres soumis à un cisaillement oscillatoire, où de petites amplitudes de déformation conduisent à augmenter la stabilité du verre (Leishangthem et al., 2017; Yeh et al., 2020). La comparaison à ce stade reste cependant qualitative puisque le modèle élasto-plastique utilisé n'est pas basé sur une description énergétique du système amorphe. Une étude plus approfondie de ces aspects requiérerait par exemple d'utiliser un modèle élasto-plastique continu basé sur un paysage énergétique, tel qu'étudié par Jagla (2007).

Une autre similitude avec les verres cisaillés sous protocole oscillatoire concerne la contrainte moyenne dans le système, qui présente un pic ("overshoot" en anglais) pour une valeur d'amplitude de déformation active a_c, indiquant une transition nette entre deux états. Alors que dans les verres cisaillés, peu de plasticité est en général observée avant le dépassement de contrainte, nous constatons ici que la plasticité dans la phase supposée solide est non négligeable. Ceci peut s'expliquer par le fait que le forçage dans le cas actif est hétérogène, conduisant à l'existence de sites soumis à un forçage grand devant les barrières d'énergie maximales du système. Il se trouve en outre que, au voisinage de la transition, la plasticité n'est pas homogène dans le système mais semble s'organiser en régions avec une activité plastique finie (et ne dépendant pas du forçage au voisinage du dépassement de contrainte) et en régions inactives, évoquant les bandes de cisaillement dans les verres cisaillés avec un protocole oscillatoire. Dans la suite, il faudrait étudier les corrélations entre évènements plastiques afin de mieux comprendre l'organisation spatiale de la plasticité au voisinage de la transition.

Notre modèle élasto-plastique est basé sur l'hypothèse que les réarrangements plastiques dans le matériau sont activés par un forçage actif produit par la déformation locale active des particules. Nous avons donc négligé les fluctuations locales de densité induites par l'activité. La densité joue toutefois un rôle important dans la dynamique des amorphes, puisqu'une région moins dense aura une propension plus grande à subir un réarrangement de particules. Estimer les variations de densité dans le modèle de particules et étudier la corrélation entre densité locale et réarrangement plastiques permettrait donc de mieux comprendre les mécanismes en jeu dans la fluidisation

du système. Enfin, Tjhung et al. (2017) suggèrent dans leur étude que l'existence d'évènements plastiques réversibles dans la phase solide est un élément crucial pour observer une transition de fluidisation discontinue d'après les données de trajectoires de particules. Il serait donc intéressant de modifier le modèle élasto-plastique actif de façon à décrire des évènements plastiques réversibles (en modifiant le critère pour générer un évènement plastique par exemple).

Enfin, le chapitre 6 est un peu à part du reste de la thèse puisqu'il consistait à étudier l'émergence d'oscillations mécaniques dans un modèle de monocouches épithéliales confinées sur un substrat d'étendue limitée en lien avec des expériences menées au sein du laboratoire. Notre étude est basée sur un modèle de type Voronoi incluant l'autopropulsion des cellules, avec un mécanisme de rétroaction entre la direction d'autopropulsion et la vitesse des cellules afin d'obtenir des oscillations. Bien que notre étude ait été principalement guidée par les résultats expérimentaux de Petrolli (2019), des liens peuvent cependant être établis entre les questions abordées dans le chapitre 6 et le reste de la thèse. En effet, plusieurs travaux soulèvent le lien entre fluidisation et migration collective dans les monocouches épithéliales. La forme des cellules, la motilité cellulaire ainsi que la division et la mort cellulaire contrôlent des transitions solide-fluide dans des modèles de vertex ou Voronoi de monocouches confluentes (transitions indépendantes de la densité) (Bi et al., 2015; Bi et al., 2016; Czajkowski et al., 2019). Les mécanismes d'alignement tel que celui considéré dans le chapitre 6 conduisent en outre à une solidification de la couche épithéliale, dans le sens où ils favorisent la migration coordonnée des cellules en limitant les réarrangements cellulaires (Giavazzi et al., 2018). Lorsque le temps typique d'alignement est grand devant le temps typique de diffusion de la direction d'autopropulsion (polarité), alors le bruit généré par l'autopropulsion agit comme une température effective qui permet de franchir les barrières d'énergie associées aux réarrangements de cellules (de type T1) (Bi et al., 2016), alors que lorsque le mécanisme d'alignement est plus rapide que la diffusion, les cellules se déplacent de façon plus coordonnée. Giavazzi et al. (2018) proposent de décrire cet effet à l'aide d'une température effective proportionnelle au ratio de la constante de diffusion rotationnelle de la polarité et du taux d'alignement. Étant données les similitudes entre l'émergence de mouvements collectifs dans le modèle SPV avec alignement avec des conditions aux limites périodiques (sans confinement) et l'émergence d'oscillations de vitesse dans le même modèle mais avec des conditions de bord répulsives (induisant un confinement), nous attendons également un effet de solidification induit par l'alignement dans le cas confiné.

On peut se demander si de tels mécanismes d'auto-propulsion avec alignement pourraient être inclus dans un modèle élasto-plastique actif. La phénoménologie décrite par Giavazzi et al. (2018) suggère que la migration cellulaire (dans un modèle avec alignement) peut résulter en un déplacement "solide" de cellules coordonnant leur mouvement, ou en déplacement plus localisés faisant intervenir des réarrangements de particules. Le cadre actuel des modèles élasto-plastiques semble plutôt adapté à décrire le deuxième type de migration, où les mécanismes d'alignement sont négligeables. Dans ce cas, le type de dynamique observée dépend cependant de façon importante du régime de persistance de la force d'autopropulsion. La dynamique observée dans le régime de faible temps de persistance de la polarité est analogue à celle d'un verre avec une température effective $T_{\text{eff}} \propto f_0^2$ (avec f_0 la force d'autopropulsion) (Bi et al., 2016; Mandal et al., 2016). Dans le cas, où, au contraire, le temps de persistance de la polarité est infini, une transition entre un solide athermique et un état fluide athermique est observée, pour une valeur critique de la force d'autopropulsion (qui dépend de la fraction volumique) (Liao et al., 2018; Mandal et al., 2020a). Cette

force critique est analogue à la contrainte seuil dans les solides amorphes athermiques cisaillés (Liao et al., 2018). Dans le cas de temps de persistance intermédiaires, Mandal et al. (2020a) ont mis en évidence une dynamique intermittente résultant de phases d'arrêt suivies de réarrangements plastiques associés à des déplacements non affines de particules de type Eshelby.

Une première utilisation naïve de modèle élasto-plastique pour décrire un système de particules auto-propulsées pourrait consister à introduire des évènements plastiques d'orientation aléatoire, avec des règles d'activation à spécifier, tel que proposé par exemple à la fin du chapitre 4. Alors que ce type d'approche pourrait en effet décrire la phase fluide d'un système de particules auto-propulsés, le lien entre la force d'autopropulsion des particules à l'échelle microscopique et le taux d'activation d'évènements resterait cependant phénoménologique. Cette approche ne permettrait en outre pas d'étudier la transition solide-fluide induite par l'auto-propulsion.

Pour aller plus loin, une première étape serait d'introduire un champ de polarité dans le modèle mésoscopique. Ce champ de polarité devrait sans doute être défini sur un réseau avec une maille plus fine que celle fixée par la taille typique des réarrangements plastiques. Une étude détaillée des évènements plastiques dans des simulations de particules comme celles réalisées par Mandal et al. (2020a) serait donc nécessaire pour éclaircir le lien entre force d'autopropulsion et polarité locales et contrainte locale nécessaire pour engendrer un évènement plastique. Par exemple, on peut se demander si les évènements plastiques décrits par Mandal et al. (2020a) se produisent quand plusieurs particules voisines ont des polarités alignées de telle sorte qu'elles peuvent exercer localement une contrainte de cisaillement suffisante pour induire un réarrangement. En s'inspirant des méthodes de Puosi et al. (2014) and Patinet et al. (2016), on pourrait imaginer construire des groupes de particules actives au sein d'un système de particules passives et varier soit le nombre de particules actives, soit leur polarité, soit leur force d'autopropulsion afin de déterminer les conditions dans lesquelles un évènement plastique se produit.

Pour conclure, le projet de construire un modèle élasto-plastique décrivant un système de particules auto-propulsées, même dans le scénario le plus simple sans mécanisme d'alignement et avec un temps de persistance infini, requièrerait un travail d'investigation numérique conséquent dans des simulations de particules, qui n'a pas pu être effectué au cours de cette thèse. Des travaux très récents de Morse et al. (2020) and Mandal et al. (2020b) offrent en outre des perspectives intéressantes concernant l'analogie entre cisaillement et auto-propulsion dans le régime de temps de persistance infini. Dans leur étude, Morse et al. (2020) proposent un nouveau protocole de simulation consistant à déplacer aléatoirement des particules de façon quasi-statique (correspondant au cas de l'autopropulsion dans la limite de vitesse nulle et d'un bruit rotationnel nul), permettant une comparaison directe entre systèmes actifs et systèmes athermiques cisaillés (suivant un protocole quasi-statique). Les résultats numériques obtenus sont en accord avec les résultats d'un modèle champ moyen (en dimension infinie) suggérant qu'appliquer un champ de force aléatoire ou une déformation de cisaillement perturbe un solide amorphe de la même façon. Les exposants critiques décrivant les avalanches de plasticité sont similaires dans les deux cas, et les préfacteurs dépendent de la longueur de corrélation du champ de déplacement appliqué : de l'ordre d'un rayon de particule dans le cas de particules auto-propulsées (sans bruit rotationnel) et de l'ordre de la taille du système dans le cas du cisaillement. Le cisaillement global apparaît alors comme un cas particulier de forçage aléatoire. Leurs résultats montrent par ailleurs qu'un solide amorphe soumis à un champ de déplacement aléatoire présente aussi une transition vers l'écoulement ("yielding") dépendant de la stabilité du verre, tel qu'observé sous cisaillement. Les auteurs soulèvent également la

question de la localisation de l'écoulement dans les systèmes actifs au voisinage de la transition, où le forçage n'impose pas de symétrie à l'échelle macroscopique, question également abordée dans le chapitre 5. Mandal et al. (2020b) proposent une méthode pour étudier les systèmes actifs denses dans la limite des temps de persistance infinie, et étudient les réarrangements plastiques de type Eshelby induits par l'activité, montrant que leur orientation est isotrope dans le matériau. Ces deux études suggèrent donc que modéliser l'autopropulsion (persistante) comme une forme de cisaillement localisé peut être une piste pertinente pour le développement de modèles à l'échelle mésoscopique. On peut également se demander si le cadre théorique développé par Morse et al. (2020) s'applique au cas d'un système de particules se déformant de façon isotrope, comme étudié dans le Chapitre 5, en prenant une limite quasi-statique du modèle.

7.2 Conclusion and perspectives

We studied in this thesis different aspects of the dynamics and rheology of amorphous and dense active materials. We considered two main classes of systems: athermally sheared amorphous materials with additional sources of mechanical noise as well as active amorphous materials in which the biological activity can also induce additional mechanical noise. The motivation to study these two classes of systems in a (at least partly) common framework comes from the numerous analogies recently proposed between the physics of thermal or driven amorphous materials and the physics of dense active systems such as epithelial tissues (Janssen, 2019; Berthier et al., 2019). Recent works have for instance proposed to describe epithelial tissues as yield stress fluids fluidized by a local biological activity, acting as an additional source of mechanical noise (Matoz-Fernandez et al., 2017a; Popović et al., 2018). Some works have also proposed that the biological activity itself acts as a local shear (Tjhung et al., 2017; Tjhung et al., 2020; Morse et al., 2020), suggesting a strong analogy between active and sheared materials.

In this thesis, we have studied how the dynamics of amorphous solids is affected by diverse sources of mechanical noise, and how a local biological activity can be modeled at a mesoscopic level by analogy with sheared systems. We have considered distinct sources of noise, either endogenous noise leading to self-fluidization or rate-weakening (e.g., due to inertial dynamics or long restructuring times in the plastic deformation of amorphous solids) as well as external (i.e., rate independent) sources of noise (e.g., vibrations, biological activity).

We studied in chapter 3 the effect of inertial dynamics on the organization of the flow of amorphous solids. According to Salerno et al. (2012), inertia enables successive energy barrier crossings when a plastic rearrangement occurs, thus facilitating the exploration of low energy states of the system and inducing an increased stress relaxation compared to the overdamped case. In other words, persistent oscillations due to inertia will induce new plastic rearrangements in a more efficient way (Karimi et al., 2016). This self-fluidization mechanism leads to nonmonotonic flow curves, as observed in particle-based simulations or in a continuum elasto-plastic model for the flow of amorphous solids (Nicolas et al., 2016; Karimi et al., 2016), although no shear bands were reported in particle-based simulations. Shear bands were observed in the continuum model (Karimi et al., 2016) and were shown not to obey a lever rule, although the authors attributed this finding to the small system size used in their study. In chapter 3, we further investigated the existence and the nature of shear bands in amorphous solids with underdamped dynamics. We followed the approach proposed

by Nicolas et al. (2016) consisting in modeling inertia as a shear rate-dependent kinetic temperature in the material inducing a rate-dependent fluidization. The results obtained by V. Vashist using underdamped particle-based simulations show that shear bands are observed when considering large systems sizes and that these bands do not follow a lever rule either, as observed by Karimi et al. (2016). Our continuum model, based on a kinetic temperature description of inertia, can predict the minimum system size required to observe shear bands and also predicts steady states shear-banded profiles that do not follow a lever rule (finding that we can rationalize using a mechanical analogy). These results contribute to clarifying the question of the existence and the nature of shear bands associated with a nonmonotonic flow curve due to an inertial dynamics raised by Nicolas et al. (2016) and Karimi et al. (2016). Our findings also support the description of inertia by a kinetic temperature field proposed by Nicolas et al. (2016).

Studies of inertial soft frictionless particles like ours or that of Salerno et al. (2012), Nicolas et al. (2016), Karimi et al. (2016), and Karimi et al. (2017) remain however quite fundamental since they do describe a specific experimental system. Typical materials where inertia is thought to play an important role are granular materials (see Chapter 1, Fig. 1.1). However granular materials are most often made of hard frictional grains, and friction itself is also thought to induce nonmonotonic flow curves and flow instabilities (DeGiuli et al., 2017). A complete study should thus account for these different sources of instability (friction, inertia, etc.).

We mainly focused in Chapter 3 on the steady state properties of sheared underdamped systems exhibiting permanent shear localization. Underdamped disordered solids also exhibit a rich transient dynamics to reach steady state, and studying this transient dynamics constitutes a possible perspective for future work. Regarding the macroscopic properties, it appears in Fig. B.4(a) that, when the homogeneous flow is unstable (nonmonotonic flow curve), the macroscopic stress first relaxes to its homogeneous steady state value, and if the system is large enough, then relaxes during a second step to a steady state value corresponding to a heterogeneous flow. This feature is also captured by the continuum model, and many questions remain open. How long does it take to reach the heterogeneous steady state? How does this depend on the system size? How does it depend on initial conditions? The evolution of flow profiles in particle-based simulations also exhibits a rich dynamics: several bands can form at the early stages of the dynamics and then coarsen until a single banded profile is reached in steady state. What governs this coarsening dynamics also remains an open question. Observing multiple bands in the early dynamics of the continuum model would however require to study a large system, which could not be achieved due to numerical stability issues with our explicit Euler scheme as discussed in section 3.2.6. One would need to use more sophisticated methods such as pseudo-spectral methods to prevent these numerical instabilities and access larger system sizes to study the coarsening dynamics in the continuum model.

Another interesting perspective (which was actually the initial motivation for this project) would be to study the effect of an external fluidizing noise on the shear bands induced by an inertial dynamics. Whether combining a rate weakening mechanism due to inertial dynamics with external vibrations leads to critical dynamics remains an open question. A preliminary work regarding the effect of vibration in particle-based simulations of a dense system of soft spheres was conducted by V. Vasisht, evidencing a fluidization mechanism akin to that reported for breathing particles in Chapter 4 (with a vanishing yield stress above a critical vibration magnitude), but different from the random activation of events considered in Chapter 4 (vanishing yield stress for any vibration magnitude). Further, the shear bands observed in the underdamped system

are very different from the ones observed in Picard's elasto-plastic model, since e.g. no lever rule is reported in the former case (Martens et al., 2012). With so much differences between the type of phase separation and the effect of the fluidizing noise between the EPM of Chapter 4 and the model glass studied in Chapter 3, it would be of great interest to see if the critical point scenario proposed in Chapter 4 holds in the latter case.

We studied in Chapter 4 the fluidization of yield stress fluids by external (rate-independent) sources of noise. The systems where such fluidization mechanisms can be at play are diverse, encompassing amorphous solids such as granular media or gels subjected to mechanical vibrations (Dijksman et al., 2011; Gibaud et al., 2020), foams or emulsions undergoing coalescence (Cohen-Addad et al., 2004), or active materials where local (biological) activity can induce additional mechanical noise (Mandal et al., 2016; Matoz-Fernandez et al., 2017a; Tjhung et al., 2017).

In Chapter 4, we restricted our work to the study of a generic fluidizing noise model responsible for the random activation of plastic events in a lattice-based elasto-plastic model (independently of the shear-induced events). This type of noise induces, by construction, a vanishing yield stress (because some plastic events are induced even at infinitesimally low stress). It is thus not suited to model the fluidization induced for instance by ultrasonic vibrations in colloidal gels, where the yield stress vanishes upon a critical vibration magnitude. The type of elasto-plastic model used in Chapter 5, where the magnitude of the local additional stress due to the source of noise is fixed (rather than an activation rate), predicts instead a vanishing yield stress upon a critical noise magnitude.

In the models of random activation considered in Chapter 4, we found that the low shear rate rheology depends on the type of activation rule. A linear rheology is obtained when a constant activation rate is considered while an activation rate depending upon the local stress in an Arrhenius fashion leads to a logarithmic-like rheology.

Next, we applied this random activation noise to simulations of the elasto-plastic model accounting for a shear banding instability (due to a long restructuring time as proposed by Coussot et al. (2010)). We found that for small noise magnitudes the rheology is nonmonotonic, with a fluidized branch at low shear rate, followed by an unstable regime where shear bands are observed at intermediate shear rates and a rheology that remains unchanged compared to the case without noise at high shear rates. When increasing the noise magnitude (i.e., the activation rate), the unstable (phase-separated) region decreases until it vanishes at a critical noise magnitude for which a homogeneous flow regime is reached. We studied the evolution of both macroscopic quantities and fluctuations in the vicinity of the transition, and found that it can be interpreted as a critical point in the framework of non-equilibrium phase transitions. The critical behavior, as characterized by a set of critical exponents, is found to be similar for the two types of activation rules considered in Chapter 4. The exponents are moreover found to be consistent with the experiments of Wortel et al. (2016) on sheared and vibrated granular materials. These findings suggest a possible generic scenario for the emergence of criticality at finite shear rate when self-fluidization competes with external fluidization mechanisms. There is however no theoretical framework that could help rationalizing the values of the critical exponents found in our study and in the experimental work of Wortel et al. (2016). We found that some of the exponents values, in particular those related to average quantities, are consistent with a mean-field Landau-like description as noted by Wortel et al. (2016). This is however not the case for the exponents describing the evolution of

spatial and temporal correlations in the vicinity of the transition, suggesting a slower decay than equilibrium mean field.

It is also interesting to point out that the rheology of the fluidized elasto-plastic model depends neither on the tensoriality of the model nor on the orientation of the randomly activated events (random or in the same direction as shear). This suggest that the fluidization behavior is mainly explained by local stress relaxation, and that correlations between plastic events play only a little role in this regime. We did however not study how the critical behavior depends upon the tensoriality, the spatial dimension or the orientation of activated events. Studying these effects would give more insights into the role of spatial correlations in the finite shear rate critical behavior.

Other perspectives for this work include for instance pushing further the characterization of the transition by measuring e.g. response functions to small perturbations in the critical regime, as well as performing direct measurements of the correlation length in the Arrhenius-like model of activation. Finally, it would be of interest to test this critical point scenario in other experimental or numerical models of disordered solids, with distinct sources of endogenous and external noise. In the context of the systems studied in this thesis, this could be done using for instance inertial dynamics as source of self-fluidizing noise (Chapter 3) and internal active noise as flow-independent fluidizing noise (Chapter 5).

In Chapter 5, we proposed a generalization of the elasto-plastic approach to account for local (active) driving. Our aim was to study the fluidization of yield stress fluids by specifying this time a particular type of noise, induced by active fluctuations of the volume of particles. It was found that fluctuations of the cell volume in epithelial tissues can occur periodically and affect the large scale velocity fields (Zehnder et al., 2015a; Zehnder et al., 2015b). Based on the particle-based model introduced by Tjhung et al. (2017), we built an active tensorial elasto-plastic model in which we describe the average response to a dilating or contracting particle as stress redistribution in the surrounding elastic medium via an elastic propagator.

We studied the dynamics of this active elasto-plastic model (AEPM), with the only source of driving originating from periodic oscillations of the local active deformation, mimicking the oscillations of the particle radius studied by Tjhung et al. (2017). Our preliminary results suggest that upon an increase of the active deformation amplitude, the system undergoes a transition from a solid-like state (with no plastic activity) to a fluid-like state with a finite rate of plastic events. This transition occurs for a finite value of the active deformation amplitude, as reported by Tjhung et al. (2017). It is however difficult to determine the nature of the transition from the data of average plasticity or from the tracer particle trajectories, due to the fact that the system exhibits an increasingly slow dynamics in the vicinity of the transition (and the first results shown in this chapter were obtained with rather short simulation runs). This slow dynamics is accompanied by a progressive increase of the average value of the local yielding thresholds (renewed after each plastic events) with the number of active deformation cycles. This effect is reminiscent of the "mechanical annealing" effect observed in some glasses sheared with an oscillatory shear protocol (Leishangthem et al., 2017; Yeh et al., 2020). The comparison remains however qualitative since our elasto-plastic model is not based on an energy landscape description of the system. Understanding how the energy landscape is explored upon active driving would thus require to use energy-based continuum elasto-plastic models, as introduced by Jagla (2007).

Another strong similarity with oscillatory-sheared glasses is observed in the macroscopic stress response to active deformation, where a stress overshoot is observed for an active deformation amplitude a_c. Although very little plasticity is observed for strain amplitudes below the threshold in sheared glasses, we report in our case a finite plastic activity for values of $a < a_c$. This can be explained by the heterogeneity of the active driving: depending upon the distribution of phases of oscillations, some sites may undergo a strong driving, i.e., the stress they receive due to the surrounding oscillating sites exceeds the maximum of the stress threshold distribution. Since plasticity is observed both before and after the overshoot, we can thus wonder what are the dynamical features of the plasticity associated with the macroscopic stress overshoot. It appears that below the overshoot, a macroscopic fraction of plastic events is due only to the active driving (and not to other plastic events in the system), while an increased cooperativity is observed above the threshold. This plastic flow further seems to be associated with some spatial organization of the plasticity into plastic and arrested regions, reminiscent of flow localization is sheared glasses. The nature of the localization is however different from the sheared cases (where shear bands are observed) due to the absence of macroscopic symmetry of the driving.

We based our elasto-plastic model on the assumption that the dominant mechanism for fluidization was due to the displacement and stress fields induced in the surrounding medium by dilating or contracting particles. We have thus neglected the density fluctuations induced by the active driving. It is however known that the local yield stress distribution depends on the density, and the role of density fluctuations in the fluidization should thus be investigated (Puosi et al., 2015). Further, Tjhung et al. (2017) argue that reversible plastic rearrangements are an important feature to explain the existence of a solid-phase (with non-zero plasticity) in simulations of actively deforming particles. Our current active elasto-plastic model does not account for such reversible plastic events, and it would be of interest to include this type of events in the dynamics (by changing the rules for yielding for instance) in order to see if the discontinuous character of the transition appears more clearly from particle trajectories.

As future perspectives, we expect that the effect of other types of activity such as cell division and cell death could be easily studied within the framework of our active elasto-plastic model (by describing the elastic response to each type of event, the case of self-propulsion will be further discussed at the end of this chapter). Along the same lines as what was proposed previously, it would also be of interest to test the genericity of the critical point scenario of Chapter 4 using the noise induced by the local active dynamics of Chapter 5 as an external fluidizing noise (and the same rate-weakening mechanism as in Chapter 4, i.e., a long restructuring time to recover an elastic behavior locally). Another interesting perspective, as mentioned briefly in Chapter 1, would be to build a Kinetic Elasto-Plastic (KEP) model based on the active tensorial model proposed in Chapter 5, with the objective of deriving fluidity equations for an active system (Bocquet et al., 2009). This would require first to introduce a tensorial version of KEP model, in the same spirit as it was done for the Hébraud-Lequeux model by Olivier et al. (2013). Then, writing tensorial KEP equations for the active elasto-plastic model of Chapter 5 would lead to two distinct non-local Boltzmann-like operators (one for the non-locality due to the driving and another one for the non-locality due to stress redistribution following plastic events). Following the approach of (Bocquet et al., 2009), a series of approximations including an expansion of the Boltzmann-like operators could lead to an analytical expression for the stress probability distribution, thus enabling one to compute the average stress and obtain fluidity-like equations.

The work presented in Chapter 6 is a bit aside the rest of the thesis since it was first motivated by experiments conducted by collaborators in the lab (Petrolli, 2019; Petrolli et al., 2019). It consisted in studying the emergence of mechanical waves in confined epithelial layers using a Voronoi-based model. We used a Self-Propelled Voronoi model (SPV) encoding adhesion and cortical tension mechanisms at play in epithelial tissues as well as self-propulsion of Voronoi centers with a delayed coupling mechanism between the direction of self-propulsion (polarity) and the cell velocity. We found oscillations of the cells velocity akin to that reported in the experiments on MDCK epithelial layers conducted by Petrolli (2019).

Although our study was mainly guided by the experimental results of Petrolli (2019), some links can be established between the questions raised in Chapter 6 and the rest of the thesis. Several works highlight indeed the link between fluidization and collective cell migration in epithelial layers. Cell shape, cell deformation, cell division and apoptosis as well as cell motility control density-independent solid-to-fluid transitions in vertex or Voronoi-based models (Bi et al., 2015; Bi et al., 2016; Czajkowski et al., 2019; Krajnc, 2020). It was morever proposed by Giavazzi et al. (2018) that alignment mechanisms like the one considered in our work promote the solidification of the monolayer due to the formation of flocks in which cells migrate collectively, thus limiting the number of cell rearrangements. The fluid- or solid-like state of the monolayer thus results from a subtle interplay between the fluidization induced by cell motility and the solidification induced by the coupling between cell polarity and cell velocity. Although this system is far from equilibrium, Giavazzi et al. (2018) further proposed to describe this effect with an effective temperature depending upon the ratio of the rotational diffusion of polarity and the alignment rate: when alignment mechanisms are faster than rotational diffusion, the effective temperature is too low to overcome the energy barriers associated with cell rearrangements and the migration is coordinated over large lengthscales (flocking behavior). Given the similarities between the phase diagram of flocks in the bulk SPV (with periodic boundary conditions (Giavazzi et al., 2018)) and the emergence of oscillations in the confined SPV, we expect these effects of solidification induced by alignment to be also at play in our case.

We now present possible perspectives to the work presented in Chapter 6. The Self-Propelled Voronoi model used in Chapter 6 could be refined with more realistic dynamics, by including for instance the velocity modulus in the coupling term between the direction of self-propulsion and the direction of velocity. This would probably prevent the oscillation of the cell velocity in a nearly immobile layer, as observed in our current simulations for small values of p_0 and v_0. Further, we considered in Chapter 6 interactions between cells deriving from a vertex energy plus some soft core repulsion for numerical stability issues (Barton et al., 2017). Preliminary tests using only soft core repulsion and turning off the vertex-like interactions (thus reducing to a repulsive particle model) yielded similar oscillations as in the full vertex-based model. Features such as the linear evolution of the period with the confining length were also observed using particle-based simulations (Deforet et al., 2014) and a phase-field model (Peyret et al., 2019) with similar coupling mechanisms. The robustness of the oscillation features thus seems to indicate that the velocity waves could be modeled including two minimal ingredients: elasticity and a delayed feedback mechanism playing the role of an effective inertia. Following the approach of Henkes et al. (2011), one could build a continuum model based on an elastic description of the monolayer, to get predictions regarding the wave velocity in the monolayer as a function of the elastic moduli and the feedback timescale τ_{al}. Microscopic simulations could be used to test such continuum model. Macroscopic elastic properties of the SPV model were

characterized by Sussman et al. (2018), who established a link between the local elastic constants (area and perimeter elasticity) and the shear and bulk moduli. To which extent these relations hold for a confined tissue (where the average area and perimeter may differ from their target values) remains however to be investigated. Using simpler microscopic models (e.g., particle or spring-based models) could also be a way to test such a continuum approach. Further, we can speculate that knowing the wave velocity from experiments and assuming that the shear and bulk moduli can be measured, one could then estimate the value of the feedback timescale τ_{al} (although measurements of tissue elastic properties may be difficult to perform in a controlled manner, see Chapter 1, section 1.16). This could be compared to more direct measurements of the feedback timescale τ_{al} like the ones performed by Peyret et al. (2019) by measuring the delay between velocity and traction force in experiments.

Finally, we can also ask whether cell motility with alignment mechanisms could be modeled within a mesoscale active elasto-plastic model. The phenomenology described by Giavazzi et al. (2018) suggests that cell migration can either occur in the form of "solid" flocks where cells coordinate their motion or in a more localized fashion involving cell plastic rearrangements. The current framework of elasto-plastic models seems more adapted to describe the second type of migration, observed when alignments mechanism play only a little role. In this case, the type of dynamics observed in particle-based simulations is found to depend upon the persistence time of the self-propulsive force (i.e. the rotational noise) (Mandal et al., 2020a; Henkes et al., 2020). For small persistence times, the behavior is analogous to that of a glass-forming system described by an effective temperature $T_{\text{eff}} \propto f_0^2$ (with f_0 the magnitude of the self-propulsion force) (Bi et al., 2016; Mandal et al., 2016). On the other hand, for infinite persistence times, a transition between an athermal solid and an athermal fluid occurs for a critical value of the force magnitude (that depends upon the volume fraction) (Liao et al., 2018; Mandal et al., 2020a). This critical force is found to be analogous to the yield stress in sheared athermal systems (Liao et al., 2018). For intermediate persistence times, Mandal et al. (2020a) report intermittent dynamics resulting in arrested phases followed by bursts of plastic rearrangements with Eshelby-like non-affine displacement fields.

These findings suggest a strong analogy between self-propelled particles and sheared systems in the intermediate and infinite persistence time regimes. This analogy was actually demonstrated very recently (in the case of infinite persistence) at the theoretical level by Morse et al. (2020). A first naive use of elasto-plastic models to account for self-propulsion would be to activate plastic events with a random orientation (with an activation rule that remains to be specified) as proposed at the end of Chapter 4. Although this type of approach could describe the fluid phase in a system of self-propelled particles, the link between the self-propulsion force and the activation rule would remain phenomenological and would not enable us to study the solid-to-fluid transition induced by self-propulsion. To go further, a first step would be to introduce a polarity field in the EPM. This polarity field should probably be defined on a finer grid than that defined by the typical size of plastic rearrangements. A detailed study of the plastic rearrangements induced by self-propulsion in particle-based simulations should be conducted in order to understand the mechanisms by which self-propulsion triggers plasticity. We can for instance ask if, in the intermittent regime described by Mandal et al. (2020a), plastic events are triggered when a specific combination of polarity of neighboring particles is met such that the resulting force exceeds a local yield force. Is there a typical configuration of polarities leading to plastic rearrangements? Taking inspiration from the methods developed by Puosi et al. (2014) and Patinet et al. (2016), we could imagine building clusters of self-propelled particles embedded

in a system of passive particles, and, by varying the self-propulsion magnitude, the number of active particles and their polarity, determine the conditions under which plastic rearrangements occurs. To conclude, the project of building a self-propelled elasto-plastic model, even in the simplest scenario of infinite persistence and without any alignement mechanisms, would require an extensive work of numerical investigation, that could not be achieved during this PhD.

The recent work of Morse et al. (2020) further offers interesting perspectives regarding the analogy between shear and self-propulsion. Beside the theoretical framework (mean-field model in infinite dimension) predicting a formal analogy between shear and self-propulsion, they developed a novel driving protocol enabling a direct comparison between quasi-static shear and quasi-static self-propulsion with infinite persistence. By modeling self-propulsion as imposing a random displacement field in a quasi-static manner, they find the same dynamical behavior as for sheared systems (e.g., avalanches exponent), with differences explained by the correlation length of the displacement field. While self-propulsion corresponds to a correlation length equal to the particle size, shear corresponds to a correlation length of the order of the system size. Shear is thus seen as a particular case of a random displacement field. Their results also show that an amorphous solid driven with a random displacement field also undergoes a yielding transition that depends on glass stability. The authors also raise the question of the nature of flow localization in active systems, where there is no macroscopic symmetry imposed by shear, as discussed in Chapter 5. Finally, we may also wonder whether the theoretical framework developed by Morse et al. (2020) applies to the case of dilating and contracting particles as studied in Chapter 5, by taking a quasi-static limit of our model.

Appendix A

Appendices to Chapter 2

A.1 Numerical approach

We explain in this part our numerical approach to solve the dynamics of the elasto-plastic model introduced in Chapter 2. We explain in details the numerical strategy in the case of a 2d tensorial version of the model in the case of an imposed strain rate along the xy direction: $\dot{\gamma} \equiv \dot{\gamma}_{xy}$. Note that we also use a mesh refining procedure for the stress and strain fields to compute the convolutions in Fourier space (as done by Nicolas et al. (2013a)). The other variants used in the thesis (stress-controlled protocol, scalar model) are simple adaptations of the protocol explained below.

A.1.1 Algorithm

Our system is described by a 2d tensorial stress field with components $\sigma_{xx}(x)$ and $\sigma_{xy}(x)$ and a state variable field $n(x)$. We discretize these fields onto a 2d lattice of size $L_x \times L_y$ where a node (i, j) corresponds to the discretized spatial coordinates along the directions x and y respectively. We discretize also the time t by choosing a small discrete timestep $dt = 10^{-2}$, kept constant during the simulations. The equation of motion to simulate is given in the main text of the chapter by Eq. 2.43.

We choose initial conditions satisfying mechanical equilibrium. We typically initialize the system with: $\sigma_{xx}(x) = 0$, $\sigma_{xy}(x) = 0$ and $n(x) = 0$. We can also initialize the system using a configuration saved from a former simulation.

Once the system is initialized, we compute the evolution of the fields by numerically solving Eq. 2.31 (or Eq. 2.43 in discrete coordinates) using a simple Euler scheme. This reads, for instance, for the σ_{xy} component:

$$\begin{aligned}\sigma_{xy}(i,j)[t+dt] = \sigma_{xy}(i,j)[t] + \mu\dot{\gamma}dt + \mu \sum_{i',j'} G^{\text{2d,shear}}_{xy,xx}(i,j,i',j') \frac{n(i',j')\sigma_{xx}(i',j')}{\mu\tau} dt \\ + \mu \sum_{i',j'} G^{\text{2d,shear}}_{xy,xy}(i,j,i',j') \frac{n(i',j')\sigma_{xy}(i',j')}{\mu\tau} dt\end{aligned} \tag{A.1}$$

After each integration step, we update the state variable $n(i, j)$ according to the stochastic rules selected (Picard's model or yield stress distribution). In the case of stochastic rules based on a yield stress distribution, a new local threshold $\sigma_{\text{y}}(i, j)$ is drawn from the distribution (as explained in the main text) when yielding occurs locally.

Boundary conditions

We have discussed in the main text the elastic response to a localized shear transformation in an infinite continuum space. In the numerical implementation of the elasto-plastic model, we consider a discretized space (lattice) and it is convenient to work with a bounded system with periodic boundary conditions when focusing on bulk properties. Note that other types of boundary conditions have been implemented in the literature, enabling to study the effect of walls on the rheology (Picard et al., 2004; Nicolas et al., 2013b). The choice of periodic boundary conditions also simplifies the numerical method since it allows for the use of pseudo-spectral methods.

Pseudo-spectral method

The second term in Eq. 2.31 is an integral over the entire space since the elastic propagator $G^{2d,\text{shear}}(\vec{x}-\vec{x'})$ is long-ranged. If we take the Fourier transform of this term with respect to $\vec{x'}$, we obtain, instead of an integral over space, independent products for each Fourier modes $\vec{q}$:

$$\int d^d\vec{x'} G^{2d,\text{shear}}_{\alpha\beta,\gamma\delta}(\vec{x}-\vec{x'}) n(\vec{x'}) \sigma_{\gamma\delta}(\vec{x'}) \quad \rightarrow \quad \tilde{G^{2d,\text{shear}}}(\vec{q}) \tilde{n}(\vec{q}) \tilde{\sigma_{\gamma\delta}}(\vec{q}) \tag{A.2}$$

This operation thus transform a non local sum over all the spatial coordinates into a local operation in Fourier space, well suited to a parallel implementation. The stress evolution can thus be computed in Fourier space, but the step of update of the local state variable $n(\vec{x'})$ must be performed in real space. Two Fourier transforms (one forward and one backward) are thus performed at each timestep. This pseudo-spectral technique allows for a reduction of the computing time for the convolution from $O(N^2)$ to $O(N\log(N))$ (Liu et al., 2016).

We presented one possible method to handle the long range propagator in a discretized periodic space. Let us discuss now the different possible approaches and their limitations.

A.1.2 Different approaches for elastic propagators in discretized periodic space

The most straightforward approach to construct a continuous period elastic kernel is perhaps to sum the periodic images of each plastic events in real space. Due to the long range character of the kernel, this sum is only conditionally convergent and has to be performed in an order compatible with convergence (Budrikis et al., 2013). The kernel is then discretized in real space.

We use another method, which consists in computing analytically the Fourier transform of the kernel for an infinite system and discretize it onto discrete Fourier modes. We set the value of modes $q = 0$ (that is, the mean of the kernel in real space) to a value respecting the symmetries of the system (0 for a stress-controlled protocol, -1 for a shear rate controlled protocol) (Nicolas et al., 2018a). Transforming this discretized kernel back to real space ensures periodization. However, as discussed by Nicolas et al. (2013a) and Tyukodi (2016), this method induces some nonphysical, high frequency oscillations of the kernel in real space, due to the truncation of the high frequency terms in the inverse transform. This effect is visible for the σ_{xx} component of the stress in particular (Nicolas et al., 2013a). Using a finer mesh for the computation of the Fourier transformations, i.e., by dividing each block into four sub-blocks, so that each plastic event now spans four sub-blocks enables to obtain a smooth stress

field. We use this mesh refining procedure when dealing with tensorial versions of the model (in Chapter 5).

The two methods (image sum and Fourier discretization) are nearly equivalent in the far field, but differ in their near-field response (Budrikis et al., 2013) (the $1/r^2$ nature of the infinite system kernel at small distances is preserved with the image sum method while some distortions appear with the Fourier method). The choice of a particular kernel may thus impact the organization of the flow on short lengthscales.

A.1.3 GPU-based parallel implementation

We use a GPU-based parallel implementation to perform simulations of the elasto-plastic model. We build our code onto the code developed by Liu et al. (2016) (available at
https://bitbucket.org/ezeferrero/epm). The main changes include: generalizing it to a tensorial implementation with a mesh refining procedure, including a stress-controlled protocol and all the model-specific additions related to Chapter 4 and 5. Simulations were ran on Kepler architecture (GK208) GPUs, the Tesla K20.

Algorithm to solve the elasto-plastic dynamics

The dynamics for the local stress is solved in several steps:

1. Computation of the local plastic strain rate in real space on a lattice of size L: $\dot{\gamma}^{\mathrm{pl}}_{xx}(\vec{x}) = n(\vec{x})\sigma_{xx}(\vec{x})/\mu\tau$ (and respectively for $\dot{\gamma}^{\mathrm{pl}}_{xy}$).
2. Mesh refining step: the plastic strain field is copied onto a larger mesh of size $2L \times 2L$: $\dot{\gamma}^{\mathrm{pl}}_{xx}(\vec{x}) \rightarrow \dot{\gamma}^{\mathrm{pl,2L}}_{xx}(\vec{x})$
3. Discrete Fourier Transform of $\dot{\gamma}^{\mathrm{pl,2L}}_{xx}(\vec{x}) \rightarrow \tilde{\dot{\gamma}}^{\mathrm{pl,2L}}_{xx}(\vec{q})$
4. Pointwise multiplication of the plastic strain rate and the elastic propagator in Fourier space, yielding the stress rate increment: $\delta\tilde{\sigma}^{\mathrm{2L}}_{xx}/\delta t(\vec{q}) = \tilde{G}^{\mathrm{2d,shear,2L}}(\vec{q})\tilde{\dot{\gamma}}^{\mathrm{pl,2L}}_{xx}(\vec{q})$
5. Inverse discrete Fourier transform of the resulting stress rate increment $\delta\tilde{\sigma}^{\mathrm{2L}}_{xx}/\delta t(\vec{q}) \rightarrow \delta\sigma^{\mathrm{2L}}_{xx}/\delta t(\vec{x})$
6. Mesh averaging step: the stress rate increment field computed over a lattice $2L \times 2L$ is reduced to a lattice $L \times L$: $\delta\sigma^{\mathrm{2L}}_{xx}/\delta t(\vec{x}) \rightarrow \delta\sigma^{\mathrm{L}}_{xx}/\delta t(\vec{x})$
7. Euler integration step in real space on a lattice $L \times L$: $\sigma^{\mathrm{L}}_{xx}(\vec{x}) = \mu\dot{\gamma}dt + \left(\delta\sigma^{\mathrm{L}}_{xx}/\delta t(\vec{x})\right) dt$
8. Update the state variable $n(\vec{x})$ (and, depending upon the model, the local threshold $\sigma_{\mathrm{y}}(\vec{x})$)

The tasks are parallelized using CUDA kernels and Thrust functions. Discrete Fourier transforms are computed using the cuFFT library (see the Supplemental Materials of Liu et al. (2016) for more details).

A.2 Rheology in Picard's model

Fig. A.1 depicts the macroscopic flow curves obtained using a scalar version of Picard's model (Picard et al., 2005) for various values of the parameters τ_{pl} (panel (a)) and τ_{el} (panel (b)). The stress plateau observed on the flow curves corresponding to $\tau_{\mathrm{el}} = 10$ and $\tau_{\mathrm{el}} = 15$ in Fig. A.1(b) is associated with permanent shear bands. The negative slope observed for shear rates $\dot{\gamma}_{xy} \simeq 10^{-3}$ is due to finite size effects.

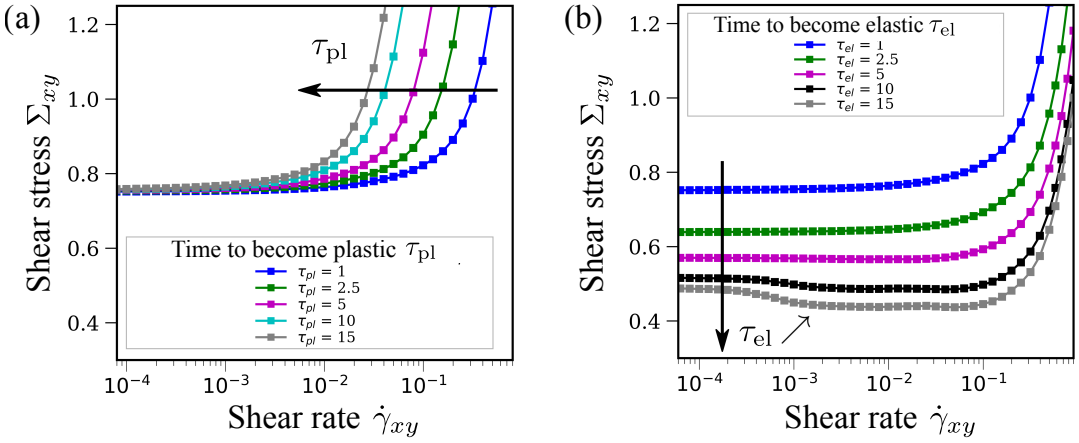

FIGURE A.1: **Macroscopic flow curve (stress versus strain rate) in a scalar version of Picard's model** for a system size $N = 256 \times 256$. (a) For $\tau_{\rm el} = 1$ and different values of $\tau_{\rm pl}$. (b) For $\tau_{\rm pl} = 1$ and different values of $\tau_{\rm el}$.

A.3 Single site elasto-plastic model

Martens et al. (2012) showed that the bulk rheology of Picard's model can be captured using an analytically solvable mean field approximation, by considering an effective single site dynamics. The derivation of this model is described below as we will extend this model in Chapter 4 to compute the low shear rate rheology in the presence of an external fluidizing noise.

In the scalar elasto-plastic model, the dynamics of the stress on a site (i, j) is written as:

$$\frac{\partial \sigma(i,j)}{\partial t} = \dot{\gamma}^{\rm eff}(i,j) + G(0,0)n(i,j)\sigma(i,j) \tag{A.3}$$

with $G(0,0) < 0$ the value of the stress propagator at the origin (describing the local plastic relaxation) and $\dot{\gamma}^{\rm eff}(i,j)$ the effective local shear rate due to the external driving and to the stress redistribution due to plastic events elsewhere in the system, $\dot{\gamma}^{\rm eff}(i,j) = \dot{\gamma} + \sum_{i',j'} G(i-i', j-j')n(i',j')\sigma(i',j')$. By assuming that this effective shear rate is spatially homogeneous and by neglecting any fluctuations around its mean value $\dot{\Gamma}$, the evolution of stress $\sigma(t)$ on a single site reads:

$$\frac{\partial \sigma(t)}{\partial t} = \dot{\Gamma} - g n(t)\sigma(t) \tag{A.4}$$

with $g = |G(0,0)|$ the absolute value of the stress propagator at the origin, which can depend on the system size in the spatial model, but which remains approximately constant for large systems ($g \simeq 0.57$). The dynamics of the activity $n(t)$ remains unchanged with respect to the spatial model (see section 2.2.3). In order to compute the steady state flow curve in this mean field approximation, we need to compute the time averaged stress $\langle \sigma \rangle_t$ as a function of $\dot{\Gamma}$.

We define σ_+ as the stress value when the site becomes plastic and σ_- as the stress value when the site becomes elastic. In the inactive state ($n = 0$), the stress increases linearly in time, starting from σ_-: $\sigma(t)_{n=0} = \sigma_- + \dot{\Gamma} t$. In the active state ($n = 1$), it comes from integrating Eq. A.4: $\sigma(t)_{n=1} = \frac{\dot{\Gamma}}{g} + (\sigma_+ + \frac{\dot{\Gamma}}{g})e^{-gt}$.

We further assume that the driving is sufficiently slow $\dot{\Gamma} < g$ and $\tau_{\rm el}$ sufficiently large to decorrelate the typical stress values for the change of activity. Under these

assumptions, the typical stress value at which a site becomes elastic is given by

$$\overline{\sigma_-} = \frac{\dot{\Gamma}}{g} + \frac{\overline{\sigma_+} - \dot{\Gamma}/g}{1 + g\tau_{\rm el}} \tag{A.5}$$

and the typical stress at which a site becomes plastic is

$$\overline{\sigma_+} = 1 + \dot{\Gamma}\tau_{\rm pl} \tag{A.6}$$

The time averaged stress $\langle\sigma\rangle_t$ can be computed as

$$\langle\sigma\rangle_t = \frac{\tau_{\rm in}\langle\sigma_{\rm in}\rangle_t + \tau_{\rm act}\langle\sigma_{\rm act}\rangle_t}{\tau_{\rm in} + \tau_{\rm act}} \tag{A.7}$$

with $\tau_{\rm in}$ and $\tau_{\rm act}$ the typical times spent in the inactive and active phase respectively, and $\langle\sigma_{\rm in}\rangle_t$ and $\langle\sigma_{\rm act}\rangle_t$ the associated average stress values.

In the inactive phase, the stress linearly increases in time between σ_- and σ_+, and the duration of the phase is given by $\frac{\sigma_+ - \sigma_-}{\dot{\Gamma}}$. To compute an ensemble average of the stress in the inactive phase, one needs to average over the values of σ_- and σ_+:

$$\langle\sigma_{\rm in}\rangle_t = \frac{1}{\tau_{\rm in}} \int_0^\infty d\sigma_- P_-(\sigma_-) \int_0^\infty d\sigma_+ P + -(\sigma_+) \left(\frac{\sigma_+ + \sigma_-}{2}\right) \left(\frac{\sigma_+ - \sigma_-}{\dot{\Gamma}}\right) \tag{A.8}$$

The time spent in the inactive phase can also be written as the sum of the time to reach the yield stress ($\sigma_y = 1$) and the typical time to yield once to yield stress is overcome, $\tau_{\rm pl}$.

$$\tau_{\rm in} = \frac{\overline{\sigma_+} - \overline{\sigma_-}}{\dot{\Gamma}} = \frac{1 - \overline{\sigma_-}}{\dot{\Gamma}} + \tau_{\rm pl} \tag{A.9}$$

This leads to

$$\langle\sigma_{\rm in}\rangle_t = \frac{\overline{\sigma_+^2} - \overline{\sigma_-^2}}{2(\overline{\sigma_+} - \overline{\sigma_-})} \tag{A.10}$$

In order to compute the values of $\overline{\sigma_+^2}$ and $\overline{\sigma_-^2}$, we consider the probability distributions of the time spent in the active phase $p_{\rm act}(t_{\rm act})$ and in the inactive phase once the stress has overcome the yield stress $p_{\rm in}(t_{\rm in})$:

$$p_{\rm act}(t_{\rm act}) = \frac{1}{\tau_{\rm el}} e^{-\frac{t_{\rm act}}{\tau_{\rm el}}} \tag{A.11}$$

$$p_{\rm in}(t_{\rm in}) = \frac{1}{\tau_{\rm pl}} e^{-\frac{t_{\rm in}}{\tau_{\rm pl}}} \tag{A.12}$$

We get

$$\overline{\sigma_+^2} = \int_0^\infty dt_{\rm in} p_{\rm in}(t_{\rm in}) \left(1 + \dot{\Gamma} t_{\rm in}\right)^2 = 1 + 2\dot{\Gamma}\tau_{\rm pl}\overline{\sigma_+} \tag{A.13}$$

and

$$\overline{\sigma_-^2} = \int_0^\infty dt_{\rm act} p_{\rm act}(t_{\rm act}) \left(\frac{\dot{\Gamma}}{g} + (\sigma_+ - \frac{\dot{\Gamma}}{g}) e^{-g t_{\rm act}}\right)^2 \tag{A.14}$$

$$\overline{\sigma_-^2} = \left(\frac{\dot{\Gamma}}{g}\right)^2 + 2\frac{\dot{\Gamma}}{g}\frac{\overline{\sigma_+} - \dot{\Gamma}/g}{1 + g\tau_{\rm el}} + \frac{\overline{\sigma_+^2} + 2(\dot{\Gamma}/g)\overline{\sigma_+} + (\dot{\Gamma}/g)^2}{1 + 2g\tau_{\rm el}} \tag{A.15}$$

To compute the average stress in the active phase, one needs to compute the time average of the stress during the active phase while taking an ensemble average of the

duration of the active phase:

$$\langle \sigma_{\mathrm{act}} \rangle_t = \frac{1}{\tau_{\mathrm{el}}} \int_0^\infty dt_{\mathrm{act}} p_{\mathrm{act}}(t_{\mathrm{act}}) \int_0^{t_{\mathrm{act}}} dt' \left(\frac{\dot{\Gamma}}{g} + (\sigma_+ - \frac{\dot{\Gamma}}{g}) e^{-gt'} \right) \tag{A.16}$$

We get

$$\langle \sigma_{\mathrm{act}} \rangle_t = \frac{\dot{\Gamma}}{g} + \frac{\overline{\sigma_+} - \dot{\Gamma}/g}{1 + g\tau_{\mathrm{el}}} = \overline{\sigma_-} \tag{A.17}$$

The typical time spent in the active phase is given by $\tau_{\mathrm{act}} = \tau_{\mathrm{el}}$.

Using Eq. A.7 and the analytical expressions in the above paragraph, we can express the steady state stress $\langle \sigma \rangle_t$ as a function of the shear rate $\dot{\Gamma}$.

Appendix B

Appendices to chapter 3

B.1 Details on particle-based simulations

The details of the particle based model, as well as the methods used for a quantitative comparison between the simulations and the model are provided in the Appendix of the paper submitted to *Soft Matter* and summarized below.

B.1.1 Particle-based model

The model disordered system is characterized by an interaction potential defined by $U(r) = 4\varepsilon\left[(a_{ij}/r_{ij})^{12} - (a_{ij}/r_{ij})^{6}\right] + \varepsilon$, for $r_{ij} \leq 2^{1/6}a_{ij}$, else $U(r_{ij}) = 0$. Here $a_{ij} = (a_i + a_j)/2$ defines the distance between the center of particles i (with diameter a_i) and j (with diameter a_j) at contact and the unit energy $\varepsilon = 1$ for all particles. The diameters of the particles are drawn from a Gaussian distribution with a variance of 10%. The initial configurations are prepared by quenching an equilibrated liquid configuration at a volume fraction $\phi = 0.70$, with a chosen set of simulation box dimensions (L_x, L_y and L_z). The quench rate used here is $\Gamma = 5 \cdot 10^{-3}\epsilon/(k_B\tau_0)$ and we find that the steady state flow features do not depend on the preparation protocol. Before subjecting the sample to shear, we take the system to the zero temperature limit using conjugate gradient energy minimization technique. Samples are then subjected to a shear deformation at finite shear rate using Lees-Edwards boundary conditions, using Dissipative Particle Dynamics (DPD):

$$m\frac{d^2\vec{r}_i}{dt^2} = -\zeta \sum_{j(\neq i)} \omega(r_{ij})(\hat{r}_{ij} \cdot \vec{v}_{ij})\hat{r}_{ij} - \nabla_{\vec{r}_i} U \tag{B.1}$$

where the first term in the right hand side (RHS) is the damping force which depends on the damping coefficient ζ and m is the mass of the particle. The relative velocity $\vec{v}_{ij} = \vec{v}_j - \vec{v}_i$ is computed over a cut-off distance $r_{ij} \leq 2.5a_{ij}$, with the weight factor $\omega(r_{ij}) = 1$. The second term in the RHS is the force due to interactions between particles. As a measure of the extent of over damping, we define an inertial quality factor $Q = \tau_{\text{damp}}/\tau_{\text{vib}}$, where $\tau_{\text{damp}} = m/\zeta$ is the viscous timescale and $\tau_{\text{vib}} = \sqrt{ma^2/\varepsilon}$ defines an elastic timescale. The inertial quality factor measures the number of inertial oscillation within the damping time. The shear rate in our simulations is defined in the units τ_{vib}^{-1}.

B.1.2 Steady-state flow

We make sure that a sample has indeed reached a steady state flow, by monitoring the macroscopic load curve as well as the microscopic flow profiles (V_x *vs.* Y) and stress profiles. Reaching steady state, the macroscopic load curve fluctuates over a

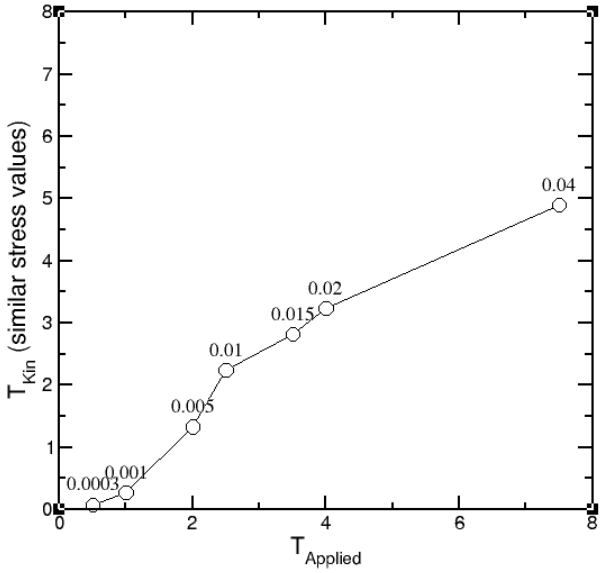

FIGURE B.1: **Kinetic temperature in an underdamped athermal system versus applied temperature in an overdamped thermal systems for similar stress and strain rates values.** The labels indicate the shear rates at which the kinetic temperature is measured.

mean stress value. Similarly the flow profiles as well as local stress do not evolve with time (strain).

B.1.3 Kinetic temperature in underdamped systems vs true temperature in overdamped systems

We plot in Fig. B.1 the kinetic temperature measured in simulations of a sheared underdamped athermal system as a function of the temperature corresponding to the same stress and shear rate value for sheared thermal overdamped systems. Although the correspondence is not perfect between the kinetic and the true temperature, we see a good correlation between these two quantities, related by a slope of about 0.6.

B.1.4 Herschel-Bulkley fitting parameters

Herschel-Bulkley (HB) fitting parameters for overdamped systems ($Q = 1$) at finite temperature are obtained by performing particle-based simulations over shear rates ranging between $\dot{\gamma} = 10^{-5}\tau_{\text{vib}}^{-1}$ to $\dot{\gamma} = 10^{-1}\tau_{\text{vib}}^{-1}$, of a system of 10^4 particles (keeping all other parameters the same as the under-damped simulations). Overdamped HB parameters at finite temperature (σ_{y}, A and n) are extracted from simulation data that have reached system state, for each temperature considered (ranging between $T = 0\varepsilon/k_B$ to $T = 7.5\varepsilon/k_B$).

B.1.5 Minimum length to accommodate an instability in molecular simulations

In order to obtain the minimum length scale to accommodate the flow instability, using the Eq. 3.16, one needs to compute the thermal conductivity λ_T, the heat capacity c_{v}, the time associated with the relaxation of kinetic energy τ, along with the derivative of stress with respect to temperature $\partial_T\sigma$ and to shear rate $\partial_{\dot{\gamma}}\sigma$ (first form of Eq. 3.16),

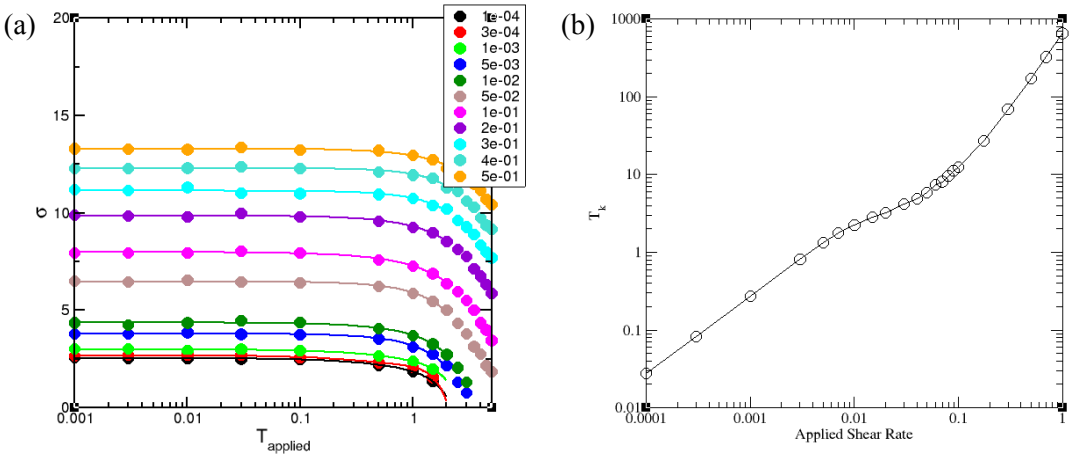

FIGURE B.2: **Stress in overdamped simulations for different temperatures and kinetic temperature dependence on the shear rate in underdamped simulations**. (a) Steady-state shear stress as a function of temperature measured in overdamped thermal simulations for various shear rates. (b) Kinetic temperature as a function of the applied shear rate measured in athermal underdamped simulations ($Q = 10^4$).

or directly the derivative of kinetic temperature with respect to the imposed shear rate $\partial_{\tilde{\gamma}\tilde{T}}$ (second form of Eq. 3.16).

λ_T is computed for a system size of $N = 10^5$, using the reverse non-equilibrium molecular dynamics method introduced by Müller-Plathe (1997) and its value is $\lambda_T = 30$ (LJ units). A slow quenching run is performed to prepare the initial sample. From this data, the heat capacity is computed as the slope of the total energy versus temperature, yielding a value $c_v = 3.0$ (LJ units), used in the computation of ℓ_c. To compute the relaxation time associated with the kinetic energy, the dissipation of kinetic energy is monitored in time at a fixed dissipation constant corresponding to $Q = 10^4$ and, yielding a value $\tau_{\mathrm{KE}} \equiv \tau \approx 350\tau_{\mathrm{vib}}$.

Using the first form of Eq. 3.16, one needs to compute the partial derivative of stress with respect to temperature ($\partial_T\sigma$) and shear rate ($\partial_{\dot{\gamma}}\sigma$). The value of $\partial_{\dot{\gamma}}\sigma$ can be obtained from the Herschel-Bulkley equation with fitting parameters obtained from the flow curve for $Q = 1$ (overdamped). The value of $\partial_T\sigma$ can be obtained by measuring, at a given shear rate, the stress in the finite temperature simulations in overdamped simulation conditions ($Q = 1$), as shown in Fig. B.2(a), and by computing the numerical derivative.

Another way is to use the second form of Eq. 3.16 and measure, in underdamped simulations ($Q = 10^4$), the evolution of kinetic temperature with the applied shear rate (Fig. B.2(b)). The data shown in Chapter 3 is obtained using this second method. We are currently working on comparing the two proposed methods in order to check that they yield similar estimates for ℓ_c.

B.1.6 Shear-concentration coupling effects

To be sure that in our case it is really the local heating effect that plays the role for the instability to occur we also provide additional measurements to disentangle potential mass migration effects from local kinetic temperature effects. To do so we measure alongside the local shear-rate profile also the steady state density profiles in the unstable region, shown in Fig. B.3(a) and (b). The question is whether these

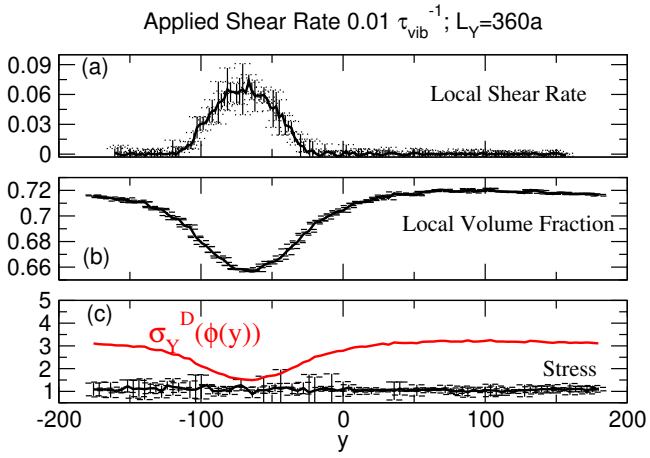

FIGURE B.3: **Concentration coupling effects in particle-based simulations**. Steady state measurement of (a) Local shear rate, (b) Local volume fraction and (c) Local stress and yield stress for a underdamped system ($Q = 10^4$) with a system size $L_y = 360a$, sheared at $\dot{\gamma} = 10^{-2}\tau_{\text{vib}}^{-1}$.

variations in the local volume fraction could as well explain the instability. To answer this question we also measure the yield stress dependence on density. We estimate the yield stress values for the range of different packing fractions that we observe in the density profiles of the simulations. And indeed we find that these are all above the actual homogeneous stress value, as shown in Fig. B.3. This means that the change of local volume fraction cannot induce an instability in our dynamics. However, the change of the local yield stress due to a finite kinetic temperature is much more drastic within the temperature range that we measure in the profiles. Therefore temperature is indeed inducing an instability to make the system flow in the high kinetic temperature regions where the temperature dependent yield stress is smaller than the homogeneous stress value. This is for us a strong enough indication that the observed migration is not the source of the instability but rather a consequence of another type of instability induced by the heating effect.

B.2 Dynamics in the continuum model and in particle-based simulations

The time (or strain) evolution of the macroscopic stress is shown for different system sizes and a shear rate $\dot{\gamma} = 10^{-2}$ in particle-based simulations (Fig. B.4(a)) and $\dot{\gamma} = 10^{-3}$ in the continuum model (Fig. B.4(b)).

For small systems where no shear banding is observed ($L_y < L_c$), the macroscopic stress reaches a plateau whose value is determined, for the continuum model, by the solution of the model for an homogeneous steady state (see main text). For larger systems in which shear banding occurs, the steady state stress is lowered compared to the homogeneous case. Interestingly, even if the steady state of the system is shear banded, the system can transiently reach the homogeneous stress value, as shown in Fig. B.4(b). The time to depart from this homogeneous solution increases as the system size is decreased towards its critical value L_c for the instability to occur.

The steady state in the continuum model is characterized by a constant macroscopic stress as well as constant stress profiles (Fig. B.5(b)), while the kinetic temperature and shear rate profiles remain banded (Fig. B.5(a) and Fig. 3.7(b)).

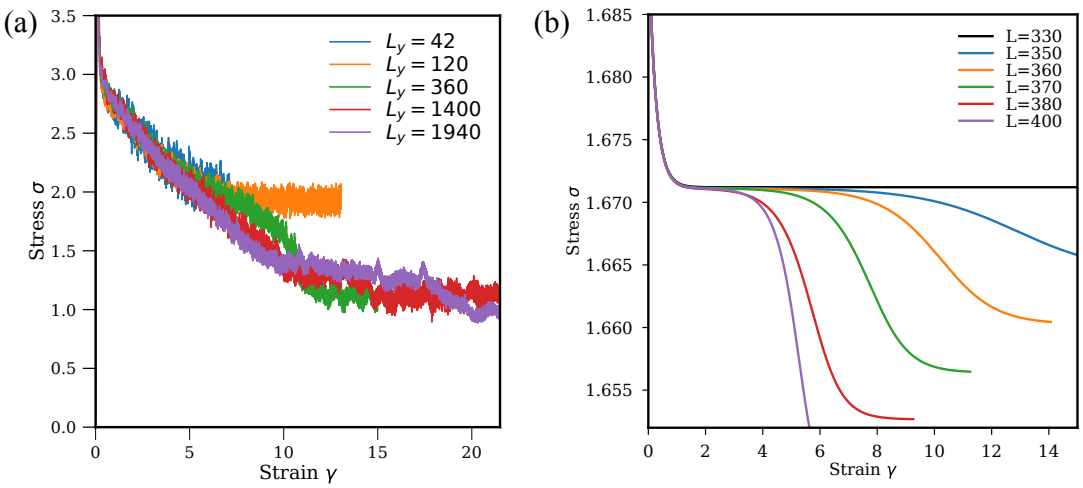

FIGURE B.4: **Stress as a function of strain for various system sizes along the gradient direction** L_y (a) In particle-based simulations, for an imposed shear rate $\dot{\gamma} = 10^{-2}$ and system sizes: $L_y = 42, 120, 360, 1400, 1940$. (b) In the continuum model, for an imposed shear rate$\dot{\gamma} = 10^{-3}$ and different system sizes: $L_y = 330, 350, 360, 370, 380, 400$.

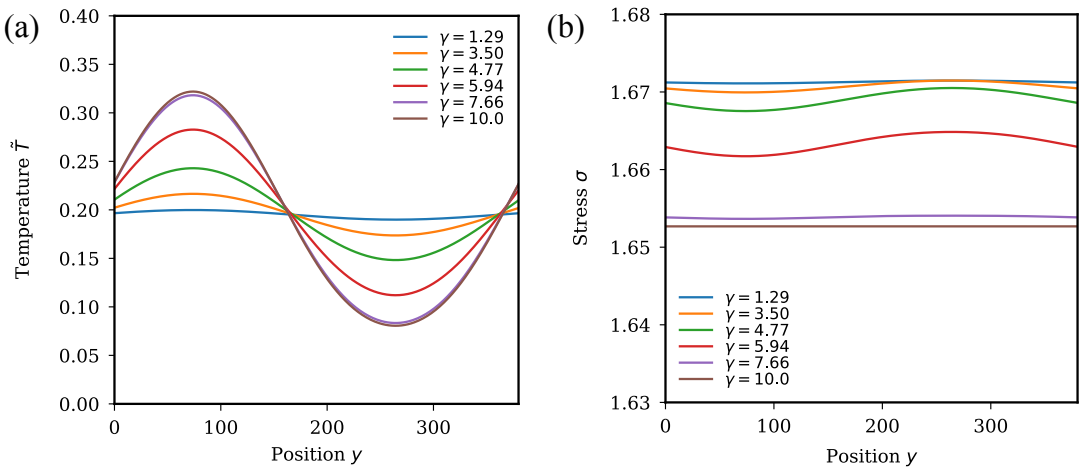

FIGURE B.5: **Temperature and stress profiles in the continuum model**.(a) Temperature profiles and (b) stress profiles for $L = 380$ at various strain values indicated by colored dots in Fig. 3.7(a)

Appendix C

Appendices to Chapter 4

C.1 Low shear rate rheology

In this part we study the low shear rate rheology in presence of external noise. We consider the regime where the plasticity is dominated by the external noise, and neglect the events activated by shear. We first consider the "0d" model (effective one site dynamics) and show that, in this regime, the rheology is linear and find an analytical expression for the viscosity in good agreement with simulations of the 2d spatial elasto-plastic model. We then use a further simplifying assumption of total stress relaxation to compute the flow curve for the two different models of noise considered in this study (random activation and Arrhenius-like activation).

C.1.1 Low shear rate rheology for a constant activation rate $k_{\mathbf{vib}} = \tau_{\mathbf{vib}}^{-1}$ in the single-site model

We consider the case where the activation of plastic events is dominated by the external noise, through a rate of activation $k_{\text{vib}} = 1/\tau_{\text{vib}}$, and neglect the activation of plastic events due to shear. In this case, following the computation of Appendix A (A.3), the average stress in the inactive (elastic) phase ($n = 0$) is given by:

$$\langle \sigma_{\text{in}} \rangle = \overline{\sigma_-} + \frac{\mu \dot{\Gamma} \tau_{\text{vib}}}{2} \tag{C.1}$$

with $\overline{\sigma_-}$ the typical stress when a site becomes plastic (under the same assumptions as those explained in Chapter 2, i.e., that the shear rate $\dot{\Gamma}$ is small enough and the restructuring time τ_{el} is large enough to decorrelate the typical stress values for the change of activity n). The typical time spent in the inactive state is simply given by

$$\tau_{\text{in}} = \tau_{\text{vib}} \tag{C.2}$$

The average stress in the active phase remains unchanged with respect to the case of shear induced plastic events as derived in Chapter 2:

$$\langle \sigma_{\text{act}} \rangle = \overline{\sigma_-} \tag{C.3}$$

and the duration of the active phase also remains

$$\tau_{\text{act}} = \tau_{\text{el}} \tag{C.4}$$

As previously, $\overline{\sigma_-}$ corresponds to the typical stress to become elastic, and is given by

$$\overline{\sigma_-} = \frac{\mu \dot{\Gamma}}{g} + \frac{\overline{\sigma_+} - \mu \dot{\Gamma}/g}{1 + g\tau_{\text{el}}} \tag{C.5}$$

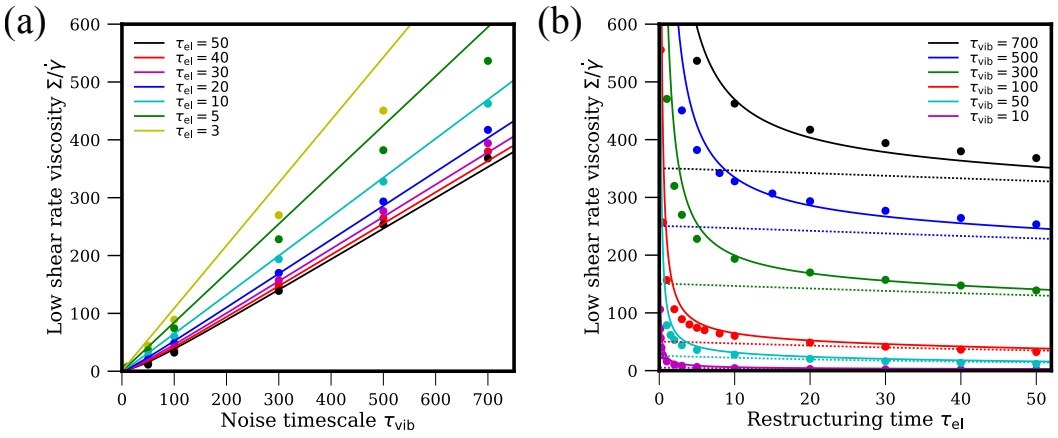

FIGURE C.1: Low shear rate viscosity $\Sigma/\dot{\gamma}$ (a) as a function of $\tau_{\rm vib}$ for various values of the restructuring time $\tau_{\rm el}$ and (b) as a function of $\tau_{\rm el}$ for various noise magnitudes $\tau_{\rm vib}$. The solid circles indicate spatial (2D) simulation points, the solid lines indicate the mean field model accounting for the noise-induced activation and the dotted line represents the model with a further assumption of total stress relaxation.

.

which, using $\overline{\sigma_+} = \overline{\sigma_-} + \mu\dot{\Gamma}\tau_{\rm vib}$, yields:

$$\overline{\sigma_-} = \frac{1}{g^2\tau_{\rm el}}\left(g\tau_{\rm el} + \mu\tau_{\rm vib}\right)\dot{\Gamma} \tag{C.6}$$

We can thus compute analytically the average stress

$$\langle\sigma\rangle = \frac{\tau_{\rm in}\sigma_{\rm in} + \tau_{\rm act}\sigma_{\rm act}}{\tau_{\rm in} + \tau_{\rm act}} = c\dot{\Gamma} \tag{C.7}$$

with

$$c = \left(\frac{1}{\tau_{\rm el} + \tau_{\rm vib}}\right) g\tau_{\rm el} + \tau_{\rm vib}\left(\frac{\mu}{g^2} + \frac{1}{g} + \frac{\mu\tau_{\rm vib}}{g^2\tau_{\rm el}} + \frac{\mu\tau_{\rm vib}}{2}\right) \tag{C.8}$$

We find a linear rheology behavior (consistent with numerical simulations of the model, see Fig. 4.2(a)) and compute the viscosity $\eta = \Sigma/\dot{\Gamma}$ for various values of $\tau_{\rm vib}$ and $\tau_{\rm el}$ as shown in Fig. C.1. We compare the viscosity obtained within the mean field model (solid lines) with numerical simulations of the spatially resolved model in 2 dimensions (solid dots). In Fig. C.1(a), we show the viscosity as a function of the timescale associated with noise $\tau_{\rm vib}$ for various values of restructuring time $\tau_{\rm el}$. Unsurprinsingly, the viscosity increases linearly with $\tau_{\rm vib}$. A good agreement between the mean field model and the spatial model is found for rather large values of $\tau_{\rm el}$, consistent with the hypothesis made in the calculations that the restructuring time is large enough to decorrelate the typical stress values for the change of activity n. Note that another source of discrepancy between mean field and spatial models comes from the fact that the "effective shear rate" ($\dot{\Gamma}$) in the one-site effective dynamics is actually different from the externally imposed shear rate $\dot{\gamma}$ (Martens et al., 2012). The approximation that we made that all the plastic activity is induced by the external noise and not by shearing is expected to be valid in the limit of large noise magnitudes $\tau_{\rm vib}^{-1}$. This is what is observed in Fig. C.1(b), where the agreement between our mean field approximation (solid line) and the spatial sinulations (solid circles) becomes better as $\tau_{\rm vib}^{-1}$ is increased (lower curves).

A further approximation could consist in assuming that the stress relaxation is total, so that the typical stress is the elastic phase is simply given by $\langle \sigma_{\rm in} \rangle_t = \frac{\mu \dot{\Gamma} \tau_{\rm vib}}{2}$. The viscosity thus obtained is shown by the dotted lines in Fig. C.1(b). This approximation becomes valid in the limit of large values of the restructuring time $\tau_{\rm el}$, and for large activation rates. However, it doesn't capture the strong increase of viscosity when $\tau_{\rm el}$ is decreased, indicating that this increase is due to incomplete local stress relaxation.

C.1.2 Simplified calculation for the low shear rate rheology for the two models of noise

We provide here a simplified calculation of the flow curve $\Sigma(\dot{\gamma})$ in the low shear-rate regime, under several simplifying assumptions. First, we assume that in this regime, the internal mechanical noise can be neglected with respect to the external noise. Second, we assume that the local stress fully relaxes during a plastic event, and that the duration of plastic events can be neglected as compared to the duration of elastic phases.

Under these strong assumptions, the local elastic stress is expressed as $\sigma = \mu \dot{\gamma} \Delta t$, where Δt is the time elapsed since the last plastic event, which relaxed the stress to $\sigma = 0$. Introducing the probability density function $p(\Delta t)$ of the time interval Δt, we get

$$\Sigma = \mu \dot{\gamma} \int_0^{\Delta t_{\rm max}} \Delta t \, p(\Delta t) \, d\Delta t \, . \tag{C.9}$$

The upper bound $\Delta t_{\rm max}$ may be estimated by the condition $\mu \dot{\gamma} \Delta t_{\rm max} = \sigma_c$, from which we deduce $\Delta t_{\rm max} = \sigma_c / (\mu \dot{\gamma})$. It follows that $\Delta t_{\rm max} \to \infty$ when $\dot{\gamma} \to 0$, and we can thus take the upper bound of the integral of Eq. (C.9) as infinite in the low shear-rate regime.

We now need to evaluate $p(\Delta t)$ for both models. On general grounds, for an activation rate $k_{\rm vib}(\sigma)$, one can write using $\sigma = \mu \dot{\gamma} \Delta t$,

$$\frac{dp}{d\Delta t} = -k_{\rm vib}(\mu \dot{\gamma} \Delta t) \, p(\Delta t) \, , \tag{C.10}$$

from which we get

$$p(\Delta t) = p_0 \, \exp \left[- \int_0^{\Delta t} k_{\rm vib}(\mu \dot{\gamma} t') \, dt' \right] \tag{C.11}$$

where p_0 is a normalization constant.

For Model 1, where $k_{\rm vib}$ is a constant, we get $p(\Delta t) = k_{\rm vib} \, e^{-k_{\rm vib} \Delta t}$ and thus

$$\Sigma = \frac{\mu}{k_{\rm vib} \, \dot{\gamma}} \, . \tag{C.12}$$

For Model 2, we have

$$k_{\rm vib}(\sigma) = k_0 \, e^{\lambda(\sigma - \sigma_c)} \, , \tag{C.13}$$

and thus

$$p(\Delta t) = p_0 \, \exp \left[-a \left(e^{\lambda \mu \dot{\gamma} \Delta t} - 1 \right) \right] , \tag{C.14}$$

where we have defined

$$a = \frac{k_0 \, e^{-\lambda \sigma_c}}{\lambda \mu \dot{\gamma}} \, . \tag{C.15}$$

After some straightforward algebra, we find that the normalization constant is given by $p_0 = \lambda \mu \dot{\gamma} \, e^{-a} / I(a)$, and the average stress by $\Sigma = J(a) / [\lambda \, I(a)]$, where we have

defined the auxiliary integrals

$$I(a) = \int_1^\infty \frac{du}{u}\, e^{-au}\,, \quad J(a) = \int_1^\infty \frac{du}{u}\, (\ln u)\, e^{-au} \tag{C.16}$$

(the integration variable u is obtained from the change of variable $u = e^{\lambda\mu\dot\gamma\Delta t}$). To get a more explicit expression in terms of $\dot\gamma$, we try to perform an asymptotic expansion of the integrals $I(a)$ and $J(a)$. At first sight, one would guess that a is large because $a \propto 1/\dot\gamma$ and $\dot\gamma$ is small. However, looking explicitly at the typical values of the parameter a in the shear rate regimes explored numerically, we find that $a \ll 1$ as long as

$$\dot\gamma \gg \frac{k_0\, e^{-\lambda\sigma_c}}{\lambda\mu} \sim 10^{-14} \tag{C.17}$$

with the parameter values used in the simulation (the extremely small value 10^{-14}, comes from the factor $e^{-\lambda\sigma_c} \sim e^{-30}$). In the regime $a \ll 1$, the exponential factor e^{-au} acts as a cut-off, thus providing an effective upper bound $\sim 1/a$ in the integrals that would otherwise diverge logarithmically without the exponential factor. As a simple approximation, we may thus write

$$I(a) \approx \int_1^{1/a} \frac{du}{u} = \ln\frac{1}{a}\,, \quad J(a) \approx \int_1^{1/a} \frac{du}{u}\, \ln u = \frac{1}{2}\left(\ln\frac{1}{a}\right)^2. \tag{C.18}$$

We thus eventually find

$$\Sigma = \frac{J(a)}{\lambda I(a)} \approx \frac{1}{2\lambda}\ln\frac{1}{a} = \frac{\sigma_c}{2} + \frac{1}{2\lambda}\ln\left(\frac{\lambda\mu}{k_0}\,\dot\gamma\right). \tag{C.19}$$

This logarithmic regime is valid in a finite shear-rate window: $\dot\gamma$ has to be larger than the (very small) lower bound given in Eq. (C.17), but it has to be small enough for the duration of plastic events and for the internal mechanical noise to be neglected.

C.2 Analogy with equilibrium critical phenomena with long-range interactions

Given that the exponents found for the correlation length and time are different from the equilibrium mean-field exponents for systems with short-range interactions, it is natural to wonder if including long-range interactions in an equilibrium analogue of our model may lead to the exponents $\nu = 1$ and $\mu = 1$. For the sake of simplicity, we briefly discuss this issue here in the language of spin models, where a magnetization field $m(\mathbf{r})$ is introduced. The above values of the exponents are suggestive of an effective Hamiltonian of the form (in the Gaussian approximation)

$$H \propto \int d\mathbf{q} \int d\mathbf{q}'(\varepsilon + |\mathbf{q}|)\hat m(\mathbf{q})\hat m(-\mathbf{q}) \tag{C.20}$$

where ε is the dimensionless deviation from the critical point, and $\hat m(\mathbf{q})$ is the spatial Fourier transform of the field $m(\mathbf{r})$. Such a Gaussian form leads to a divergence of the correlation length $\xi \sim \varepsilon^{-1}$, and thus to $\nu = 1$. However, this form corresponds to interactions decaying as $1/r^{d+1}$ (where d is the space dimension, $d = 2$ in our model), and not as $1/r^d$ as the Eshelby propagator.

Note that in terms of dynamics, a simple Langevin relaxational dynamics with the effective Hamiltonian (C.20) would lead, at the critical point, to

$$\partial_t \hat{m} = -|\mathbf{q}|\hat{m}(\mathbf{q}) + \xi(\mathbf{q}, t) \tag{C.21}$$

with $\xi(\mathbf{q}, t)$ a white noise. At a heuristic level, the scaling 'time $\sim$ length' suggests a dynamical exponent $z = 1$, corresponding to $\mu = z\nu = 1$.

Appendix D

Appendices to Chapter 5

D.1 Point-force model of contracting inclusion

We presented in Chapter 5 the computation of the displacement and stress fields in response to a contracting/dilating inclusion modeled as a set of two orthogonal pairs of forces. We followed the real-space computation of Lechner et al. (2009) for a compressible elastic medium. We present here a Fourier space computation similar to that presented in Chapter 2 to compute the response to a plastic transformation for an incompressible elastic medium.

We consider the same force density as presented in the main text, i.e.,

$$f_\alpha(x_\beta) = -f_0 h \frac{\partial \delta(x_\beta)}{\partial x_\alpha} \tag{D.1}$$

We assume that the elastic medium is incompressible and mechanical equilibrium reads

$$-\frac{\partial P}{\partial x_\alpha} + \mu \frac{\partial^2 u_\alpha}{\partial x_\beta^2} + f_\alpha = 0 \tag{D.2}$$

This equation can be solved in Fourier space, with $\tilde{f}_\alpha = i f_0 h q_\alpha$.

$$i q_\alpha \tilde{P} - \mu q_\beta q_\beta \tilde{u}_\alpha + \tilde{f}_\alpha = 0 \tag{D.3}$$

and

$$-i q_\alpha \tilde{u}_\alpha = 0 \tag{D.4}$$

It comes that the pressure field is homogeneous and the Oseen tensor reads

$$\tilde{u}_\alpha = \frac{\tilde{f}_\alpha}{\mu q^2} = \frac{i f_0 h q_\alpha}{\mu q^2} \tag{D.5}$$

Then, using $\sigma_{\alpha\beta} = 2\mu\varepsilon_{\alpha\beta}$, with $\varepsilon_{\alpha\beta} = -(i/2)(q_\alpha u_\beta + q_\beta u_\alpha)$, we get:

$$\tilde{\sigma}_{\alpha\beta} = 2 f_0 h \frac{q_\alpha q_\beta}{q^2} \tag{D.6}$$

As in the work of Picard et al. (2004), the force f_0 can be related to the active volumetric strain occurring in the inclusion $\varepsilon^{\mathrm{act}}$ as (Tyukodi, 2016):

$$f_0 = \mu \pi h \varepsilon^{\mathrm{act}} \tag{D.7}$$

For simplicity, we rewrite the above equation as

$$\tilde{\sigma}_{\alpha\beta} = \mu\alpha \frac{q_\alpha q_\beta}{q^2} \gamma^{\mathrm{act}} \tag{D.8}$$

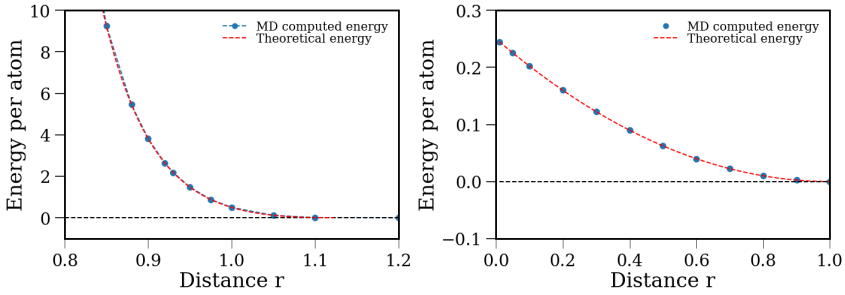

FIGURE D.1: **Potential energy per atom as a function of the distance between 2 atoms**. (Left) Truncated and shifted Lennard-Jones potential. (Right): Short-ranged harmonic potential.

with $\alpha = \pi h^2$ a constant related to the inclusion (that we set to 1 in the mesoscale simulations) and $\gamma^{\text{act}} = 2\varepsilon^{\text{act}}$.

D.2 Particle-based simulations

The two types of repulsive interaction potentials used in our simulations are shown in Fig. D.1.

D.3 Active Elasto-Plastic Model

D.3.1 Transient dynamics

Fig. D.2 depicts the evolution of several quantities as a function of the number of cycles (with a period $T = 1000$) (for a system size $L = 64$): (a) the fraction of sites undergoing plastic deformation, (b) the spatially average barrier to yield, (c) the fraction of plastic events induced by the active driving only (no contribution from the mechanical noise due to other plastic rearrangements in the system) and (d) the cumulated plasticity per cycle (same as Fig. 5.10)(a)) for two independent samples (by choosing different distributions for the phases of oscillation of the active drive).

For all these observables, a long transient regime is observed for amplitudes of the active drive close to the transition; long simulation runs are thus required in order to characterize the transition. The comparison of two independent samples in Fig. D.2(d) suggests that sample-to-sample variations may be relatively small - for the cumulated plasticity at least-. Averaging over few independent samples will nonetheless be performed in future work in order to characterize the transition.

D.3.2 Dynamics of tracer particles in the AEPM

In Fig. D.3(a), we plot the probability distribution of one-cycle displacements of tracer particles $\delta x_i = |x_i(t+T) - x_i(t)|$ (averaged over x and y directions) for a few values of a in the vicinity of the transition (computed after running the simulations for about 5000 cycles). Although we see that the one-cycle displacement reaches larger values for increasing values of a, there is no sign of discontinuity in these first data, that have not yet reached steady state.

In Fig. D.3(b), we compute the mean squared displacement of the tracer particles, which exhibits a diffusive behavior in the fluid phase (red curve for $a = 30$, diffusive behavior indicated by the black dashed line). Measurements in steady state and over

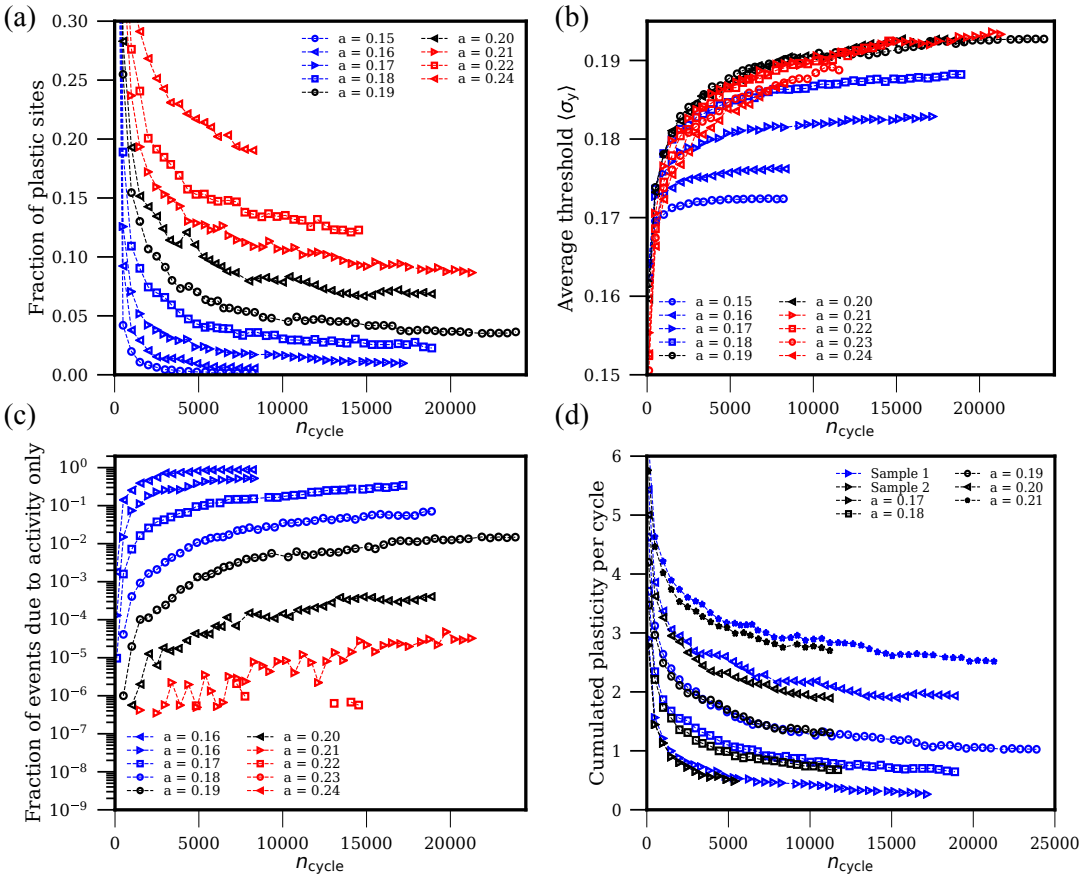

FIGURE D.2: **Transient dynamics in the AEPM.** (a) Fraction of sites undergoing plastic events as a function of the number of cycles of oscillation n_{cycle}. (b) Average local threshold σ_y as a function of n_{cycle}. (c) Fraction of plastic events triggered by the active driving only (no contribution of the mechanical noise due to Eshelby plastic rearrangements) as a function of n_{cycle}. (d) Cumulated plasticity per cycle as a function of n_{cycle} for two independent samples (i.e. two different distributions of phases of oscillation for the active drive).

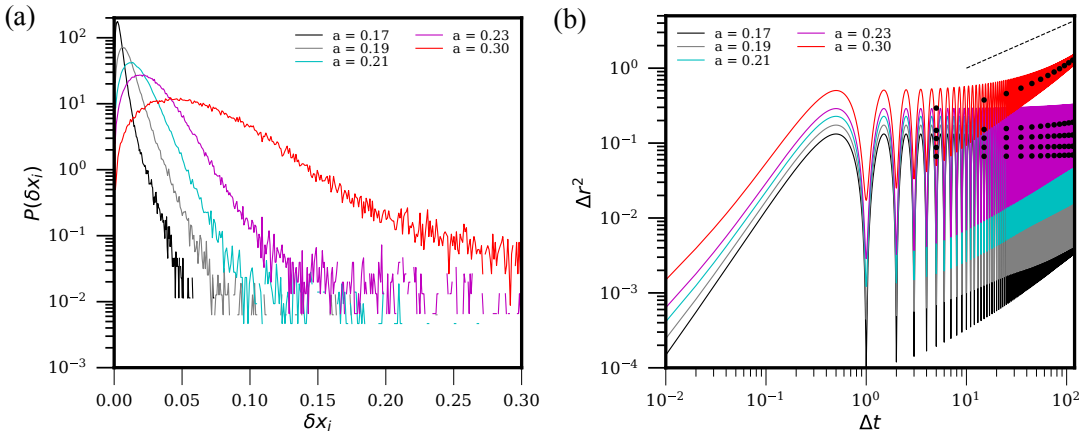

FIGURE D.3: **Dynamics of tracer particles in the AEPM**. (a) Probability distribution of the one-cycle displacement for various values of the active driving amplitude a. (b) Mean squared displacement (diffusive behavior indicated by the black dashed line). The black dots indicate the data averaged over one cycle.

longer durations should be performed to assess the behavior of particles trajectories in the vicinity of the transition.

D.3.3 Characteristics of the active drive

At each timestep, a site receives stress increments due to actively deforming sites in the system. The resulting stress is computed from the convolution of the field of active deformation γ^{act} with the elastic propagator F describing the far-field response to an actively deforming inclusion. The stress received due to the active drive by a given site varies in time due to the fact that the active deformation in all the surrounding sites has its own oscillatory dynamics.

We measure the two components (σ_{xx}^{act} and σ_{xy}^{act}) of the stress received by each site at timesteps separated by an interval $\Delta t = 10$ during one cycle of oscillations $T = 1000$. We show in Fig. D.4(a) an example of stress received in a single site due to the active drive on all the other sites of the system.

We then measure the maximum of the Von Mises stress received by each site (in the example of Fig. D.4(a) it is approximately equal to 0.077). We depict in Fig. D.4(b) the distribution of the maximum Von Mises stress $\sigma_{\text{v}}^{\text{act,MAX}}$ received during one cycle in each site, which exhibits a maximum at $\sigma_{\text{v}}^{\text{act,MAX}} = a$.

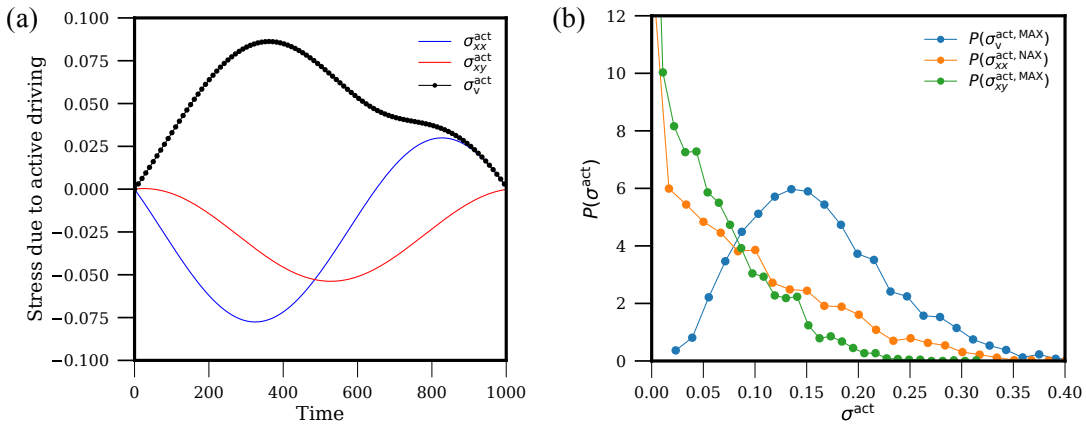

FIGURE D.4: **Characteristics of the active driving**. (a) Example of stress received due to the active drive during one cycle of oscillation for a system size $L = 64$ and a driving amplitude $a = 0.15$. The Von Mises stress is given by $\sigma_{\rm v}^{\rm act} = \sqrt{\sigma_{xy}^{\rm act\,2} + \sigma_{xx}^{\rm act\,2}}$. (b) Probability distribution of the maximum active driving stress $\sigma^{\rm act,MAX}$ received in each site.

Appendix E

Appendices to Chapter 6

E.1 Details on numerical methods and simulation parameters

E.1.1 Confinement in the SPV model

In SAMoS, the boundaries are imposed through a special type of particles (called "boundary" particles, and denoted b in the parameters list) that form a "boundary line" that delineates between the monolayer and its surrounding (described through a boundary line tension λ_b and a bending stiffness κ_b). The confinement is introduced through a rectangular assembly of immobile particles ("wall" of dimensions (L_X , L_Y), denoted w in the parameters) that interact through a repulsive potential with the cells, characterized by a stiffness k_{cw} and a characteristic length a_w. Note that the boundary particles do not represent cells and hence do not interact with the confining layer of immobile particles (interaction potential $k_{bw} = 0$ between the boundary and the wall).

E.1.2 Simulation methods and parameters

We integrate the above model using Brownian dynamics (Barton et al., 2017). We first prepare the monolayer configurations and oscillations are then studied in steady state with a fixed number of cells. The layer is initialized with a cell number that is fixed by the system size $N_{\text{init}} = (L_X - 2)(L_Y - 1)$, and cells are able to divide during a time T_{growth} at a rate $d = d_0(1 - z/\rho_{\text{max}})$ (with z the number of neighbors and ρ_{max} a parameter describing the maximum number of neighbors), to achieve a given cell number density. Division is then turned off and the study focuses on times $t > T_{\text{growth}}$. The total duration of simulation T_{run} depends on the time period of oscillations T but is usually $T_{\text{run}} > 10T$. The parameters of the vertex model (A_0, P_0, K and Γ) are chosen such that the monolayer is in a solid-like state ($p_0 = P_0/\sqrt{A_0} = 2.5$) and cells are mostly hexagonal. Note that keeping very low values of p_0 is important in order to avoid having only square cells due to the rectangular confinement constraints, and to prevent shear flow induced by the boundaries, that prevents the onset of oscillations. Note that in our simulations, the confinement induces additional geometrical constraints on the monolayer: for an imposed value of $p_0 = 3.1$, the average value of the shape factor $p = \langle P/\sqrt{A}\rangle \simeq 3.75$, mainly due to the fact that the average area ($\langle A\rangle \simeq 0.7$) is smaller than the target area ($A_0 = 1$). The value of self-propulsion velocity is set to $v_0 = 0.2$, but note that changing the value of v_0 doesn't affect the features of the oscillations much (it only dictates the amplitude of velocity oscillations). The rotational diffusion coefficient D_r is set to a constant value. The values of all the parameters are listed in the following tables.

TABLE E.1: **Vertex-energy, boundary and potential parameters**. Raw simulation parameters

Parameter	Meaning	Value
K	Area stiffness	1.0
Γ	Perimeter stiffness	1.0
A_0	Target area	1.0
P_0	Target perimeter	between 2.5 and 3.8
k_{cc}	Repulsive potential strength	5.0
a_{cc}	Repulsive potential length	1.0
k_{cw}	Confinement strength (cells)	5.0
k_{bw}	Confinement strength (boundary)	0.0
a_w	Confinement potential length	1.0
κ	Boundary bending	0.1
λ	Line tension	0.1

TABLE E.2: **Dynamics parameters**

Parameter	Meaning	Value
v_0	Self propulsion velocity	0.1 or 0.2
γ	Friction	1.0
γ_r	Orientational friction	1.0
μ	Mobility	1.0
μ_r	Rotational mobility	1.0
ν_r	Rotational noise (rate)	0.1

E.1.3 Simulation data analysis (SPV model)

Custom-made codes were developed for data analysis in Python. Similarly as for processing experimental data, once in the steady state regime, we average the horizontal component of the centroids velocity along the transverse direction and generate the kymographs of x-velocity by displaying this average value as a function of time and space along the horizontal direction x.

Wavelength and period

The period and wavelength of oscillations are then extracted from the autocorrelation of the kymograph of the x-component of the velocity, as shown in Fig. E.1.

Propagation velocity

The propagation velocity of oscillations can be measured either from the space-time kymograph of the x-component of the velocity or from its 2d-autocorrelation. We use a method to detect the "lines" delimitating the leftward and rightward motions using the Hough transform (Hough, 1962), either on the space-time kymograph of the cell velocity (Fig.E.2(a)) or on its autocorrelation (Fig.E.2(b)). We use Hough transform algorithms from the *Scikit-image* image processing Python library (https://scikit-image.org).

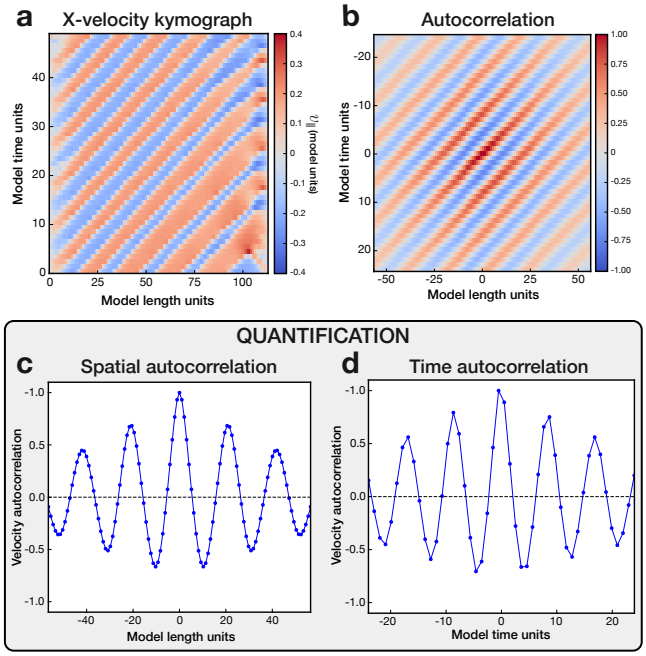

FIGURE E.1: **Illustration of simulation data analysis**. (a) Kymograph of the x-component of the velocity averaged along the y-direction. (b) Auto-correlation of the kymograph. (c) Spatial autocorrelation used to extract the wavelength of oscillations. (d) Time autocorrelation used to extract the time period of oscillations.

E.2 Velocity oscillation for different values of v_0

We show in Fig. E.3 the evolution in time of the x-component of the velocity averaged over the the whole system (in the small system regime where global oscillations are observed) for three different values of the self-propulsion speed v_0. All the data can be approximately collapsed by normalizing the velocity with the value of v_0.

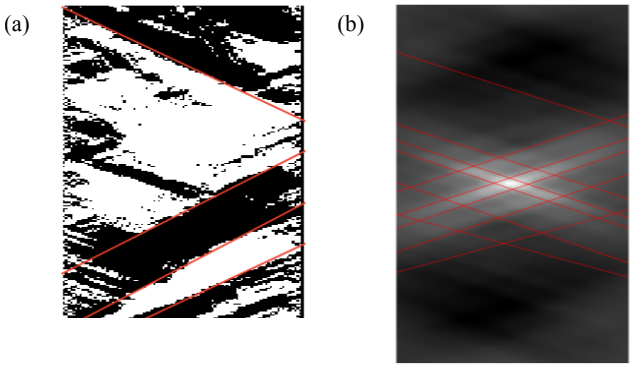

FIGURE E.2: **Examples of line detection using the Hough transform to measure the wave velocity** in (a) the space-time kymograph of the x-component of the velocity averaged along the y dimension and (b) the autocorrelation of the space-time kymograph of the velocity.

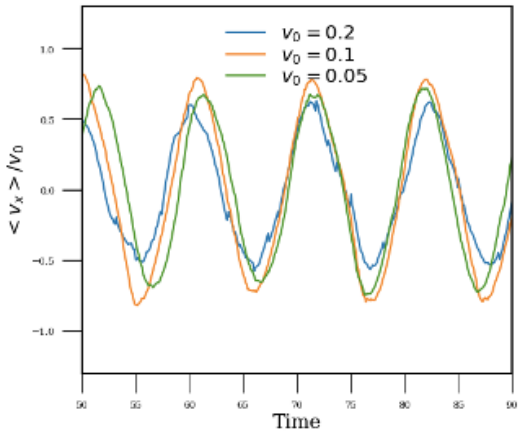

FIGURE E.3: **Velocity oscillation for different values of the self-propulsion speed** v_0. Velocity averaged over the system for a small system ($L_X = 15$) rescaled by v_0.

Bibliography

Agoritsas, Elisabeth, Eric Bertin, Kirsten Martens, and Jean-Louis Barrat (2015). "On the relevance of disorder in athermal amorphous materials under shear". In: *European Physical Journal E* 38.7, p. 71.

Albaret, T, A Tanguy, F Boioli, and D Rodney (2016). "Mapping between atomistic simulations and Eshelby inclusions in the shear deformation of an amorphous silicon model". In: *Physical Review E* 93.5, p. 053002.

Alert, Ricard and Xavier Trepat (2019). "Physical Models of Collective Cell Migration". In: *Annual Review of Condensed Matter Physics* 11.

Amon, Axelle, Ary Bruand, Jérôme Crassous, Eric Clément, et al. (2012). "Hot spots in an athermal system". In: *Physical Review Letters* 108.13, p. 135502.

Andreotti, Bruno, Yoël Forterre, and Olivier Pouliquen (2013). *Granular media: between fluid and solid*. Cambridge University Press.

Angelini, Thomas E, Edouard Hannezo, Xavier Trepat, Manuel Marquez, Jeffrey J Fredberg, and David A Weitz (2011). "Glass-like dynamics of collective cell migration". In: *Proceedings of the National Academy of Sciences* 108.12, pp. 4714–4719.

Angell, CA (1991). "Relaxation in liquids, polymers and plastic crystals—strong/fragile patterns and problems". In: *Journal of Non-Crystalline Solids* 131, pp. 13–31.

Aoki, Kazuhiro, Yohei Kondo, Honda Naoki, Toru Hiratsuka, Reina E Itoh, and Michiyuki Matsuda (2017). "Propagating wave of ERK activation orients collective cell migration". In: *Developmental cell* 43.3, pp. 305–317.

Argon, AS (1979). "Plastic deformation in metallic glasses". In: *Acta metall.* 27.1, pp. 47–58.

Argon, AS and HY Kuo (1979). "Plastic flow in a disordered bubble raft (an analog of a metallic glass)". In: *Materials science and Engineering* 39, pp. 101–109.

Banerjee, Shiladitya and M Cristina Marchetti (2019). "Continuum models of collective cell migration". In: *Cell Migrations: Causes and Functions*. Springer, pp. 45–66.

Banerjee, Shiladitya, Kazage JC Utuje, and M Cristina Marchetti (2015). "Propagating stress waves during epithelial expansion". In: *Physical review letters* 114.22, p. 228101.

Barbot, Armand, Matthias Lerbinger, Anier Hernandez-Garcia, Reinaldo García-García, Michael L Falk, Damien Vandembroucq, and Sylvain Patinet (2018). "Local yield stress statistics in model amorphous solids". In: *Physical Review E* 97.3, p. 033001.

Barés, Jonathan, Dengming Wang, Dong Wang, Thibault Bertrand, Corey S O'Hern, and Robert P Behringer (2017). "Local and global avalanches in a two-dimensional sheared granular medium". In: *Physical Review E* 96.5, p. 052902.

Baret, Jean-Christophe, Damien Vandembroucq, and Stéphane Roux (2002). "Extremal model for amorphous media plasticity". In: *Physical Review Letters* 89.19, p. 195506.

Barton, Daniel L, Silke Henkes, Cornelis J Weijer, and Rastko Sknepnek (2017). "Active vertex model for cell-resolution description of epithelial tissue mechanics". In: *PLoS computational biology* 13.6, e1005569.

Bécu, Lydiane, Sébastien Manneville, and Annie Colin (2006). "Yielding and flow in adhesive and nonadhesive concentrated emulsions". In: *Physical Review Letters* 96.13, p. 138302.

Berthier, Ludovic (2014). "Nonequilibrium glassy dynamics of self-propelled hard disks". In: *Physical review letters* 112.22, p. 220602.

Berthier, Ludovic and Giulio Biroli (2011). "Theoretical perspective on the glass transition and amorphous materials". In: *Reviews of Modern Physics* 83.2, p. 587.

Berthier, Ludovic, Elijah Flenner, and Grzegorz Szamel (2017). "How active forces influence nonequilibrium glass transitions". In: *New Journal of Physics* 19.12, p. 125006.

— (2019). "Glassy dynamics in dense systems of active particles". In: *The Journal of chemical physics* 150.20, p. 200901.

Bertrand, Emanuel, Jerome Bibette, and Véronique Schmitt (2002). "From shear thickening to shear-induced jamming". In: *Physical Review E* 66.6, p. 060401.

Bertrand, Thibault, Joseph d'Alessandro, Ananyo Maitra, Shreyansh Jain, Barbara Mercier, René-Marc Mège, Benoit Ladoux, and Raphaël Voituriez (2020). "Clustering and ordering in cell assemblies with generic asymmetric aligning interactions". In: *arXiv preprint arXiv:2012.00785*.

Besseling, Rut, Lucio Isa, Pierre Ballesta, G Petekidis, ME Cates, and WCK Poon (2010). "Shear banding and flow-concentration coupling in colloidal glasses". In: *Physical review letters* 105.26, p. 268301.

Bi, Dapeng, JH Lopez, JM Schwarz, and M Lisa Manning (2015). "A density-independent rigidity transition in biological tissues". In: *Nature Physics* 11.12, p. 1074.

Bi, Dapeng, Jorge H Lopez, JM Schwarz, and M Lisa Manning (2014). "Energy barriers and cell migration in densely packed tissues". In: *Soft Matter* 10.12, pp. 1885–1890.

Bi, Dapeng, Xingbo Yang, M Cristina Marchetti, and M Lisa Manning (2016). "Motility-driven glass and jamming transitions in biological tissues". In: *Physical Review X* 6.2, p. 021011.

Binder, Kurt and Dieter W Heermann (2010). *Monte Carlo Simulation in Statistical Physics: An Introduction*. Springer Science & Business Media.

Blanch-Mercader, C, R Vincent, Elsa Bazellières, X Serra-Picamal, X Trepat, and J Casademunt (2017a). "Effective viscosity and dynamics of spreading epithelia: a solvable model". In: *Soft Matter* 13.6, pp. 1235–1243.

Blanch-Mercader, Carles and Jaume Casademunt (2017b). "Hydrodynamic instabilities, waves and turbulence in spreading epithelia". In: *Soft matter* 13.38, pp. 6913–6928.

Bocquet, Lydéric, Annie Colin, and Armand Ajdari (2009). "Kinetic theory of plastic flow in soft glassy materials". In: *Physical review letters* 103.3, p. 036001.

Bonn, Daniel, Morton M Denn, Ludovic Berthier, Thibaut Divoux, and Sébastien Manneville (2017). "Yield stress materials in soft condensed matter". In: *Reviews of Modern Physics* 89.3, p. 035005.

Boocock, Daniel, Naoya Hino, Natalia Ruzickova, Tsuyoshi Hirashima, and Edouard Hannezo (2020). "Theory of mechano-chemical patterning and optimal migration in cell monolayers". In: *bioRxiv*.

Bouchaud, Jean-Philippe (1992). "Weak ergodicity breaking and aging in disordered systems". In: *Journal de Physique I* 2.9, pp. 1705–1713.

Bouzid, Mehdi, Adrien Izzet, Martin Trulsson, Eric Clément, Philippe Claudin, and Bruno Andreotti (2015). "Non-local rheology in dense granular flows". In: *The European Physical Journal E* 38.11, p. 125.

Brader, Joseph M, Th Voigtmann, Michael E Cates, and Matthias Fuchs (2007). "Dense colloidal suspensions under time-dependent shear". In: *Physical review letters* 98.5, p. 058301.

Brader, Joseph M, Thomas Voigtmann, Matthias Fuchs, Ronald G Larson, and Michael E Cates (2009). "Glass rheology: From mode-coupling theory to a dynamical yield criterion". In: *Proceedings of the National Academy of Sciences* 106.36, pp. 15186–15191.

Bragg, William Lawrence and JF Nye (1947). "A dynamical model of a crystal structure". In: *Proceedings of the Royal Society of London. Series A. Mathematical and Physical Sciences* 190.1023, pp. 474–481.

Bricard, Antoine, Jean-Baptiste Caussin, Nicolas Desreumaux, Olivier Dauchot, and Denis Bartolo (2013). "Emergence of macroscopic directed motion in populations of motile colloids". In: *Nature* 503.7474, pp. 95–98.

Brodland, G Wayne (2015). "How computational models can help unlock biological systems". In: *Seminars in cell & developmental biology*. Vol. 47. Elsevier, pp. 62–73.

Budrikis, Zoe, David Fernandez Castellanos, Stefan Sandfeld, Michael Zaiser, and Stefano Zapperi (2017). "Universal features of amorphous plasticity". In: *Nature communications* 8.1, pp. 1–10.

Budrikis, Zoe and Stefano Zapperi (2013). "Avalanche localization and crossover scaling in amorphous plasticity". In: *Physical Review E* 88.6, p. 062403.

Bulatov, VV and AS Argon (1994). "A stochastic model for continuum elasto-plastic behavior. I. Numerical approach and strain localization". In: *Modelling and Simulation in Materials Science and Engineering* 2.2, p. 167.

Buttenschön, Andreas and Leah Edelstein-Keshet (2020). "Bridging from single to collective cell migration: A review of models and links to experiments". In: *arXiv preprint arXiv:2011.10873*.

Caballero-Robledo, G. A. and E. Clément (2009). "Rheology of a sonofluidized granular packing". In: *European Physical Journal E* 30.4, p. 395.

Camley, Brian A and Wouter-Jan Rappel (2017). "Physical models of collective cell motility: from cell to tissue". In: *Journal of physics D: Applied physics* 50.11, p. 113002.

Campbell, Charles S and Christopher E Brennen (1985). "Computer simulation of granular shear flows". In: *Journal of Fluid Mechanics* 151, pp. 167–188.

Cantat, Isabelle and Olivier Pitois (2006). "Stokes experiment in a liquid foam". In: *Physics of Fluids* 18.8, p. 083302.

Cao, Xiangyu, Alexandre Nicolas, Denny Trimcev, and Alberto Rosso (2018). "Soft modes and strain redistribution in continuous models of amorphous plasticity: the Eshelby paradigm, and beyond?" In: *Soft matter* 14.18, pp. 3640–3651.

Cates, Michael E and Julien Tailleur (2015). "Motility-induced phase separation". In: *Annu. Rev. Condens. Matter Phys.* 6.1, pp. 219–244.

Chattoraj, Joyjit, Christiane Caroli, and Anaël Lemaître (2010). "Universal additive effect of temperature on the rheology of amorphous solids". In: *Physical Review Letters* 105, p. 266001.

Chaudhuri, Pinaki, Ludovic Berthier, and Lydéric Bocquet (2012). "Inhomogeneous shear flows in soft jammed materials with tunable attractive forces". In: *Physical Review E* 85.2, p. 021503.

Chen, Kan, Per Bak, and SP Obukhov (1991). "Self-organized criticality in a crack-propagation model of earthquakes". In: *Physical Review A* 43.2, p. 625.

Chiang, M and D Marenduzzo (2016). "Glass transitions in the cellular Potts model". In: *EPL (Europhysics Letters)* 116.2, p. 28009.

Cloitre, Michel (2018). "Microscopic Design of Glassy Suspensions Using Soft Colloids". In: *Talk at the KITP conference "Physics of dense suspensions"*.

Cloitre, Michel, Régis Borrega, Fabrice Monti, and Ludwik Leibler (2003). "Glassy dynamics and flow properties of soft colloidal pastes". In: *Physical review letters* 90.6, p. 068303.

Cohen-Addad, Sylvie, Reinhard Höhler, and Yacine Khidas (2004). "Origin of the slow linear viscoelastic response of aqueous foams". In: *Physical Review Letters* 93.2, p. 028302.

Collinet, Claudio, Matteo Rauzi, Pierre-François Lenne, and Thomas Lecuit (2015). "Local and tissue-scale forces drive oriented junction growth during tissue extension". In: *Nature cell biology* 17.10, pp. 1247–1258.

Coulais, Corentin, Antoine Seguin, and Olivier Dauchot (2014). "Shear modulus and dilatancy softening in granular packings above jamming". In: *Physical review letters* 113.19, p. 198001.

Coussot, Philippe, Quoc Dzuy Nguyen, HT Huynh, and Daniel Bonn (2002a). "Avalanche behavior in yield stress fluids". In: *Physical Review Letters* 88.17, p. 175501.

Coussot, Philippe and Guillaume Ovarlez (2010). "Physical origin of shear-banding in jammed systems". In: *European Physical Journal E* 33.3, pp. 183–188.

Coussot, Philippe, JS Raynaud, F Bertrand, P Moucheront, JP Guilbaud, HT Huynh, S Jarny, and D Lesueur (2002b). "Coexistence of liquid and solid phases in flowing soft-glassy materials". In: *Physical review letters* 88.21, p. 218301.

Cubuk, Ekin D, Samuel Stern Schoenholz, Jennifer M Rieser, Brad Dean Malone, Joerg Rottler, Douglas J Durian, Efthimios Kaxiras, and Andrea J Liu (2015). "Identifying structural flow defects in disordered solids using machine-learning methods". In: *Physical review letters* 114.10, p. 108001.

Curran, Scott, Charlotte Strandkvist, Jasper Bathmann, Marc de Gennes, Alexandre Kabla, Guillaume Salbreux, and Buzz Baum (2017). "Myosin II controls junction fluctuations to guide epithelial tissue ordering". In: *Developmental cell* 43.4, pp. 480–492.

Czajkowski, Michael, Daniel M. Sussman, M. Cristina Marchetti, and M. Lisa Manning (2019). "Glassy dynamics in models of confluent tissue with mitosis and apoptosis". In: *Soft Matter* 15 (44), pp. 9133–9149.

Dafermos, Constantine M and Ling Hsiao (1983). "Adiabatic shearing of incompressible fluids with temperature-dependent viscosity". In: *Quarterly of applied mathematics* 41.1, pp. 45–58.

Dahmen, Karin A, Yehuda Ben-Zion, and Jonathan T Uhl (2009). "Micromechanical model for deformation in solids with universal predictions for stress-strain curves and slip avalanches". In: *Physical Review Letters* 102.17, p. 175501.

D'anna, G, P Mayor, A Barrat, V Loreto, and Franco Nori (2003). "Observing brownian motion in vibration-fluidized granular matter". In: *Nature* 424.6951, p. 909.

Das, Amit, Srikanth Sastry, and Dapeng Bi (2020). "Controlled neighbor exchanges drive glassy behavior, intermittency and cell streaming in epithelial tissues". In: *bioRxiv*.

Dasgupta, Agnik, Matthias Merkel, Madeline J Clark, Andrew E Jacob, Jonathan Edward Dawson, M Lisa Manning, and Jeffrey D Amack (2018). "Cell volume changes contribute to epithelial morphogenesis in zebrafish Kupffer's vesicle". In: *Elife* 7, e30963.

Deforet, M, V Hakim, HG Yevick, G Duclos, and P Silberzan (2014). "Emergence of collective modes and tri-dimensional structures from epithelial confinement". In: *Nature communications* 5, p. 3747.

DeGiuli, E and M Wyart (2017). "Friction law and hysteresis in granular materials". In: *Proceedings of the National Academy of Sciences* 114.35, pp. 9284–9289.

Delarue, Morgan, Jörn Hartung, Carl Schreck, Pawel Gniewek, Lucy Hu, Stephan Herminghaus, and Oskar Hallatschek (2016). "Self-driven jamming in growing microbial populations". In: *Nature physics* 12.8, pp. 762–766.

Deseigne, Julien, Olivier Dauchot, and Hugues Chaté (2010). "Collective motion of vibrated polar disks". In: *Physical review letters* 105.9, p. 098001.

Desmond, Kenneth W and Eric R Weeks (2015). "Measurement of stress redistribution in flowing emulsions". In: *Physical review letters* 115.9, p. 098302.

Dhont, Jan KG (1999). "A constitutive relation describing the shear-banding transition". In: *Physical Review E* 60.4, p. 4534.

Dhont, Jan KG and Wim J Briels (2008). "Gradient and vorticity banding". In: *Rheologica acta* 47.3, pp. 257–281.

Dijksman, Joshua A, Geert H Wortel, Louwrens TH van Dellen, Olivier Dauchot, and Martin van Hecke (2011). "Jamming, yielding, and rheology of weakly vibrated granular media". In: *Physical review letters* 107.10, p. 108303.

Dimitriou, Christopher J and Gareth H McKinley (2014). "A comprehensive constitutive law for waxy crude oil: a thixotropic yield stress fluid". In: *Soft Matter* 10.35, pp. 6619–6644.

Divoux, Thibaut, Marc A Fardin, Sebastien Manneville, and Sandra Lerouge (2016). "Shear banding of complex fluids". In: *Annual Review of Fluid Mechanics* 48, pp. 81–103.

Divoux, Thibaut, Hervé Gayvallet, and Jean-Christophe Géminard (2008). "Creep motion of a granular pile induced by thermal cycling". In: *Physical review letters* 101.14, p. 148303.

Divoux, Thibaut, David Tamarii, Catherine Barentin, and Sébastien Manneville (2010). "Transient shear banding in a simple yield stress fluid". In: *Physical review letters* 104.20, p. 208301.

Doxzen, Kevin, Sri Ram Krishna Vedula, Man Chun Leong, Hiroaki Hirata, Nir S Gov, Alexandre J Kabla, Benoit Ladoux, and Chwee Teck Lim. In: ().

Drasdo, Dirk, Stefan Hoehme, and Michael Block (2007). "On the role of physics in the growth and pattern formation of multi-cellular systems: What can we learn from individual-cell based models?" In: *Journal of Statistical Physics* 128.1-2, p. 287.

Duclos, G, C Blanch-Mercader, V Yashunsky, G Salbreux, J-F Joanny, J Prost, and Pascal Silberzan (2018a). "Spontaneous shear flow in confined cellular nematics". In: *Nature physics* 14.7, pp. 728–732.

Duclos, Guillaume, Maxime Deforet, Hannah G Yevick, Olivier Cochet-Escartin, Flora Ascione, Sarah Moitrier, Trinish Sarkar, Victor Yashunsky, Isabelle Bonnet, Axel Buguin, et al. (2018b). "Controlling Confinement and Topology to Study Collective Cell Behaviors". In: *Cell Migration*. Springer, pp. 387–399.

Eiser, E, F Molino, G Porte, and O Diat (2000). "Nonhomogeneous textures and banded flow in a soft cubic phase under shear". In: *Physical Review E* 61.6, p. 6759.

Ellenbroek, Wouter G, Martin van Hecke, and Wim van Saarloos (2009). "Jammed frictionless disks: Connecting local and global response". In: *Physical Review E* 80.6, p. 061307.

Eshelby, JD (1954). "Distortion of a crystal by point imperfections". In: *Journal of Applied Physics* 25.2, pp. 255–261.

Eshelby, John D (1957). "The determination of the elastic field of an ellipsoidal inclusion, and related problems". In: *Proceedings of the Royal Society of London A*. Vol. 241. 1226. The Royal Society, pp. 376–396.

Etournay, Raphaël, Marko Popović, Matthias Merkel, Amitabha Nandi, Corinna Blasse, Benoît Aigouy, Holger Brandl, Gene Myers, Guillaume Salbreux, Frank Jülicher, et al. (2015). "Interplay of cell dynamics and epithelial tension during morphogenesis of the Drosophila pupal wing". In: *Elife* 4, e07090.

Falk, Michael L and James S Langer (1998). "Dynamics of viscoplastic deformation in amorphous solids". In: *Physical Review E* 57.6, p. 7192.

Fardin, Marc-Antoine, TJ Ober, Cyprien Gay, Guillaume Grégoire, GH McKinley, and S Lerouge (2012). "Potential ways of thinking about the shear-banding phenomenon". In: *Soft Matter* 8.4, pp. 910–922.

Farhadifar, Reza, Jens-Christian Röper, Benoit Aigouy, Suzanne Eaton, and Frank Jülicher (2007). "The influence of cell mechanics, cell-cell interactions, and proliferation on epithelial packing". In: *Current Biology* 17.24, pp. 2095–2104.

Ferrero, Ezequiel E and Eduardo A Jagla (2019). "Criticality in elastoplastic models of amorphous solids with stress-dependent yielding rates". In: *Soft matter* 15.44, pp. 9041–9055.

Fielding, SM, ME Cates, and P Sollich (2009). "Shear banding, aging and noise dynamics in soft glassy materials". In: *Soft Matter* 5.12, pp. 2378–2382.

Fielding, Suzanne M (2014). "Shear banding in soft glassy materials". In: *Reports on Progress in Physics* 77.10, p. 102601.

— (2020). "Elastoviscoplastic rheology and aging in a simplified soft glassy constitutive model". In: *Journal of Rheology* 64.3, pp. 723–738.

Fielding, Suzanne M and Peter D Olmsted (2003). "Flow phase diagrams for concentration-coupled shear banding". In: *The European Physical Journal E* 11.1, pp. 65–83.

Fielding, Suzanne M, Peter Sollich, and Michael E Cates (2000). "Aging and rheology in soft materials". In: *Journal of Rheology* 44.2, pp. 323–369.

Fily, Yaouen, Silke Henkes, and M Cristina Marchetti (2014). "Freezing and phase separation of self-propelled disks". In: *Soft matter* 10.13, pp. 2132–2140.

Fiocco, Davide, Giuseppe Foffi, and Srikanth Sastry (2014). "Encoding of memory in sheared amorphous solids". In: *Physical review letters* 112.2, p. 025702.

Fletcher, Alexander G, Miriam Osterfield, Ruth E Baker, and Stanislav Y Shvartsman (2014). "Vertex models of epithelial morphogenesis". In: *Biophysical journal* 106.11, pp. 2291–2304.

Fletcher, Daniel A and R Dyche Mullins (2010). "Cell mechanics and the cytoskeleton". In: *Nature* 463.7280, pp. 485–492.

Fuchs, Matthias and Michael E Cates (2002). "Theory of nonlinear rheology and yielding of dense colloidal suspensions". In: *Physical review letters* 89.24, p. 248304.

Garcia, Simon, Edouard Hannezo, Jens Elgeti, Jean-François Joanny, Pascal Silberzan, and Nir S Gov (2015). "Physics of active jamming during collective cellular motion in a monolayer". In: *Proceedings of the National Academy of Sciences* 112.50, pp. 15314–15319.

Gaudel, Naïma, Sébastien Kiesgen de Richter, Nicolas Louvet, Mathieu Jenny, and Salaheddine Skali-Lami (2017). "Bulk and local rheology in a dense and vibrated granular suspension". In: *Physical Review E* 96.6, p. 062905.

Géminard, Jean-Christophe and Eric Bertin (2010). "Aging of the frictional properties induced by temperature variations". In: *Physical Review E* 82.5, p. 056108.

Giavazzi, Fabio, Matteo Paoluzzi, Marta Macchi, Dapeng Bi, Giorgio Scita, M Lisa Manning, Roberto Cerbino, and M Cristina Marchetti (2018). "Flocking transitions in confluent tissues". In: *Soft matter* 14.18, pp. 3471–3477.

Gibaud, Thomas, Noémie Dagès, Pierre Lidon, Guillaume Jung, L Christian Ahouré, Michael Sztucki, Arnaud Poulesquen, Nicolas Hengl, Frédéric Pignon, and Sébastien

Manneville (2020). "Rheoacoustic Gels: Tuning Mechanical and Flow Properties of Colloidal Gels with Ultrasonic Vibrations". In: *Physical Review X* 10.1, p. 011028.

Gnoli, Andrea, Antonio Lasanta, Alessandro Sarracino, and Andrea Puglisi (2016). "Unified rheology of vibro-fluidized dry granular media: From slow dense flows to fast gas-like regimes". In: *Scientific reports* 6, p. 38604.

Goldstein, Martin (1969). "Viscous liquids and the glass transition: a potential energy barrier picture". In: *The Journal of Chemical Physics* 51.9, pp. 3728–3739.

Goyon, J, A Colin, G Ovarlez, A Ajdari, and L Bocquet (2008). "Spatial cooperativity in soft glassy flows". In: *Nature* 454.7200, p. 84.

Graner, François and James A Glazier (1992). "Simulation of biological cell sorting using a two-dimensional extended Potts model". In: *Physical review letters* 69.13, p. 2013.

Griffa, M, B Ferdowsi, RA Guyer, EG Daub, PA Johnson, C Marone, and J Carmeliet (2013). "Influence of vibration amplitude on dynamic triggering of slip in sheared granular layers". In: *Physical Review E* 87.1, p. 012205.

Gross, Markus and Fathollah Varnik (2018). "Shear-density coupling for a compressible single-component yield-stress fluid". In: *Soft matter* 14.22, pp. 4577–4590.

Guevorkian, Karine, Marie-Josée Colbert, Mélanie Durth, Sylvie Dufour, and Françoise Brochard-Wyart (2010). "Aspiration of biological viscoelastic drops". In: *Physical review letters* 104.21, p. 218101.

Guillot, Charlène and Thomas Lecuit (2013). "Mechanics of epithelial tissue homeostasis and morphogenesis". In: *Science* 340.6137, pp. 1185–1189.

Hakim, Vincent and Pascal Silberzan (2017). "Collective cell migration: a physics perspective". In: *Reports on Progress in Physics* 80.7, p. 076601.

Hancock, GJ (1953). "The self-propulsion of microscopic organisms through liquids". In: *Proceedings of the Royal Society of London. Series A. Mathematical and Physical Sciences* 217.1128, pp. 96–121.

Hanotin, Caroline (2014). "Rhéophysique des suspensions granulaires vibrées". In: *Université de Lorraine*.

Hanotin, Caroline, S Kiesgen De Richter, Philippe Marchal, Laurent J Michot, and Christophe Baravian (2012). "Vibration-induced liquefaction of granular suspensions". In: *Physical Review Letters* 108.19, p. 198301.

Harris, Andrew R, Loic Peter, Julien Bellis, Buzz Baum, Alexandre J Kabla, and Guillaume T Charras (2012). "Characterizing the mechanics of cultured cell monolayers". In: *Proceedings of the National Academy of Sciences* 109.41, pp. 16449–16454.

Hébraud, P, F Lequeux, JP Munch, and DJ Pine (1997). "Yielding and rearrangements in disordered emulsions". In: *Physical Review Letters* 78.24, p. 4657.

Hébraud, Pascal and François Lequeux (1998). "Mode-coupling theory for the pasty rheology of soft glassy materials". In: *Physical Review Letters* 81.14, p. 2934.

Henkes, Silke, Yaouen Fily, and M Cristina Marchetti (2011). "Active jamming: Self-propelled soft particles at high density". In: *Physical Review E* 84.4, p. 040301.

Henkes, Silke, Kaja Kostanjevec, J Martin Collinson, Rastko Sknepnek, and Eric Bertin (2020). "Dense active matter model of motion patterns in confluent cell monolayers". In: *Nature communications* 11.1, pp. 1–9.

Herschel, Winslow H and Ronald Bulkley (1926). "Konsistenzmessungen von gummibenzollösungen". In: *Colloid & Polymer Science* 39.4, pp. 291–300.

Hinkle, Adam R, Chris H Rycroft, Michael D Shields, and Michael L Falk (2017). "Coarse graining atomistic simulations of plastically deforming amorphous solids". In: *Physical Review E* 95.5, p. 053001.

Hohenberg, P. C. and B. I. Halperin (1977). "Theory of dynamic critical phenomena". In: *Reviews of Modern Physics* 49, p. 435.

Horbach, Jürgen and Walter Kob (2001). "Relaxation dynamics of a viscous silica melt: The intermediate scattering functions". In: *Physical Review E* 64.4, p. 041503.

Hough, Paul VC (1962). *Method and means for recognizing complex patterns*. US Patent 3,069,654.

Hunter, Gary L and Eric R Weeks (2012). "The physics of the colloidal glass transition". In: *Reports on progress in physics* 75.6, p. 066501.

Idema, Timon, Julien O Dubuis, Louis Kang, M Lisa Manning, Philip C Nelson, Tom C Lubensky, and Andrea J Liu (2013). "The syncytial Drosophila embryo as a mechanically excitable medium". In: *PloS one* 8.10, e77216.

Ikeda, Atsushi, Ludovic Berthier, and Peter Sollich (2012). "Unified study of glass and jamming rheology in soft particle systems". In: *Physical Review Letters* 109, p. 018301.

Ishihara, Shuji, Philippe Marcq, and Kaoru Sugimura (2017). "From cells to tissue: A continuum model of epithelial mechanics". In: *Physical Review E* 96.2, p. 022418.

Jacquin, Hugo, Ludovic Berthier, and Francesco Zamponi (2011). "Microscopic mean-field theory of the jamming transition". In: *Physical review letters* 106.13, p. 135702.

Jagla, EA (2007). "Strain localization driven by structural relaxation in sheared amorphous solids". In: *Physical Review E* 76.4, p. 046119.

Jaiswal, Prabhat K, Itamar Procaccia, Corrado Rainone, and Murari Singh (2016). "Mechanical yield in amorphous solids: A first-order phase transition". In: *Physical Review Letters* 116.8, p. 085501.

Janssen, Liesbeth MC (2019). "Active glasses". In: *Journal of Physics: Condensed Matter* 31.50, p. 503002.

Jia, X, Th Brunet, and J Laurent (2011). "Elastic weakening of a dense granular pack by acoustic fluidization: Slipping, compaction, and aging". In: *Physical Review E* 84.2, p. 020301.

Jiang, Yi, Pieter J Swart, Avadh Saxena, Marius Asipauskas, and James A Glazier (1999). "Hysteresis and avalanches in two-dimensional foam rheology simulations". In: *Physical Review E* 59.5, p. 5819.

Jin, Howon, Kyongok Kang, Kyung Hyun Ahn, and Jan KG Dhont (2014). "Flow instability due to coupling of shear-gradients with concentration: non-uniform flow of (hard-sphere) glasses". In: *Soft matter* 10.47, pp. 9470–9485.

Jin, Yuliang, Pierfrancesco Urbani, Francesco Zamponi, and Hajime Yoshino (2018). "A stability-reversibility map unifies elasticity, plasticity, yielding, and jamming in hard sphere glasses". In: *Science advances* 4.12, eaat6387.

Kaliman, Sara, Christina Jayachandran, Florian Rehfeldt, and Ana-Sunčana Smith (2016). "Limits of applicability of the Voronoi tessellation determined by centers of cell nuclei to epithelium morphology". In: *Frontiers in physiology* 7, p. 551.

Karimi, Kamran and Jean-Louis Barrat (2016). "Role of inertia in the rheology of amorphous systems: A finite-element-based elastoplastic model". In: *Physical Review E* 93.2, p. 022904.

Karimi, Kamran, Ezequiel E Ferrero, and Jean-Louis Barrat (2017). "Inertia and universality of avalanche statistics: the case of slowly deformed amorphous solids". In: *Physical Review E* 95.1, p. 013003.

Katsaounis, Theodoros, Julien Olivier, and Athanasios E Tzavaras (2017). "Emergence of coherent localized structures in shear deformations of temperature dependent fluids". In: *Archive for Rational Mechanics and Analysis* 224.1, pp. 173–208.

Kawasaki, Kyozi, Tatsuzo Nagai, and Katsuya Nakashima (1989). "Vertex models for two-dimensional grain growth". In: *Philosophical Magazine B* 60.3, pp. 399–421.

Kawasaki, Takeshi and Ludovic Berthier (2016). "Macroscopic yielding in jammed solids is accompanied by a nonequilibrium first-order transition in particle trajectories". In: *Physical Review E* 94.2, p. 022615.

Kermouche, G, G Guillonneau, J Michler, J Teisseire, and E Barthel (2016). "Perfectly plastic flow in silica glass". In: *Acta Materialia* 114, pp. 146–153.

Khalilgharibi, Nargess, Jonathan Fouchard, Pierre Recho, Guillaume Charras, and Alexandre Kabla (2016). "The dynamic mechanical properties of cellularised aggregates". In: *Current Opinion in Cell Biology* 42, pp. 113–120.

Kim, Sangwoo, Marie Pochitaloff, Georgina Stooke-Vaughan, and Otger Campas (2020). "Embryonic Tissues as Active Foams". In: *bioRxiv*.

Klongvessa, Natsuda, Félix Ginot, Christophe Ybert, Cécile Cottin-Bizonne, and Mathieu Leocmach (2019a). "Active glass: ergodicity breaking dramatically affects response to self-propulsion". In: *Physical Review Letters* 123.24, p. 248004.

— (2019b). "Nonmonotonic behavior in dense assemblies of active colloids". In: *Physical Review E* 100.6, p. 062603.

Koch, Jeremy A, Daniel I Castaneda, Randy H Ewoldt, and David A Lange (2019). "Vibration of fresh concrete understood through the paradigm of granular physics". In: *Cement and Concrete Research* 115, pp. 31–42.

Kollmannsberger, Philip and Ben Fabry (2011). "Linear and nonlinear rheology of living cells". In: *Annual review of materials research* 41, pp. 75–97.

Krajnc, Matej (2020). "Solid–fluid transition and cell sorting in epithelia with junctional tension fluctuations". In: *Soft Matter* 16.13, pp. 3209–3215.

Krajnc, Matej, Sabyasachi Dasgupta, Primož Ziherl, and Jacques Prost (2018). "Fluidization of epithelial sheets by active cell rearrangements". In: *Physical Review E* 98.2, p. 022409.

Kruse, Karsten, Jean-Francois Joanny, Frank Jülicher, Jacques Prost, and Ken Sekimoto (2005). "Generic theory of active polar gels: a paradigm for cytoskeletal dynamics". In: *The European Physical Journal E* 16.1, pp. 5–16.

Ladoux, Benoit and René-Marc Mège (2017). "Mechanobiology of collective cell behaviours". In: *Nature Reviews Molecular Cell Biology* 18.12, p. 743.

Langer, JS (2004). "Dynamics of shear-transformation zones in amorphous plasticity: Formulation in terms of an effective disorder temperature". In: *Physical Review E* 70.4, p. 041502.

Lauridsen, John, Michael Twardos, and Michael Dennin (2002). "Shear-induced stress relaxation in a two-dimensional wet foam". In: *Physical review letters* 89.9, p. 098303.

Le Bellac, M. (1992). *Quantum and statistical field theory*. Clarendon Press.

Le Bouil, Antoine, Axelle Amon, Sean McNamara, and Jérôme Crassous (2014). "Emergence of cooperativity in plasticity of soft glassy materials". In: *Physical review letters* 112.24, p. 246001.

Leach, Andrew R and Andrew R Leach (2001). *Molecular modelling: principles and applications*. Pearson education.

Lechner, Wolfgang and Christoph Dellago (2009). "Point defects in two-dimensional colloidal crystals: simulation vs. elasticity theory". In: *Soft Matter* 5.3, pp. 646–659.

Lecuit, Thomas and Pierre-Francois Lenne (2007). "Cell surface mechanics and the control of cell shape, tissue patterns and morphogenesis". In: *Nature reviews Molecular cell biology* 8.8, pp. 633–644.

Leishangthem, Premkumar, Anshul DS Parmar, and Srikanth Sastry (2017). "The yielding transition in amorphous solids under oscillatory shear deformation". In: *Nature Communications* 8, p. 14653.

Lemaître, Anaël and Christiane Caroli (2009). "Rate-dependent avalanche size in athermally sheared amorphous solids". In: *Physical Review Letters* 103.6, p. 065501.

Lerouge, Sandra and Jean-François Berret (2009). "Shear-induced transitions and instabilities in surfactant wormlike micelles". In: *Polymer Characterization*. Springer, pp. 1–71.

Liao, Qinyi and Ning Xu (2018). "Criticality of the zero-temperature jamming transition probed by self-propelled particles". In: *Soft Matter* 14.5, pp. 853–860.

Lin, Jie, Edan Lerner, Alberto Rosso, and Matthieu Wyart (2014). "Scaling description of the yielding transition in soft amorphous solids at zero temperature". In: *Proceedings of the National Academy of Sciences* 111.40, pp. 14382–14387.

Liu, Andrea J and Sidney R Nagel (1998). "Nonlinear dynamics: Jamming is not just cool any more". In: *Nature* 396.6706, p. 21.

— (2010). "The jamming transition and the marginally jammed solid". In: *Annu. Rev. Condens. Matter Phys.* 1.1, pp. 347–369.

Liu, Chen (2016). "Critical dynamics at the yielding transition and creep behavior of amorphous systems: mesoscopic modeling". PhD thesis. Université Grenoble Alpes.

Liu, Chen, Suman Dutta, Pinaki Chaudhuri, and Kirsten Martens (2020a). "An elastoplastic approach based on microscopic insights for the steady state and transient dynamics of sheared disordered solids". In: *arXiv preprint arXiv:2007.07162*.

Liu, Chen, Ferrero, Jagla, Martens, Rosso, and Talon (2020b). "Oscillatory quasistatic shear deformation of amorphous materials: a mesoscopic approach". In: *arXiv preprint arXiv:2012.15310v*.

Liu, Chen, Ezequiel E Ferrero, Kirsten Martens, and Jean-Louis Barrat (2018). "Creep dynamics of athermal amorphous materials: a mesoscopic approach". In: *Soft Matter* 14.41, pp. 8306–8316.

Liu, Chen, Ezequiel E Ferrero, Francesco Puosi, Jean-Louis Barrat, and Kirsten Martens (2016). "Driving rate dependence of avalanche statistics and shapes at the yielding transition". In: *Physical Review Letters* 116.6, p. 065501.

Lootens, Didier, Henri Van Damme, and Pascal Hébraud (2003). "Giant stress fluctuations at the jamming transition". In: *Physical Review Letters* 90.17, p. 178301.

Losert, W, L Bocquet, TC Lubensky, and Jerry P Gollub (2000). "Particle dynamics in sheared granular matter". In: *Physical review letters* 85.7, p. 1428.

Malinverno, Chiara, Salvatore Corallino, Fabio Giavazzi, Martin Bergert, Qingsen Li, Marco Leoni, Andrea Disanza, Emanuela Frittoli, Amanda Oldani, Emanuele Martini, et al. (2017). "Endocytic reawakening of motility in jammed epithelia". In: *Nature materials* 16.5, p. 587.

Malmi-Kakkada, Abdul N, Xin Li, Himadri S Samanta, Sumit Sinha, and Dave Thirumalai (2018). "Cell growth rate dictates the onset of glass to fluidlike transition and long time superdiffusion in an evolving cell colony". In: *Physical Review X* 8.2, p. 021025.

Maloney, Craig and Anael Lemaitre (2004). "Subextensive scaling in the athermal, quasistatic limit of amorphous matter in plastic shear flow". In: *Physical review letters* 93.1, p. 016001.

Maloney, Craig E and Anaël Lemaître (2006). "Amorphous systems in athermal, quasistatic shear". In: *Physical Review E* 74.1, p. 016118.

Mandal, Rituparno, Pranab Jyoti Bhuyan, Pinaki Chaudhuri, Chandan Dasgupta, and Madan Rao (2020a). "Extreme active matter at high densities". In: *Nature Communications* 11.1, pp. 1–8.

Mandal, Rituparno, Pranab Jyoti Bhuyan, Madan Rao, and Chandan Dasgupta (2016). "Active fluidization in dense glassy systems". In: *Soft Matter* 12.29, pp. 6268–6276.

Mandal, Rituparno and Peter Sollich (2020b). "How to Study a Persistent Active Glassy System?" In: *arXiv preprint arXiv:2012.01195*.

Manning, ML, JS Langer, and JM Carlson (2007). "Strain localization in a shear transformation zone model for amorphous solids". In: *Physical Review E* 76.5, p. 056106.

Mansard, Vincent, Annie Colin, Pinaki Chaudhuri, and Lydéric Bocquet (2013). "A molecular dynamics study of non-local effects in the flow of soft jammed particles". In: *Soft matter* 9.31, pp. 7489–7500.

Mansard, Vincent, Annie Colin, Pinaki Chauduri, and Lyderic Bocquet (2011). "A kinetic elasto-plastic model exhibiting viscosity bifurcation in soft glassy materials". In: *Soft Matter* 7.12, pp. 5524–5527.

Marée, Athanasius FM, Verônica A Grieneisen, and Paulien Hogeweg (2007). "The Cellular Potts Model and biophysical properties of cells, tissues and morphogenesis". In: *Single-cell-based models in biology and medicine*. Springer, pp. 107–136.

Marmottant, Philippe and François Graner (2007). "An elastic, plastic, viscous model for slow shear of a liquid foam". In: *European Physical Journal E* 23.4, pp. 337–347.

Marmottant, Philippe, Abbas Mgharbel, Jos Käfer, Benjamin Audren, Jean-Paul Rieu, Jean-Claude Vial, Boudewijn Van Der Sanden, Athanasius FM Marée, François Graner, and Hélène Delanoë-Ayari (2009). "The role of fluctuations and stress on the effective viscosity of cell aggregates". In: *Proceedings of the National Academy of Sciences* 106.41, pp. 17271–17275.

Martens, Kirsten, Lydéric Bocquet, and Jean-Louis Barrat (2011). "Connecting diffusion and dynamical heterogeneities in actively deformed amorphous systems". In: *Physical Review Letters* 106.15, p. 156001.

— (2012). "Spontaneous formation of permanent shear bands in a mesoscopic model of flowing disordered matter". In: *Soft Matter* 8.15, pp. 4197–4205.

Martz, Eric and Malcolm S Steinberg (1972). "The role of cell-cell contact in "contact" inhibition of cell division: A review and new evidence". In: *Journal of cellular physiology* 79.2, pp. 189–210.

Matoz-Fernandez, DA, Elisabeth Agoritsas, Jean-Louis Barrat, Eric Bertin, and Kirsten Martens (2017a). "Nonlinear rheology in a model biological tissue". In: *Physical review letters* 118.15, p. 158105.

Matoz-Fernandez, DA, Kirsten Martens, Rastko Sknepnek, JL Barrat, and Silke Henkes (2017b). "Cell division and death inhibit glassy behaviour of confluent tissues". In: *Soft matter* 13.17, pp. 3205–3212.

Mattiello, Maddalena (2018). "Structure et dynamique de suspensions concentrées des colloïdes déformables molles avec liaisons associatives accordables". PhD thesis.

Mattsson, Johan, Hans M Wyss, Alberto Fernandez-Nieves, Kunimasa Miyazaki, Zhibing Hu, David R Reichman, and David A Weitz (2009). "Soft colloids make strong glasses". In: *Nature* 462.7269, pp. 83–86.

Mayor, Roberto and Carlos Carmona-Fontaine (2010). "Keeping in touch with contact inhibition of locomotion". In: *Trends in cell biology* 20.6, pp. 319–328.

McNamara, Sean, Jérôme Crassous, and Axelle Amon (2016). "Eshelby inclusions in granular matter: theory and simulations". In: *Physical Review E* 94.2, p. 022907.

Melhus, Martin F and Igor S Aranson (2012). "Effect of vibration on solid-to-liquid transition in small granular systems under shear". In: *Granular matter* 14.2, pp. 151–156.

Mizuno, Hideyuki, Stefano Mossa, and Jean-Louis Barrat (2013). "Measuring spatial distribution of the local elastic modulus in glasses". In: *Physical Review E* 87.4, p. 042306.

Moeendarbary, Emad, Léo Valon, Marco Fritzsche, Andrew R Harris, Dale A Moulding, Adrian J Thrasher, Eleanor Stride, L Mahadevan, and Guillaume T Charras (2013). "The cytoplasm of living cells behaves as a poroelastic material". In: *Nature materials* 12.3, pp. 253–261.

Møller, PCF, Stéphane Rodts, MAJ Michels, and Daniel Bonn (2008). "Shear banding and yield stress in soft glassy materials". In: *Physical Review E* 77.4, p. 041507.

Mongera, Alessandro, Payam Rowghanian, Hannah J Gustafson, Elijah Shelton, David A Kealhofer, Emmet K Carn, Friedhelm Serwane, Adam A Lucio, James Giammona, and Otger Campàs (2018). "A fluid-to-solid jamming transition underlies vertebrate body axis elongation". In: *Nature* 561.7723, p. 401.

Moorcroft, Robyn L, Michael E Cates, and Suzanne M Fielding (2011). "Age-dependent transient shear banding in soft glasses". In: *Physical review letters* 106.5, p. 055502.

Morse, Peter K, Sudeshna Roy, Elisabeth Agoritsas, Ethan Stanifer, Eric I Corwin, and M Lisa Manning (2020). "A direct link between active matter and sheared granular systems". In: *arXiv preprint arXiv:2009.07706*.

Moure, Adrian and Hector Gomez (2019). "Phase-Field Modeling of Individual and Collective Cell Migration". In: *Archives of Computational Methods in Engineering*, pp. 1–34.

Müller-Plathe, Florian (1997). "A simple nonequilibrium molecular dynamics method for calculating the thermal conductivity". In: *The Journal of chemical physics* 106.14, pp. 6082–6085.

Nandi, Saroj Kumar and Nir S Gov (2017). "Nonequilibrium mode-coupling theory for dense active systems of self-propelled particles". In: *Soft Matter* 13.41, pp. 7609–7616.

Newman, Timothy J (2005). "Modeling multi-cellular systems using sub-cellular elements". In: *arXiv preprint q-bio/0504028*.

Ni, Ran, Martien A Cohen Stuart, and Marjolein Dijkstra (2013). "Pushing the glass transition towards random close packing using self-propelled hard spheres". In: *Nature communications* 4.1, pp. 1–7.

Nichol, Kiri, Alexey Zanin, Renaud Bastien, Elie Wandersman, and Martin van Hecke (2010). "Flow-induced agitations create a granular fluid". In: *Physical Review Letters* 104.7, p. 078302.

Nicolas, Alexandre and Jean-Louis Barrat (2013a). "A mesoscopic model for the rheology of soft amorphous solids, with application to microchannel flows". In: *Faraday discussions* 167, pp. 567–600.

— (2013b). "Spatial cooperativity in microchannel flows of soft jammed materials: A mesoscopic approach". In: *Physical review letters* 110.13, p. 138304.

Nicolas, Alexandre, Jean-Louis Barrat, and Jörg Rottler (2016). "Effects of inertia on the steady-shear rheology of disordered solids". In: *Physical Review Letters* 116.5, p. 058303.

Nicolas, Alexandre, Ezequiel E Ferrero, Kirsten Martens, and Jean-Louis Barrat (2018a). "Deformation and flow of amorphous solids: Insights from elastoplastic models". In: *Reviews of Modern Physics* 90.4, p. 045006.

Nicolas, Alexandre, Kirsten Martens, and Jean-Louis Barrat (2014a). "Rheology of athermal amorphous solids: Revisiting simplified scenarios and the concept of mechanical noise temperature". In: *EPL (Europhysics Letters)* 107.4, p. 44003.

Nicolas, Alexandre, Kirsten Martens, Lydéric Bocquet, and Jean-Louis Barrat (2014b). "Universal and non-universal features in coarse-grained models of flow in disordered solids". In: *Soft Matter* 10.26, pp. 4648–4661.

Nicolas, Alexandre, Francesco Puosi, Hideyuki Mizuno, and Jean-Louis Barrat (2015). "Elastic consequences of a single plastic event: towards a realistic account of structural disorder and shear wave propagation in models of flowing amorphous solids". In: *Journal of the Mechanics and Physics of Solids* 78, pp. 333–351.

Nicolas, Alexandre and Jörg Rottler (2018b). "Orientation of plastic rearrangements in two-dimensional model glasses under shear". In: *Physical Review E* 97.6, p. 063002.

Ninarello, Andrea, Ludovic Berthier, and Daniele Coslovich (2017). "Models and algorithms for the next generation of glass transition studies". In: *Physical Review X* 7.2, p. 021039.

Nishizawa, Kenji, Kei Fujiwara, Masahiro Ikenaga, Nobushige Nakajo, Miho Yanagisawa, and Daisuke Mizuno (2017). "Universal glass-forming behavior of in vitro and living cytoplasm". In: *Scientific reports* 7.1, pp. 1–12.

Nnetu, Kenechukwu David, Melanie Knorr, Steve Pawlizak, Thomas Fuhs, and Josef A Käs (2013). "Slow and anomalous dynamics of an MCF-10A epithelial cell monolayer". In: *Soft Matter* 9.39, pp. 9335–9341.

Notbohm, Jacob, Shiladitya Banerjee, Kazage JC Utuje, Bomi Gweon, Hwanseok Jang, Yongdoo Park, Jennifer Shin, James P Butler, Jeffrey J Fredberg, and M Cristina Marchetti (2016). "Cellular contraction and polarization drive collective cellular motion". In: *Biophysical journal* 110.12, pp. 2729–2738.

Ogura, Yosuke, Fu-Lai Wen, Mustafa M Sami, Tatsuo Shibata, and Shigeo Hayashi (2018). "A switch-like activation relay of EGFR-ERK signaling regulates a wave of cellular contractility for epithelial invagination". In: *Developmental cell* 46.2, pp. 162–172.

Okuzono, Tohru and Kyozi Kawasaki (1995). "Intermittent flow behavior of random foams: a computer experiment on foam rheology". In: *Physical Review E* 51.2, p. 1246.

Olivier, Julien and Michael Renardy (2013). "On the generalization of the Hébraud–Lequeux model to multidimensional flows". In: *Archive for Rational Mechanics and Analysis* 208.2, pp. 569–601.

Olmsted, Peter D (2008). "Perspectives on shear banding in complex fluids". In: *Rheologica Acta* 47.3, pp. 283–300.

Oswald, Linda, Steffen Grosser, David M Smith, and Josef A Käs (2017). "Jamming transitions in cancer". In: *Journal of physics D: Applied physics* 50.48, p. 483001.

Ovarlez, Guillaume, Quentin Barral, and Philippe Coussot (2010). "Three-dimensional jamming and flows of soft glassy materials". In: *Nature materials* 9.2, pp. 115–119.

Ovarlez, Guillaume, Sylvie Cohen-Addad, Kapil Krishan, Julie Goyon, and Philippe Coussot (2013). "On the existence of a simple yield stress fluid behavior". In: *Journal of Non-Newtonian Fluid Mechanics* 193, pp. 68–79.

Oxtoby, David W and ADJ Haymet (1982). "A molecular theory of the solid–liquid interface. II. Study of bcc crystal–melt interfaces". In: *The Journal of Chemical Physics* 76.12, pp. 6262–6272.

Oyama, Norihiro, Takeshi Kawasaki, Hideyuki Mizuno, and Atsushi Ikeda (2019). "Glassy dynamics of a model of bacterial cytoplasm with metabolic activities". In: *Physical Review Research* 1.3, p. 032038.

Ozawa, Misaki, Ludovic Berthier, Giulio Biroli, Alberto Rosso, and Gilles Tarjus (2018). "Random critical point separates brittle and ductile yielding transitions in amorphous materials". In: *Proceedings of the National Academy of Sciences* 115.26, pp. 6656–6661.

Pajic-Lijakovic, Ivana Dusan and Milan Milivojevic (2020). "Mechanical oscillations in 2D collective cell migration: the elastic turbulence". In: *Frontiers in Physics* 8, p. 456.

Palmieri, Benoit, Yony Bresler, Denis Wirtz, and Martin Grant (2015). "Multiple scale model for cell migration in monolayers: Elastic mismatch between cells enhances motility". In: *Scientific reports* 5.1, pp. 1–13.

Park, Jin-Ah, Lior Atia, Jennifer A Mitchel, Jeffrey J Fredberg, and James P Butler (2016). "Collective migration and cell jamming in asthma, cancer and development". In: *Journal of cell science* 129.18, pp. 3375–3383.

Park, Jin-Ah, Jae Hun Kim, Dapeng Bi, Jennifer A Mitchel, Nader Taheri Qazvini, Kelan Tantisira, Chan Young Park, Maureen McGill, Sae-Hoon Kim, Bomi Gweon, et al. (2015). "Unjamming and cell shape in the asthmatic airway epithelium". In: *Nature materials* 14.10, p. 1040.

Parry, Bradley R, Ivan V Surovtsev, Matthew T Cabeen, Corey S O'Hern, Eric R Dufresne, and Christine Jacobs-Wagner (2014). "The bacterial cytoplasm has glass-like properties and is fluidized by metabolic activity". In: *Cell* 156.1-2, pp. 183–194.

Pastore, Raffaele, Massimo Pica Ciamarra, and Antonio Coniglio (2011). "'Flow and jam'of frictional athermal systems under shear stress". In: *Philosophical Magazine* 91.13-15, pp. 2006–2013.

Patinet, Sylvain, Armand Barbot, Matthias Lerbinger, Damien Vandembroucq, and Anaël Lemaître (2020). "Origin of the Bauschinger Effect in Amorphous Solids". In: *Physical Review Letters* 124.20, p. 205503.

Patinet, Sylvain, Damien Vandembroucq, and Michael L Falk (2016). "Connecting local yield stresses with plastic activity in amorphous solids". In: *Physical Review Letters* 117.4, p. 045501.

Petitjean, L., M. Reffay, E. Grasland-Mongrain, M. Poujade, B. Ladoux, A. Buguin, and P. Silberzan. "Velocity fields in a collectively migrating epithelium". In: *Biophysical Journal* 9 (), pp. 1790–1800. ISSN: 15420086.

Petridou, Nicoletta I and Carl-Philipp Heisenberg (2019). "Tissue rheology in embryonic organization". In: *The EMBO journal* 38.20.

Petrolli, Vanni (2019). "Transition entre des modes oscillatoires de migration cellulaire induite par le confinement". PhD thesis. Université Grenoble Alpes.

Petrolli, Vanni, Thomas Boudou, Martial Balland, and Giovanni Cappello (2020). "Oscillations in collective cell migration". In:

Petrolli, Vanni, Magali Le Goff, Monika Tadrous, Kirsten Martens, Cédric Allier, Ondrej Mandula, Lionel Hervé, Silke Henkes, Rastko Sknepnek, Thomas Boudou, et al. (2019). "Confinement-Induced Transition between Wavelike Collective Cell Migration Modes". In: *Physical review letters* 122.16, p. 168101.

Peyret, Gregoire, Romain Mueller, Joseph d'Alessandro, Simon Begnaud, Philippe Marcq, Rene-Marc Mege, Julia M Yeomans, Amin Doostmohammadi, and Benoit Ladoux (2019). "Sustained oscillations of epithelial cell sheets". In: *Biophysical journal*.

Phillips, HM and MS Steinberg (1978). "Embryonic tissues as elasticoviscous liquids. I. Rapid and slow shape changes in centrifuged cell aggregates". In: *Journal of cell science* 30.1, pp. 1–20.

Picard, Guillemette, Armand Ajdari, François Lequeux, and Lydéric Bocquet (2004). "Elastic consequences of a single plastic event: A step towards the microscopic modeling of the flow of yield stress fluids". In: *The European Physical Journal E* 15.4, pp. 371–381.

— (2005). "Slow flows of yield stress fluids: Complex spatiotemporal behavior within a simple elastoplastic model". In: *Physical Review E* 71.1, p. 010501.

Plimpton, Steve (1995). "Fast parallel algorithms for short-range molecular dynamics". In: *Journal of computational physics* 117.1, pp. 1–19.

Pons, Adeline, Axelle Amon, Thierry Darnige, Jérôme Crassous, and Eric Clément (2015). "Mechanical fluctuations suppress the threshold of soft-glassy solids: the secular drift scenario". In: *Physical Review E* 92.2, p. 020201.

Popović, Marko, Tom WJ de Geus, and Matthieu Wyart (2018). "Elastoplastic description of sudden failure in athermal amorphous materials during quasistatic loading". In: *Physical Review E* 98.4, p. 040901.

Popovic, Marko, Valentin Druelle, Natalie A Dye, Frank Jülicher, and Matthieu Wyart (2020). "Inferring the plasticity of epithelial tissues from their geometry". In: *arXiv preprint arXiv:2002.05133*.

Popović, Marko, Amitabha Nandi, Matthias Merkel, Raphaël Etournay, Suzanne Eaton, Frank Jülicher, and Guillaume Salbreux (2017). "Active dynamics of tissue shear flow". In: *New Journal of Physics* 19.3, p. 033006.

Preziosi, Luigi, Davide Ambrosi, and Claude Verdier (2010). "An elasto-visco-plastic model of cell aggregates". In: *Journal of theoretical biology* 262.1, pp. 35–47.

Priezjev, Nikolai V (2018). "Molecular dynamics simulations of the mechanical annealing process in metallic glasses: Effects of strain amplitude and temperature". In: *Journal of Non-Crystalline Solids* 479, pp. 42–48.

Princen, HM and AD Kiss (1986). "Rheology of foams and highly concentrated emulsions: III. Static shear modulus". In: *Journal of Colloid and Interface Science* 112.2, pp. 427–437.

Prost, Jacques, Frank Jülicher, and Jean-François Joanny (2015). "Active gel physics". In: *Nature physics* 11.2, pp. 111–117.

Puliafito, Alberto, Lars Hufnagel, Pierre Neveu, Sebastian Streichan, Alex Sigal, D Kuchnir Fygenson, and Boris I Shraiman (2012). "Collective and single cell behavior in epithelial contact inhibition". In: *Proceedings of the National Academy of Sciences* 109.3, pp. 739–744.

Puosi, Francesco, Julien Olivier, and Kirsten Martens (2015). "Probing relevant ingredients in mean-field approaches for the athermal rheology of yield stress materials". In: *Soft Matter* 11.38, pp. 7639–7647.

Puosi, Francesco, Joerg Rottler, and Jean-Louis Barrat (2014). "Time-dependent elastic response to a local shear transformation in amorphous solids". In: *Physical Review E* 89.4, p. 042302.

Radhakrishnan, Rangarajan and Suzanne M Fielding (2016). "Shear banding of soft glassy materials in large amplitude oscillatory shear". In: *Physical review letters* 117.18, p. 188001.

Ragouilliaux, Alexandre, Guillaume Ovarlez, Noushine Shahidzadeh-Bonn, Benjamin Herzhaft, Thierry Palermo, and Philippe Coussot (2007). "Transition from a simple yield-stress fluid to a thixotropic material". In: *Physical Review E* 76.5, p. 051408.

Raina, Arun and Christian Miehe (2016). "A phase-field model for fracture in biological tissues". In: *Biomechanics and modeling in mechanobiology* 15.3, pp. 479–496.

Ranft, Jonas, Markus Basan, Jens Elgeti, Jean-François Joanny, Jacques Prost, and Frank Jülicher (2010). "Fluidization of tissues by cell division and apoptosis". In: *Proceedings of the National Academy of Sciences*.

Ravazzano, Linda, Maria Chiara Lionetti, Maria Rita Fumagalli, Silvia Bonfanti, Roberto Guerra, Oleksandr Chepizhko, Caterina A. M. La Porta, and Stefano Zapperi (2020). "Unjamming of active rotators". In: *arXiv preprint arXiv:2003.06239*.

Recho, Pierre, Thibaut Putelat, and Lev Truskinovsky (2019). "Force-induced repolarization of an active crawler". In: *New Journal of Physics* 21.3, p. 033015.

Regev, Ido, John Weber, Charles Reichhardt, Karin A Dahmen, and Turab Lookman (2015). "Reversibility and criticality in amorphous solids". In: *Nature communications* 6.1, pp. 1–8.

Richard, David, Geert Kapteijns, Julia A Giannini, M Lisa Manning, and Edan Lerner (2020). "A simple and broadly-applicable definition of shear transformation zones". In: *arXiv preprint arXiv:2007.08181*.

Rodríguez-Franco, Pilar, Agustí Brugués, Ariadna Marín-Llauradó, Vito Conte, Guiomar Solanas, Eduard Batlle, Jeffrey J Fredberg, Pere Roca-Cusachs, Raimon Sunyer, and Xavier Trepat (2017). "Long-lived force patterns and deformation waves at repulsive epithelial boundaries". In: *Nature materials* 16.10, p. 1029.

Romanczuk, Pawel, Markus Bär, Werner Ebeling, Benjamin Lindner, and Lutz Schimansky-Geier (2012). "Active brownian particles". In: *The European Physical Journal Special Topics* 202.1, pp. 1–162.

Rottler, Jörg, Samuel S Schoenholz, and Andrea J Liu (2014). "Predicting plasticity with soft vibrational modes: From dislocations to glasses". In: *Physical Review E* 89.4, p. 042304.

Rowlinson, JS and B Widom (1982). "Molecular Theory of Capillarity, The International Series of Monographs on Chemistry". In: *Clarendon: Oxford, UK*.

Sadati, Monirosadat, Nader Taheri Qazvini, Ramaswamy Krishnan, Chan Young Park, and Jeffrey J Fredberg (2013). "Collective migration and cell jamming". In: *Differentiation* 86.3, pp. 121–125.

Salerno, K Michael, Craig E Maloney, and Mark O Robbins (2012). "Avalanches in strained amorphous solids: does inertia destroy critical behavior?" In: *Physical Review Letters* 109.10, p. 105703.

Saramito, Pierre (2007). "A new constitutive equation for elastoviscoplastic fluid flows". In: *Journal of Non-Newtonian Fluid Mechanics* 145.1, pp. 1–14.

Schall, Peter and Martin van Hecke (2010). "Shear bands in matter with granularity". In: *Annual Review of Fluid Mechanics* 42, pp. 67–88.

Schall, Peter, David A Weitz, and Frans Spaepen (2007). "Structural rearrangements that govern flow in colloidal glasses". In: *Science* 318.5858, pp. 1895–1899.

Schiller, Ulf D, Timm Krüger, and Oliver Henrich (2018). "Mesoscopic modelling and simulation of soft matter". In: *Soft matter* 14.1, pp. 9–26.

Schoetz, Eva-Maria, Marcos Lanio, Jared A Talbot, and M Lisa Manning (2013). "Glassy dynamics in three-dimensional embryonic tissues". In: *Journal of The Royal Society Interface* 10.89, p. 20130726.

Serra-Picamal, Xavier, Vito Conte, Romaric Vincent, Ester Anon, Dhananjay T Tambe, Elsa Bazellieres, James P Butler, Jeffrey J Fredberg, and Xavier Trepat (2012). "Mechanical waves during tissue expansion". In: *Nature Physics* 8.8, p. 628.

Shi, Yunfeng, Michael B Katz, Hui Li, and Michael L Falk (2007). "Evaluation of the disorder temperature and free-volume formalisms via simulations of shear banding in amorphous solids". In: *Physical review letters* 98.18, p. 185505.

Smeets, Bart, Jiri Pesek, Thomas Deckers, Gabriella Nilsson Hall, Maxim Cuvelier, Steven Ongenae, Veerle Bloemen, Frank P Luyten, Ioannis Papantoniou, and Herman Ramon (2019). "Compaction dynamics during progenitor cell self-assembly reveal granular mechanics". In: *BioRxiv*, p. 699447.

Sollich, Peter, François Lequeux, Pascal Hébraud, and Michael E Cates (1997). "Rheology of soft glassy materials". In: *Physical Review Letters* 78.10, p. 2020.

Spring, Kenneth R and Ann-Christin Ericson (1982). "Epithelial cell volume modulation and regulation". In: *The Journal of membrane biology* 69.3, pp. 167–176.

Srivastava, Ishan, Leonardo E Silbert, Gary S Grest, and Jeremy B Lechman (2019). "Flow-Arrest Transitions in Frictional Granular Matter". In: *Physical review letters* 122.4, p. 048003.

Stoker, MGP and H Rubin (1967). "Density dependent inhibition of cell growth in culture". In: *Nature* 215.5097, p. 171.

Streitberger, Kaspar-Josche, Ledia Lilaj, Felix Schrank, Jürgen Braun, Karl-Titus Hoffmann, Martin Reiss-Zimmermann, Josef A Käs, and Ingolf Sack (2020). "How tissue fluidity influences brain tumor progression". In: *Proceedings of the National Academy of Sciences* 117.1, pp. 128–134.

Subramaniyan, Arun K and CT Sun (2008). "Continuum interpretation of virial stress in molecular simulations". In: *International Journal of Solids and Structures* 45.14-15, pp. 4340–4346.

Sussman, Daniel M and Matthias Merkel (2018). "No unjamming transition in a Voronoi model of biological tissue". In: *Soft matter* 14.17, pp. 3397–3403.

Szabo, Balint, GJ Szöllösi, B Gönci, Zs Jurányi, David Selmeczi, and Tamás Vicsek (2006). "Phase transition in the collective migration of tissue cells: experiment and model". In: *Physical Review E* 74.6, p. 061908.

Szamel, Grzegorz (2014). "Self-propelled particle in an external potential: Existence of an effective temperature". In: *Physical Review E* 90.1, p. 012111.

Szamel, Grzegorz, Elijah Flenner, and Ludovic Berthier (2015). "Glassy dynamics of athermal self-propelled particles: Computer simulations and a nonequilibrium microscopic theory". In: *Physical Review E* 91.6, p. 062304.

Talamali, Mehdi, Viljo Petäjä, Damien Vandembroucq, and Stéphane Roux (2011). "Avalanches, precursors, and finite-size fluctuations in a mesoscopic model of amorphous plasticity". In: *Physical Review E* 84.1, p. 016115.

Tanguy, Anne, Fabien Leonforte, and J-L Barrat (2006). "Plastic response of a 2D Lennard-Jones amorphous solid: Detailed analysis of the local rearrangements at very slow strain rate". In: *The European Physical Journal E* 20.3, pp. 355–364.

Taylor, E Wilfred (1949). "Plastic deformation of optical glass". In: *Nature* 163.4139, pp. 323–323.

Telford, Mark (2004). "The case for bulk metallic glass". In: *Materials today* 7.3, pp. 36–43.

Tjhung, Elsen and Ludovic Berthier (2017). "Discontinuous fluidization transition in time-correlated assemblies of actively deforming particles". In: *Physical Review E* 96.5, p. 050601.

— (2020). "Analogies between growing dense active matter and soft driven glasses". In: *Physical Review Research* 2.4, p. 043334.

Tlili, S, M Durande, C Gay, B Ladoux, F Graner, and H Delanoë-Ayari (2020). "Migrating Epithelial Monolayer Flows Like a Maxwell Viscoelastic Liquid". In: *Physical Review Letters* 125.8, p. 088102.

Tlili, Sham, Estelle Gauquelin, Brigitte Li, Olivier Cardoso, Benoît Ladoux, Hélène Delanoë-Ayari, and François Graner (2018). "Collective cell migration without proliferation: density determines cell velocity and wave velocity". In: *Royal Society open science* 5.5, p. 172421.

Tlili, Sham, Cyprien Gay, François Graner, Philippe Marcq, François Molino, and Pierre Saramito (2015). "Colloquium: Mechanical formalisms for tissue dynamics". In: *The European Physical Journal E* 38.5, p. 33.

Trepat, Xavier, Michael R Wasserman, Thomas E Angelini, Emil Millet, David A Weitz, James P Butler, and Jeffrey J Fredberg (2009). "Physical forces during collective cell migration". In: *Nature physics* 5.6, p. 426.

Tsamados, Michel, Anne Tanguy, Chay Goldenberg, and Jean-Louis Barrat (2009). "Local elasticity map and plasticity in a model Lennard-Jones glass". In: *Physical Review E* 80.2, p. 026112.

Tyukodi, Botond (2016). "A depinning approach of amorphous plasticity and dewetting". PhD thesis. Paris 6.

Tyukodi, Botond, Claire A Lemarchand, Jesper S Hansen, and Damien Vandembroucq (2016a). "Finite-size effects in a model for plasticity of amorphous composites". In: *Physical Review E* 93.2, p. 023004.

Tyukodi, Botond, Sylvain Patinet, Stéphane Roux, and Damien Vandembroucq (2016b). "From depinning transition to plastic yielding of amorphous media: A soft-modes perspective". In: *Physical Review E* 93.6, p. 063005.

Tyukodi, Botond, Damien Vandembroucq, and Craig E Maloney (2018). "Diffusion in mesoscopic lattice models of amorphous plasticity". In: *Physical Review Letters* 121.14, p. 145501.

Van Hecke, Martin (2009). "Jamming of soft particles: geometry, mechanics, scaling and isostaticity". In: *Journal of Physics: Condensed Matter* 22.3, p. 033101.

Vasisht, Vishwas V and Emanuela Del Gado (2019). "A computational study of transient shear banding in soft jammed solids". In: *arXiv preprint arXiv:1908.03943*.

Vasisht, Vishwas V, Magali Le Goff, Kirsten Martens, and Jean-Louis Barrat (2018). "Permanent shear localization in dense disordered materials due to microscopic inertia". In: *preprint arXiv:1812.03948*.

Verdier, Claude, Jocelyn Etienne, Alain Duperray, and Luigi Preziosi (2009). "Rheological properties of biological materials". In: *Comptes Rendus Physique* 10.8, pp. 790–811.

Vicsek, Tamás, András Czirók, Eshel Ben-Jacob, Inon Cohen, and Ofer Shochet (1995). "Novel type of phase transition in a system of self-driven particles". In: *Physical review letters* 75.6, p. 1226.

Vignaud, Timothée, Hajer Ennomani, and Manuel Théry. In: ().

Vincent, Romaric, Elsa Bazellières, Carlos Pérez-González, Marina Uroz, Xavier Serra-Picamal, and Xavier Trepat (2015). "Active tensile modulus of an epithelial monolayer". In: *Physical review letters* 115.24, p. 248103.

Walton, Otis R and Robert L Braun (1986). "Viscosity, granular-temperature, and stress calculations for shearing assemblies of inelastic, frictional disks". In: *Journal of rheology* 30.5, pp. 949–980.

Weaire, Denis, Joseph D Barry, and Stefan Hutzler (2010). "The continuum theory of shear localization in two-dimensional foam". In: *Journal of Physics: Condensed Matter* 22.19, p. 193101.

Weeks, John D, David Chandler, and Hans C Andersen (1971). "Role of repulsive forces in determining the equilibrium structure of simple liquids". In: *The Journal of chemical physics* 54.12, pp. 5237–5247.

Wessel, Alok D, Maheshwar Gumalla, Jörg Grosshans, and Christoph F Schmidt (2015). "The mechanical properties of early Drosophila embryos measured by high-speed video microrheology". In: *Biophysical journal* 108.8, pp. 1899–1907.

Wisitsorasak, Apiwat and Peter G Wolynes (2017). "Dynamical theory of shear bands in structural glasses". In: *Proceedings of the National Academy of Sciences* 114.6, pp. 1287–1292.

Wortel, Geert, Olivier Dauchot, and Martin van Hecke (2016). "Criticality in vibrated frictional flows at a finite strain rate". In: *Physical review letters* 117.19, p. 198002.

Wortel, Geert H, Joshua A Dijksman, and Martin van Hecke (2014). "Rheology of weakly vibrated granular media". In: *Physical Review E* 89.1, p. 012202.

Wuttke, J, W Petry, and S Pouget (1996). "Structural relaxation in viscous glycerol: Coherent neutron scattering". In: *The Journal of chemical physics* 105.12, pp. 5177–5182.

Wyatt, Tom, Buzz Baum, and Guillaume Charras (2016). "A question of time: tissue adaptation to mechanical forces". In: *Current opinion in cell biology* 38, pp. 68–73.

Xie, Yuesong, Oleksandr G Kravchenko, R Byron Pipes, and Marisol Koslowski (2016). "Phase field modeling of damage in glassy polymers". In: *Journal of the Mechanics and Physics of Solids* 93, pp. 182–197.

Yeh, Wei-Ting, Misaki Ozawa, Kunimasa Miyazaki, Takeshi Kawasaki, and Ludovic Berthier (2020). "Glass stability changes the nature of yielding under oscillatory shear". In: *Physical Review Letters* 124.22, p. 225502.

Yerushalmi, Joseph, Stanley Katz, and Reuel Shinnar (1970). "The stability of steady shear flows of some viscoelastic fluids". In: *Chemical Engineering Science* 25.12, pp. 1891–1902.

Zehnder, Steven M, Melanie Suaris, Madisonclaire M Bellaire, and Thomas E Angelini (2015a). "Cell volume fluctuations in MDCK monolayers". In: *Biophysical journal* 108.2, pp. 247–250.

Zehnder, Steven M., Marina K. Wiatt, Juan M. Uruena, Alison C. Dunn, W. Gregory Sawyer, and Thomas E. Angelini (2015b). "Multicellular density fluctuations in epithelial monolayers". In: *Phys. Rev. E* 92 (3), p. 032729.

Zhang, Ge, Sean Ridout, and Andrea J Liu (2020). "Interplay of rearrangements, strain, and local structure during avalanche propagation". In: *arXiv preprint arXiv:2009.11414*.

Zhou, EH, X Trepat, CY Park, G Lenormand, MN Oliver, SM Mijailovich, C Hardin, DA Weitz, JP Butler, and JJ Fredberg (2009). "Universal behavior of the osmotically compressed cell and its analogy to the colloidal glass transition". In: *Proceedings of the National Academy of Sciences* 106.26, pp. 10632–10637.